



Universiteit
Antwerpen

DEPARTEMENT FYSICA, FACULTEIT WETENSCHAPPEN,
UNIVERSITEIT ANTWERPEN

**Quasiparticles in out-of-equilibrium
quantum systems:
correlations and equilibration**

**Quasideeltjes in kwantumsystemen uit evenwicht:
correlaties en equilibratie**

Author:

Mathias Van Regemortel

Supervisors:

Prof. Dr. Michiel Wouters
Dr. Iacopo Carusotto

Proefschrift voorgelegd ter verkrijging van de graad
doctor in de wetenschappen fysica

april 2018

Members of the jury

- Prof. Dr. Michiel Wouters – Universiteit Antwerpen
- Prof. Dr. Iacopo Carusotto – Università di Trento
- Prof. Dr. Jo Verbeeck – Universiteit Antwerpen
- Prof. Dr. François Peeters – Universiteit Antwerpen
- Prof. Dr. Cristiano Ciuti – Université Paris Diderot
- Prof. Dr. Sebastian Diehl – University of Cologne

This research is financially supported by the Research Foundation - Flanders (FWO) in the form of a PhD fellowship.

Dankwoord

Een onderzoek van meer dan vier jaar kan je uiteraard niet uitvoeren zonder de nodige hulp en steun van anderen. Naast de intense arbeid – ik hoor hier en daar wat gelach klinken – is er even goed nood aan ontspanning buiten het werk. Zowel in Antwerpen als in Trento, waar ik deel van dit werk heb uitgevoerd, heb ik altijd kunnen vertrouwen op anderen – zowel tijdens als na de werkuren. Ik zou dan ook graag een heleboel mensen willen bedanken zonder wie dit werk onmogelijk tot een goed einde gebracht zou zijn.

Om te beginnen dienen uiteraard mijn promotors vermeld te worden – twee in totaal, een in België en een in Italië. Met Michiel in Antwerpen heb ik steeds een uitstekende verstandhouding gehad. Zijn inzichten en ideeën hebben mij keer op keer verder geholpen; wanneer ik even het bos niet meer zag door de bomen, maar ook als ik wel op het juiste pad leek te zitten. Aan de andere kant van de Alpen, in Trento, kon ik dan weer onvoorwaardelijk rekenen op de steun van Iacopo. Ook zijn heldere inzichten en kritiek hebben mij telkens verder geholpen en door moeilijke punten getrokken. Verder heb ik ook veel hulp gehad van mijn medeauteurs Dries, Wim en Hadrien, en natuurlijk van zowel de groep in Antwerpen als in Trento. Als laatste wou ik ook graag de leden van mijn doctoraatsjury bedanken, vooral dan Sebastian en Cristiano, die helemaal zijn afgezakt naar Antwerpen om hun deskundige bedenkingen op mijn werk te kunnen uiten.

Buiten de werkuren heb ik dan weer telkens kunnen rekenen op anderen voor de nodige ontspanning. Op de eerste plaats dient hier natuurlijk mijn familie vermeld te worden, die mij gedurende de hele periode ondersteund heeft. In Antwerpen heb ik bovendien regelmatig mijn aandacht kunnen verzetten door vrijpostig muziek te spelen, waarvoor ik al mijn medemuzikanten wil bedanken. Daarnaast zijn ook mijn vrienden van groot belang geweest om dit werk tot een goed einde te kunnen brengen. Ook zou ik graag de mensen in Trento willen vermelden, die mij op regelmatige wijze de prachtige omgeving hebben laten zien en vaak te vinden waren om na het werk iets te eten of te drinken.

Een speciale dank gaat uit naar twee vrienden die ik onderweg verloren heb. An-Sophie, achtergebleven terwijl ze deed wat ze altijd wilde doen – de wereld rondreizen – en Seppe, die altijd wel op één of andere manier de wereld aan het rondreizen was, desondanks de omstandigheden.

Nederlandstalige samenvatting

De term *niet-evenwicht* heeft gedurende de laatste decenia een buitengewone interesse aangetrokken binnen de kwantummechanica. Zodoende tracht dit werk een kleine – maar betekenisvolle – bijdrage te leveren aan het grotere geheel van algemene kennis hieromtrent. In het bijzonder wordt de intrigerende rol van *quasideeltjes* uitgelicht; fictieve deeltjes die men invoert om de relevante fysica uit te drukken in termen van effectieve vrije deeltjes. In ons geval – maar dat hoeft niet altijd zo te zijn – zijn deze deeltjes het typerende product van een *kwadratische* benadering van het veeldeeltjesmodel, waarbij we de interacties tussen de deeltjes tot op tweede orde in storingstheorie meenemen. Aangezien de informatie die een volledige kwantumtoestand van veel deeltjes bevat ver boven het bevattingsvermogen van een simpele mens uitstijgt, gaat onze interesse in eerste instantie uit naar lokale observabelen die experimenteel gemeten kunnen worden, zoals *correlatiefuncties*, waarvan we verwachten dat ze na lange tijd *equilibreren* en een evenwichtswaarde vinden.

In het eerste deel onderzoeken we hoe de evolutie van een kwantummechanisch systeem bestaande uit veel deeltjes zich vertaalt in een verandering van correlatiefuncties wanneer het systeem plotseling uit evenwicht wordt gebracht. Hiertoe beschouwen we een eenvoudig kwadratisch model van deeltjes die op één dimensionaal rooster leven en waarvan we abrupt een parameter in het model veranderen. In het bijzonder wordt uitgelicht hoe een langedrachtspotentiaal (een afvallende machtswet) tussen de deeltjes de spreiding van de correlaties doorheen het rooster beïnvloedt. Merkwaardig genoeg besluiten we dat de langedrachtspotentiaal de mogelijkheid tot transmissie van informatie, direct terug te leiden tot de evolutie van correlatiefuncties, niet wezenlijk versnelt. Meer bepaald kunnen we vanuit het model een lichtkegel bepalen waarbinnen correlaties zich bewegen, met nagenoeg geen superluminale correcties. Een analyse met behulp van vrije quasideeltjes laat ons in dit geval toe om alle details van dit eenvoudige model te begrijpen en uit te werken.

We gaan dan verder in het tweede deel met het bestuderen van een volledige andere invulling van het concept niet-evenwicht. Meer precies ligt onze focus nu op fotonen in een microcaviteit, waar het continue gedreven en dissipatieve karakter van het systeem uitmondt in een stabiele toestand, van die aard dat de niet-evenwichtsomstandigheden uitdrukkelijk weerspiegeld worden. We lichten hier uit hoe een – eerder zwakke – interactie tussen fotonen in de microcaviteit kan leiden tot een licht niet-klassiek karakter van het licht dat eruit komt. Niet-klassiek wil hier zeggen dat we geen evenwaardige beschrijving in termen van klassieke

elektromechanica kunnen vinden om de geobserveerde fenomenen te verklaren en, bijgevolg, dat het uitdrukkelijke kwantummechanische karakter van individuele fotonen moet worden in rekening genomen. Vervolgens illustreren we hoe een selectie- en interferentie-experiment, opgesteld achter de microcaviteit, bij benadering een trein van individuele fotonen kan opleveren wanneer deze licht niet-klassieke toestand als input wordt gegeven. Ook hier laten effectieve quasideeltjes in de microcaviteit ons toe om de fysica van dit model – terug bij benadering kwadratisch – grondig door te lichten en uit te buiten.

Ten slotte dan, in het laatste deel, gaan we een stapje verder en zoeken we uit hoe interacties tussen quasideeltjes ons toelaten om fenomenen voorbij een vereenvoudigde kwadratische benadering van een veeldeeltjesmodel te bestuderen. Als eerste voorbeeld bekijken we terug een fotonisch model – deze keer niet één enkele caviteit, maar een hele resem aan elkaar gekoppelde caviteiten. De gedreven-dissipatieve stabiele toestand van deze keten vertoont dan kenmerkende tekenen van onderliggende interacties tussen de quasideeltjes. Deze bevinding is op zijn minst merkwaardig te noemen, want zeer algemene overwegingen, zoals de tweede hoofdwet van de thermodynamica, leiden ons ertoe om in een thermisch evenwicht te veronderstellen dat de evenwichtstoestand geen extra informatie kan bevatten over de dynamica van het systeem (maximale entropie). Dit brengt ons dan vanzelf bij de laatste studie, waar we bekijken hoe een gas van zwak interagerende atomen een evenwicht hervindt nadat plotseling de interacties tussen de deeltjes worden opgedreven. We besluiten dat het systeem doorheen twee afzonderlijke relaxatiefases gaat. Voor korte tijden kan het model opnieuw benaderd worden als kwadratisch, waardoor de dynamica van de vrije quasideeltjes zal leiden tot een eerste quasi-evenwicht, doorgaans de *prethermische* toestand genoemd. Veel later blijken dan de interacties tussen de quasideeltjes het systeem te beïnvloeden, waardoor een veel tragere beweging ontstaat naar de finale *thermische* toestand. We illustreren dat deze twee relaxatiemechanismen terug te vinden zijn in de evolutie van een lokale observabele, zoals de dichtheidscorrelaties, wat maakt dat deze fenomenologie relevant is voor hedendaagse experimenten met ultrakoude atomaire gassen.

Contents

1	Introduction	1
I	The creation of quasiparticles following a sudden quench	3
2	Quenches in conservative quantum systems	5
2.1	The initial state: the ground state of a many-body quantum system	6
2.2	The time evolution: how fast are distant points correlated?	7
2.3	Relaxation: back to thermal equilibrium?	8
3	A long-range interacting chain of fermions	11
3.1	The transverse-field Ising model	12
3.2	The long-range Kitaev model	13
3.2.1	The Hamiltonian	14
3.2.2	Solving the model: quasiparticles	15
3.2.3	The quasiparticle dispersion and group velocities	16
3.2.4	The ground state and initial state before the quench	18
3.3	The spreading of correlations following a quench	19
3.3.1	The Lieb-Robinson bound	20
3.3.2	A bound on correlation functions	21
3.4	Correlations in the long-range Kitaev chain	22
3.4.1	The short-range limit	23
3.4.2	The fate of long-range interactions	24
3.5	Living inside a finite subsystem	26
3.5.1	Building up the local density matrix	27
3.5.2	Entanglement entropy	29
3.5.3	Mutual information	33
3.6	Relaxation and integrability: the generalized Gibbs ensemble	35
3.6.1	The generalized Gibbs ensemble	36
3.6.2	Relaxation in quadratic models	37
3.7	Some relevant experiments	38

3.7.1	Spreading of correlations in trapped-ion lattices	38
3.7.2	The Lieb-Robinson bound with cold atoms	40
3.7.3	Integrability in a one-dimensional condensate	42
3.8	Conclusive remarks	43
II Engineering nonclassical light from quasiparticles		45
4	Photonic systems	47
4.1	Dissipative dynamics	47
4.1.1	The Lindblad master equation	47
4.1.2	Simulation of dissipative systems	49
4.2	Optical systems	50
4.2.1	Nonclassical light: photon antibunching	50
4.2.2	The photon blockade	52
4.2.3	The unconventional photon blockade	53
5	A quantum fluid of light inside a planar microcavity	57
5.1	Microcavities	57
5.1.1	Quality factor	58
5.1.2	The photon dispersion	59
5.1.3	Quantum-well excitons	59
5.2	Exciton-polaritons inside the quantum well	60
5.2.1	The free Hamiltonian	60
5.2.2	Adding interactions	62
5.2.3	Pumping	63
5.2.4	The full Hamiltonian	63
5.3	Coupling to a reservoir: the quantum Langevin equation	64
5.3.1	Including the reservoir: the total Hamiltonian	64
5.3.2	The quantum Langevin equation	65
5.4	The Bogoliubov approximation	66
5.4.1	The mean field equation	66
5.4.2	The evolution of the quantum fluctuations	67
5.4.3	The quadratic correlation functions in the steady state	69
6	Constructing Gaussian states from the output of a planar microcavity	71
6.1	The unconventional photon blockade with Gaussian states	71
6.1.1	Gaussian states: a brief overview	72
6.1.2	Antibunching in Gaussian states	74
6.2	Engineering squeezed coherent output states from a microcavity	74
6.2.1	The setup: selecting and interfering momentum modes	76

6.2.2	Squeezing in the output state	77
6.2.3	Optimizing the antibunched emission	79
6.3	Manipulating and probing photon statistics with a wide-aperture lens . . .	81
6.3.1	Intensity correlations in position space	82
6.3.2	The density-density correlation function	82
6.3.3	Lightcone-like correlations in the high-density regime	83
6.3.4	Spatial pattern formation with diffusive modes	86
6.4	Conclusive remarks	87
III Interacting quasiparticles: Beliaev-Landau scattering		89
7	Beliaev-Landau scattering	91
7.1	The decay of a phonon	91
7.2	Equilibrium vs. out-of-equilibrium	94
8	Interacting quasiparticles in a cavity array	95
8.1	Cavity arrays	95
8.1.1	Semiconductor microcavities	96
8.1.2	Superconducting circuits	97
8.2	The model	98
8.2.1	The Hamiltonian of a cavity array	99
8.2.2	Dissipative photon losses	99
8.2.3	Expanding the photon field operator	100
8.2.4	Free quasiparticles: the Bogoliubov approximation	101
8.3	The truncated Wigner approximation	103
8.3.1	The Wigner quasiprobability distribution	103
8.3.2	Truncating the equation of motion	105
8.3.3	A TWA simulation of the cavity array	106
8.4	Quasiparticle interactions: Beliaev-Landau channels	108
8.4.1	Resonant scattering channels	108
8.4.2	The origin of the breakdown of TWA	109
8.5	Constructing a hierarchy of correlation functions	111
8.5.1	Deriving the hierarchy	111
8.5.2	The momentum distribution in the HOC scheme	114
8.5.3	The third-order correlation functions	115
8.6	The footprint of spontaneous Beliaev-Landau scattering in an array of semi-conductor micropillars	116
8.6.1	Measuring the momentum distribution	118
8.6.2	The role of disorder	119
8.6.3	Measuring the third-order correlator	120

9	Prethermalization to thermalization crossover following a quench in a weakly interacting Bose gas	121
9.1	The weakly interacting Bose gas	121
9.1.1	The full Hamiltonian	122
9.1.2	Hamiltonian in Bogoliubov basis	124
9.2	The approximately integrable dynamics	127
9.2.1	An interaction ramp: the dynamical Casimir effect	127
9.2.2	Prethermalization	129
9.3	Constructing a hierarchy of correlation functions	130
9.3.1	Equation of motion of the quasiparticle operator	130
9.3.2	The hierarchy of correlations	131
9.4	The kinetic description of the problem	133
9.4.1	Deriving the kinetic equations for the quasiparticles	133
9.4.2	Approaching a thermal ensemble	135
9.5	The evolution of the density correlations	135
9.5.1	The density correlations	136
9.5.2	The two-stage relaxation of local observables	137
9.6	Conclusive remarks and outlook	137
10	Final discussion and open questions	141
A	Extra info on the long-range Kitaev chain	147
A.1	Relaxation to the GGE	147
A.2	Derivation of the correlation function	148
B	Extra info on exciton-polaritons in planar microcavities	149
B.1	The quantum Langevin equation	149
B.2	The Bogoliubov transformation revisited	151
B.2.1	Evolution of the quasiparticle operators	151
B.2.2	Regular modes	151
B.2.3	Diffusive-like modes	152
B.3	The time evolution of the particle operators	153
B.4	Main noise sources	153
B.4.1	Disorder	154
B.4.2	Pure dephasing	155
B.4.3	Other noise sources	155
C	Details on the construction of a hierarchy of equations	157
C.1	Derivation of the correlation hierarchy for the cavity array	157
C.2	Different truncation schemes and comparison	159

Contents

C.3	Discretization of the hierarchy of correlation functions in three spatial dimensions	165
C.3.1	The kinetic equations	165
C.3.2	Discretization of the full hierarchy	165
C.4	Comparison between the hierarchy and the kinetic equations	166
C.4.1	The quasiparticle occupation numbers	167
C.4.2	The density-density correlations at short times	167

Chapter 1

Introduction

Out-of-equilibrium is a notion that has attracted an intense attention in quantum mechanics over the last decades, in theory as well as in experiment. As such, this thesis aims to add a – small but meaningful – fragment to the common knowledge of the question how a quantum many-body system behaves in a nonequilibrium scenario. As a central guideline throughout this work, the role of *quasiparticles* will be highlighted; fictitious particles devised to capture the relevant degrees of freedom of a model. While the information contained in a full quantum many-body wave function is generally vast and far beyond the possible understanding of a human being, our primary focus lies on the dynamics of few-body observables – such as *correlations* – and how they may seemingly approach *equilibration*.

For this work, we generally distinguish between two different notions of out-of-equilibrium. In a first part, we deal with the unitary dynamics of a many-body quantum system suddenly kicked out of equilibrium; a *quantum quench*. Here, the whole system is brought out of equilibrium at a *specific* instant in time, after which the ensuing dynamics is conservative, meaning that the total energy of the system is a conserved quantity. We then continue in a second part with *open quantum systems*; systems that are continuously held out of equilibrium at *all* times through a nonnegligible interaction with their environment. In particular, we will concentrate on *photonic* platforms, where the coupling with the environment relates to the continuous injection and escape processes of photons in the system.

Part I of this thesis is concentrated on the behavior of spinless fermions living inside a one-dimensional lattice. After an abrupt quench of some global parameter in the model, these fermions start to behave in a nontrivial way and cause an overall time-dependence of correlation functions. It is then illustrated how quasiparticles emerge after the quench and encode information that is carried through the chain. Our aim is to investigate how the range of the interaction potential between the fermions affects the general properties of information propagation through the chain, leading to the eventual relaxation of local observables when a new equilibrium is found.

In Part II we move our attention to the nonequilibrium nature of photonic systems. It

is studied how quasiparticles arise in a *quantum fluid of light* inside a planar microcavity device. The continuous driving and dissipation of the system establishes a nonequilibrium population of quasiparticles in the steady state. We illustrate how these quasiparticles are responsible for the generation of output light with a slightly *nonclassical* nature. Nonclassical, in this context, means that the resulting light bears features that cannot be understood from the classical wave picture of electromagnetism and, consequently, that the individual particle character of the photons needs to be considered. Our work then focuses on how we can amplify these nonclassical features by orders of magnitude with a selection and interference scheme placed *after* the cavity, thereby rendering the output light strongly nonclassical.

Finally, in Part III we study how we can go beyond a standard Gaussian approximation of a quantum many-body system by taking into account interactions among the emergent quasiparticles; traditionally called *Beliaev-Landau collisions*. We start by considering a chain of coupled cavities, in which photons can hop from one cavity to its neighbour. It is then illustrated how we can witness footprints of the quasiparticle interactions by measuring observables in the steady state of the driven-dissipative chain; we attribute this to the strong nonequilibrium nature of the setting. We then move on with analyzing how the same collisions drive a gas of trapped bosonic atoms towards a thermal equilibrium after an abrupt quench of the interparticle interaction strength.

Part I

The creation of quasiparticles following a sudden quench

Chapter 2

Quenches in conservative quantum systems

In this part, we deal with the unitary dynamics of a quantum many-body system after kicking it abruptly out of equilibrium. Usually, it is then studied how the nonequilibrium dynamics generates a time-dependence of correlation functions, which eventually approach a new equilibrium after a relaxation stage. We will briefly review the common concepts of this field of research in this chapter, before we continue with the theoretical analysis of a chain of long-range interacting fermions in Chapter 3.

In general, we consider a quantum system that is at rest under Hamiltonian $\hat{H}(g)$, where g is some coupling that we can tune. The protocol for the quench is then the following.

1. Prepare the quantum system (in total isolation) as an equilibrium state of Hamiltonian $\hat{H}(g_i)$. Here, equilibrium means a thermal equilibrium and, if not specified otherwise, we assume temperature to be zero, such that the system is in the ground state $|\Psi_0\rangle$ of $\hat{H}(g_i)$.
2. Abruptly make a change $\hat{H}(g_i) \rightarrow \hat{H}(g_f)$, fast enough so that the system cannot respond in time. The key idea is that this change occurs *instantaneously*, i.e. faster than any relevant time scale¹. At any rate, the system is no longer at equilibrium under the new Hamiltonian $\hat{H}(g_f)$ and will therefore evolve non-trivially according to $|\Psi(t)\rangle = e^{-i\hat{H}(g_f)t/\hbar}|\Psi_0\rangle$.
3. As the system evolves in time, the dynamics of observables $\langle \hat{O} \rangle_t$ (usually few-body) in the quantum system is followed.

Typical questions that present themselves in this context are of the following kind:

- *How much time does operator \hat{O} need in order to feel that the system was changed by the quench?*

¹Here we implicitly make some assumptions about the spectrum of the Hamiltonian. We will come back to this later.

- At late times, does a few-body observable $\langle \hat{O} \rangle_t$ become stationary?
- If so, can these equilibrium values in any way be associated with a new equilibrium ensemble?

In this thesis, we study quantum quenches in two different systems. We investigate in Chapter 3 how the range of interactions affects the dynamics of quantum lattice models after an abrupt quench. A toy model of long-range interacting fermions on a chain will serve as a guide to outline the common concepts in this context. In Chapter 9, at the very end of this work, we will then continue with studying the dynamics in a weakly interacting gas of ultracold bosonic particles after an abrupt ramp of the interparticle interaction strength. Today, this is an extremely relevant experimental setup and our results will therefore be focused on measurable observables.

As a central guide, we aim to highlight the special role of *quasiparticles*, effective particles that spontaneously arise after a quench, to understand the nonequilibrium quantum dynamics of a many-body quantum system. We refer the interested reader to Ref. [1] for a broad overview on quench physics and a summary of important recent experiments.

2.1 The initial state: the ground state of a many-body quantum system

Before we abruptly change a coupling parameter in the many-body Hamiltonian for the quench, we assume that the system has had sufficient time to equilibrate. Based on very general arguments, such as the second law of thermodynamics, we are then led to propose a thermal ensemble for the many-body density matrix

$$\hat{\rho} \sim \exp \{ - \beta \hat{H} \}, \quad (2.1)$$

with \hat{H} the many-body Hamiltonian and $\beta = 1/k_B T$ the inverse temperature. In the limit of zero temperature, or $\beta \rightarrow \infty$, we will find the system in the *ground state* of \hat{H} .

Typical many-body Hamiltonians in the context of condensed-matter physics and quantum-information science are inherently *local*. When an underlying lattice structure is assigned to the system, the interaction terms between different degrees of freedom are often restricted to a domain of neighboring sites only. The local structure of interactions is then directly reflected in the correlation functions from the ground state. Provided the Hamiltonian is not *critical*, which means that there is a nonzero gap between the ground-state energy and the first excited level, a correlation function between two distant points in the lattice always exhibits an exponentially decaying behavior at large distances [2].

Furthermore, this has profound implications on the scaling of entropy in the ground state of a short-range interacting Hamiltonian. While a system at thermal equilibrium has a *volume* law for entropy, in accordance with our intuitive picture that entropy is an extensive thermodynamic quantity, the entropy of a ground state generally follows an *area*

2.2. The time evolution: how fast are distant points correlated?

law [3, 4]: when we separate a subregion from the rest of the lattice, the entanglement entropy of this block merely scales with its area, not with its volume. This observation has a profound impact on various – seemingly unrelated – fields in physics, such as condensed matter physics, information theory and black hole physics, where it is often referred to as the *holographic principle* – all information of a quantum system is encoded on its surface.

The specific structure of correlation functions in the ground state has deep implications on the difficulty to simulate a quantum system on a classical computer. When correlations decay exponentially and the entanglement entropy of a block assumes an area law, the true quantum state can always be approximated with a *matrix product state*, with an exponential convergence in the bond dimension of the matrices that build up the state. The *density matrix renormalization group* (DMRG) provides a variational method to determine the ground state of a quantum many-body Hamiltonian within the class of matrix product states [5, 6]. We refer to Refs. [7, 8] for excellent review articles on this topic.

While the area law is expected to emerge for any non-critical Hamiltonian with finite-range interactions, we explicitly seek to investigate the influence of a long-range (power-law) interaction potential upon a many-body quantum state. In this case, an exponential decay of correlation functions may dominate at short distances, but the general behavior at large distances is usually algebraic, reflecting the underlying structure of interactions [9, 10].

2.2 The time evolution: how fast are distant points correlated?

Once a coupling in the Hamiltonian is abruptly quenched, the quantum system is suddenly brought out of equilibrium and starts to evolve nontrivially. We, as observer or experimenter, want to gain information from the system by performing measurements on it. Nevertheless, the probing tools that we have at hand are limited and usually restricted to measurements of a handful of degrees of freedom at a time, while the ones that build up the whole system are vast and beyond reach. Consequently, categorizing the coherence that is contained and preserved in the evolving wavefunction of the entire many-body quantum state requires far more resources than an experimenter could potentially dream of.

For this reason, our main interest lies in studying the evolution of typical *few-body* observables, generated from the evolving quantum many-body wavefunction. Of particular importance are *correlation functions* between distant points in the system. How long does it take for point A to become correlated with point B when they are a distance d away from each other? In an attempt to address this question, a series of rigid results has been established over the years, which have turned out to revolutionize our understanding of many-body quantum dynamics at a very general level.

The first statement in this context was proposed and proven by Elliott H. Lieb and Derek Robinson in 1972 and commonly goes under the name of the *Lieb-Robinson* bound

today. They considered a lattice composed of spin-like constituents at each site. Formulated in terms of a bound on the commutator of two observables, one situated at point A and the other at point B , they succeeded in proving that a notion of locality is emergent in a many-body quantum system with short-range interactions, even without imposing Lorentz invariance. They found that the effect of a local perturbation cannot be measured elsewhere in the lattice outside an effective *lightcone*, with a characteristic velocity that can be derived from the Hamiltonian spectrum. In later works, this bound was shown to have severe implications on the development of correlations between two separate points in a quantum system [11] and the scaling of entanglement entropy after a quench [12].

Part of this work aims to investigate Lieb-Robinson-like bounds in quantum systems with *long-range* interactions. Several attempts have been made to prove similar bounds for lattice models with constituents that interact with a power-law potential. In a first work by Hastings [2], it was found that such systems are inherently subject to a *logarithmic* lightcone, suggesting that the causal region may expand exponentially fast in time, rather than linearly. Nevertheless, this bound was reconsidered in a later stage, where they concluded that the lightcone follows a power-law behavior at most, provided the power-law exponent of interactions is sufficiently high [9].

In any case, a bound is merely a bound and it is never clear beforehand whether a particular observable in a specific system approaches it or not. With this work, we seek to shed a light on this problem by analyzing the correlations in a fermionic toy model with long-range interactions. We can anticipate at this point that a linearly growing lightcone is found within good approximation, in spite of the long-range nature of interactions. As far as we are aware, it is still an open question which systems approach the established Lieb-Robinson bound for long-range interacting lattice models and which give rise to an approximately linear lightcone.

2.3 Relaxation: back to thermal equilibrium?

Ever since the development of quantum mechanics in the early days, a central question has been how unitary time evolution of a quantum state of many particles may generate a seemingly thermal ensemble in the long-time limit. On the level of the density matrix that is associated to the system, this means that it must evolve somehow from a pure state $\hat{\rho}(t) = |\psi(t)\rangle\langle\psi(t)|$, with $|\psi(t)\rangle$ the quantum state, to a formulation for the density matrix of form (2.1), at least in the eyes of an observer with limited tools to probe the system.

Essentially, this convergence must relate to two different phenomena. First of all, the time dependence of the density matrix has to vanish in order to produce an apparent *stationary ensemble*. It is not difficult to see that this must be the case by expanding the many-body wave function in the basis of eigenstates of the Hamiltonian; $|\psi(t)\rangle = \sum_j c_j e^{-i\omega_j t} |\hat{\phi}_j\rangle$, with $\hbar\omega_j$ an energy level of \hat{H} and $|\hat{\phi}_j\rangle$ the corresponding eigenstate.

2.3. Relaxation: back to thermal equilibrium?

The expectation value of a typical few-body observable $\hat{A}(t)$ can then be expressed as

$$\langle \hat{A}(t) \rangle = \langle \psi(t) | \hat{A} | \psi(t) \rangle = \sum_{j,l} c_j^* c_l e^{i(\omega_j - \omega_l)t} A_{j,l}, \quad (2.2)$$

where we used the notation $A_{j,l} = \langle \phi_j | \hat{A} | \phi_l \rangle$. In the absence of degeneracies in the Hamiltonian spectrum² the long-time average of $\langle \hat{A}(t) \rangle$ is then expected to converge to

$$\bar{A} = \lim_{t \rightarrow \infty} \frac{1}{t} \int_0^t dt \langle \hat{A}(t) \rangle = \sum_j |c_j|^2 A_{j,j}. \quad (2.3)$$

This is also the expectation value of \hat{A} predicted in the *diagonal ensemble* [13].

According to the *eigenstate thermalization hypothesis* (ETH) the $A_{j,j}$ are expected to be approximately constant³ inside the energy window $E + \Delta E$, with $E = \langle \hat{H} \rangle$ the total energy of the system and ΔE the energy variance, which dominates the sum in (2.3) [14, 15]. Therefore, ETH states the equality of the time-averaged expectation value (2.3) and the predicted value in the *microcanonical* ensemble, provided the system is sufficiently large. The hypothesis has been numerically verified for a variety of chaotic quantum systems [16, 17].

Since it relies on the assumption of *ergodicity*, a class of systems where ETH is not expected to hold are *integrable* quantum systems. Here, the system contains an extensive number of conserved quantities besides the thermodynamic energy, such that the motion of the many-body quantum system is constrained to a small subspace of the entire Hilbert space. However, in the same spirit as ETH, a *representative* eigenstate of the integrable Hamiltonian can be identified, which produces the same expectation values for *local* observables as the relevant stationary ensemble [18]. The ensemble, in turn, is in this case not given by a Gibbs or microcanonical ensemble, but by a *generalized Gibbs ensemble* that contains all the conserved quantities \hat{I} in its definition [19]. Following very general arguments, as originally postulated in the seminal paper by E.T. Jaynes [20], this ensemble is then found as

$$\hat{\rho}_{\text{GGE}} \propto \exp \left\{ - \sum_k \lambda_k \hat{I}_k \right\}. \quad (2.4)$$

Here, the \hat{I}_k are independent constants of motion of the Hamiltonian, such that $[\hat{H}, \hat{I}_k] = 0$ and $[\hat{I}_k, \hat{I}_j] = 0$. The λ_k are Lagrange multipliers that have to be fixed from the initial pure quantum state. Interestingly, they can be regarded as effective inverse temperatures for *each* conserved quantity separately.

Another way to define an integrable quantum system relies on the *level statistics* of a quantum many-body Hamiltonian: how many energy levels do we find inside an energy interval δE ? When a system is not integrable, and therefore is expected to satisfy ETH,

²Degeneracies in an interacting many-body problem are extremely ungeneric and must be related to additional symmetries.

³Actually the statement is that $A_{j+1,j+1} - A_{j,j}$ is exponentially small in system size.

the Hamiltonian can be seen as a random matrix with corresponding level statistics. An integrable quantum system, on the other hand, is typically characterized by Poissonian level statistics [21]. In this sense, also *many-body localized* quantum systems, systems where a high amount of disorder prevents thermalization, exhibit a form of integrability [22].

In this part, we study relaxation in a toy model of long-range interacting fermions on a chain. We conclude in Sec. 3.6 that the system does not thermalize, but that it indeed approaches a state described by a generalized Gibbs ensemble. At the very end of this thesis, in Chapter 9, we study how a weakly interacting bosonic gas first relaxes to a *prethermal state* due to the approximate integrability of the model. On a much longer time scale, the integrability is broken and higher-order particle interactions lead the system to the final state: a thermal ensemble.

Chapter 3

A long-range interacting chain of fermions

In this chapter, we exploit an exactly solvable model of fermions living on a 1D lattice to guide us through the key concepts of quenches in many-body quantum systems. In particular, we will show interest in how the long-range nature of interactions among the fermions influences the subsequent dynamics in the system. While the Lieb-Robinson bound for short-range interacting lattice models poses severe restrictions on the development of correlations, the fate of a long-range interaction potential remains obscure and is – in part for this reason – currently a trending topic in the community.

Ironically, the discussion actually starts with the definition of long-range interactions itself. In the literature you can find many interpretations, but usually the criterion separating a short-range from a long-range interaction is expressed through the two-body interaction potential, which is taken to follow a power-law decay $V(r) \sim r^{-\alpha}$ [23].

The two most common criteria applied to distinguish a long-range interaction potential are then

- $\alpha < D$, with D the dimension of the system: In this case the system's thermodynamic energy is not *additive*, we will come back to this later.
- $V(r)$ falls off slower than exponentially, meaning that any power-law interaction is considered long-ranged in nature.

In practice, we will mainly apply the first criterion to make the distinction between short and long range. We will, however, often explicitly take the limit $\alpha \rightarrow \infty$, which can be seen as the second criterion, to study short-range features.

To set the stage, we first discuss a short-range interacting model (according to the second criterion) of spins on a lattice, which will then naturally lead us to the central model of this chapter, the *long-range Kitaev chain*.

3.1 The transverse-field Ising model

Formulated and solved for the first time in 1970 by Pfeuty [24], the *transverse-field Ising* model bears a long history of intensive research. Probably, the reason why it has become such a widely studied model is twofold [25]. First of all, as we will see in a bit, it is exactly solvable, in the sense that the ground state and all elementary excitations can be found analytically. Second, the model can be regarded as a simplified theory to describe magnetism on a quantum mechanical level. In particular, the ground state shows a *quantum phase transition* from a paramagnetic to a ferromagnetic phase with long-range order upon varying the external magnetic field [26].

The system here is composed of L spins positioned on a 1D lattice, with only nearest-neighbor interactions between them. The Hamiltonian of the model is then formulated as

$$\hat{H}_{TFI} = -t \sum_{j=1}^L \hat{S}_j^x \hat{S}_{j+1}^x - h \sum_{j=1}^L \hat{S}_j^z, \quad (3.1)$$

with spin operators $\hat{S}_j^\alpha = \frac{1}{2} \hat{\sigma}_j^\alpha$ and the Pauli matrices

$$\hat{\sigma}^x = \begin{pmatrix} 0 & 1 \\ 1 & 0 \end{pmatrix}, \quad \hat{\sigma}^y = \begin{pmatrix} 0 & -i \\ i & 0 \end{pmatrix}, \quad \hat{\sigma}^z = \begin{pmatrix} 1 & 0 \\ 0 & -1 \end{pmatrix}. \quad (3.2)$$

Here, we see that the spins interact with each other according to their spin along the x -axis, while the magnetic field is oriented in the z -direction, in the transverse plane – hence the name.

A few years before Pfeuty formulated his model, Mattis, Lieb and Schultz [27] had discovered that a certain class of 1D spin systems allowed for an exact solution by mapping the spin operators onto fermionic ones. For this they needed to associate a fermion operator with a spin operator on each lattice site j through the following correspondences

$$\hat{\sigma}_j^- \leftrightarrow \hat{c}_j, \quad \hat{\sigma}_j^+ \leftrightarrow \hat{c}_j^\dagger, \quad \hat{\sigma}_j^z \leftrightarrow 2\hat{c}_j^\dagger \hat{c}_j - 1, \quad (3.3)$$

with $\hat{\sigma}_j^\pm = \hat{S}_j^x \pm i\hat{S}_j^y$ the raising and lowering operator of spin j . We therefore want to associate the absence or presence of a fermion on lattice site j with a spin up or down.

Yet, there is one problem if we want to implement these associations directly in Hamiltonian (3.1); spins and fermions do *not* follow the same canonical commutation relations. While the on-site commutations are already reproduced correctly, $\{\hat{\sigma}_j^+, \hat{\sigma}_j^-\} = \{\hat{c}_j^\dagger, \hat{c}_j\} = 1$, we see that the difficulty comes with the commutation relations at different sites: $[\hat{c}_j^\dagger, \hat{c}_l] \neq [\hat{\sigma}_j^+, \hat{\sigma}_l^-] = 0$ when $j \neq l$.

We can remedy this by introducing the *string* operator $\hat{S}_j = \exp\left(-i\pi \sum_{l=1}^{j-1} \hat{c}_l^\dagger \hat{c}_l\right)$, which essentially counts all the fermions sitting on the left of site j and then gives a sign ‘+’ or ‘−’ depending on whether that number is even or odd. Notice that this operator is highly non-local and that boundary conditions as well as the choice of site labeling (in particular in

3.2. The long-range Kitaev model

higher dimensions [28]) may be important. However, upon representing the spin operators as

$$\hat{\sigma}_j^+ = \hat{S}_j \hat{c}_j, \quad \hat{\sigma}_j^- = \hat{S}_j^\dagger \hat{c}_j^\dagger, \quad \hat{\sigma}_j^z = 2\hat{c}_j^\dagger \hat{c}_j - 1, \quad (3.4)$$

it is easy to verify that $[\hat{\sigma}_j^+, \hat{\sigma}_l^-] = 0$. In 1928 this transformation was introduced by Jordan and Wigner and bears their names since [29].

Eventually, the nonlocal string operator magically cancels everywhere except at the boundaries when we perform these substitutions in (3.1). Upon taking a large enough system, such that we can neglect the boundary term, and after a shift of ground-state energy, we find a fermionic Hamiltonian that can be formulated as [30]

$$\begin{aligned} \hat{H}_{\text{SRK}} = & -J \sum_{j=1}^L \left(\hat{c}_j^\dagger \hat{c}_{j+1} + \hat{c}_{j+1}^\dagger \hat{c}_j \right) + \Delta \sum_{j=1}^L \left(\hat{c}_j \hat{c}_{j+1} + \hat{c}_{j+1}^\dagger \hat{c}_j^\dagger \right) \\ & - \mu \sum_{j=1}^L \left(\hat{c}_j^\dagger \hat{c}_j - \frac{1}{2} \right). \end{aligned} \quad (3.5)$$

Traditionally, the model with Hamiltonian (3.5) is referred to as the *Kitaev chain* [31]. We have now ended up with a number of spinless fermions living on a lattice, which are represented by the creation operators \hat{c}_j and obey fermionic commutation relations

$$\{\hat{c}_j, \hat{c}_l^\dagger\} = \delta_{j,l} \quad \{\hat{c}_j, \hat{c}_l\} = \{\hat{c}_j^\dagger, \hat{c}_l^\dagger\} = 0. \quad (3.6)$$

The fermions can hop from a site j to the neighbouring site $j + 1$ and vice versa with a tunneling rate J . Additionally, there is a chance to make two fermions vanish when they are sitting next to each other, or to create a pair of two fermions on two adjacent sites with a rate Δ . In the context of superconductivity this can be seen – at least on mean-field level – as two fermions being converted into a Cooper pair or, the other way around, a Cooper pair breaking up into two separate fermions.

As we will show in the following, the model is readily solved starting from (3.5). A few decades of intensive investigation of this model have yielded a plethora of (semi)analytical results for all sorts of physical quantities, so that it has provided an invaluable amount of information on the nature of many-body quantum mechanics. Throughout this chapter, we will therefore frequently refer back to long-established results of the transverse-field Ising model (or the Kitaev model, as you like, since they are practically equivalent) to situate our results within the existing literature.

3.2 The long-range Kitaev model

Although long-range interactions are omnipresent in nature – think of the Coulomb interaction, gravity, Van der Waals etc. – they are often not perceived as such. The reason is that the underlying long-range nature of interactions is usually *screened* in realistic materials. For the case of Coulomb interactions in a metal, this can be pictured as an electron that

pushes away other nearby electrons, thereby leaving a positively charged cloud around it coming from the positive lattice background. At large distances, the negative charge of the electron is then largely canceled, so that it gives rise to a *Yukawa*-like potential for electron-electron interactions, which is short-ranged in nature because it decays exponentially. This story, of course, does not hold for gravitating systems, as there is no oppositely charged background, but generally we do not need quantum mechanics to describe the interactions between massive bodies¹.

The recent interest in long-range interacting quantum systems, however, stems from the development of a number of experimental platforms where they are naturally simulated. Most notably, experiments with trapped ions can be interpreted as *quantum simulators* for long-range interacting spin lattices [32]. We refer the interested reader to Sec. 3.7.1, where we briefly explain the setup and review some recent experiments.

By applying the Jordan-Wigner transformation to the transverse-field Ising model, we were able to transform a short-range interacting spin model into a short-range fermionic model. As expected, the string operators from (3.4) turn into a total mess as soon as interactions between the spins in the chain are not only between nearest neighbors. One therefore has to resort to numerical simulations to study the ground state or dynamical properties of a lattice of long-range interacting spins.

We can, however, attempt to shed a light on the nature of long-range interacting quantum systems by looking into a fermionic model that exhibits some long-range features. As we are coming to, quadratic fermionic models, such as (3.5), are solved in a few steps, making them an ideal playground to investigate the principles lying at the heart of various sophisticated quantum phenomena. We would like to emphasize that the model that we are about to formulate here is merely a toy model and has – as far as we are aware – no immediate experimental relevance. Yet, its simplicity permits us to illuminate many features of nonequilibrium quantum dynamics in an elegant way, with the additional freedom to examine the impact of a long-range interaction potential.

3.2.1 The Hamiltonian

Starting from (3.5) we would like to introduce a long-range interaction potential between the fermions. To this end, we have opted to investigate the impact of a long-range *pairing* interaction [33]. Notice that this was merely a choice, as one could also consider a long-range *hopping* term, which was the topic of Ref. [34].

The *long-range Kitaev model*, the central model of this chapter, is then formulated in

¹Quantum gravity is another story, but we are not going into that for the purposes of this work.

3.2. The long-range Kitaev model

terms of the Hamiltonian

$$\begin{aligned} \hat{H}_{\text{LRK}}(J, \mu, \Delta) = & -J \sum_{j=1}^L \left(\hat{c}_j^\dagger \hat{c}_{j+1} + \hat{c}_{j+1}^\dagger \hat{c}_j \right) - \mu \sum_{j=1}^L \left(\hat{c}_j^\dagger \hat{c}_j - \frac{1}{2} \right) \\ & + \Delta \sum_{j=1}^L \sum_{l=1}^{j-1} \left(\frac{\hat{c}_j \hat{c}_l + \hat{c}_l^\dagger \hat{c}_j^\dagger}{|l-j|^\alpha} \right). \end{aligned} \quad (3.7)$$

The first term, scaling with J , describes the hopping of a fermion that sits on site j to the adjacent site $j+1$ and vice versa. The second term introduces an effective chemical potential μ and the last term, scaling with Δ , represents a *long-range* pairing interaction. It tells us that fermions interact with a strength Δ/r^α when they are sitting $r = |l-j|$ sites apart from each other. It is clear that when we send $\alpha \rightarrow \infty$, the pairing interaction reduces to nearest neighbours only and we *exactly* recover the *short-range* Kitaev model, presented in (3.5). Consequently, the parameter α quantifies the long-range nature of our model and it interpolates neatly between a short-range ($\alpha \rightarrow \infty$) and an all-to-all interaction ($\alpha \rightarrow 0$). In practice, we set the parameters $J = \Delta = 1$ and we will study the model in the thermodynamic limit, by sending $L \rightarrow \infty$ – although we will explicitly come back to this a couple of times.

3.2.2 Solving the model: quasiparticles

Being *exactly* solvable, this toy model provides an ideal setting to investigate the impact of a long-range interaction potential upon the nonequilibrium dynamics of a many-body quantum system. Exact – in this case – means that we can find a new set of fermions, which we represent by the operators $\hat{\xi}_q$, that behave as if they were free particles under \hat{H}_{LRK} . Here the index $q = 1, \dots, L$ labels the basis of the new operators. In a few steps we can find what they look like.

We first start by expressing \hat{H}_{LRK} in momentum space by introducing the operators

$$\hat{c}_k = \frac{1}{\sqrt{L}} \sum_{l=1}^L e^{-ikl} \hat{c}_l, \quad \hat{c}_k^\dagger = \frac{1}{\sqrt{L}} \sum_{l=1}^L e^{ikl} \hat{c}_l^\dagger, \quad (3.8)$$

with lattice momentum $k = 2\pi(n+1/2)/L$. After some algebra, the transformed Hamiltonian is then found as

$$H_{\text{LRK}} = \sum_k \left[-(\cos k + \mu) \hat{c}_k^\dagger \hat{c}_k + f^{(\alpha)}(k) \left(\hat{c}_k \hat{c}_{-k} + \hat{c}_{-k}^\dagger \hat{c}_k^\dagger \right) \right],$$

for which we have introduced the family of functions $f^{(\alpha)}(k) = \sum_{u=1}^L \sin ku / u^\alpha$.

The next step consists of introducing new momentum-space operators via a *Bogoliubov transformation*, which mixes the creation and annihilation operators for a momentum mode k ,

$$\hat{c}_k = u_k \hat{\xi}_k - iv_{-k} \hat{\xi}_{-k}^\dagger, \quad \hat{c}_k^\dagger = u_k \hat{\xi}_k^\dagger + iv_{-k} \hat{\xi}_{-k}. \quad (3.9)$$

One immediately concludes that the transformation coefficients must be expressed as a rotation, $u_k = \cos(\theta_k/2)$ and $v_k = \sin(\theta_k/2)$, in order to preserve the fermionic commutation relations from (3.6) for the set of $\hat{\xi}_k$ operators. Upon choosing the rotation angle as

$$\tan \theta_k = -f^{(\alpha)}(k)/(\mu + \cos k), \quad (3.10)$$

we finally arrive at

$$\hat{H}_{\text{LRK}} = E_0 + \sum_k \epsilon(k) \hat{\xi}_k^\dagger \hat{\xi}_k. \quad (3.11)$$

Here is a first example of how the introduction of a set of *quasiparticles* permits us to find an – in this case – exact solution to a nontrivial interacting quantum many-body problem. Recall that we started from a Hamiltonian with long-range interactions and that with a few linear transformations we ended up with a set of new fermions, represented by the $\hat{\xi}_k$ operators, which behave as if they were free under the dynamics of \hat{H}_{LRK} .

3.2.3 The quasiparticle dispersion and group velocities

As the quasiparticles travel through the chain with a lattice momentum k , they carry an intrinsic energy with them. The relation between quasiparticle energy and momentum is given by a dispersion relation, which we read off from the spectrum of (3.11) [10]

$$\epsilon(k) = \sqrt{(\cos k + \mu)^2 + f^{(\alpha)}(k)^2}. \quad (3.12)$$

In Fig. 3.1(a-b) the dispersion relation (3.12) is shown for $\mu = \pm 1$ and for different ranges of pairing interactions, as set by α .

By sending $\alpha \rightarrow \infty$, we recover the short-range limit. This yields the well-known result for the spectrum of the transverse-field Ising chain (3.1)

$$\epsilon_{\text{TFI}}(k) = \sqrt{(\cos k + \mu)^2 + \sin^2 k}, \quad (3.13)$$

with corresponding rotation angle, found from (3.10),

$$\tan \theta_k^{\text{TFI}} = -\frac{\sin k}{\mu + \cos k} \quad (3.14)$$

Virtually all the relevant dynamics of a quadratic model is encoded in the spectrum of quasiparticles (3.12). We will frequently come back to the dispersion to situate the phenomena that we encounter in the upcoming analysis. However, it is already worthwhile to illuminate a few things before continuing. As we see on Fig. 3.1(a)–(b), the dispersion is, in general, not a monotonous function of momentum. We can anticipate that this may lead to unexpected features in the dynamics upon quenching the model. Furthermore, when $\alpha < 1$ (or $\alpha < D$, with D the dimensionality in general) it is clear from (3.7) that the total energy $\langle \hat{H}_{\text{LRK}} \rangle$ is not additive and scales *superextensively*. Essentially, this indicates that the interaction energy of one fermion with all the other fermions in the chain is diverging,

3.2. The long-range Kitaev model

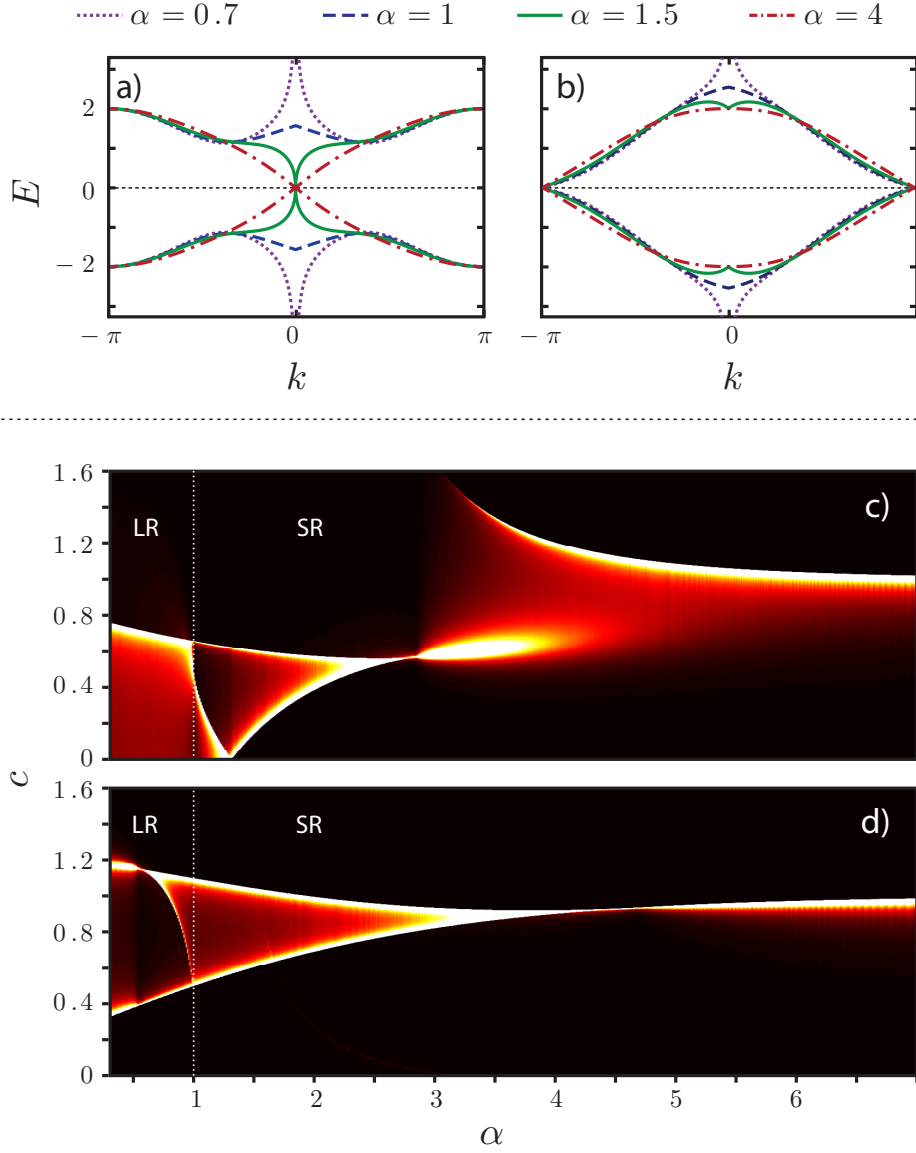


Figure 3.1: (a-b) The quasiparticle dispersions of the LRK model for $\mu = -1$ (a) and $\mu = 1$ (b) and for different α . When $\alpha < 1$, the interactions have a true long-range nature, as is signaled by the diverging $k = 0$ mode. For the case $\alpha = 4$, the spectrum is practically indistinguishable from the transverse-field Ising result, which we find in the limit $\alpha \rightarrow \infty$. (c-d) Distribution of quasiparticle group velocities (vertical slices) for varying α (arbitrary units). Bright colors indicate a high density of quasiparticles having a particular velocity c in a system with pairing-interaction exponent α .

causing the energy density, i.e. the energy per lattice site, to diverge upon sending $L \rightarrow \infty$. Notably, this observation is also reflected in the quasiparticle dispersion. When $\alpha < 1$, the spectrum diverges for $k \rightarrow 0$ as $\epsilon_k \sim k^{\alpha-1}$, which we can see in Fig. 3.1. In that case, we conclude that it takes a large amount of energy to create a long-wavelength excitation.

Once a quasiparticle with momentum k is inserted in the chain, it will travel at a speed corresponding to the quasiparticle *group velocity*

$$c_k = \frac{\partial \epsilon(k)}{\partial k}. \quad (3.15)$$

One of the key quantities that we use for the analysis is the *group-velocity distribution*, denoted by $\mathcal{N}(c)$, which is a quantity that can be derived from the quasiparticle spectrum. We compute the quasiparticle group velocity c_k for each momentum k from (3.15). Then, we count all velocities c_k that fall within an interval $c + \Delta c$ and build up a histogram accordingly. The result of this analysis is the image shown in Fig. 3.1(c)–(d), which we obtain after gluing all the histograms (a single vertical slice) together while varying α for both the cases $\mu = \pm 1$. A bright color signals that many modes in the spectrum exhibit that particular group velocity at that specific value of α , while dark regions show velocities that are not (or barely) present in the spectrum.

A few words of explanation are in place at this point. We see that the velocity distribution is sharply concentrated around well-defined velocities, producing the observed pattern of bright stripes. The presence of a peak in the distribution means that many spectral modes travel in phase – at the same velocity – creating a *ballistic* wavefront of quasiparticles upon excitation. As can be anticipated, a later analysis will show that this has a profound impact on the spreading of correlations through the system. In the limit $\alpha \rightarrow \infty$, there remains only a single peak, which approaches $c = 1$ in both the cases $\mu = \pm 1$. From (3.13) we see that this coincides with the group velocity of modes close to $k = 0$ ($\mu = -1$) or $k = \pi$ ($\mu = 1$). Strangely, while we expect the presence of modes with a divergent group velocity when $\alpha < 1$ (or even $\alpha < 2$ when $\mu = -1$), we see that they are hardly represented in the distribution of group velocities in Fig. 3.1(c)–(d). We conclude that, in general, the largest weight of quasiparticles is concentrated in sharp velocity peaks. Therefore, the generation of ballistic wavefronts of many quasiparticles together will be a vital ingredient to our understanding of the dynamical behavior of this system.

3.2.4 The ground state and initial state before the quench

From expression (3.11) we conclude that we can conveniently express the energy of this many-body system in terms of the $\hat{\xi}_k$ fermions

$$E_{\text{LRK}} = \langle \hat{H}_{\text{LRK}} \rangle = E_0 + \sum_k \epsilon(k) n_k^{(\xi)}, \quad (3.16)$$

with $n_k^{(\xi)} = \langle \hat{\xi}_k^\dagger \hat{\xi}_k \rangle$. Consequently, it is readily seen that we find the minimum of $E_{\text{LRK}} = E_0$ by setting $n_k^{(\xi)} = 0$ for all k , corresponding to the vacuum of the $\hat{\xi}$ -fermions.

3.3. The spreading of correlations following a quench

Clearly, the vacuum of the $\hat{\xi}$ -fermions does in general not coincide with the one from the original \hat{c} -fermions in the chain. From (3.9) we find immediately that we can change to the correlations in the basis of \hat{c} -fermions with the relations

$$\begin{aligned} n_k \equiv \langle \hat{c}_k^\dagger \hat{c}_k \rangle &= u_k^2 \langle \hat{\xi}_k^\dagger \hat{\xi}_k \rangle + v_k^2 \langle \hat{\xi}_{-k} \hat{\xi}_{-k}^\dagger \rangle - 2iu_k v_k \Im \{ \langle \hat{\xi}_{-k} \hat{\xi}_k \rangle \} \\ &= (u_k^2 - v_k^2) n_k^{(\xi)} + v_k^2 - 2iu_k v_k \Im \{ m_k^{(\xi)} \}, \end{aligned} \quad (3.17)$$

$$m_k \equiv \langle \hat{c}_{-k} \hat{c}_k \rangle = u_k^2 \langle \hat{\xi}_{-k} \hat{\xi}_k \rangle + v_k^2 \langle \hat{\xi}_k^\dagger \hat{\xi}_{-k}^\dagger \rangle + iu_k v_k \left(\langle \hat{\xi}_{-k} \hat{\xi}_{-k}^\dagger \rangle - \langle \hat{\xi}_k^\dagger \hat{\xi}_k \rangle \right) \quad (3.18)$$

$$= u_k^2 m_k^{(\xi)} + v_k^2 m_k^{(\xi)*} + iu_k v_k (1 - 2n_k^{(\xi)}). \quad (3.19)$$

Here, we defined $m_k^{(\xi)} = \langle \hat{\xi}_{-k} \hat{\xi}_k \rangle$ and we used that $u_k = u_{-k}$ and $v_k = -v_{-k}$ and applied the fermion anticommutation relations from (3.6). In the ground state, which is void of $\hat{\xi}$ -fermions, it is then easily seen that

$$n_k = v_k^2, \quad m_k = iu_k v_k. \quad (3.20)$$

Alternatively, we can express the ground state in terms of the original \hat{c} -fermions in the form of a BCS-type state

$$|GS\rangle = \prod_k (u_k - iv_k \hat{c}_k^\dagger \hat{c}_{-k}^\dagger) |0\rangle, \quad (3.21)$$

with $|0\rangle$ denoting the vacuum of \hat{c} -fermions, reproducing the correlations from (3.20).

It has long been understood that the ground state of the transverse-field Ising model, obtained by sending $\alpha \rightarrow \infty$, contains a *quantum phase transition* [26] from a ferromagnetic state with long-range order $|\mu| < 1$ to a paramagnetic phase $|\mu| > 1$, with an exact symmetry $\mu \leftrightarrow -\mu$ [24]. This symmetry vanishes when a long-range interaction potential is considered in (3.7). Moreover, while the critical point $\mu = +1$ persists, the one at $\mu = -1$ disappears when $\alpha < 1$, meaning that we can continuously move between a ferromagnetic and a paramagnetic phase in the model [35]. We can understand this aspect from the quasiparticle dispersion in Fig. 3.1(a), where we see a spectral divergence for $k \rightarrow 0$ when $\alpha < 1$; exactly at the momentum where the spectral gap normally closes for the critical point $\mu = -1$.

For our analysis, however, we will take the system to be in the ground state of \hat{H}_{LRK} with $\mu \rightarrow -\infty$ before the quench. In this case, we derive from (3.7) that it requires an infinite amount of energy to insert a fermion into the chain, making us conclude that the chain must be empty; corresponding to the vacuum state $|0\rangle$ of the \hat{c} -fermions. Since interactions between the fermions do not matter in this limit, we will also refer to it as the *noninteracting* ground state. From there on, we will abruptly quench μ to a finite value at $t = 0$ and study the subsequent dynamics.

3.3 The spreading of correlations following a quench

Before we duck into calculations of observables in the long-range Kitaev model (3.7), we make a brief excursion to a few long-established results in the context of information propagation in quantum lattice models. In particular, they apply to the case of short-range

interactions, which we naturally retrieve in the long-range Kitaev model by sending $\alpha \rightarrow \infty$. At the end of this section, we will then briefly discuss if there is anything general that we can say about the long-range interacting case (finite α).

3.3.1 The Lieb-Robinson bound

In special relativity, the speed of light sets a universal upper limit on the speed at which information can be transmitted through space-time. In nonrelativistic quantum systems there is, in principle, no limit to the rate at which we can send signals through. Does this mean that we can *instantly* send information from point A to point B , separated by a distance R , through a nonrelativistic system?

In their seminal paper from 1972, titled *The finite group velocity of quantum spin systems* [36], Elliott H. Lieb and Derek Robinson addressed exactly this question and their conclusions had a profound impact on our understanding of condensed matter physics and quantum information theory today. After a long and rather technical derivation, which you can find back in the paper, the conclusion of their work can be summarized as follows.

Given a D -dimensional lattice Γ of which we send the total volume to infinity. We now assign a local Hilbert space to each lattice site i , which we denote as \mathcal{H}_i . In the original work, the dimension of the local Hilbert space (i.e. on each lattice site) was taken to be finite – hence the specification *spin systems* in the title – but this was later generalized to infinite local Hilbert spaces as well, in the form of harmonic oscillators [37].

Let \hat{H} be a Hamiltonian acting on the lattice Γ that we can decompose as

$$\hat{H} = \sum_{X \subset \Gamma} \hat{h}_X. \quad (3.22)$$

Here, the \hat{h}_X are operators that act only on a subsystem $X \subset \Gamma$ and are assumed to be of *finite range*: each X covers only a *finite* number of lattice sites². The easiest example you can think of is a nearest-neighbor interaction term, which only connects two sites at a time for each \hat{h}_X .

Let us now take two operators \hat{O}_A and \hat{O}_B which are supported only on a *finite* set: $A, B \subset \Gamma$. Additionally, we assume that the sets A and B are separated from each other by a distance $R = \min_{i \in A, j \in B} D(i, j)$, with $D(i, j)$ some distance measure defined on the lattice. The evolution of the operator \hat{O}_A under Hamiltonian \hat{H} can then be written in the Heisenberg picture as

$$\hat{O}_A(t) = e^{i\hat{H}t} \hat{O}_A e^{-i\hat{H}t}, \quad (3.23)$$

and analogous for $\hat{O}_B(t)$.

The central question is then the following: *How long does it take – expressed in terms of evolution time t – for \hat{O}_B to feel that the system was perturbed with \hat{O}_A , at a distance*

²In reality \hat{h}_X may have an exponentially decaying overlap with other sites outside of X , but that is a mere technical detail.

3.3. The spreading of correlations following a quench

R away? This question was answered by Lieb and Robinson by deriving a bound on the commutator of both operators, which can be formulated as follows,

$$\| [\hat{O}_A(t), \hat{O}_B] \| \leq a \exp \left\{ - \frac{|R - v_{\text{LR}}t|}{\xi} \right\}. \quad (3.24)$$

Here a and ξ are (positive) constants that depend on the details of \hat{O}_A and \hat{O}_B and the norm $\| \cdot \|$ can be any suitable operator norm, like the Hilbert-Schmidt norm or the trace norm. The importance of this result, however, lies in the form of the exponent. Essentially it states that one can *never* extract information about changes in point B by doing any *local* measurement at point A , a distance R away, before a time $\tau(R) = R/v_{\text{LR}}$ has passed – up to exponentially suppressed corrections. The fundamental constant v_{LR} is dubbed the *Lieb-Robinson velocity* and is here to be understood as a *finite* propagation speed of perturbations that limits the rate at which information can spread through a quantum system. Intriguingly, v_{LR} enters in exactly the same form as the speed of light c in a relativistic context and it therefore establishes a notion of causality in an explicit *nonrelativistic* quantum theory. It should come as no surprise that this bound is often referred to as the *lightcone effect*.

3.3.2 A bound on correlation functions

The presentation of the Lieb-Robinson bound by means of a bound on a commutator of two observables can be somewhat inconvenient in a practical context. Of more direct relevance to us is the question how fast correlations can build up between two distant points in a quantum system after a quench. Obviously, the creation of correlations on itself should not be limited by a fundamental speed, as entanglement cannot be used to transfer information at a superluminal rate – this is exactly the central argument in the EPR paradox [39]. It is, however, illustrated in Ref. [11] that the *spreading* of entanglement after a perturbation can be understood from a Lieb-Robinson-like bound as well.

For this they considered the time-evolved connected correlation function and proved that

$$\left| \langle \hat{O}_A \hat{O}_B \rangle_t \right| \equiv \left| \langle \Psi(0) | e^{i\hat{H}t} \hat{O}_A \hat{O}_B e^{-i\hat{H}t} | \Psi(0) \rangle \right| \leq \tilde{a} \exp \left\{ - \frac{|R - 2v_{\text{LR}}t|}{\tilde{\xi}} \right\}. \quad (3.25)$$

where \tilde{a} and $\tilde{\xi}$ are again two positive constants that depend on the details of \hat{O}_A and \hat{O}_B . Furthermore, we denote $|\Psi(0)\rangle$ as the quantum state at $t = 0$, the time instant when the quench takes place. The form of this expression is very similar in shape as the original formulation of the Lieb-Robinson bound from (3.24), but an important difference comes with the extra factor two in the exponent: the spreading of correlations appears to go at twice the rate of the propagation of perturbations.

In Ref. [38] a natural explanation for this was introduced in terms of the *quasiparticle view*. At the time of the quench, a population of quasiparticles is abruptly inserted into the

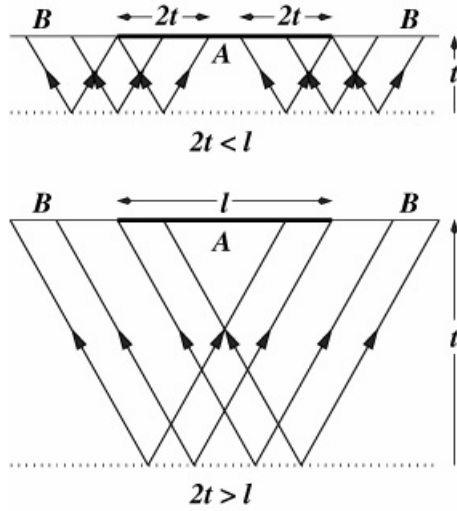


Figure 3.2: The quasiparticle view: at the time of the quench a population of quasiparticles is abruptly injected in the system. These start traveling through the system at a speed given by the quasiparticle group velocity. On the image, the quasiparticles with a maximal group velocity are pictured as they move along the emergent lightcone. The extra factor 2 in the bound of (3.25) is attributed to the entanglement of two counterpropagating quasiparticles, which were created at the same spatio-temporal point. Picture from Ref. [38], where this interpretation was originally presented.

quantum system. From there on, these start propagating through the lattice at a speed set by their quasiparticle group velocity, derived from the spectrum through (3.15). The origin of the factor two is then intuitively understood by noticing that quasiparticles are always created in pairs where both quasiparticles propagate in opposite directions. In Fig. 3.2 this picture is schematically illustrated.

3.4 Correlations in the long-range Kitaev chain

We consider quenches of the parameter μ in the Hamiltonian \hat{H}_{LRK} of the long-range Kitaev model (3.7). Although this might not be the most convenient parameter to quench in experiment – remember that this is a toy model anyway – one of the central points is that many features in the dynamics of correlation functions are universal. In practice, we set $\mu \rightarrow \infty$ at times $t < 0$ and abruptly quench to either $\mu = 1$ or $\mu = -1$, which are the critical points in the short-range Kitaev model (see Sec. 3.2.4).

We take the system to be initially in the ground state of the prequench Hamiltonian (see Sec. 3.2.4). Since it takes an infinite amount of energy to insert a fermion in the lattice when $\mu \rightarrow \infty$, we conclude that the lattice must be void of particles and, consequently, that the vacuum of the original \hat{c}_k fermions in this case coincides with the one from the rotated $\hat{\xi}_k$ Bogoliubov fermions.

3.4. Correlations in the long-range Kitaev chain

Quasiparticles play a key role in the understanding of the time evolution of a many-body quantum system. The complex dynamics can be understood by noticing that the time evolution of the quasiparticle operators in the Heisenberg picture is particularly simple and found as

$$i\dot{\hat{\xi}}_k = [\hat{\xi}_k, H_{\text{LRK}}] = \epsilon_k \hat{\xi}_k, \quad (3.26)$$

which is readily seen from \hat{H}_{LRK} written in form (3.11). This makes that a quasiparticle traveling with momentum k oscillates in time as $\hat{\xi}_k(t) = \hat{\xi}_k e^{-i\epsilon_k t}$, as it is dictated by the dispersion relation from (3.12). By transforming back to the true fermions with (3.9), we find the time evolution of the \hat{c} -operators as

$$\hat{c}_k(t) = u_k e^{-i\epsilon_k t} \hat{\xi}_k(0) - i v_{-k} e^{i\epsilon_k t} \hat{\xi}_{-k}^\dagger(0). \quad (3.27)$$

As illustrated in Sec. (3.2.4), the initial state is conveniently expressed in momentum space by the quadratic correlation functions $\langle \hat{c}_k^\dagger \hat{c}_{k'} \rangle_t = n_k(t) \delta_{k,k'}$ and $\langle \hat{c}_k \hat{c}_{k'} \rangle_t = m_k(t) \delta_{k,-k'}$, where the δ -functions reflect the spatial homogeneity of the system. The initial state is void of fermions, so that $n_k(0) = 0$ and $m_k(0) = 0$.

We then find the time evolution of the correlation functions from the time-evolved operators (3.26)

$$\begin{aligned} n_k(t) &= 4u_k^2 v_k^2 \sin^2(\epsilon_k t) = \sin^2 \theta_k \sin^2(\epsilon_k t) \\ m_k(t) &= 2u_k v_k \sin(\epsilon_k t) \left(u_k^2 e^{-i\epsilon_k t} + v_k^2 e^{-i\epsilon_k t} \right) \end{aligned} \quad (3.28)$$

$$= \sin \theta_k \sin(\epsilon_k t) \left(\cos^2 \theta_k e^{-i\epsilon_k t} + \sin^2 \theta_k e^{i\epsilon_k t} \right) \quad (3.29)$$

From (3.8), we see that the spatial correlation functions are evaluated as the Fourier transforms of the quadratic correlation functions in momentum space

$$G^{(n)}(r) \equiv \langle \hat{c}_m^\dagger \hat{c}_n \rangle_t = \frac{1}{L} \sum_{k,k'} e^{-ikm} e^{ik'n} \langle \hat{c}_k^\dagger \hat{c}_{k'} \rangle_t = \frac{1}{L} \sum_k e^{-ikr} n_k(t), \quad (3.30)$$

$$G^{(a)}(r) \equiv \langle \hat{c}_m \hat{c}_n \rangle_t = \frac{1}{L} \sum_{k,k'} e^{ikm} e^{ik'n} \langle \hat{c}_k \hat{c}_{k'} \rangle_t = \frac{1}{L} \sum_k e^{-ikr} m_k(t), \quad (3.31)$$

with the lattice distance $r = |m - n|$. In the following, we will refer to these as the *normal* and *anomalous* correlations respectively.

3.4.1 The short-range limit

With expressions (3.30)–(3.31), we have access to quantities *exactly* of the form (3.25). Recall that one of the prerequisites for the Lieb-Robinson bound to hold was that interactions are *short-ranged* in nature. As the name of our model suggests, there is nothing we can say about the spreading of correlations in the long-range Kitaev chain based on general arguments from the Lieb-Robinson bound. However, we now consider the limit $\alpha \rightarrow \infty$ to recover a short-range interacting model.

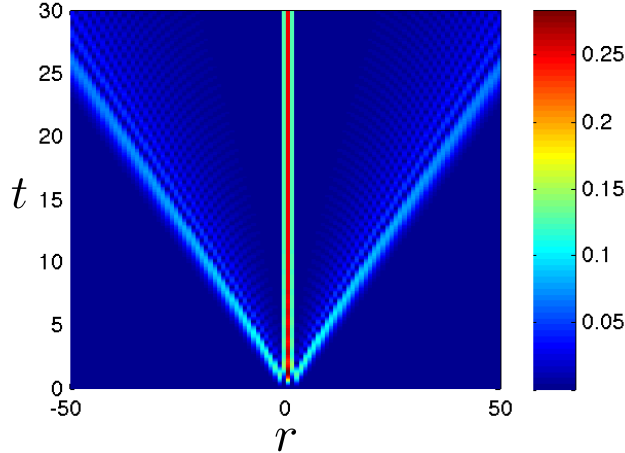


Figure 3.3: The normal correlation function $G^{(n)}(r, t) \equiv \langle \hat{c}_j^\dagger \hat{c}_{j+r} \rangle_t$ of the short-range Kitaev model (with $\alpha \rightarrow \infty$) after an abrupt quench to $\mu = -1$. A light cone is visible in the correlation pattern, as is expected from the Lieb-Robinson bound (3.25).

In Fig. (3.3) we show the evolution of the normal correlation function, given in (3.30). Here we clearly observe how an emergent *light cone* prevents the building up of correlations between two distant points outside an effective causal region. If we take a look back at Fig. 3.1(c-d), we see that at large α there is only a single peak left in the quasiparticle group-velocity distribution, which shifts to $c = 1$ (for $|\mu| = 1$). If we analyze the light cone in Fig. (3.3) more carefully, we find that it is characterized by the curve $t = R/2c$ (with $c = 1$ in this case), exactly with the extra factor 2 that was needed for the Lieb-Robinson-like bound from (3.25).

By quenching the model, the vacuum state is abruptly changed and we insert pairs of quasiparticles into the system, which then start to travel in opposite directions, following the *quasiparticle view* introduced in Ref. [38]. The shape of the spectrum gives rise to a sharp peak in the quasiparticle velocity distribution $\mathcal{N}(c)$ at $c = \pm 1$, signaling that many of those quasiparticles share the same velocity and form a wavefront. Since a quasiparticle and its partner travel in opposite directions, their entangled information spreads at twice the rate of the quasiparticle velocity c , as was illustrated in Fig. 3.2.

3.4.2 The fate of long-range interactions

Can we, at this point, already make a statement about the general case of long-range interactions, with finite α ? In Fig. (3.4) we show the correlation function (3.30) for $\alpha < 1$ and we conclude that correlations between two distant point are not exponentially suppressed when they are lying outside of each others light cone. In fact, in Appendix A.2 we derive for $\alpha < 1$ that at large $r = |m - n|$ the correlations behave as

3.4. Correlations in the long-range Kitaev chain

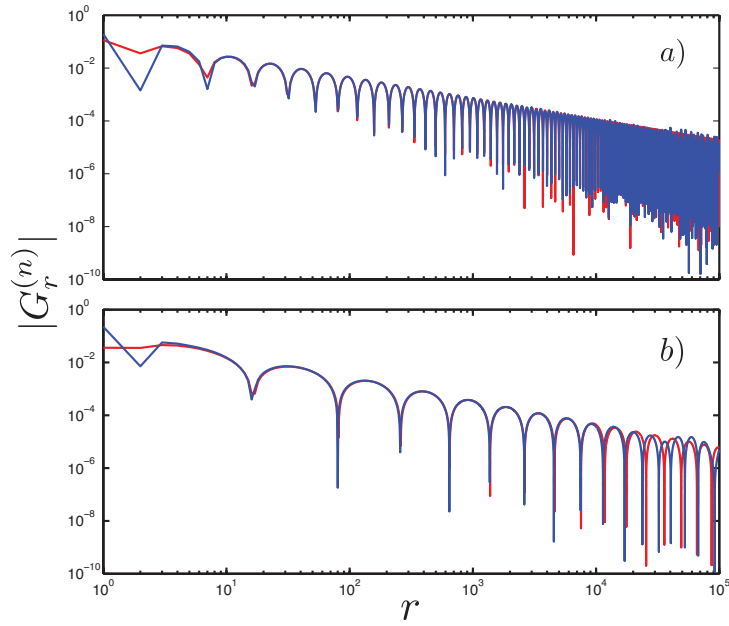


Figure 3.4: The normal correlation function $G^{(n)}(r) \equiv \langle \hat{c}_n^\dagger \hat{c}_{n+r} \rangle_t$ of the long-range Kitaev model with (a) $\alpha = 0.3$ and (b) $\alpha = 0.7$ for a quench to $\mu = -1$ at a time frame $t = 1$. The long-range nature of interactions impedes the emergence of a clearly distinguishable light cone. Rather, a power-law decay of the correlation function is seen at large distances. The red line is the true correlation function, obtained with (3.30) and the blue is the result obtained with a saddle-point approximation of the integral, explained in Appendix A.2.

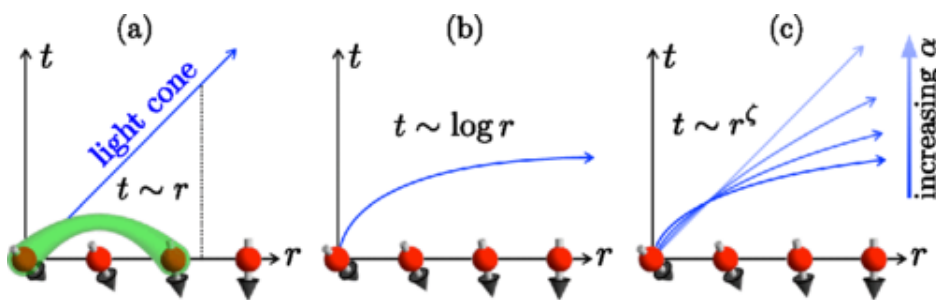


Figure 3.5: (a) According to the Lieb-Robinson bound, short-range interacting spin systems give rise to a linearly growing causal region. (b) [2, 40] suggest that the causal region may grow exponentially for the case of a power-law interaction. (c) In [35] it is shown that, in general, the causal region may grow as a power law $t \sim r^\zeta$, with $\zeta < 1$ but approaching 1 for shorter-ranged interactions. Picture taken from Ref. [35].

$\langle c_m^\dagger c_n \rangle = i \langle c_m c_n \rangle = -\mathcal{F}^{(\alpha)}(r, t) \cos[\eta^{(\alpha)}(r, t)]$. The envelope has a power-law dependence in both time and distance: $\mathcal{F}^{(\alpha)}(r, t) = C^{(\alpha)} \cdot t^\gamma r^{-\chi}$, with $C^{(\alpha)}$ a constant. The exponents are then derived as

$$\gamma = \frac{1}{2(2-\alpha)}, \quad \chi = \frac{3-\alpha}{2(2-\alpha)}. \quad (3.32)$$

Does this mean that we can transmit information instantly from point A to point B by utilizing the long-range nature of interactions in the model?

If one naively generalizes the original bound from Lieb and Robinson, one would conclude that the emergent ‘light cone’ in long-range interacting systems is characterized by $t \sim \log r$, suggesting that the effective causal region may grow exponentially, rather than linearly in time [2, 40]. In a recent work [35], however, the problem of generalizing the Lieb-Robinson bound for long-range interactions was reconsidered. In particular, they studied Hamiltonians with interaction terms dropping as $V(r) \sim r^{-\alpha}$, with $\alpha > 2D$ and concluded that then the light cone is actually characterized by a power law $t \sim r^\zeta$, with $\zeta < 1$. In the limit $\alpha \rightarrow \infty$ it was then illustrated that $\zeta \rightarrow 1$, thus recovering a linear light cone for short-range interactions. See Fig. 3.5 for a schematic illustration of their results.

How does this translate to the *propagation of information* in the long-range Kitaev model? After all, a bound is only bound and no claims whatsoever are made as to how accurately it is approached in a specific model. Before we make an attempt to answer this question, let us investigate in more detail how we can quantify ‘transmitting information’ through a quantum system more properly; correlation functions between two distant points can be somewhat arbitrary because they come in many forms.

3.5 Living inside a finite subsystem

Imagine that you, as an observer, only have access to lattice points situated within a subsystem that is composed of a finite number of sites. What information can you collect

3.5. Living inside a finite subsystem

by merely investigating that particular region? In any case, we must be able to observe the initial stage of quasiparticle creation after the quench in the subsystem, but as soon as these travel outside of your region and they are gone, we expect something to happen.

3.5.1 Building up the local density matrix

The most general representation of a quantum state is its density matrix $\hat{\rho}$. In the case of a *pure* quantum state $|\psi\rangle$, one that is not entangled with any other state, we can represent the density matrix as $\hat{\rho}_{\text{pure}} = |\psi\rangle\langle\psi|$. When a quantum state is not pure, we call it *mixed* and in that case we can always find a set of $|\phi_i\rangle$, such that $\hat{\rho}_{\text{mixed}} = \sum_i p_i |\phi_i\rangle\langle\phi_i|$ with $\sum_i p_i = 1$.

When we take the system as a whole, i.e. the entire chain of fermions, it is a pure quantum state and, importantly, unitary time evolution implies that it remains so at any time. However, when we separate a subsystem \mathcal{A} , composed of only a finite number of lattice sites, from the rest of the chain and consider the *local* quantum state, it will generally be entangled with the outside and no longer be pure. In that case, we have to formulate the quantum state in terms of a mixed ensemble

$$\hat{\rho}_{\mathcal{A}} \equiv \text{tr}_{\bar{\mathcal{A}}}\hat{\rho} = \text{tr}_{\bar{\mathcal{A}}}\left\{|\psi\rangle\langle\psi|\right\} = \sum_i p_i |\phi_i\rangle\langle\phi_i|, \quad (3.33)$$

where $\text{tr}_{\bar{\mathcal{A}}}\{\cdot\}$ means tracing over the entire chain except the sites in \mathcal{A} .

This section is devoted to investigating how we can construct the local density matrix $\hat{\rho}_{\mathcal{A}}$ of a subsystem \mathcal{A} in the chain of fermions. Let us therefore start by gathering all the information that we can find inside a subsystem. Given that Hamiltonian (3.7) is quadratic, it means that we can apply *Wick's* theorem at all times, provided the initial state can be expressed as such³. Conveniently, this has the consequence that all higher-order correlation functions can be factorized into different products of second-order correlation functions [41]. But we already know these at *all times* from expressions (3.30)–(3.31). Consequently, all information about our subsystem that we could possibly think of must be somehow encoded in these quadratic correlations.

Since we have access to all information contained in the subsystem by probing the quadratic correlation functions, we must be able to construct the local density matrix in terms of those. To this end, we start by formulating a general Gaussian form for the density matrix of subsystem \mathcal{A} , which reflects the quadratic nature of our model, as it was first proposed by Peschel [42],

$$\hat{\rho}_{\mathcal{A}}(t) = \frac{1}{\mathcal{Z}} \exp \left\{ - \sum_q \Omega_q(t) \hat{\gamma}_q^\dagger(t) \hat{\gamma}_q(t) \right\}. \quad (3.34)$$

³This is certainly the case, since we start from the fermionic vacuum. In general, one can prove that the ground state of a quadratic Hamiltonian always exhibits a Wick theorem [25].

For this representation of the density matrix, we have introduced a new set of modes $\hat{\gamma}_q$, which live inside the subsystem only, with $q = 1, \dots, N_{\mathcal{A}}$ an index labeling the degrees of freedom of the subsystem. In general, the $\hat{\gamma}_q$ can be obtained at all times as a linear transform from the original \hat{c} -fermions that live on the lattice sites of the subsystem

$$\hat{\gamma}_q(t) = \sum_{j \in \mathcal{A}} \left(U_{qj}(t) \hat{c}_j(t) + iV_{qj}(t) \hat{c}_j^\dagger(t) \right). \quad (3.35)$$

If we want the $\hat{\gamma}$ -fermions to satisfy fermionic anticommutation relations (3.6), we derive two identities for the transformation matrices

$$UU^\dagger + VV^\dagger = \mathbb{1}, \quad UV^T + VU^T = 0. \quad (3.36)$$

Expectation values of observables \hat{O} defined on \mathcal{A} are then given by $\text{tr}\{\rho_{\mathcal{A}}\hat{O}\}$, where the trace over states on \mathcal{A} can be evaluated by expressing it as

$$\text{tr}\{\cdot\} = \sum_{n_1^{(\gamma)}=0,1} \cdots \sum_{n_{N_{\mathcal{A}}}^{(\gamma)}=0,1} \langle n_1^{(\gamma)} \cdots n_{N_{\mathcal{A}}}^{(\gamma)} | \cdot | n_1^{(\gamma)} \cdots n_{N_{\mathcal{A}}}^{(\gamma)} \rangle, \quad (3.37)$$

meaning that we sum over all possibilities to have one or zero fermions in the different $\hat{\gamma}$ -modes. By requiring that $\text{tr}\hat{\rho}_{\mathcal{A}} \equiv 1$, the partition sum is then readily evaluated as $\mathcal{Z} = \prod_q n_q^{(\gamma)}$, with

$$n_q^{(\gamma)} \equiv \langle \hat{\gamma}_q^\dagger \hat{\gamma}_q \rangle = (1 + e^{-\Omega_q})^{-1}. \quad (3.38)$$

Not surprisingly, the parameters Ω_q bear the name *pseudo-energies*, which we associate to the modes $\hat{\gamma}_q$ in \mathcal{A} .

Since both $\rho_{\mathcal{A}}$ and the second-order correlation functions (3.30-3.31) necessarily contain all relevant information about the subsystem, there must exist a map between the two. In practice, we can reconstruct $\rho_{\mathcal{A}}$ by demanding that it correctly reproduces the quadratic correlation functions as expectation values. We then require that the second-order correlation functions from (3.30) inside the subsystem \mathcal{A} are reproduced by $\rho_{\mathcal{A}}$,

$$G_{ij}^{(n)}(t) = \text{tr}\{\rho_{\mathcal{A}}(t)\hat{c}_i^\dagger\hat{c}_j\} \quad \text{and} \quad G_{ij}^{(a)}(t) = \text{tr}\{\rho_{\mathcal{A}}(t)\hat{c}_i\hat{c}_j\}. \quad (3.39)$$

By evaluating (3.39) we conclude that the transformation matrices U and V and the pseudo-energies Ω_q are obtained by solving two linear systems of equations

$$P\mathcal{G}_{\mathcal{A}}^{(+)} = \Lambda_{\mathcal{A}}Q \quad \text{and} \quad Q\mathcal{G}_{\mathcal{A}}^{(-)} = \Lambda_{\mathcal{A}}P, \quad (3.40)$$

with

$$\mathcal{G}_{\mathcal{A}}^{(\pm)} = \begin{pmatrix} 2G_{\mathcal{A}}^{(n)} - \mathbb{1} & \pm 2G_{\mathcal{A}}^{(a)} \\ \pm 2G_{\mathcal{A}}^{(a)*} & 2G_{\mathcal{A}}^{(n)} - \mathbb{1} \end{pmatrix}, \quad \Lambda_{\mathcal{A}} = \begin{pmatrix} \Xi & 0 \\ 0 & \Xi \end{pmatrix}, \quad (3.41)$$

with $\Xi_{qp} = \delta_{qp} (2n_q^{(\gamma)} - 1)$. Furthermore, the matrices are found as

$$P = \begin{pmatrix} U & V \\ V^* & U^* \end{pmatrix}, \quad Q = \begin{pmatrix} U & -V \\ -V^* & U^* \end{pmatrix}, \quad (3.42)$$

3.5. Living inside a finite subsystem

with the U and V matrices defined for the Bogoliubov transformation of (3.35). Having built up the density matrix $\hat{\rho}_{\mathcal{A}}$ of subsystem \mathcal{A} , we have, in principle, access to all observables of interest defined on the interior of \mathcal{A} .

It is illuminating to note that the local density matrix (3.34) is actually of the form

$$\hat{\rho}_{\mathcal{A}}(t) \sim \exp\{-\hat{H}_{\text{mod}}(t)\}. \quad (3.43)$$

Here, $\hat{H}_{\text{mod}}(t) = \Omega_q(t)\hat{\gamma}_q^\dagger(t)\hat{\gamma}_q(t)$ is called the *modular* or *entanglement* Hamiltonian of the system and $\Omega_q(t)$, the eigenvalues of $\hat{H}_{\text{mod}}(t)$, are often referred to as the *entanglement spectrum*. It is striking that, while the entire quantum system is in a pure state with $\hat{\rho} = |\psi\rangle\langle\psi|$, a *local* observer inside a finite subsystem does not perceive it like this, merely due to his lack of knowledge of the outside. From (3.43) we are tempted to say that a local observer's perception is that the subsystem is in a *thermal state* of the local (time-dependent) Hamiltonian $\hat{H}_{\text{mod}}(t)$ with temperature $k_B T = 1$. This is also seen in (3.38), where we find the local $\hat{\gamma}$ -modes to have a thermal occupation with a pseudo-energy $\Omega_q(t)$. Although this observation is appropriate for many quantum systems in the long-time limit, we explain in Sec. 3.6 that we must take care with these considerations in our case.

3.5.2 Entanglement entropy

We want to have a way to quantify to what extent the subsystem that we live in is connected – or entangled – with the outside. Any information that is encoded in correlations between our subsystem and the rest of the world, which we cannot probe, is inevitably lost. Now that we have a method to construct the local density matrix, we have access to any observable related to lattice points that we can probe inside subsystem \mathcal{A} . One way to quantify the ‘missing information’, the information encoded in correlations with the outside, is by evaluating the *entanglement* entropy of \mathcal{A} , defined as the Von Neumann entropy of the local density matrix

$$S_{\mathcal{A}} = -\text{tr}\{\hat{\rho}_{\mathcal{A}} \log \hat{\rho}_{\mathcal{A}}\}. \quad (3.44)$$

With the form (3.34), we can evaluate the entanglement entropy in terms of the entanglement spectrum of the modular Hamiltonian $S_{\mathcal{A}} = \sum_q h(n_q^{(\gamma)})$. Each mode $\hat{\gamma}_q$, with occupation $n_q^{(\gamma)}$ given in (3.38), therefore carries an intrinsic entropy

$$h(x) = -x \log x - (1-x) \log(1-x). \quad (3.45)$$

A pure state is characterized by having zero Von Neumann entropy. Therefore the entanglement entropy of a subsystem, always a positive number, can be regarded as a measure to quantify the degree of entanglement of the subsystem with the rest of the chain.

We can now look at how much information an observer in subsystem \mathcal{A} loses in time after an abrupt quench. Roughly speaking, we expect the quasiparticles, which enter \mathcal{A} after the quench, to entangle the subsystem with the outside. At $t = 0$, just before the quench, the total quantum state is a product of the states at different lattice points because

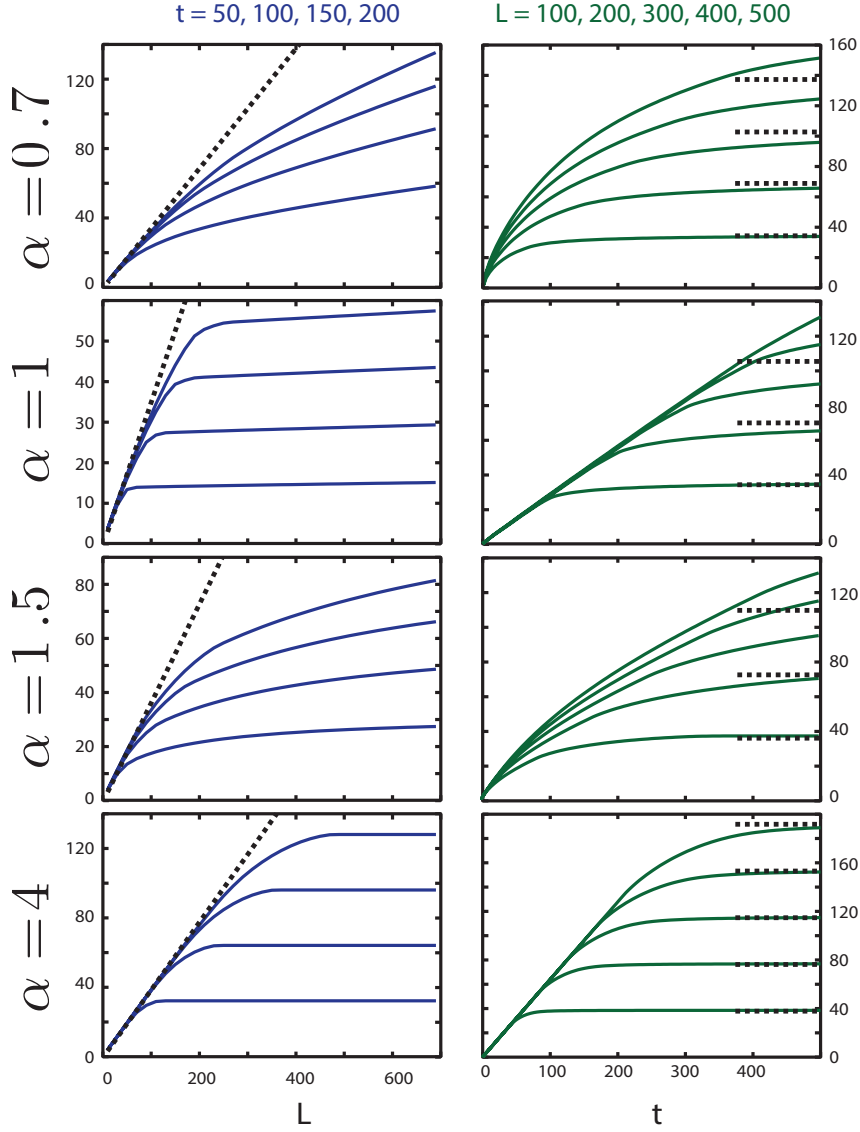


Figure 3.6: The scaling of entanglement entropy as a function of subsystem size (left) and time (right) for quenches in the LRK chain to $\mu = -1$ and different ranges of interactions α . The dotted lines indicate the stationary result predicted by the generalized Gibbs ensemble (see Sec. 3.6).

3.5. Living inside a finite subsystem

the chain is void of fermions (in the case $\mu \rightarrow \infty$). As we can see in the left panels of Fig. 3.5.2, this means that we have $S_{\mathcal{A}}(t = 0) = 0$. From there on, $S_{\mathcal{A}}$ starts growing until it saturates at some value, indicated by the dotted lines. The bigger we choose the subsystem, the longer it appears to take to reach a stationary value and the higher the entanglement entropy of the stationary state.

Alternatively, we can look at fixed time frames and study how $S_{\mathcal{A}}$ scales as function of subsystem size, i.e. the number of points contained in \mathcal{A} – this is shown in the left panels of Fig. 3.5.2. Let us first discuss the limit of high α (the two lower panels on Fig. 3.5.2), for which the quasiparticle view has proven its importance before. When the quasiparticle pairs are generated with the quench, we saw that they are entangled and start propagating in opposite directions. It is now easy to picture that every time one of those quasiparticles leaves the subsystem, we lose some information, thereby causing a rise in entropy. When all the pairs initially created inside the subsystem have lost at least one of their partners, there is no way we can increase entropy further and it saturates. The pair that is created exactly in the middle of the system will take the longest time to leave, $t_c = L/2c$, with L the subsystem size and $c = 1$ the speed of the quasiparticles. We see that this is exactly the time instant at which the entropy curves turn abruptly over and saturate, confirming our intuition. At a fixed time frame, on the other hand, this is perceived as a linear rise in entropy as we make a subsystem larger, until it also saturates. At the saturation point, we have reached the size of a region that encompasses a distance larger than the maximal distance traveled by quasiparticles since the quench: $L = 2ct$. At later times, this distance is larger, so that also a larger subsystem is needed before saturation is reached. In Ref. [12], very general entanglement scaling laws were derived in the context of quenches with local Hamiltonians and, in particular, it was shown that the entanglement entropy of distinguished subsystem saturates as a function of its size. The entanglement entropy of a finite subsystem therefore follows an *area law*, rather than a volume law, under local Hamiltonians – as we had anticipated in Sec. 2.1.

This picture does not hold when we increase the range of interactions (decrease α). While entropy still saturates at late times, the rise is, in general, no longer linear and no abrupt saturation point can be distinguished. In Fig. 3.5.2(a) we show the same curves on a log-log scale and see that the growth of entropy in a chain with $\alpha < 1$ follows a power law $S_{\mathcal{A}} \sim t^\beta$, with $\beta < 1$. Surprisingly, this is in contrast with other results for the LRK model [10], for long-range spin chains [43] and for coupled harmonic oscillators [44], where the initial entropy growth was reported to be logarithmic. Furthermore, at a fixed time frame we see that entanglement entropy does not saturate as function of subsystem size. More specifically, we see that it keeps on growing linearly with system size, suggesting a *volume law* or extensive entropy for Hamiltonians with long-range interactions.

In Fig. 3.5.2(b) we show how long it takes for chains with different interaction range α to reach 95% of the stationary value of entanglement entropy after the quench. Notably, for $\mu = -1$ there is a substantial delay in equilibration at the value $\alpha \approx 1.3$, which can

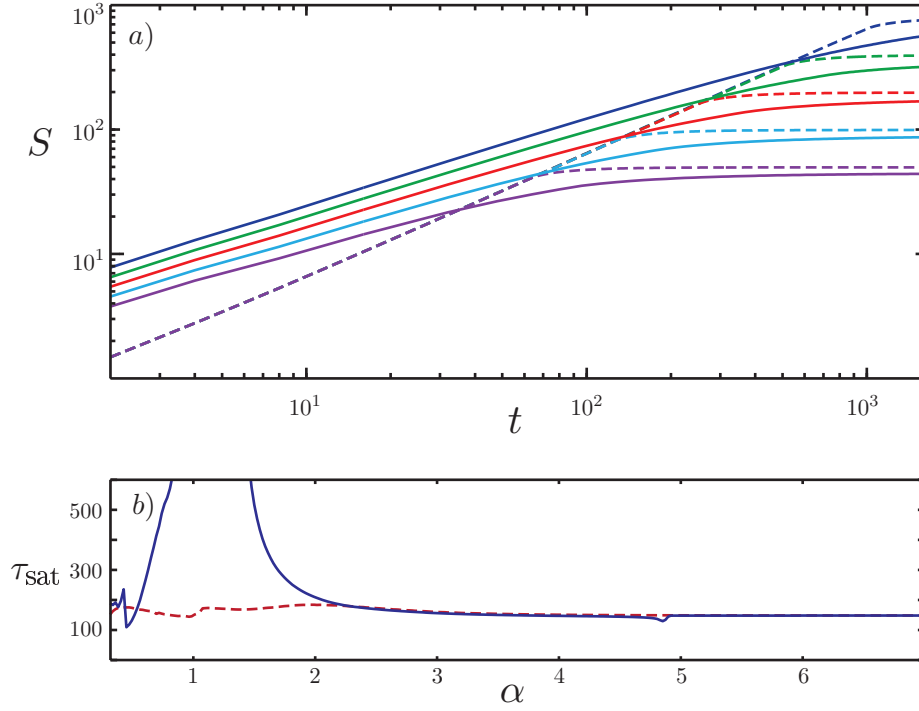


Figure 3.7: (a) Entanglement entropy as a function of time after a quench to $\mu = 1$ in the LRK chain with $\alpha = 0.7$ (solid lines) and $\alpha = 10$ (dashed lines). Results are shown for subsystem sizes from 128 to 2048 sites. (b) The time t_{sat} it takes to reach 95% of the stationary entropy (given by the GGE ensemble, see Sec. 3.6) after the quench for quenches to $\mu = -1$ (blue solid line) and $\mu = 1$ (red dashed line).

3.5. Living inside a finite subsystem

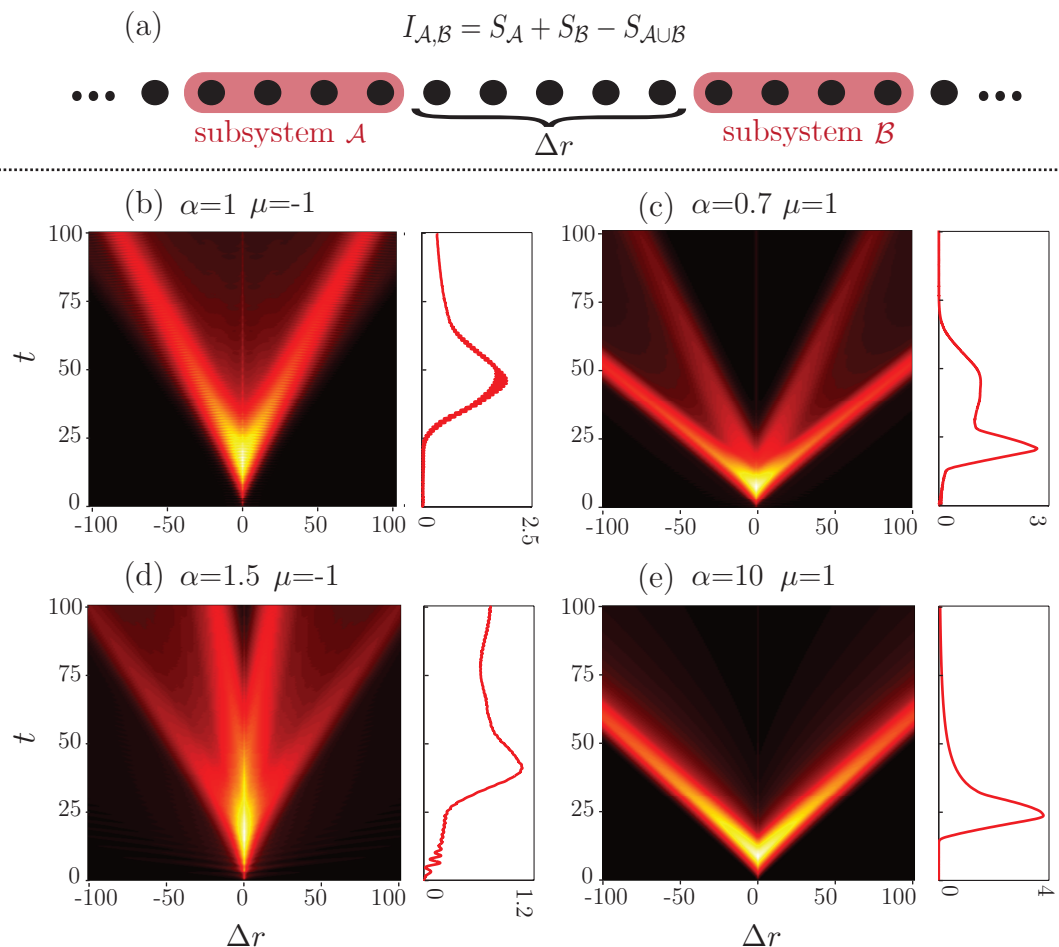


Figure 3.8: Mutual information in the LRK chain after a global quantum quench as a function of subsystem separation (Δr) and time (t), as schematically depicted in (a). Subsystems are composed of 16 sites. All quenches start from the noninteracting ground state ($\mu \rightarrow -\infty$) and go to the values indicated above the figures. The side panels show the mutual information at a fixed separation of 30 sites.

understood by considering the velocity distributions shown in Fig. 3.1(c). We see that at this specific value of α there is a peak that shifts towards $c = 0$, meaning that there is quasiparticle front that propagates at nearly zero velocity.

3.5.3 Mutual information

Having investigated how one subsystem becomes entangled with its environment after the quench, we now want to move our attention back to the question how fast we can transmit information from one subsystem to another, situated at a nonzero distance away. Previously, we have attempted to answer this question by studying correlations between two distant points i and j in the chain. However, many different sorts of correlation functions can be

formulated and, while they may share some common features, it is difficult to make general statements based solely on those.

In this respect, a much more solid and general quantity is provided by the *mutual information* between two subsystems \mathcal{A} and \mathcal{B} , formulated as

$$I_{\mathcal{A},\mathcal{B}} = S_{\mathcal{A}} + S_{\mathcal{B}} - S_{\mathcal{A}\cup\mathcal{B}}. \quad (3.46)$$

It is defined as the difference between the sum of the entropies of systems \mathcal{A} and \mathcal{B} and the entropy of the joint system $\mathcal{A}\cup\mathcal{B}$; it can therefore be regarded as the ‘shared’ information between systems \mathcal{A} and \mathcal{B} . Furthermore, one can prove that the mutual information provides an upper bound on *any* correlation function between the two subsystems [45]. Intuitively, this can be understood by noticing that we also needed *all* relevant (i.e. quadratic, if there is a Wick theorem) correlation functions to construct the local density matrix (3.34).

The propagation of mutual information between two distant subsystems after a quench in the long-range Kitaev model is illustrated in Fig. 3.5.3 for different ranges of interactions α . The plots show the mutual information between two subsystems of size 16 for varying distance between them (Δr) and time (t). In the case of short-range interactions (see (e) with $\alpha = 10$), the intuitive picture of traveling quasiparticles comes into play again. Quasiparticles initially created in subsystem \mathcal{A} start traversing the chain and enter subsystem \mathcal{B} at some point, and vice versa, thereby leading to a rise in mutual information. When those quasiparticles exit the other subsystem again, there is a drop of mutual information that goes all the way to zero again, meaning that the subsystems are left uncorrelated. The emergent light cone neatly follows the curve $t = \Delta r/2c$, with $c = 1$, as we also saw for the correlation functions before. For a short-ranged interacting system, it should be no surprise that mutual information shows a lightcone-like pattern: any correlation function between points in the two subsystems is subject to the Lieb-Robinson bound (3.25) and, therefore, we expect that mutual information between the subsystems, which sets some upper bound on correlations, shares this feature as well.

Things become more interesting when we consider the effects of a long-range interaction potential on the spreading of mutual information. Recall that, as for now, the only true claim for long-range interactions is that we can associate a power-law light cone $t \sim r^\zeta$, with $\zeta < 1$, to the spreading of a local perturbation, provided $\alpha > 2D$ (see Sec. 3.4.2). Moreover, in Sec. 3.2.3 we have illustrated how true long-range interactions ($\alpha < D$) may give rise to quasiparticles with a diverging group velocity, which can in principle transfer information instantly.

It is therefore striking to observe how, at first glance, all panels (b)–(e) seem to exhibit a well-bound light cone in spite of the long-ranged nature of interactions. When we take a closer look, in particular at panels (c)–(d), we see that some of the information indeed leaks out of the light cone due these fast-propagating modes. All in all, however, we conclude that the bulk of information neatly propagates inside an emergent light cone after the quench.

We can even distinguish different fronts of quasiparticles that propagate ballistically

3.6. Relaxation and integrability: the generalized Gibbs ensemble

through the chain. Each of those fronts leads to a lightcone-like pattern in the mutual information, characterized by a curve $t = \Delta r/2\tilde{c}$. In turn, each \tilde{c} exactly corresponds to a peak in the distribution of quasiparticle velocities $\mathcal{N}(c)$, plotted in Fig. 3.1(c-d). We therefore conclude that the majority of information in the long-range Kitaev model propagates ballistically through the chain and that superluminal modes barely affect the rate at which we can transmit information from one subsystem to another.

In a recent work [46], the spreading of correlations in two different models was compared: a spin chain (Ising model) with a long-range spin-spin interaction and a bosonic chain (Bose-Hubbard model) with long-range density-density interactions. Strikingly, they found that the long-range nature of interactions influences the spreading of correlations radically differently in both models. While the spin model gave rise to an instantaneous propagation of correlations (not bound by a light cone), the Bose-Hubbard model exhibited some sort of, what they called, ‘protected quasilocality’. In essence, the results from [46] for the Bose-Hubbard model were very similar to ours. Within a quadratic approximation they found that, while there are quasiparticles with a divergent velocity, the bulk propagates within a well-bound emergent light cone. It is still an open question as to what extent this behavior of ‘protected quasilocality’ is generic for long-range interacting quantum systems and, if so, what the general mechanism is that lies at the heart of it.

Now that we have come to understand how information is transmitted through the chain after a quench, we can move our attention to how a new equilibrium is eventually established inside a subsystem.

3.6 Relaxation and integrability: the generalized Gibbs ensemble

We expect that we can associate an equilibrium ensemble to a density matrix if we wait sufficiently long. The question is, however, what kind of ensemble we have to look for if we only have access to lattice sites within a finite subsystem of the lattice. In general, we would be prompted to formulate a thermal density matrix for an equilibrated isolated quantum system, i.e $\rho \sim \exp\{-\beta\hat{H}\}$, where \hat{H} is the system Hamiltonian and $\beta = 1/k_B T$ is the inverse temperature. Consequently, the system pertains no memory of the initial state, other than the total injected energy, to which we can associate an equilibrium temperature. In other words, regardless of how we perturb the system exactly, we solely need to know the injected energy to predict the equilibrium ensemble that emerges if we wait long enough. How does this notion apply to the long-range interacting Kitaev chain, for which we have identified an extensive number of conserved quantities?

3.6.1 The generalized Gibbs ensemble

The occupation numbers of the Bogoliubov modes $n_k^{(\xi)} = \langle \hat{\xi}_k^\dagger \hat{\xi}_k \rangle$ are conserved in time, which we can see from $[\hat{\xi}_k^\dagger \hat{\xi}_k, \hat{H}_{\text{LRK}}] = 0$. If these observables are conserved under time evolution with \hat{H}_{LRK} , it means that the system *does* pertain a memory of the initial state – in terms of the initial values for $n_k^{(\xi)}$ that cannot change. Quantum systems with a Hamiltonian to which we can associate an *extensive* number of commuting conserved quantities are called *integrable* quantum systems⁴.

But then, if we can determine an infinite set of operators \hat{O}_k , such that $[\hat{O}_k, \hat{H}] = 0$ for all k and also $[\hat{O}_k, \hat{O}_{k'}] = 0$ for all k and k' , what is the equilibrium ensemble that we can associate to the system? Clearly, adjusting only the equilibrium temperature, so as to correctly reproduce the injected energy, will not suffice; not only energy is a conserved quantity under Hamiltonian evolution. Following the seminal paper of E.T. Jaynes from 1957 [20], it was proposed that the equilibrium ensemble of an integrable quantum system must contain all the conserved quantities in its formulation. Moreover, it is the *least-biased* estimate that will prevail and describe the correct statistics once the system is equilibrated [19].

Mathematically, this is formulated as follows. Given an operator \hat{A} that is defined within a *finite-sized* subsystem \mathcal{A} . At late times the expectation value of \hat{A} is found as

$$\lim_{t \rightarrow \infty} \lim_{L \rightarrow \infty} \langle \hat{A} \rangle_t = \text{tr} \{ \hat{\rho}_{\text{GGE}} \hat{A} \}, \quad (3.47)$$

with the *generalized Gibbs ensemble*

$$\hat{\rho}_{\text{GGE}} = \frac{1}{\mathcal{Z}} \exp \left\{ - \sum_k \lambda_k \hat{O}_k \right\}. \quad (3.48)$$

A few important remarks are in place here. First of all, we emphasize again that the statement holds only for *local* operators \hat{A} , while the total system size is sent to infinity. Consequently, nothing can be said about, for example, quantities in momentum space⁵. Second, the order of limits in (3.47) is of crucial importance. One is to take the limit of infinite system size *first* and only then the limit of late times, otherwise the statement is not well defined. The reason is that a finite system will always *revive*, or return to its initial state, if one waits long enough [48]. In a recent experiment this was seen in the correlation pattern following a sudden quench [49]. The time scale on which this revival occurs is typically exponentially long in system size. Therefore, one first needs to send the volume to infinity and only then study late times to find an equilibrium ensemble.

⁴A consistent definition of integrability for quantum systems is, contrary to integrability in classical systems, not so straightforward. Another – perhaps more accurate – definition relies on the level statistics of the Hamiltonian [21].

⁵In [47] it is explained how the GGE can be extended to make claims about nonlocal quantities as well.

3.6.2 Relaxation in quadratic models

Quadratic Hamiltonians, such as the long-range Kitaev chain from (3.7), always possess a set of conserved quantities. In our case, the conserved quantities are the occupation numbers of the Bogoliubov fermions $\langle \hat{O}_k \rangle \equiv n_k^{(\xi)} = \langle \hat{\xi}_k^\dagger \hat{\xi}_k \rangle$. The λ_k from (3.48) are Lagrange multipliers that are set by the initial conditions $\langle \hat{O}_k \rangle_{t=0} \equiv \text{tr}\{\hat{O}_k \hat{\rho}_{\text{GGE}}\}$. We can obtain them by fixing

$$n_k^{(\xi)} \equiv \text{tr}\{\hat{n}_k^{(\xi)} \rho_{\text{GGE}}\} = \frac{1}{\mathcal{Z}} \text{tr}\left\{\hat{n}_k^{(\xi)} e^{-\sum_q \lambda_q \hat{n}_q^{(\xi)}}\right\}. \quad (3.49)$$

The trace is evaluated by summing over all possible values for the $\hat{n}_k^{(\xi)}$, in the same spirit as (3.37). After evaluation, we find that $\mathcal{Z} = \prod_k (1 + e^{-\lambda_k})$ and

$$\begin{aligned} n_k^{(\xi)} &\equiv \prod_q (1 + e^{-\lambda_q})^{-1} \times \prod_q \sum_{\hat{n}_q^{(\xi)}=0,1} e^{-\lambda_q \hat{n}_q^{(\xi)}} \hat{n}_k^{(\xi)} \\ &= \prod_q (1 + e^{-\lambda_q})^{-1} \prod_{q \neq k} (1 + e^{-\lambda_q}) e^{-\lambda_k} \\ &= \frac{1}{1 + e^{\lambda_k}} \end{aligned} \quad (3.50)$$

Presented in this form, we recognize a Fermi-Dirac-like distribution for each mode $\hat{\xi}_k$. Interestingly, we can now associate an effective temperature $T_k^{\text{eff}} = \epsilon_k / \lambda_k$ (in units with $k_B = 1$) to *each* of the $\hat{\xi}_k$ operators independently, for which the value is set by the initial conditions of the quench. We had already found that $n_k^{(\xi)} = v_k^2$, such that we can compare with (3.50) to fix the Lagrange multipliers,

$$\lambda_k = \log(1/v_k^2 - 1) = 2 \log(\tan \theta_k). \quad (3.51)$$

If the late-time value of any *local* observable $\langle \hat{A} \rangle$ can be predicted according to statement (3.47), we can as well say that the density matrix $\hat{\rho}_{\mathcal{A}}(t)$ from (3.34) – containing any information on observables inside a finite-size subsystem \mathcal{A} – must converge to ρ_{GGE} at late times. More precisely, starting from definition (3.34), we want to have that

$$\begin{aligned} \text{tr}_{\bar{\mathcal{A}}}\{\hat{\rho}(t)\} = \hat{\rho}_{\mathcal{A}}(t) &= \frac{1}{\mathcal{Z}(t)} e^{-\sum_q \Omega_q(t) \hat{\gamma}_q^\dagger(t) \hat{\gamma}_q(t)} \\ &\quad \downarrow t \rightarrow \infty \\ \text{tr}_{\bar{\mathcal{A}}}\{\hat{\rho}_{\text{GGE}}\} &= \frac{1}{\mathcal{Z}} \text{tr}_{\bar{\mathcal{A}}}\left\{e^{-\sum_k \lambda_k \hat{n}_k^{(\xi)}}\right\}, \end{aligned} \quad (3.52)$$

where $\text{tr}_{\bar{\mathcal{A}}}\{\cdot\}$ means again tracing over the entire system, except subsystem \mathcal{A} .

In Appendix A.1 we provide a proof of statement (3.52) that holds for any quadratic fermionic Hamiltonian with conserved quantities in momentum space. Also, when looking back at Fig. 3.5.2, we see that the entanglement entropy of a subsystem converges at late times to the result predicted by the generalized Gibbs ensemble (dotted lines). We therefore

conclude in this section that integrable quantum systems do not reach a thermal state in the long-time limit. This prediction was confirmed in a recent cold-atom experiment with a one-dimensional system that is nearly integrable [50]. See 3.7.3 for more information.

Furthermore, since the entropy of a generalized Gibbs ensemble is always smaller than that of the corresponding Gibbs ensemble with the same energy, we can think of extracting work from an integrable quantum system by increasing its entropy. In Ref. [51] it is explained how this can be achieved by applying a series of Bragg pulses.

3.7 Some relevant experiments

To conclude this part, we would like to highlight some recent experiments in the context of the presented results. While the central model that we presented, the long-range Kitaev chain (3.7) is merely a toy model, many of the introduced concepts are generic and apply to a variety of systems. In particular, cold atoms and trapped ions provide an increasingly versatile platform to test theoretical predictions. The latter platform has the additional advantage that it can be used as a quantum simulator for long-range interacting spin lattices.

3.7.1 Spreading of correlations in trapped-ion lattices

The main interest in long-range interacting quantum systems stems from recent advances on the experimental side. Most notably, experiments with trapped ions can be interpreted as *quantum simulators* for long-range interacting spin lattices [32]. The system, depicted in Fig. 3.7.1, consists of numerous ions (~ 100) that are trapped in a magnetic field. Due to repulsive Coulomb interactions, the ions form a lattice after cooling, which can be 1D or 2D, depending on the configuration of the magnetic trap. The ions themselves have a long-lived electronic transition, such that they can be regarded as an effective two-level system – a spin. Due to the lattice structure, the transition is dressed with a number of Raman side bands, which originate from the absorption or creation of a lattice phonon, along with a spin excitation. When a laser is shone close to resonance with one of these Raman transitions, the phonons mediate an effective long-range interaction among the spins after being integrated out. This can be captured by an approximate spin-spin interaction Hamiltonian of the form,

$$\hat{H}_{\text{int}} = \frac{1}{2} \sum_{i,j;\gamma} J_{i,j}^{\gamma} \hat{S}_i^{\gamma} \hat{S}_j^{\gamma}, \quad (3.53)$$

where i, j label the lattice sites and $\gamma = x, y, z$ is the spin polarization. The coupling constants are found to follow an approximate power law $J_{i,j}^{\gamma} \propto |i - j|^{-\alpha}$. By varying the configuration of the driving lasers, the polarization of the interaction can be chosen and the power-law exponent can be tuned between $0 \leq \alpha \leq 3$, interpolating between an all-to-all and a short-range interaction.

A recent experiment in the group of C. Roos [53] studies the propagation of a spin excitation through a chain of 15 ions trapped in a 1D configuration. The dynamics of

3.7. Some relevant experiments

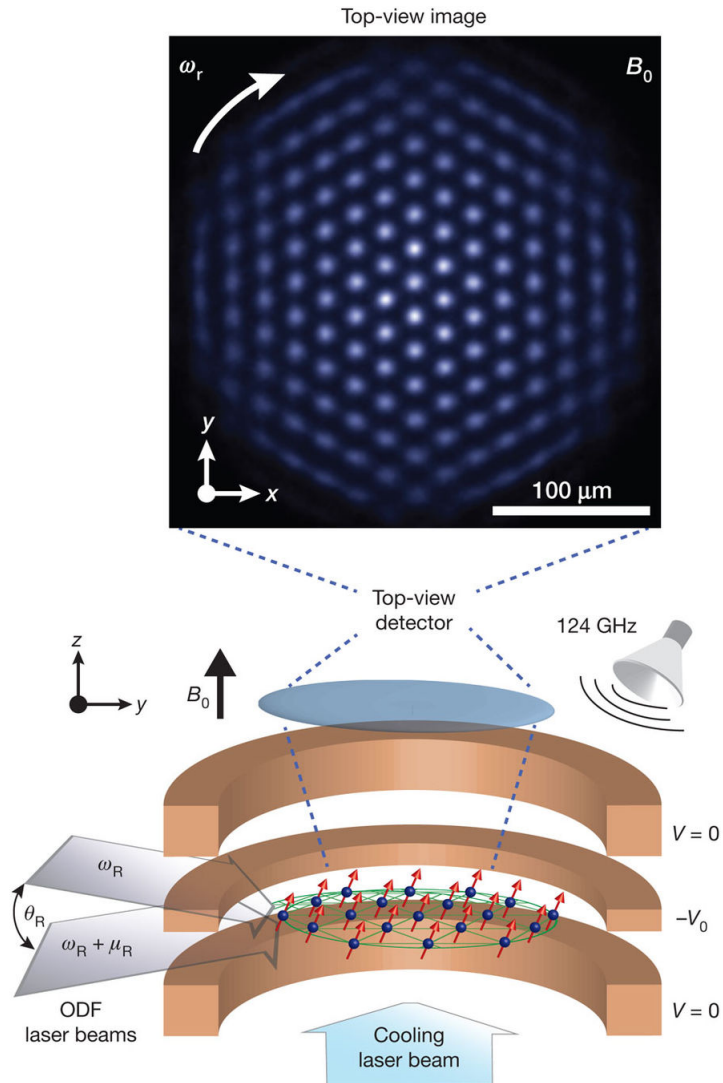


Figure 3.9: An image of a trapped-ion experiment. The ions are trapped in a magnetic field and organize themselves on a lattice after cooling. The phononic lattice modes mediate an effective power-law interaction between different spins in the lattice. Picture taken from Ref. [52].

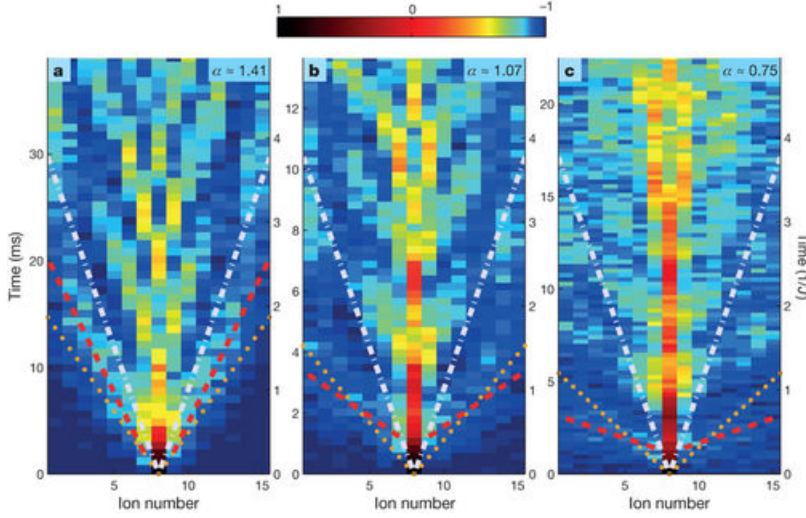


Figure 3.10: The evolution of magnetization $\langle \hat{S}_j^z(t) \rangle$ after a sudden flip of the middle spin for different ranges of interactions in the chain. The white and orange lines represent different ways to obtain an emergent lightcone in the system. The red lines are fits of the observed arrival time of the spin excitation. (a) For short-range interactions the perturbation remains well within the prediction of the orange lightcone. (b-c) The long-range interacting regime is accompanied by perturbations that leak out of the lightcone. Picture from [53].

the chain was analyzed after an abrupt spin flip of the middle spin. Depending on the effective range of interactions between the spins, according to Hamiltonian 3.53, a radically different behavior was observed in the propagation of the spin excitation. While a short-range potential gives rise to an approximate lightcone-like propagation of the magnetization $\langle \hat{S}_j^z(t) \rangle$, an almost instantaneous effect of the middle spin upon other spins in the chain is observed in the case of long-range interactions. In Fig. 3.10 the propagation of the spin excitation through the chain is illustrated.

3.7.2 The Lieb-Robinson bound with cold atoms

The Lieb-Robinson bound in its strict sense, as explained in Sec. (3.4.2), is expected to hold for lattice models with short-range interactions. When ultracold (bosonic) atoms are loaded into an optical lattice, this can be described by means of a lattice model where the atoms only interact locally (i.e. on the same lattice site) while they can tunnel from one site to an adjacent. The atoms are trapped by the *ac Stark effect* in the wells generated by two copropagating laser beams that form the lattice. In this way, one can create a one, two or three dimensional configuration for the atoms [55].

In a recent experiment [54], the dynamics of a one-dimensional chain of ultracold atoms was studied after abruptly lowering the lattice wells, thereby quenching the tunneling rate of atoms from one site to the next. The initial state was prepared such that a single atom was trapped on each lattice site. In the subsequent dynamics it is seen how elementary

3.7. Some relevant experiments

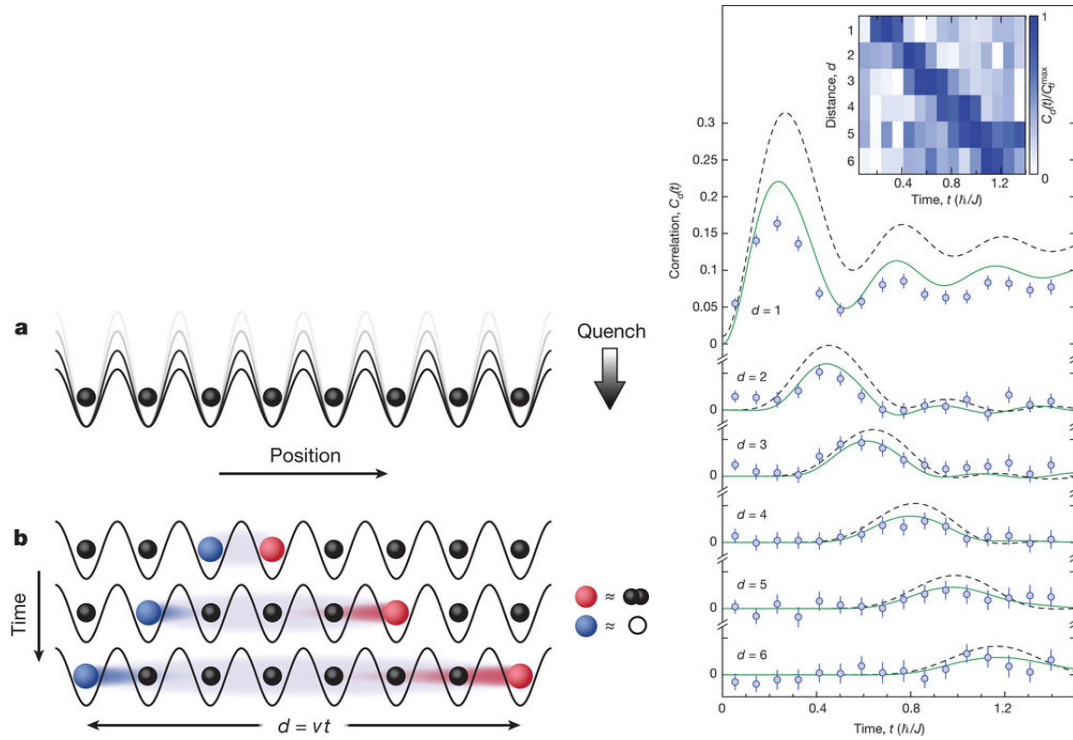


Figure 3.11: The Lieb-Robinson bound has been observed in a cold-atom system. (left) The height of the wells building up the lattice is abruptly lowered, thereby creating elementary excitations in the form of holons (empty sites) and doublons (doubly occupied sites) that travel through the chain at a velocity v . (right) The lightcone-like spreading of correlations is visible in the parity correlations between two different lattice sites in the chain. The larger the distance d between the two sites (lower lines), the longer it takes before a change in the correlation pattern is observed. From [54].

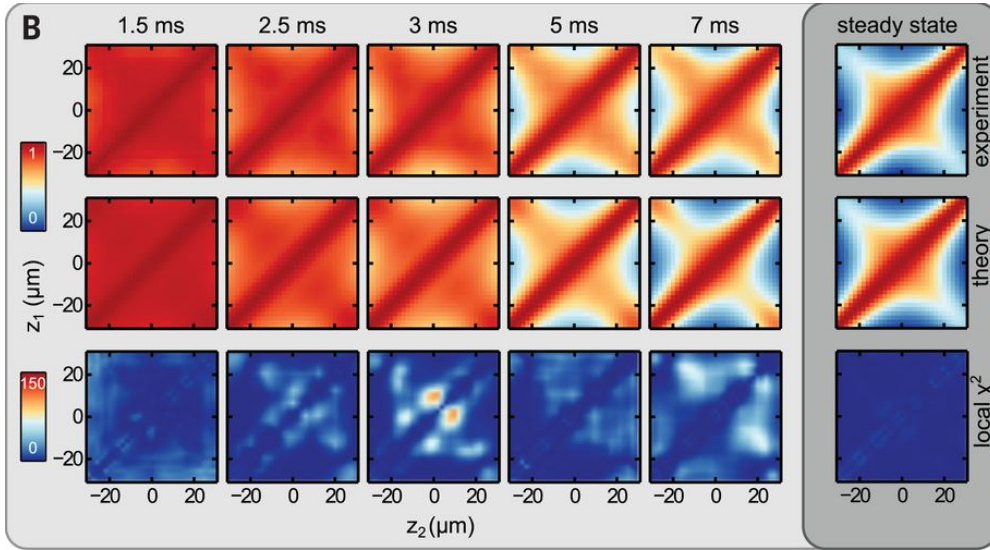


Figure 3.12: The evolution of the two-point phase correlation function after an abrupt split of a one-dimensional condensate, as measured in [50]. At late times, a dephasing process leads the system to a quasisteady or prethermal state that is described in terms of a generalized Gibbs ensemble (see Sec. 3.6). A different temperature is associated with each conserved quantity

excitations in the form of *doublons*, two atoms per site, are formed and propagate through the chain. The speed at which these excitations travel, however, is bound by a maximal velocity that can be derived from the model; this establishes a *lightcone-like* propagation of correlations. In Fig. 3.11 we show the results of the experiment.

3.7.3 Integrability in a one-dimensional condensate

Integrable quantum models in nature only exist approximately. That is, in some situations a set of fast degrees of freedom can be distinguished, which may relax on a short time scale and lead the system to a quasisteady state, often called *prethermal* state, before actual thermalization takes place. In Chapter 9 we see how this is the case for a cold bosonic gas.

One of the prototypical integrable quantum models is the *Lieb-Liniger liquid* [56], a one-dimensional gas of bosonic atoms that interact with a contact potential; this is a model that can be solved exactly with the *Bethe ansatz* [57]. An infinite number of nontrivial conserved quantities can be identified, which relate to the scattering properties of the fluid. When a three-dimensional condensate is trapped in a cigar-like configuration with strong lateral confinement, it can be shown that the low energy physics is approximately described by the Lieb-Liniger model [58].

Recently, a number of experiments were run in the group of J. Schmiedmayer to study the relaxation of the phase dynamics of an abruptly split one-dimensional condensate [50]. It was then seen how a dephasing stage at short times leads the system to a quasisteady

3.8. Conclusive remarks

(commonly called prethermal) state, described in terms of a generalized Gibbs ensemble with the conserved quantities of the model (see Sec. 3.6). Rather than fixing only a single temperature, a different temperature needs to be introduced for *each* of the conserved quantities, in order to account for the observed correlations. In Fig. 3.12 we show the measured two-point phase correlation function at different times after the quench. At late times, it converges to the values predicted by the GGE ensemble, while a thermal Gibbs ensemble with a single temperature would give substantially different predictions.

3.8 Conclusive remarks

In this part, we have studied the propagation of information and relaxation in long-range interacting quantum many-body systems. Throughout, we have used a toy model of fermions on a lattice, the long-range Kitaev chain (3.7), to introduce the concepts of nonequilibrium quantum dynamics after a sudden quench. The Lieb-Robinson bound provides a solid bound to the rate at which information can propagate through a short-range interacting lattice model. An emergent light cone limits the spreading of correlations to an effective causal region in the lattice. For long-range interacting quantum systems, no such bound exist. At best, it was shown that correlations propagate inside a power-law light cone characterized by $t \propto r^\zeta$, with $\zeta < 1$, provided $\alpha > 2D$ (see Fig. 3.5).

However, we have seen that this bound is not at all attained in the long-range Kitaev model. Instead, the largest fraction of information neatly propagates inside an emergent (linear) light cone that we can obtain from the Hamiltonian spectrum (see Fig. 3.5.3). This effect was attributed to the excitation of a wavefront of quasiparticles after the quench, which then propagates ballistically through the chain at a well-defined velocity (see Fig. 3.1). It is still an open question whether this behavior is generic for a class of long-range interacting quantum lattice models.

Contrary to our intuition, long-range interactions may drastically delay, instead of enhance, the process of relaxation in a many-body quantum system (see Fig. 3.5.2). The reason is that the quasiparticle spectrum may give rise to a wavefront of quasiparticles with velocity that approaches zero. In that case, the entanglement entropy of a block in the chain is expected to reach its equilibrium value extremely slowly.

The results of this work are summarized and published in Ref. [33].

Part II

Engineering nonclassical light from quasiparticles

Chapter 4

Photonic systems

For the second part of this thesis, we will duck into a complete different notion of out of equilibrium. Previously, we assumed that a quantum system in its entirety was abruptly taken away from equilibrium at a *specific* time instance. Yet, from there on the dynamics was fully *conservative*, ensuring that the total energy of the system is a constant in time. We now move on with looking into systems that are deliberately held out of equilibrium at *all times* due to a nonnegligible coupling with their environment. The relevant dynamics is then generated by a genuine interplay of Hamiltonian and dissipative dynamics, where the latter originates from the strong interaction with the environment. However, a larger system that contains *both* the system of interest and the environment can be taken as entirely isolated from any other environment. The dynamics of this larger system is then again governed by Hamiltonian (unitary) dynamics.

4.1 Dissipative dynamics

More precisely, we consider a Hamiltonian that can be decomposed into three different contributions, as depicted in Fig. 4.1

$$\hat{H}_{\text{tot}} = \hat{H}_S + \hat{H}_C + \hat{H}_B. \quad (4.1)$$

Here, \hat{H}_S describes the dynamics of the system of interest, without any influence of the environment. \hat{H}_B is the Hamiltonian of the reservoir (bath) and \hat{H}_C is the coupling Hamiltonian between system and reservoir.

4.1.1 The Lindblad master equation

Eventually, we are only interested in the physics that takes place inside the system and we want to incorporate the effects of the environment upon the system merely in a perturbative way. More precisely, in Ref. [59] it is explained how a *master equation* for the density matrix can be derived for the dynamics inside the system only, provided the following criteria are satisfied.

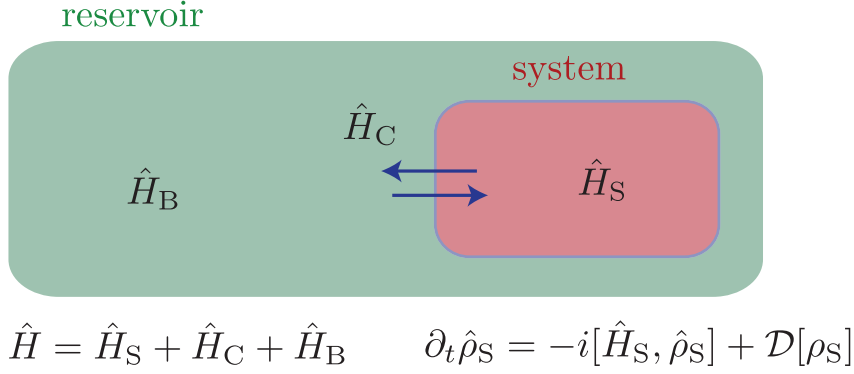


Figure 4.1: The system with Hamiltonian \hat{H}_S is embedded into a larger environment with Hamiltonian \hat{H}_B and a coupling H_C between them. We want to integrate out the dynamics generated by the \hat{H}_B , the Hamiltonian of the reservoir, to obtain an effective model for the dynamics of the system only in terms of a Lindblad master equation for the density matrix.

- **Weak-coupling limit:** The coupling between the system and its environment is assumed to be *weak*. Here, weak means that the influence of the system upon the dynamics of the reservoir is negligible. The central approximation is then called the *Born approximation*, which says that the full density matrix can be decomposed as

$$\hat{\rho}(t) = \hat{\rho}_S(t) \otimes \hat{\rho}_B. \quad (4.2)$$

With this, any dynamics of the density matrix $\hat{\rho}$ is captured in the evolution of $\hat{\rho}_S$, the density matrix of the system, while the reservoir is assumed to be roughly independent of time.

- **Markov approximation:** An additional assumption relates to a separation of time scales between the dynamics of system and environment. The correlation functions of the environment, which are in principle influenced by the interaction with the system, are expected to relax on a time scale much faster than typical time scales associated with the system dynamics. With this assumption, the time evolution for the density matrix becomes approximately local in time.

These two approximations lead to a *Lindblad master equation* for the evolution of the the density matrix of the system

$$\frac{d}{dt} \hat{\rho}_S = -i[\hat{H}, \hat{\rho}_S] + \mathcal{D}(\hat{\rho}_S) \quad (4.3)$$

Here, the first term represents the unitary evolution of the density matrix under the Hamiltonian of the system only, while the second term incorporates the effects of *dissipation* (interaction with the environment) upon the system,

$$\mathcal{D}(\hat{\rho}_S) = \sum_i \gamma_i D(\hat{L}_i) \hat{\rho}_S, \quad D(\hat{L}) \hat{\rho} = \hat{L} \hat{\rho} \hat{L}^\dagger - \frac{1}{2} (\hat{L}^\dagger \hat{L} \hat{\rho} + \hat{\rho} \hat{L}^\dagger \hat{L}). \quad (4.4)$$

4.1. Dissipative dynamics

The \hat{L}_i are commonly called the Lindblad operators of the system and they capture the coupling of the system with the environment in terms of dissipative processes. Importantly, an equation of form (4.3) constitutes the most general trace-preserving evolution of a density matrix of a quantum system [59].

While the Lindblad master equation provides a very general formalism to study dissipative dynamics, we prefer to work on the level of a stochastic operator equation. In a way, the difference is the same as the *Schrodinger* or *Heisenberg* picture at equilibrium, where the wavefunction is now replaced by the full density matrix of the quantum system. In Sec. 5.3.2 we establish this stochastic *quantum Langevin equation*, which forms the beginning point of our analysis. The more detailed derivation is given in Appendix B.1.

4.1.2 Simulation of dissipative systems

Direct numerical integration of the master equation (4.3) for a given quantum system can be an extremely difficult task when the system is substantially large. Where we only needed to evaluate the many-body wave function $|\Psi\rangle$ for a conservative quantum system, dissipative quantum systems generally require a description in terms of the full density matrix $\hat{\rho}$. For a Hilbert space of dimension N , this implies that not only N , but order N^2 degrees of freedom are to be implemented for the integration of the master equation (4.3).

One possible way to overcome to this problem is to introduce a *stochastic* wave function and to sample over various *quantum trajectories* [60]. The dissipative processes are then implemented as random *quantum jumps* during the time evolution of the stochastic wave function. These jumps have a very natural interpretation in terms of an observer watching the quantum system by performing nondestructive measurements; this was also confirmed by comparing with experiments [61, 62].

Alternatively, one can try to reduce the size of the full Hilbert space to a relevant subspace or *corner* and develop a variational method for those states only. The *corner-space renormalization method* is an iterative procedure that aims to retain only the relevant quantum states for the steady-state density matrix of the master equation (4.3) in a dissipative lattice model [63]. Also methods based on matrix product states, a formalism that has proven its value for conservative quantum systems, have been developed to integrate the master equation (4.3) [64, 65], where a variational method [66] can be particularly efficient to determine the steady state [67, 68].

A formulation that is entirely equivalent to the master equation (4.3), at least in principle, is provided by *phase-space methods*. Here, the problem is not expressed by means of the density matrix, but it is translated to phase space [69]. With a few approximations, the dynamics of the quantum fields can then be sampled with *semiclassical* trajectories of the corresponding phase-space variables. We refer to Sec. 8.3 for a derivation of this formulation in the *Wigner representation*, one of the possible phase-space representations.

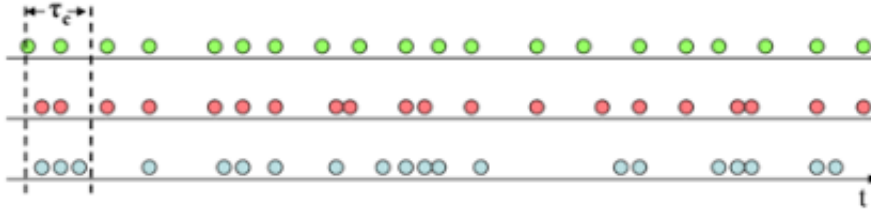


Figure 4.2: A schematic image of a train of photons as expected for (up) antibunched, (middle) Poissonian and (low) bunched photon statistics. The antibunched regime is characterized by having intensity fluctuations (4.5) $g^{(2)}(0) < 1$ and requires genuine quantum correlations in the photonic state. In the limiting case $g^{(2)}(0) \approx 0$, a train of single photons is expected to leak out of the device: *the photon blockade* (see Sec. 4.2.2). Picture from Wikipedia.

4.2 Optical systems

The open quantum systems studied in this work are *photonic* systems. Here, the system consists of a cavity or a chain of cavities coupled together, in which photons reside for some time, before they tunnel through the cavity mirrors and escape. The dissipation is, for the problems considered in this work, provided by random escape processes of photons. On the level of the Lindblad master equation, this can be captured by choosing the Lindblad operators from (4.4) as $\hat{L} \equiv \hat{a}$, where the \hat{a} operator annihilates a photon from the cavity. On the other hand, the photon losses require a constant replenishment of new photons in the cavity, in order to reach a steady photon state in the system. While different driving schemes exist, we consider a drive by a CW (continuous wave) laser beam, ensuring that a constant rate of photons is *coherently* injected into the photonic system.

4.2.1 Nonclassical light: photon antibunching

The generation of *nonclassical* states of light has been at the heart of quantum optics ever since the early days of its development. Nonclassical, in this context, means that the produced light does not have an equivalent description in terms of classical electromagnetism. Very generally, these nonclassical features can usually be attributed to the intrinsic *particle* nature of the light field, ensuring that the classical *wave* picture fails to understand the observed phenomena. Though, the distinction between *classical* and *quantum mechanical* is, in a way, merely a consequence of human perception.

One example of a class of nonclassical photon states are *Fock* states; quantum states with a well-defined number of photons and severely reduced fluctuations in their number, while having a completely arbitrary phase. Another class of nonclassical states of light are *squeezed* states. Here, the noise in one of two conjugate quadratures, such as phase and amplitude, is strongly reduced, at the cost of having larger fluctuations in the other (see

4.2. Optical systems

Fig. 6.1).

Since nonclassical features in light may arise in different forms, we need a solid criterion to classify whether a state of light is to be regarded nonclassical. We therefore need a measurable quantity that can produce an outcome that cannot be attributed to a state of light in the view of classical electromagnetism. One of the possibilities is to look at the *number* or *intensity* fluctuations of the photon field [70]. The second-order intensity correlation function of a mode \hat{a} is then defined as,

$$g^{(2)}(\tau) = \frac{\langle \hat{a}^\dagger(0) \hat{a}^\dagger(\tau) \hat{a}(\tau) \hat{a}(0) \rangle}{\langle \hat{n} \rangle^2}, \quad (4.5)$$

where $\hat{n} = \hat{a}^\dagger \hat{a}$ is the density operator. Essentially, it is the probability of detecting a first photon at time $t = 0$ and then another at a time instant $t = \tau$ later, normalized with the probability of detecting two photons coming from a random photon source with Poissonian statistics.

Our primary interest lies in the intensity correlation function at *zero* time delay, i.e. $g^{(2)}(0)$, which relates to the probability of detecting two photons at the same time. In general, three different regimes can be distinguished, as pictured in Fig. 4.2:

- $g^{(2)}(0) = 1$: The statistics of the photon source follows exactly Poissonian statistics and is called *coherent*. This value is characteristic for a beam of photons coming from a coherent laser.
- $g^{(2)}(0) > 1$: The light field has *super-Poissonian* statistics and is considered *chaotic*. All classical light fields, including thermal photon sources, fall within this category. The field is said to exhibit *bunched* photon statistics.
- $g^{(2)}(0) < 1$: The intensity fluctuations of the photon field are *sub-Poissonian*. This regime has no analog in classical electromagnetism and measuring $g^{(2)}(0) < 1$ is a manifest indication of intrinsic quantum correlations in the photon state. In this case, the photon field is said to exhibit *antibunched* photon statistics. For a *Fock* state of a single photon, we find exactly the lower limit $g^{(2)}(0) = 0$.

As a criterion to distinguish whether a state of light has intrinsic quantum properties, we will therefore apply

$$g^{(2)}(0) < 1. \quad (4.6)$$

The second-order intensity correlation function of a photon field is usually measured in a Hanbury Brown - Twiss (HBT) setup. Originally introduced to measure the angular diameter of stars emitting at radio frequencies [71], Hanbury Brown and Twiss generalized the scheme shortly thereafter to optical frequencies for measuring photon correlations [72]. The photons from the light source pass through a half-silvered mirror (what we would call a 50:50 beam splitter these days), which transmits and reflects approximately half of the photons. Measuring the coincidence rate of photons between both arms of the beam splitter,

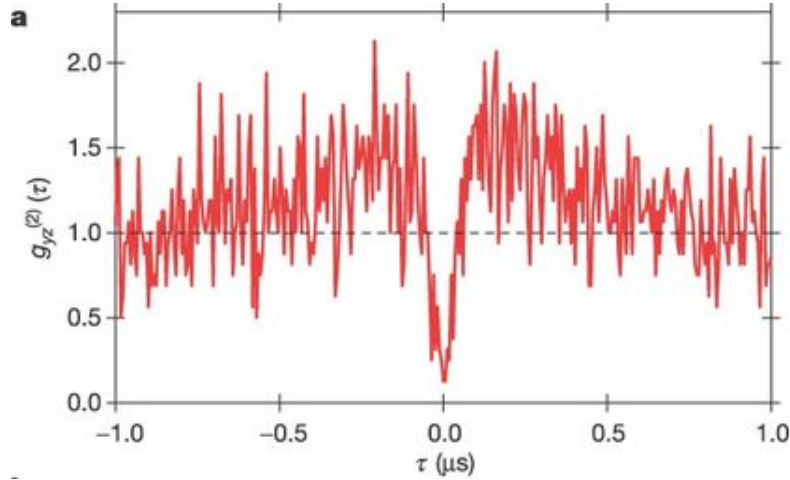


Figure 4.3: The measured delayed intensity fluctuations in the experiment from J. Kimble et al. [73]. At zero time delay, a strong suppression of intensity fluctuations is seen when a single atom is strongly coupled to the cavity mode, which is driven with a laser. This establishes $g^{(2)}(0) \approx 0$ and produces an approximate output of single photons from the cavity. The index y refers to the polarization of the incident light and z to the polarization of the measured photons.

potentially with an additional delay line in one of the arms, gives a measure for (4.5). In Fig. 6.2(d) we provide a schematic image of a HBT setup, where we need it for photon correlations after generating a nonclassical field of light.

4.2.2 The photon blockade

In the limiting case where the output of a light source produces $g^{(2)}(0) \approx 0$, the photons are expected to leak out one by one, thereby realizing a *photon turnstile device*. In the case of a (0D) cavity (see Sec. 8.1.1) this can be achieved with a strong nonlinear cavity spectrum. When a photon is sitting inside the cavity, the resonance shifts to higher energies, such that it becomes energetically forbidden for a second photon to enter: *the photon blockade* [74]. The result is that this cavity then emits one photon after the other when it is continuously pumped, thus producing a train of single photons as output.

Today, a plethora of experimental platforms have been realized to observe the photon blockade. The first experiment in this context was performed by J. Kimble et al. [73] and utilized a single atom trapped in an optical cavity. In the regime of strong coupling between the atom and the cavity, the linear cavity spectrum, being that of an harmonic oscillator, is converted into the highly anharmonic ladder of states from the *Jaynes-Cummings model*. The cavity is now pumped by a laser beam with frequency close to resonance with the $|1, \pm\rangle$ state, where the number indicates the number of photons in the cavity and \pm the state of the atom, which is treated as a two-level system. The highly nonlinear spectrum of the

4.2. Optical systems

cavity now realizes that the $|2, \pm\rangle$ -state, which would be reached by introducing a second photon from the laser in the cavity, is detuned with an energy substantially larger than the cavity linewidth. Consequently, before the first photon has escaped from the cavity, it is practically forbidden for a second to enter, resulting in a strongly antibunched output stream of photons. In Fig. 4.3 we show the measured delayed intensity correlations $g^{(2)}(\tau)$ and we see that the signal satisfies $g^{(2)}(0) \approx 0$ at zero time delay, suggesting that the cavity can only contain one photon at a time. Alternatively, when the laser frequency is tuned close to the two-photon resonance, strong bunching is seen in the statistics of the output photon beam.

In a later stage, the photon blockade was also observed by embedding a quantum dot in a photonic crystal, an optical nanostructure that establishes an effective lattice for the photons [75, 76]. Here, the quantum dot acts as an effective atom, or two-level system, which strongly couples to the photonic-crystal cavity. This produces very similar effects when the system is driven with a coherent beam of light.

Recently, the phenomenon was also reported at microwave frequencies in a superconducting circuit [77, 78], where microwave resonators are coupled to superconducting qubits. In Sec. 8.1.2 we provide a short overview of this topic in the context of *cavity arrays*. In that case, when a series of atom-resonator systems, operating in the photon-blockade regime, are coupled together, one can think of true *quantum simulation with light*. A state ‘1’ or ‘0’ can be assigned to the presence or absence of a photon in a cavity, or to two other clearly distinguishable quantum states. We refer to review articles [79, 80] for more information on this field of research.

4.2.3 The unconventional photon blockade

The photon blockade in its strict sense relies on a mechanism to generate a strong nonlinear spectrum for photons inside a cavity, such as a strong coupling between the cavity mode and an atom inside. Technically, however, this may be difficult because it requires a strong coupling of a cavity photon to microscopic structures, such as an (artificial) atom. Many systems, including the exciton-polariton systems that we discuss in Chapter 5, offer superb flexibility in terms of control and tunability, but the mediated photon-photon interactions are weak as compared to currently achievable linewidths. The reported values for $g^{(2)}(0)$ are then usually very close to 1, the value corresponding to the driving laser field, with only a minor correction coming from mediated photon interactions [82].

Recently, it was shown that the photon blockade is not necessarily a direct consequence of a strong cavity nonlinearity [83, 81, 84, 85]. Later dubbed the *unconventional photon blockade*, it was illustrated how certain setups consisting of two coupled cavities can produce a strong suppression of $g^{(2)}(0)$, in spite of having interactions that are substantially weaker than the dissipation rate of the cavity. A detailed overview of the phenomenon can be found in Ref. [86].

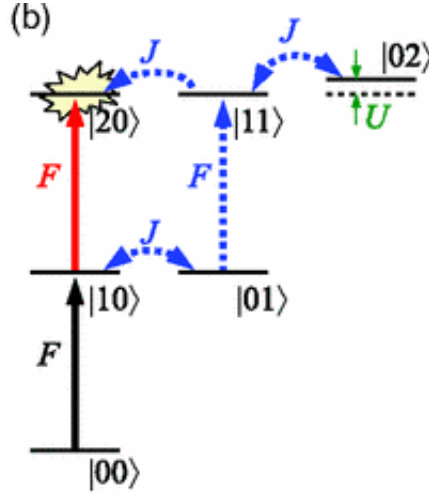


Figure 4.4: The diagram from [81] that explains the interference mechanism behind the *unconventional photon blockade*. A photon can be directly injected in the first cavity by the driving laser, or it may involve a tunneling process to the second cavity and back. When these two independent pathways are made to destructively interfere with each other, strong antibunched statistics is predicted for the output field of driven cavity.

In Fig. 4.4, we present the result from [81], where the unconventional photon blockade was first explained in terms of a subtle interference effect between two independent pathways to inject a second photon in a cavity. Here, the setup consists of two coupled microcavities, of which only the first one is pumped with a coherent laser. Photons inside the system have a probability to hop from one cavity to the other, as quantified by the tunneling rate J , while photons inside the same cavity interact with each other (see Chapter 8, where we consider a whole chain of such cavities). The nonlinearity is taken to be weak, such that only a slight shift of the cavity resonance is observed due to interactions. When there is a photon inside the first cavity, there are two possible ways to inject a second one inside this cavity. First, there is the possibility to inject another photon directly with the pumping laser beam (represented with F on the diagram) to make a transition $|10\rangle \xrightarrow{F} |20\rangle$, where the numbers label the number of photons inside each cavity. Alternatively, a photon that is already inside the driven cavity can first hop to the other, after which a new photon is injected in the cavity, such that they both contain one photon. Then, the photon in the non-driven cavity can tunnel back to the first. This is represented by the series of processes $|10\rangle \xrightarrow{J} |01\rangle \xrightarrow{F} (|11\rangle \xleftarrow{J} |02\rangle) \xrightarrow{J} |20\rangle$, where ‘ \xleftrightarrow{J} ’ represents a superposition under tunneling J . After choosing the correct detuning from the laser to the cavity resonance, these two independent pathways can be made to interfere destructively with each other, thereby making it practically forbidden for two photons to reside inside the driven cavity at the same time. It is then seen that $g^{(2)}(0) \approx 0$ for the driven cavity, thereby realizing an approximate train of single photons in a device with only weak photon-photon interactions.

4.2. Optical systems

The photon state of a device with a weak nonlinearity can usually be described in terms of a coherent field, coming from the laser, and quantum fluctuations with a Gaussian nature that arise from interactions [87]. In Ref. [88] it was explained how the strong antibunching features from the unconventional photon blockade can be understood in terms of *Gaussian states of light*, which is explained in Sec. 6.1.2. In Chapter 5, we review how weak mediated photon-photon interactions in a planar microcavity give rise to an approximate Gaussian output state. We then continue in Chapter 6 with illustrating how this output state can be manipulated in a selection and interference scheme to engineer photon states with strongly antibunched statistics, exactly in the spirit of [88].

Chapter 5

A quantum fluid of light inside a planar microcavity

A planar microcavity consists of two mirrors that are placed close to each other, on the micrometer scale, and can be utilized to generate a strong photonic field inside. When a nonlinear material is placed between the two mirrors to mediate effective photon-photon interactions, the resulting system can be regarded as a 2D fluid of photons: ‘a quantum fluid of light’ [87]. In this chapter, we go through the basics of this setup to set the stage for the next, where we exploit the photons escaping from a nonlinear planar microcavity to produce nonclassical states of light.

The content of this chapter is mainly based on the excellent review articles [87] and [89], but also on the PhD theses from Maarten Baeten [90], Selma Koghee [91] and myself (master) [92].

5.1 Microcavities

The cavities used to engineer exciton-polariton systems are semiconductor microcavities, which consist of two distributed Bragg reflectors. Chapter 6 deals with two-dimensional planar devices, where polaritons are confined in the direction perpendicular to the plane. We will then continue in Chapter 8 with the study of a chain of 0D cavities, in which photons can hop from one cavity to the other.

The distributed Bragg reflectors from a microcavity consist of alternating layers of materials with different refractive index, optimized to confine photons between the two mirrors. The reflectors consist of a number of quarter-wavelength thick layers with a varying refractive index. The photons are confined in the direction perpendicular to the cavity plane, such that a standing wave is generated between the two mirrors, thereby maximizing the radiation intensity at its antinodes. As the Bragg reflectors are not perfect mirrors, there is always an intrinsic loss rate of photons that escape from the cavity, making a pumping laser necessary to replenish the system. Furthermore, the mirrors are usually designed with

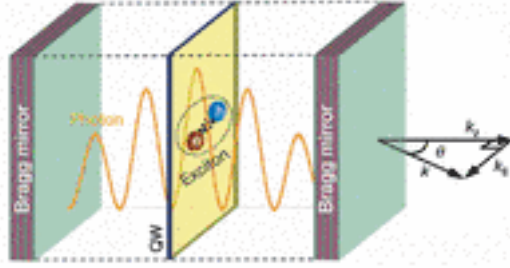


Figure 5.1: A schematic image of a microcavity. Photons are confined between two distributed Bragg mirrors and form a standing wave. At the antinode of the wave a quantum well is placed, a semiconductor material with an excitonic resonance that is close to the photon frequency of the cavity. In the strong coupling regime, the photons and excitons form new hybrid particles, the *exciton-polaritons*. A photon with in-plane momentum \mathbf{k} escapes from the cavity at an angle θ_k with $\sin \theta_k = ck/\omega_L$, where ω_L is the laser frequency and c the speed of light. Picture from [93].

a wedge, such that the distance between the mirrors varies in space. With this, also the resonance frequency of the standing wave changes throughout the 2D plane of the sample.

At the antinodes of the standing wave, a *quantum well* is placed, in which excitons are excited by the strong photonic field. The quantum well is usually made of III-V semiconductor materials, such as GaAs or AlGaAs. See figure 5.1 for a schematic image of a standard microcavity.

5.1.1 Quality factor

Photons confined between the two mirrors have a finite lifetime inside the cavity before they escape again by tunneling through one of the mirrors. The quality factor or Q-factor quantifies how well a cavity confines photons inside. It is defined as

$$Q = \frac{\omega_c}{\gamma_c}, \quad (5.1)$$

where ω_c is the frequency of the light inside and $\gamma_c = 1/\tau_c$ is the photon decay rate, with τ_c the average photon lifetime. Roughly speaking, it is therefore defined as how many times a photon bounces off the cavity mirrors before it finally tunnels through.

For this work, we will mainly focus on GaAs cavities, which have a typical photon lifetime of 10 – 100ps and operate at roughly 10^3 GHz, such that they have typical Q-factors ranging between 10^4 and 10^5 . The inevitable losses of photons on a timescale of a few picoseconds implies that the system should be actively replenished with new photons to reach a steady state. The injection mechanism of photons is typically provided by an external laser beam, shone on the cavity.

5.1. Microcavities

5.1.2 The photon dispersion

The confinement of photons between the two cavity mirrors implies that their motion in the z -direction, the axis perpendicular to the cavity plane, is quantized. The in-plane momentum, on the other hand, can be set with the angle of incidence of the laser beam and is a continuous degree of freedom.

For a cavity with distance w between the mirrors and a refractive index n , the energy of a photon inside the cavity that moves with an in-plane momentum \mathbf{k} is found as (we set $\hbar = 1$ again)

$$\omega_{\text{ph}}(\mathbf{k}) = \frac{c}{n} \sqrt{k^2 + \left(\frac{2\pi N}{w}\right)^2} \approx \omega_0 + \frac{k^2}{2m_{\text{ph}}}, \quad (5.2)$$

where N is the index of the N th transverse mode of the standing wave in the z -direction. Because the dynamics is frozen in the z -direction, we conclude that we can regard photons with low in-plane momentum inside the cavity as 2D particles with effective mass $m_{\text{ph}} = \frac{2\pi n N}{cw}$.

A photon that propagates inside the cavity plane with in-plane momentum \mathbf{k} is then expected to fly out at a nonzero angle (see Fig. 5.1). By using momentum conservation on both sides of the cavity mirror, we then derive that this angle is given by

$$\sin \theta_k = \frac{ck}{\omega_c}. \quad (5.3)$$

At this point, we can already anticipate that we will heavily exploit this property for developing a selection and interference scheme to generate nonclassical light in Chapter 6.

5.1.3 Quantum-well excitons

Excitons are quasiparticles that consist of a bound electron-hole pair in a semiconductor device. An excited electron can hop from the valence band to the conduction band and is free to start moving inside the lattice. A positively charged vacancy, a hole, is left in the lattice where the electron used to sit. Both the electron and the hole have a specific energy-momentum relation, depending on the configuration of the atoms that build up the lattice, which is known as the electronic band structure of a solid.

There can exist a number of intermediate metastable energy levels corresponding to the formation of a bound electron-hole pair. In that case, the excited electron and the hole bind by the attractive Coulomb interaction to a new quasiparticle, known as an exciton. Thanks to their dipolar structure, the excitons inside a quantum well can couple to light. Since the Bohr radius of these excitons is typically much smaller than the interparticle distance, the internal fermionic structure of an exciton can be neglected, reducing them to composite bosonic particles.

On the other hand, the binding length of an exciton is usually substantially larger than the lattice constant of the corresponding semiconductors materials. This justifies the

approximation of considering excitons as independent quasiparticles, as lattice effects are averaged out over the typical length scales that are dealt with. Furthermore, this large length scale corresponds to momenta close to the center of the Brillouin zone, where both electrons and holes have an approximately quadratic dispersion. Effectively, this means that the in-plane dispersion of an exciton inside the quantum well is found as

$$\varepsilon_{\text{ex}}(\mathbf{k}) = \varepsilon_{\text{ex}}^0 - \epsilon_b + \frac{k^2}{2m_{\text{ex}}}, \quad (5.4)$$

with $\varepsilon_{\text{ex}}^0$ the resonance energy of the exciton and ϵ_b is the intrinsic binding energy of the electron-hole pair. In analogy with a hydrogen atom, the binding energy of the n -th level is then given by

$$\epsilon_{b,n} = \left(\frac{\mu}{\epsilon^2 m_0} \right) \frac{E_R}{n^2},$$

with μ the reduced mass of the electron-hole pair, m_0 the electron rest mass, ϵ the electric permeability of the material and E_R the Rydberg constant.

The exciton mass m_{ex} , essentially the sum of the electron and hole band mass, is typically a few orders of magnitude larger than the effective photon mass that we found before; $m_{\text{ph}} \sim 10^{-4} m_{\text{ex}}$. We can therefore approximate the exciton dispersion (5.4) as roughly flat as compared to the photon dispersion from (5.2).

5.2 Exciton-polaritons inside the quantum well

We have now reviewed how, on the one hand, photons behave when they are confined inside a microcavity and how, on the other, excitons come about inside the quantum well. The main idea of these microcavity devices is to generate a strong coupling between the photons and the excitons. This gives rise to new hybrid particles: the *exciton-polaritons*. In this section, we aim to review this strong-coupling regime and to establish the final theory of exciton-polaritons inside a microcavity.

5.2.1 The free Hamiltonian

The photons inside the cavity excite excitons in the quantum well, which will in turn decay again and emit a photon in the cavity. In the strong-coupling regime, this can be described by introducing a *Rabi* coupling between the photon and exciton field operators. The free Hamiltonian, i.e. the Hamiltonian that does not yet take into account particle interactions, can then be formulated in terms of the photon and exciton field operators

$$\hat{H}_0 = \sum_{\mathbf{k},\sigma} \left(\hat{\psi}_{\mathbf{k},\sigma}^\dagger, \hat{D}_{\mathbf{k},\sigma}^\dagger \right) \begin{pmatrix} \omega_{\text{ph}}(\mathbf{k}) & \Omega/2 \\ \Omega/2 & \varepsilon_{\text{ex}}(\mathbf{k}) \end{pmatrix} \begin{pmatrix} \hat{\psi}_{\mathbf{k},\sigma} \\ \hat{D}_{\mathbf{k},\sigma} \end{pmatrix}. \quad (5.5)$$

Here, $\hat{\psi}_{\mathbf{k},\sigma}$ is the photonic and $\hat{D}_{\mathbf{k},\sigma}$ the excitonic creation operator for a particle with in-plane momentum \mathbf{k} and spin σ . While in principle both the photon and the exciton

5.2. Exciton-polaritons inside the quantum well

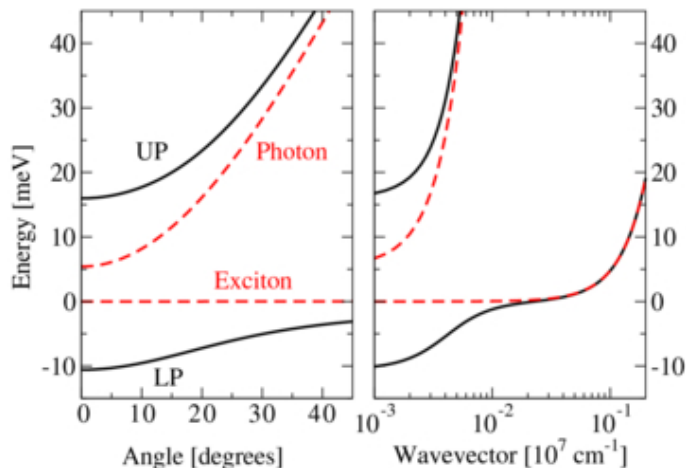


Figure 5.2: In the strong-coupling regime, the photons and excitons hybridize to form the lower and upper polariton modes. (left) The photon dispersion (5.2) and exciton dispersion (5.4) as a function of the angle of emission θ_k (6.13). Hybridization leads to the UP and LP dispersions. (right) Same, but in function of in-plane momentum \mathbf{k} . From [89], plotted for the parameters (m_e is the electron rest mass) $m_{\text{ex}} = 0.08m_e$, $m_{\text{ph}} = 3 \times 10^{-5}m_e$, $\Omega_R = 26\text{meV}$ and $\delta = 5.4\text{meV}$.

carry a spin degree of freedom, the polarization of the incident laser can be tuned such that approximately only a single spin component is populated. From now on, we will therefore omit this degree of freedom and deal with a single spin component only. The in-plane dispersion of photons $\omega_{\text{ph}}(\mathbf{k})$ and excitons $\epsilon_{\text{ex}}(\mathbf{k})$ from (5.5) is given in (5.2) and (5.4) respectively, while the Rabi coupling Ω quantifies the rate at which a photons can be converted into an exciton and vice versa.

By diagonalizing Hamiltonian (5.5), we find the energy levels of the two hybridized modes, the *upper* (UP) and *lower* (LP) polariton modes

$$E_k^{(UP,LP)} = \frac{1}{2} \left(\delta + \frac{k^2}{2m_{\text{ph}}} \pm \sqrt{\left(\delta - \frac{k^2}{2m_{\text{ph}}} \right)^2 + \Omega^2} \right), \quad (5.6)$$

with $\delta = \omega_{\text{ph}}(0) - \epsilon_{\text{ex}}(0)$ the detuning between the bottom of the photon and exciton dispersion. See Fig. 5.2 for an image of the photon and exciton dispersion, which hybridize into the upper and lower polariton modes. These modes, in turn, are found as a rotation of the photon and exciton fields

$$\begin{pmatrix} \hat{\psi}_{\mathbf{k}} \\ \hat{D}_{\mathbf{k}} \end{pmatrix} = \begin{pmatrix} \cos \theta_k & \sin \theta_k \\ -\sin \theta_k & \cos \theta_k \end{pmatrix} \begin{pmatrix} \hat{U}_{\mathbf{k}} \\ \hat{L}_{\mathbf{k}} \end{pmatrix}, \quad (5.7)$$

with rotation angle $\tan 2\theta_k = \Omega / (\omega_{\text{ph}}(k) - \epsilon_{\text{ex}}(k))$.

In practice, we assume the system to be excited by a laser beam with energy and momentum close to the lower-polariton branch. Provided the Rabi frequency Ω is substantially

larger than the linewidth of the laser and the residual temperature, we can assume that only the lower-polariton branch is populated, so that we can write down an approximate model in terms of these modes only

$$\hat{H}_0^{(LP)} = \sum_{\mathbf{k}} E_k^{(LP)} \hat{L}_{\mathbf{k}}^\dagger \hat{L}_{\mathbf{k}}, \quad (5.8)$$

with $E_k^{(LP)}$ the lower-polariton dispersion, given in (5.6).

In addition, when the laser excitation is restricted to polaritons sufficiently close to the bottom of the LP branch, where the dispersion is roughly quadratic, we can approximate further

$$E_k^{(LP)} \approx \epsilon_0^{\text{LP}} + \frac{k^2}{2m_{\text{LP}}}, \quad (5.9)$$

with the effective polariton mass

$$m_{\text{LP}} = m_{\text{ph}} \frac{\sqrt{\delta^2 + \Omega^2}}{\delta + \sqrt{\delta^2 + \Omega^2}}. \quad (5.10)$$

At this point, we have established an effective free model for the microcavity exciton-polaritons, where the dispersion is taken to be approximately quadratic with LP mass m_{LP} . The next step consists of introducing interactions between the lower polaritons.

5.2.2 Adding interactions

While photons inside the cavity do not (or only extremely weakly) interact with each another, the excitons inside the quantum well do. The main contribution to exciton-exciton interactions is a fermionic exchange interaction, repulsive in nature, which originates from exchanging a hole or an electron between two excitons. For the lower-polaritons, which are excited at the bottom of the branch, we can assume the excitonic fraction to be approximately constant for the range of momenta that we consider [87, 89].

The polariton-polariton interactions between the lower-polaritons can then be formulated with an effective interaction Hamiltonian

$$\hat{H}_{\text{int}} = \frac{1}{2} \sum_{\mathbf{k}, \mathbf{k}', \mathbf{q}} V(\mathbf{q}) \hat{L}_{\mathbf{k}'-\mathbf{q}}^\dagger \hat{L}_{\mathbf{k}+\mathbf{q}}^\dagger \hat{L}_{\mathbf{k}'} \hat{L}_{\mathbf{k}}. \quad (5.11)$$

Typically, the interaction potential $V(\mathbf{q})$ has a short-ranged nature as compared to other length scales, such as the average interparticle distance. It is therefore a good approximation to replace the true interaction potential with a *contact* potential $V(\mathbf{q}) \approx g$, making that the exchanged momentum in a collision is roughly independent of the incoming momenta \mathbf{k} and \mathbf{k}' .

The large interest in the platform of microcavity-polaritons stems in part from the mediated photon-photon interactions inside the cavity, a feature that is non-existing for

5.2. Exciton-polaritons inside the quantum well

photons in vacuum¹. However, the interaction constant is relatively small as compared to achievable cavity linewidths today. The dimensionless parameter that characterizes the ‘strength’ of interactions in a 2D system is mg (in units of $\hbar = 1$), with m the particle mass, has typical values ranging between 10^{-4} and 10^{-5} for polariton systems. Part of this work (see next chapter) consists of illustrating how the ‘quantum’ features attributed to these interactions can be severely amplified, in spite of the small coupling constant intrinsic to the photonic system.

5.2.3 Pumping

There is a constant rate of new photons that enter the cavity and others that tunnel through the mirrors and escape from the fluid; this makes exciton-polaritons in semiconductor devices an inherent nonequilibrium system. The injection of photons can be captured on the level of the Hamiltonian as they all enter coherently (i.e. with same phase) in the system that is pumped with a coherent laser beam.

For a wide enough pump spot and a perpendicularly incident laser beam, only the $k = 0$ mode of the polaritons is pumped. This can be described with the pumping Hamiltonian

$$H_{\text{pump}}(t) = F e^{-i\omega_L t} \hat{L}_0 + F^* e^{i\omega_L t} \hat{L}_0^\dagger, \quad (5.12)$$

where F is the pumping rate of the laser beam and ω_L the frequency.

Besides the coherent pumping scheme, where all polaritons are injected close to the bottom of the LP dispersion, polaritons can also be pumped incoherently. In this case, polaritons are injected with an energy much higher than the LP branch, after which they relax to lower energies through collisions. Interestingly, across a threshold point in pumping power, one can see the *spontaneous* creation of a condensate with macroscopic occupation of the $k = 0$ mode of lower polaritons; Bose-Einstein condensation (BEC) of a polaritonic system [93]. Also in the coherent pumping scheme the polaritons exhibit coherence and long-range order, but here these properties are directly inherited from the incident laser beam and are therefore not spontaneously generated.

Furthermore, in the OPO (optical parametric oscillator) scheme, the polaritons are injected close to the inflection point of the LP branch, such that a parametric down conversion process can take place and three modes are microscopically populated [94]. Finally, photons can also be injected from a non-Markovian reservoir, as studied in [95], where the bandwidth of the reservoir strongly influences the steady-state properties of the fluid.

5.2.4 The full Hamiltonian

By adding Hamiltonians (5.5), (5.11) and (5.12) together, we find the full Hamiltonian of the system of lower polaritons. We can formulate the resulting Hamiltonian in position

¹In theory, there is an extremely small photon-photon interaction in vacuum predicted by quantum field theory. This originates from two photons being converted into a virtual electron-positron pair, which then mediates a very weak interaction, completely negligible in these circumstances.

space by defining the Fourier transforms of the LP field operators

$$\hat{\Psi}(\mathbf{r}) = \frac{1}{\sqrt{V}} \sum_{\mathbf{k}} \hat{L}_{\mathbf{k}} e^{i\mathbf{k}\mathbf{r}}, \quad \hat{\Psi}^\dagger(\mathbf{r}) = \frac{1}{\sqrt{V}} \sum_{\mathbf{k}} \hat{L}_{\mathbf{k}}^\dagger e^{-i\mathbf{k}\mathbf{r}} \quad (5.13)$$

After performing the additional transformation $\hat{\Psi} \rightarrow \hat{\Psi} e^{i\omega_L t}$ to remove the time dependence of the drive, we then find that the full Hamiltonian for the lower-polaritons close to the bottom of the LP branch can be formulated as

$$\hat{H}_{\text{pol}} = \int d\mathbf{r} \left[\hat{\Psi}^\dagger \left(-\frac{\nabla^2}{2m} - \omega_L \right) \hat{\Psi} + \frac{g}{2} \hat{\Psi}^\dagger \hat{\Psi}^\dagger \hat{\Psi} \hat{\Psi} + F(\hat{\Psi} + \hat{\Psi}^\dagger) \right], \quad (5.14)$$

where we introduce simplified notation for the LP mass $m \equiv m_{\text{LP}}$. Importantly, the laser frequency ω_L enters Hamiltonian (5.14) as a tunable *chemical potential* (loosely speaking). We will later see that the freedom to tune this quantity, by simply varying the laser frequency, may have very surprising consequences.

5.3 Coupling to a reservoir: the quantum Langevin equation

At this point, we have established the Hamiltonian for lower polaritons injected close to the bottom of their branch, but we still have to deal with the explicit openness of the setup. The constant rate of coherently injected photons can be treated on a Hamiltonian footing, but the losses are inherently dissipative and cannot be described by unitary dynamics. When we consider a larger system, however, which encompasses both the system of interest and the environment, we can again assume the dynamics to be unitary.

5.3.1 Including the reservoir: the total Hamiltonian

For this we need to consider the Hamiltonian of the entire system, which consists of the polariton Hamiltonian (5.14), the Hamiltonian of the environment and a coupling between the two (see Chapter 4),

$$\hat{H} = \hat{H}_{\text{pol}} + \hat{H}_{\text{env}} + \hat{H}_{\text{coup}}. \quad (5.15)$$

The reservoir is in this case parametrized as a set of harmonic oscillators, which represent the photonic modes of the outer world,

$$\hat{H}_{\text{env}} = \sum_l \omega_l \int d\mathbf{r} \hat{b}_l^\dagger(\mathbf{r}) \hat{b}_l(\mathbf{r}), \quad (5.16)$$

where l is some arbitrary index to label the modes and ω_l is the frequency of mode l . The coupling between the system of interest, the microcavity, and the environment is then parametrized with a coupling Hamiltonian

$$\hat{H}_{\text{coup}} = \sum_l \kappa_l \int d\mathbf{r} [\hat{\Psi}(\mathbf{r}) \hat{b}_l^\dagger(\mathbf{r}) + \hat{\Psi}^\dagger(\mathbf{r}) \hat{b}_l(\mathbf{r})]. \quad (5.17)$$

5.3. Coupling to a reservoir: the quantum Langevin equation

With this, we essentially formulate that a polariton inside the cavity at position \mathbf{r} , represented by $\hat{\Psi}(\mathbf{r})$, can be transformed into one of the outer modes \hat{b}_l with a coupling κ_l by tunneling through the cavity mirrors, or vice versa.

It is our aim to establish an effective model in terms of the polariton degrees of freedom only. One possibility is to consider the density matrix of the full system and then *trace out* the degrees of freedom of the reservoir to end up with a Markovian *master equation* for the system density matrix [59]. The resulting equation is then decoupled from the environment,

$$\partial_t \hat{\rho} = -i[\hat{H}_{\text{pol}}, \hat{\rho}] + \mathcal{D}[\hat{\rho}], \quad (5.18)$$

with a dissipator of the Lindblad form to capture the incoherent photon losses,

$$\mathcal{D}[\hat{\rho}] = \frac{\gamma}{2} \int d\mathbf{r} \left(2\hat{\Psi}\hat{\rho}\hat{\Psi}^\dagger - \hat{\rho}\hat{n} - \hat{n}\hat{\rho} \right). \quad (5.19)$$

Here, $\hat{n}(\mathbf{r}) = \hat{\Psi}^\dagger(\mathbf{r})\hat{\Psi}(\mathbf{r})$ is the density of the polaritonic field $\hat{\Psi}$ at point \mathbf{r} and γ is the effective lifetime of photons inside the cavity. However, although entirely equivalent, we prefer to work on the level of a stochastic operator equation for the lower-polariton field $\hat{\Psi}(\mathbf{r}, t)$.

5.3.2 The quantum Langevin equation

In Appendix B.1 we provide a detailed derivation of the central equation for this part; the *quantum Langevin equation*. However, for now it suffices to realize that the quadratic nature of the reservoir Hamiltonian (5.16) suggests that we have to introduce noise operators $\hat{\xi}(\mathbf{r}, t)$ with a *Gaussian* character. At temperatures much lower than the relevant energy scales inside the microcavity (i.e. $k_B T \ll \omega_L$, with ω_L the laser frequency) we then conclude that this noise is characterized by the correlation functions

$$\begin{aligned} \langle \hat{\xi}(\mathbf{r}, t)\hat{\xi}(\mathbf{r}', t') \rangle &= \langle \hat{\xi}^\dagger(\mathbf{r}, t)\hat{\xi}(\mathbf{r}', t') \rangle = 0, \\ \langle \hat{\xi}(\mathbf{r}, t)\hat{\xi}^\dagger(\mathbf{r}', t') \rangle &= \delta(\mathbf{r} - \mathbf{r}')\delta(t - t'). \end{aligned} \quad (5.20)$$

Adding noise and dissipation, and evaluating the evolution of the polaritons under their own Hamiltonian (5.14), we then find an equation of motion for the polariton field operator $\hat{\Psi}(\mathbf{r}, t)$ that captures the full dynamics of the polaritons in the microcavity [87],

$$i\partial_t \hat{\Psi}(\mathbf{r}, t) = \left(-\frac{\nabla^2}{2m} - \delta + g\hat{\Psi}^\dagger(\mathbf{r}, t)\hat{\Psi}(\mathbf{r}, t) - i\frac{\gamma}{2} \right) \hat{\Psi}(\mathbf{r}, t) + \sqrt{\gamma}\hat{\xi}(\mathbf{r}, t) + F, \quad (5.21)$$

with $\delta = \omega_L - \epsilon_{\text{LP}}(0)$ the detuning of the laser frequency from the bottom of the bare LP dispersion.

Note that, while the evolution of $\hat{\Psi}(\mathbf{r}, t)$ is not generated by unitary dynamics, the inclusion of dissipative processes with the losses, derived in Appendix B.1, and the noise, given in (5.20), ensures that $\hat{\Psi}(\mathbf{r}, t)$ preserves bosonic commutation relations during its time evolution. In particular, it is easy to verify that $[\hat{\Psi}(\mathbf{r}, t), \hat{\Psi}^\dagger(\mathbf{r}', t')] = \delta(\mathbf{r} - \mathbf{r}')\delta(t - t')$ is conserved in time under (5.21).

5.4 The Bogoliubov approximation

We have seen previously that the dimensionless interaction parameter in a polaritonic system typically satisfies $m \cdot g \ll 1$, which justifies the treatment of interactions on a perturbative level. In the coherent pumping scheme, as considered here, all photons enter the cavity with the same phase, which they inherit from the pumping laser beam. Oriented perpendicularly to the microcavity, the vast majority of photons inside the well will then be found in the zero-momentum mode and form a condensate, while there is only a small *depletion* of fluctuations with nonzero momentum due to interactions.

In the spatially uniform configuration, we can then conveniently parametrize the polariton field operator as

$$\hat{\Psi}(\mathbf{r}, t) = \psi_0(t) + \hat{\phi}(\mathbf{r}, t) = \psi_0(t) + \frac{1}{\sqrt{V}} \sum_{\mathbf{k}} \hat{\phi}_{\mathbf{k}}(t) e^{i\mathbf{k} \cdot \mathbf{r}}, \quad (5.22)$$

where the *classical* field ψ_0 represents the coherent component and the quantum fields $\hat{\phi}_{\mathbf{k}}(\mathbf{r}, t)$ are the fluctuations around it, which arise from interactions. We will show interest in the situation where $n_0 \gg 1/V \sum_{\mathbf{k}} n_{\mathbf{k}}$, with $n_0 = |\psi_0|^2$ and $n_{\mathbf{k}} = \langle \hat{\phi}_{\mathbf{k}}^\dagger \hat{\phi}_{\mathbf{k}} \rangle$; i.e. when almost all photons are found in the zero-momentum mode, as is expected for weak enough interactions.

5.4.1 The mean field equation

The crudest approximation consists of neglecting any effects coming from the quantum fluctuations in (5.22). If we simply plug in the homogeneous mean-field ψ_0 in (5.21), we end up with a polynomial equation for the mean-field density n_0

$$n_0 \left(\Delta^2 + \gamma^2/4 \right) = |F|^2, \quad (5.23)$$

where we have introduced the interaction-renormalized detuning

$$\Delta = \delta - \mu, \quad (5.24)$$

with $\mu = gn_0$ the mean-field interaction energy.

We see that the mean-field equation (5.23) can have either one or two stable solutions for the density n_0 . When $\delta < \sqrt{3}\gamma/2$, we find only one solution for a given pump power F . Usually this is called the *optical limiter* regime: the more we populate the cavity, the further it will shift away from resonance by the building up of interaction energy. In the scenario $\delta > \sqrt{3}\gamma/2$, on the other hand, there is a range of pump powers F for which two stable density solutions can be found: the *bistable* regime. Upon increasing pump power, the density will abruptly jump from the low-density to the high-density branch at some critical point. When reducing pump power, the system will remain in the high-density branch until it abruptly drops down to the low-density branch at a critical point. Generally, these two critical points do not coincide, giving rise to a hysteresis curve when the pump power is

5.4. The Bogoliubov approximation

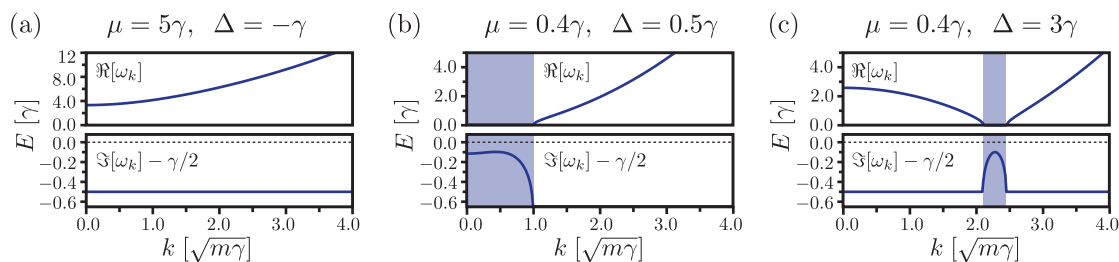


Figure 5.3: The quasiparticle spectrum from (5.27) for different mean-field configurations. (a) When $\Delta < 0$ the spectrum is gapped and there are no additional imaginary contributions. (b) When $0 < \Delta < 2\mu$, there is a disk of diffusive-like modes centered around $\mathbf{k} = 0$. These modes are characterized by having $\Re\omega_{\mathbf{k}} = 0$, while having a nonzero imaginary contribution. (c) If $\Delta > 2\mu$, the diffusive modes shift to higher momentum and form a ring in momentum space. The diffusive regions are marked with blue shades. For clarity, we plot $\Im\omega_{\mathbf{k}} - \gamma/2$, which represents the total decay rate of a Bogoliubov mode with momentum \mathbf{k} .

repeatedly increased and decreased across the bistable point [96]. The area of this hysteresis loop has been shown to depend upon pump switching time when quantum fluctuations are also included [97], as was confirmed in a recent experiment [98].

5.4.2 The evolution of the quantum fluctuations

For a given steady mean-field solution ψ_0 , we can then study the motion of quantum fluctuations in the microcavity by looking at the dynamics of the $\hat{\phi}_{\mathbf{k}}$. By plugging ansatz (5.22) into the quantum Langevin equation (5.21) and only retaining terms up to linear order in the fluctuation operator $\hat{\phi}_{\mathbf{k}}$, we arrive at the equation of motion of the quantum fluctuations

$$i\partial_t \begin{pmatrix} \hat{\phi}_{\mathbf{k}} \\ \hat{\phi}_{-\mathbf{k}}^\dagger \end{pmatrix} = (B_{\mathbf{k}} - i\frac{\gamma}{2}\mathbb{I}) \begin{pmatrix} \hat{\phi}_{\mathbf{k}} \\ \hat{\phi}_{-\mathbf{k}}^\dagger \end{pmatrix} + \sqrt{\gamma} \begin{pmatrix} \hat{\xi}_{\mathbf{k}} \\ \hat{\xi}_{-\mathbf{k}}^\dagger \end{pmatrix}, \quad B_{\mathbf{k}} = \begin{pmatrix} \varepsilon_{\mathbf{k}} + \mu & \mu \\ -\mu & -\varepsilon_{\mathbf{k}} - \mu \end{pmatrix}. \quad (5.25)$$

Here, the interaction energy $\mu = gn_0$ enters the matrix $B_{\mathbf{k}}$ as an off-diagonal coupling between creation and annihilation operators of the quantum fluctuations. The diagonal element is then found as the single-particle dispersion, but shifted with the interaction-renormalized detuning

$$\varepsilon_{\mathbf{k}} = \frac{k^2}{2m} - \Delta = \mu + \varepsilon_{LP}(0) + \frac{k^2}{2m} - \omega_L. \quad (5.26)$$

We see that the noise operator $\hat{\xi}_{\mathbf{k}}$ enters in (5.25) as a drive term for the quantum fluctuations. The random escape processes of photons from the fluids evoke small ripples in the otherwise flat density profile, thereby triggering the creation of quantum fluctuations.

The eigenvalues of $B_{\mathbf{k}}$ govern the dynamics of the quantum fluctuations once they are generated. The two eigenmodes $\pm\omega_{\mathbf{k}}$ come with opposite sign and are expressed in the same

analytical form as the Bogoliubov modes of a dilute gas of bosonic atoms at equilibrium (see Chapter 9 or Ref.[99])

$$\omega_k = \sqrt{\varepsilon_k(\varepsilon_k + 2\mu)}. \quad (5.27)$$

Nevertheless, an important difference with equilibrium condensates comes from the modified single-particle dispersion $\varepsilon_{\mathbf{k}}$, presented in (5.26). When $\Delta < 0$, with Δ the interaction-renormalized detuning from (5.24), the spectrum is positive-valued for any momentum \mathbf{k} . There is a spectral gap $|\Delta|(|\Delta| + 2\mu)$, which closes in the limit of $\Delta \rightarrow 0^{(-)}$, i. e. at the end point of the high-density branch in the bistable regime. In the other case, when $\Delta > 0$ there are regions in momentum space where the spectrum is purely imaginary, meaning that these modes have zero group velocity and a modified lifetime $\tau_{\mathbf{k}}^{(\pm)} = 1/(\gamma \pm 2\Im\omega_{\mathbf{k}})$. We refer to these modes as *diffusive-like*. Note that this regime is only parametrically stable when $2\mu < \gamma$, i.e. for low enough densities. The quasiparticle dispersion is shown for different mean-field regimes in Fig. 5.3. The properties of the different regimes are explained in more detail in Appendix B.3.

From equation (5.25), we can then find an exact analytical form of the time-evolved fluctuation operator $\hat{\phi}_{\mathbf{k}}$. This can be done by performing two subsequent Bogoliubov rotations: first a rotation to the diagonal basis, where the time evolution is trivial, and then a rotation back to the basis of $\hat{\phi}_{\mathbf{k}}$ operators. In Appendix B.3 we explain in more detail how this is done, but the calculation is very similar to the analysis presented in Sec. 3.4 in the chapter on long-range interacting fermions.

Eventually, we find that the time-evolved fluctuation operator can be written in the form

$$\hat{\phi}_{\mathbf{k}}(t) = e^{-\gamma t/2} \left(\eta_k(t) \hat{\phi}_{\mathbf{k}}(0) + \zeta_k(t) \hat{\phi}_{-\mathbf{k}}^\dagger(0) \right) + \text{noise}. \quad (5.28)$$

The expressions for the time-dependent Bogoliubov coefficients $\eta_k(t)$ and $\zeta_k(t)$ in the various mean-field regimes are derived in Appendix B.3. It should be noted, though, that the usual interpretation of the Bogoliubov operators $\hat{\chi}_{\mathbf{k}}$ as bosonic quasiparticles breaks down for the regime with a diffusive dispersion. We discuss this in more detail in Appendix B.2.

The freedom to tune the parameter Δ in the system, which merely requires a variation of pump frequency ω_L , as seen from (8.9), enables us to explore parameter regimes inaccessible to the usual conservative dynamics of dilute Bose gases at equilibrium (see Chapter 9). In previous works, this freedom has been exploited to illustrate the existence of exotic effects with no analog at equilibrium. In this context, Ref. [100] studies the superfluidity of a driven-dissipative quantum fluid when it flows past a defect. Later, also the drag force was evaluated in [101] and it was even shown in [102] that this drag force can assume *negative* values. Remarkably, it was pointed out that exactly the diffusive modes in a fluid with $\Delta > 0$ are responsible for the occurrence of this exotic effect.

5.4. The Bogoliubov approximation

5.4.3 The quadratic correlation functions in the steady state

From the stochastic equations of motion for the quantum fluctuations, presented in (5.25), we can obtain the equations for the evolution of the quadratic correlation functions by applying the product rule for derivatives. On our level of approximation, we want to know the time evolution of the density distribution $n_k = \langle \hat{\phi}_{\mathbf{k}}^\dagger \hat{\phi}_{\mathbf{k}} \rangle$ and the pair correlation $c_k = \langle \hat{\phi}_{\mathbf{k}} \hat{\phi}_{-\mathbf{k}} \rangle$. These are found as

$$\partial_t n_k = -\gamma n_k + 2\Im[g\psi_0^2 c_k^*], \quad (5.29)$$

$$i\partial_t c_k = (2\varepsilon_k + 2g|\psi_0|^2 - i\gamma)c_k + g\psi_0^2(2n_k + 1). \quad (5.30)$$

Setting the left-hand side to zero yields the equal-time quadratic correlations in the steady state, as they were first derived in [103],

$$n_k = \frac{1}{2} \frac{(gn_0)^2}{\omega_k^2 + \gamma^2/4}, \quad c_k = -\frac{g\psi_0^2 \varepsilon_k + gn_0 + i\gamma/2}{2 \frac{\omega_k^2 + \gamma^2/4}{\omega_k^2 + \gamma^2/4}}. \quad (5.31)$$

From here, the *nonequal-time* correlation function is straightforwardly obtained. In our case, we want to know the quantities $n_k(\tau) = \langle \hat{\phi}_{\mathbf{k}}^\dagger(t) \hat{\phi}_{\mathbf{k}}(t') \rangle$ and $c_k(\tau) = \langle \hat{\phi}_{\mathbf{k}}(t) \hat{\phi}_{-\mathbf{k}}(t') \rangle$, where the delayed operator $\hat{\phi}_{\mathbf{k}}(t)$ is given in (5.28). In the steady state we know that only the relative time difference $\tau = t - t'$ can be important for correlations. In this context, the quantum regression theorem [69] states that the delayed correlation function in the steady state can be obtained by merely evolving the later operator over a time $\tau \geq 0$ and then taking the expectation value. This is particularly easily seen in our case, because all contributions from the Markovian noise in (5.28) will cancel upon taking the expectation value with an operator evaluated at a different time instant.

Then, the nonequal-time quadratic correlation functions are derived as

$$n_k(\tau) = e^{-\gamma\tau/2} \left(\eta_k^*(\tau) n_k + \zeta_k^*(\tau) c_k \right), \quad c_k(\tau) = e^{-\gamma\tau/2} \left(\eta_k(\tau) c_k + \zeta_k(\tau) n_k \right), \quad (5.32)$$

with the equal-time correlations n_k and c_k from (5.31). We can therefore conclude that the delayed correlation functions mix up the normal and anomalous correlations, with an overall exponentially decaying envelop that reflects the finite excitation lifetime. The coefficients $\eta_k(\tau)$ and $\zeta_k(\tau)$ are the same as the ones found for the time-dependent Bogoliubov rotation from (5.28) and are derived in Appendix B.3.

Chapter 6

Constructing Gaussian states from the output of a planar microcavity

We have ended the previous chapter by presenting a linearized analysis of a quantum fluid of light inside a planar microcavity. In this chapter, we will continue with illustrating how we can utilize this output state in a selection and interference scheme to engineer a wide class of Gaussian states of light. In particular, we will focus on how we can amplify by orders of magnitude the *quantum nature* of the output state, attributed to the spontaneous creation of a small depletion of quantum fluctuations.

6.1 The unconventional photon blockade with Gaussian states

The downside of the photon blockade, as formulated in its traditional form, is that the phenomenon relies on a strong anharmonic spectrum of the cavity (see Sec. 4.2.2). Experimentally, this may be difficult to realize and to control as it requires some mechanism to mediate strong photon-photon interactions inside the cavity. Recently, a number of works have proposed to realize the photon blockade by utilizing an interference mechanism between two different pathways to inject a second photon in a cavity. Coined the *unconventional* photon blockade, this alternative mechanism has the advantage that it can be realized even with a weakly nonlinear cavity spectrum (see Sec. 4.2.3).

As seen previously, the dimensionless interaction constant of polaritons inside a planar microcavity has typical values of $mg \sim 10^{-4}$, with m the polariton mass and g the 2D interaction constant, thus rendering polariton interactions generally weak. While it motivated us to present a linearized analysis of the quantum field in Sec. 5.4, it also ensures that quantum corrections upon the coherent laser field are usually very small. As a consequence, the intensity fluctuations of the output field are expected to be characterized by $g^{(2)}(0) \approx 1$ [82], the value of the incident laser field, with only a minimal (antibunched) correction of

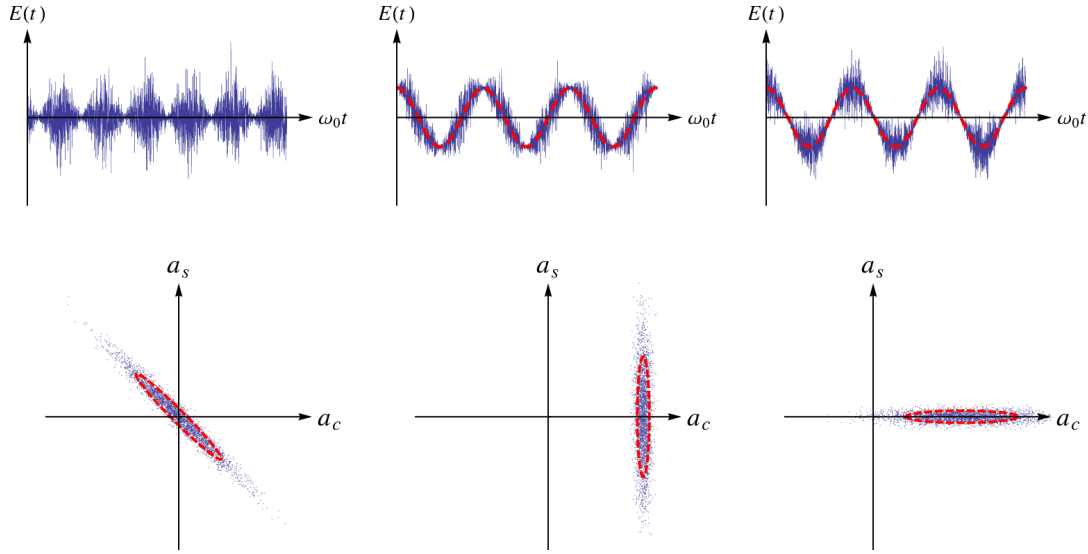


Figure 6.1: A schematic image of squeezed coherent states. The upper row shows the evolution of the electric field associated to the quantum state and the lower row is a schematic representation of the quantum state. (left) A squeezed state of the vacuum. Middle: an amplitude-squeezed state shows reduced amplitude fluctuations, at the cost of large phase fluctuations. (right) A phase-squeezed state, on the contrary, has strong amplitude fluctuations but a well-defined phase. Picture from [104].

the order of 10^{-4} coming from the quantum fluctuations.

This section is devoted to illustrating how we can amplify this minor correction with a few orders of magnitude by carefully shaping the output field of the cavity, thus engineering a strongly nonclassical photon state as output from our scheme. The proposed scheme has the advantage that it separates the squeezing and interference stage in space, thereby gaining a larger control over the setup compared to the two-cavity model (see Sec. 4.2.3). The results can be understood in the perspective of the unconventional photon blockade with Gaussian states [88].

6.1.1 Gaussian states: a brief overview

On the linearized level, such as presented in Sec. 5.4, the quantum field is characterized by a coherent amplitude coming from the incident laser field and quadratic correlations from the quantum fluctuations. Quantum states of this form are generally called *Gaussian*. We will briefly present a general overview of single-mode Gaussian states and translate the results from Sec. 5.4 to this framework.

The light field from a thermal photon source is characterized by a Gaussian density matrix with an average number of photons n_{th} ,

$$\hat{\rho}_{n_{\text{th}}} = \mathcal{Z}^{-1} \exp\{-\hbar\omega\hat{a}^\dagger\hat{a}/kT\}, \quad (6.1)$$

6.1. The unconventional photon blockade with Gaussian states

such that $n_{\text{th}} = 1/(e^{\hbar\omega/kT} - 1)$ and $\mathcal{Z} = 1/(1 - e^{-\hbar\omega/kT})$ with $\hbar\omega$ the energy of the mode and T the temperature. In the limit $T \rightarrow 0$ the number of photons goes to zero and we recover the density matrix of the vacuum. Note that we introduce the temperature T and energy $\hbar\omega$ here as completely arbitrary parameters to fix n_{th} , as if it were a photon state generated by a thermal source.

A single-mode *squeezed* Gaussian state of the mode \hat{a} can then be generated from $\hat{\rho}_{n_{\text{th}}}$ by performing the transformation

$$\hat{\rho}_{\xi, n_{\text{th}}} = \hat{S}(\xi)\hat{\rho}_{n_{\text{th}}}\hat{S}^\dagger(\xi), \quad (6.2)$$

where $\hat{S}(\xi) = \exp[\frac{1}{2}(\xi^*\hat{a}^2 - \xi\hat{a}^{\dagger 2})]$ is the squeezing operator with $\xi = re^{i\theta}$. The new density matrix $\hat{\rho}_{\xi, n_{\text{th}}}$ has now reduced fluctuations in one quadrature, while having stronger fluctuations in the other. The amount of squeezing is set by the parameter r and the quadrature is chosen with the phase θ . Alternatively, a squeezed Gaussian state is entirely characterized by its second moments and there exists a one-to-one map [96] that allows to extract the squeezing parameter ξ and the thermal density of photons n_{th} ,

$$n = \text{tr}[\hat{\rho}_{\xi, n_{\text{th}}}\hat{a}^\dagger\hat{a}] = \left(n_{\text{th}} + \frac{1}{2}\right) \cosh 2r - \frac{1}{2} \quad (6.3)$$

$$c = \text{tr}[\hat{\rho}_{\xi, n_{\text{th}}}\hat{a}\hat{a}] = -\left(n_{\text{th}} + \frac{1}{2}\right) e^{i\theta} \sinh 2r. \quad (6.4)$$

As a last step, the mode \hat{a} can be displaced with a coherent field $\alpha = \bar{\alpha}e^{i\zeta}$, leading to the new density matrix

$$\hat{\rho}_{\alpha, \xi, n_{\text{th}}} = \hat{D}(\alpha)\hat{\rho}_{\xi, n_{\text{th}}}\hat{D}^\dagger(\alpha), \quad (6.5)$$

where $\hat{D}(\alpha) = \exp[\alpha\hat{a}^\dagger - \alpha^*\hat{a}]$ is the displacement operator. The displacement field is then found back from $\hat{\rho}_{\alpha, \xi, n_{\text{th}}}$ by relating

$$\alpha = \text{tr}[\hat{\rho}_{\alpha, \xi, n_{\text{th}}}\hat{a}]. \quad (6.6)$$

In summary, any single-mode Gaussian state has a representation of form (6.5) and is fully characterized by three parameters: n_{th} (thermal density), ξ (squeezing) and α (displacement field). A quantum state of form (6.5) parametrizes a photon field that is generated with a coherent laser, as quantified by α , and fluctuations on top. The fluctuations are characterized in terms of n_{th} , their population, and squeezing ξ , which quantifies how fluctuations are distributed over two conjugate quadratures, like phase and amplitude. See Fig. 6.1 for a schematic picture of squeezed coherent states and the electric field that they are expected to produce.

Very recently, squeezed states of light have been used in an interference scheme to measure the tiny length difference that is predicted when a gravitational wave passes through earth [105]. The squeezing was necessary to reduce the fluctuations in one quadrature to attain sufficient precision for detection, beyond the standard quantum limit [104].

6.1.2 Antibunching in Gaussian states

The general mechanism from the *unconventional photon blockade* was recently understood in terms of Gaussian states exactly of form (6.5) [88]. By tuning the parameters n_{th} , ξ and α in an optimal way, the state can produce strongly antibunched photons as output.

To see this, we start by deriving the intensity fluctuations, given in expression (4.5), for a Gaussian state of form (6.5),

$$g^{(2)}(0) = 1 + \frac{2\bar{\alpha}^2 \text{Re}(n - \bar{c}e^{i(\theta-2\zeta)}) + n^2 + \bar{c}^2}{(\bar{\alpha}^2 + n)^2}, \quad (6.7)$$

where we have defined $c = \bar{c}e^{i\theta}$. The quadratic correlations n and c are given in (6.3) and the displacement field α is defined in (6.6). In order to obtain a small $g^{(2)}(0)$, we now see that we need to set $\theta = 2\zeta$, which corresponds to squeezing exactly in the amplitude quadrature, thereby severely enhancing phase fluctuations. A photon state of this form is illustrated in the middle panel of Fig. 6.1.

When the second moments n and c of the fluctuations are fixed, we can vary the displacement field α to establish optimal antibunching conditions in (6.7). By minimizing the expression for the intensity fluctuations with respect to $\bar{\alpha}$, we obtain the displacement field that realizes maximal antibunching,

$$\bar{\alpha}_{\text{opt}} = \sqrt{\frac{(\bar{c} + n)\bar{c}}{\bar{c} - n}}. \quad (6.8)$$

We then find the maximally reduced density fluctuations of a Gaussian field with fixed n and c , but with optimal $\bar{\alpha}_{\text{opt}}$ as

$$g_{\text{opt}}^{(2)}(0) = 1 - \frac{(\bar{c} - n)^2}{\bar{c}^2 + 2\bar{c}n - n^2}. \quad (6.9)$$

We will next see how we can shape the approximate Gaussian output state from the microcavity. The parameters n and c are momentum-dependent and are set by the nature of interactions inside the cavity. However, we can shape the coherent field from the incident laser before interference in the setup to approach the optimal displacement amplitude from (6.8).

6.2 Engineering squeezed coherent output states from a microcavity

Within the linearized treatment presented in Sec. 5.4, we find that the effect of quantum fluctuations on top of the coherent condensate is captured by the non-trivial quadratic correlations n_k and c_k , derived in (5.31). In the squeezing language introduced in the previous section, this means that the two modes $\pm\mathbf{k}$ form a *two-mode* squeezed state.

6.2. Engineering squeezed coherent output states from a microcavity

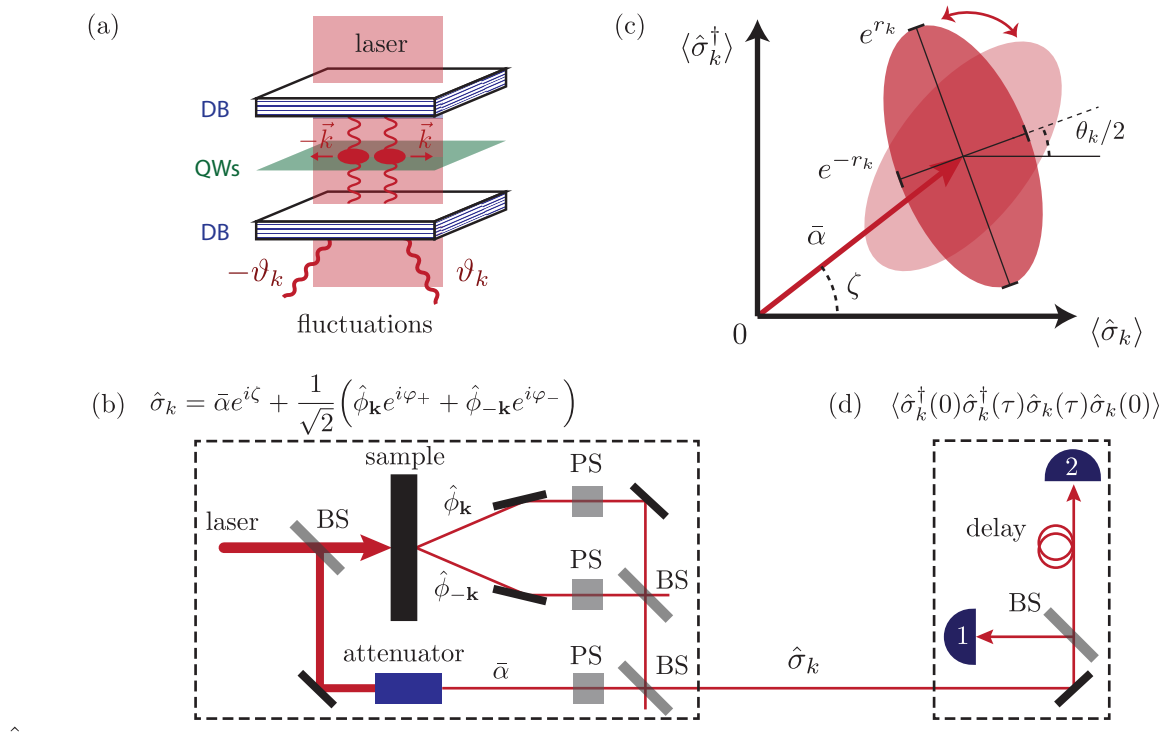


Figure 6.2: (a) A schematic image of a planar semiconductor microcavity in the strong light-matter coupling regime. A quantum well (QW) is placed between two distributed Bragg mirrors (DB) and is pumped with a coherent laser beam. Photon interactions, mediated by the optical nonlinearity of the QW, lead to a small depletion of the condensate in terms of quantum fluctuations with nonzero momentum. The excitations are formed in pairs with opposite momentum and form a two-mode squeezed Gaussian state. A fluctuation with momentum \mathbf{k} can leave the cavity as propagating radiation at an angle ϑ_k , with $\sin \vartheta_k = ck/\omega_L$, from the perpendicular axis. (b) A schematic image of the scheme, composed of linear optical building blocks, that we propose to engineer squeezed coherent states as output. The coherent field of the pumping laser is attenuated and interfered with the two-mode squeezed Gaussian state of the quantum fluctuations to construct the photon field $\hat{\sigma}_k$. (c) The output state $\hat{\sigma}_k$ can be approximately parametrized as a squeezed coherent state. The squeezing parameter r_k is momentum-dependent and can be found through (6.12). The phase between squeezing (θ_k) and displacement (ζ) can be varied with the phase shifters from (b), as given in (6.13), allowing the output field to move between an amplitude and a phase squeezed state. (d) A HBT setup to measure photon correlations of the output state. Detecting simultaneous clicks of detectors 1 and 2 allows for the measurement of the delayed intensity fluctuations of the photon field $\hat{\sigma}_k$ and gives access to quantity (6.14). 'BS' stands for a (50:50) beam splitter and 'PS' for phase shifter.

Similar to the single-mode case that we presented in (6.1), a two-mode squeezing operator is defined as $\hat{S}_2(\xi) = \exp[-\xi\hat{a}\hat{b} + \xi^*\hat{a}^\dagger\hat{b}^\dagger]$, with in our case $\hat{a} \equiv \hat{\phi}_{\mathbf{k}}$ and $\hat{b} \equiv \hat{\phi}_{-\mathbf{k}}$.

We will illustrate in the following how we can utilize the two-mode squeezed light, originating from the quantum fluctuations inside the microcavity, to engineer single-mode squeezed states of form (6.5). In Sec. 6.1.2, we have seen how these states may lead to strong antibunching in the photon statistics.

6.2.1 The setup: selecting and interfering momentum modes

The setup that we propose relies on the fact that photons with an in-plane momentum \mathbf{k} escape from the cavity at an angle ϑ_k , as found from the relation $\sin \vartheta_k = ck/\omega_L$ where c is the speed of light in vacuum and ω_L is the laser angular frequency (see Sec. 5.1.2). A coherent polariton population is created inside the microcavity by shining a laser onto the sample to (quasi)resonantly excite $\mathbf{k} \simeq 0$ polaritons. Due to polariton-polariton interactions, there will be a small depletion of quantum fluctuation populating the $\mathbf{k} \neq 0$ modes, as illustrated in Fig. 6.2(a). A quantum fluctuation traveling with a momentum \mathbf{k} then leads to photon emission from the microcavity at an angle ϑ_k , while the bulk of the photons, pumped in the $\mathbf{k} = 0$ mode, fly out along the axis perpendicular to the microcavity. Consequently, if we can isolate two modes $\pm\mathbf{k}$ and we would measure the photon statistics of these two beams, we expect them to follow the statistics of a two-mode squeezed state, characterized by the parameters n_k and c_k from (5.31).

In our scheme, we want to isolate these modes to let the photons interfere on a 50:50 beam splitter, as illustrated in Fig. 6.2(b). Thanks to the $\mathbf{k} \leftrightarrow -\mathbf{k}$ symmetry of the system, the state resulting from this interference obeys exactly the same statistics as a single-mode squeezed state, like (6.1), of which the characteristic parameters n and c are given by the expressions for n_k and c_k from (5.31).

A possible way to realize this selection is based on a series of lenses to image the Fourier plane onto two pinholes or on the cores of two single-mode fibers. When these pinholes only transmit the desired Fourier components, they can be recombined on a free-space or fiber beam splitter for the interference. Another possibility is to image the Fourier space directly on an optical fiber bundle or on a Spatial Light Modulator (see also further in Sec. 6.3) that selectively transmits the chosen modes.

As a last step, we let the engineered single-mode squeezed state interfere with a coherent field. In our setup this coherence is naturally provided by the incident laser field. Therefore, if we split a fraction of the incident laser beam off, we can use it as a coherent source to achieve the required displacement for engineering a state of form (6.5). Before interference, the coherent field is ‘shaped’ by letting it pass through an attenuator, which allows to tune the amplitude $\bar{\alpha}$, and a phase shifter, with which we can shift the phase ζ . Note that this gives us the freedom to vary the full displacement field α , such that we can closely approach condition (6.8) for the n and c as they are now given by the quadratic correlations n_k and

6.2. Engineering squeezed coherent output states from a microcavity

c_k from (5.31).

The final state of the scheme from Fig. 6.2(b) is then found to be of the form

$$\hat{\sigma}_k = \bar{\alpha}e^{i\zeta} + \frac{1}{\sqrt{2}}\left(\hat{\phi}_{\mathbf{k}}e^{i\varphi_+} + \hat{\phi}_{-\mathbf{k}}e^{i\varphi_-}\right), \quad (6.10)$$

where the φ_{\pm} represent the acquired phases of the $\pm\mathbf{k}$ modes in the interference scheme. Notice that they are not only set by the inserted phase shifters, but also by a possible path difference and the π phase shifts by reflection off a mirror. In principle, the phase shifters would allow to tune the phases of all the beams at will to match the desired conditions.

By looking at the quadratic correlations of this state

$$\langle \hat{\sigma}_k^\dagger \hat{\sigma}_k \rangle = \bar{\alpha}^2 + n_k, \quad \langle \hat{\sigma}_k \hat{\sigma}_k \rangle = \bar{\alpha}^2 e^{2i\zeta} + c_k e^{i(\varphi_+ + \varphi_-)}, \quad (6.11)$$

where n_k and c_k are given in (5.31), we immediately conclude that the mode $\hat{\sigma}_k$ can be regarded as a squeezed coherent state of form (6.5) with a displacement given by the coherent field α and quadratic correlations from (6.3), with $n \equiv n_k$ and $c \equiv c_k e^{i(\varphi_+ + \varphi_-)}$.

6.2.2 Squeezing in the output state

With the selection and interference scheme from Fig. 6.2(b) we have engineered a squeezed and displaced state $\hat{\sigma}_k$ of form (6.5) as output, such as formulated in (6.10). To make the correspondence more precise, we can next determine the effective squeezing parameter $r_k e^{i\theta_k}$ and thermal density $n_{\text{th},k}$ for the mode $\hat{\sigma}_k$. After some algebra, we find from expressions (6.3)–(6.4) the thermal density and squeezing of $\hat{\sigma}_k$ as

$$n_{\text{th},k} = \sqrt{\left(n_k + \frac{1}{2}\right)^2 + |c_k|^2} - \frac{1}{2}, \quad \tanh 2r_k = \frac{|c_k|}{n_k + \frac{1}{2}}. \quad (6.12)$$

with n_k and c_k found within the Bogoliubov framework and given in (5.31). Furthermore, we see that the squeezing phase is found as

$$\theta_k = \arg c_k + \varphi_+ + \varphi_-, \quad (6.13)$$

where φ_{\pm} are the phases that enter in (6.10). This is particularly easily seen from Expr. (6.11).

The difference between θ_k and the phase of the displacement field ζ can be tuned by varying φ_{\pm} and ζ with the phase shifters in the setup from Fig. 6.2(b). In the schematic image of the squeezed state shown in Fig. 6.2(c), this corresponds to rotating the ellipse, thereby allowing to switch between an amplitude and a phase squeezed state.

In Fig. 6.3(a)–(b) we show how the parameters r_k and $n_{\text{th},k}$ from expression (6.12) depend on the selected momentum \mathbf{k} . We show both the cases of negative (Fig. 6.3(b)) and positive (Fig. 6.3(a)) values of the interaction-renormalized detuning Δ , defined in (5.24). Very generally, excitations become more particle-like and have a larger frequency at large k where the spectrum goes roughly as $\omega_k \approx k^2/2m$ [99]. Consequently, we expect that the

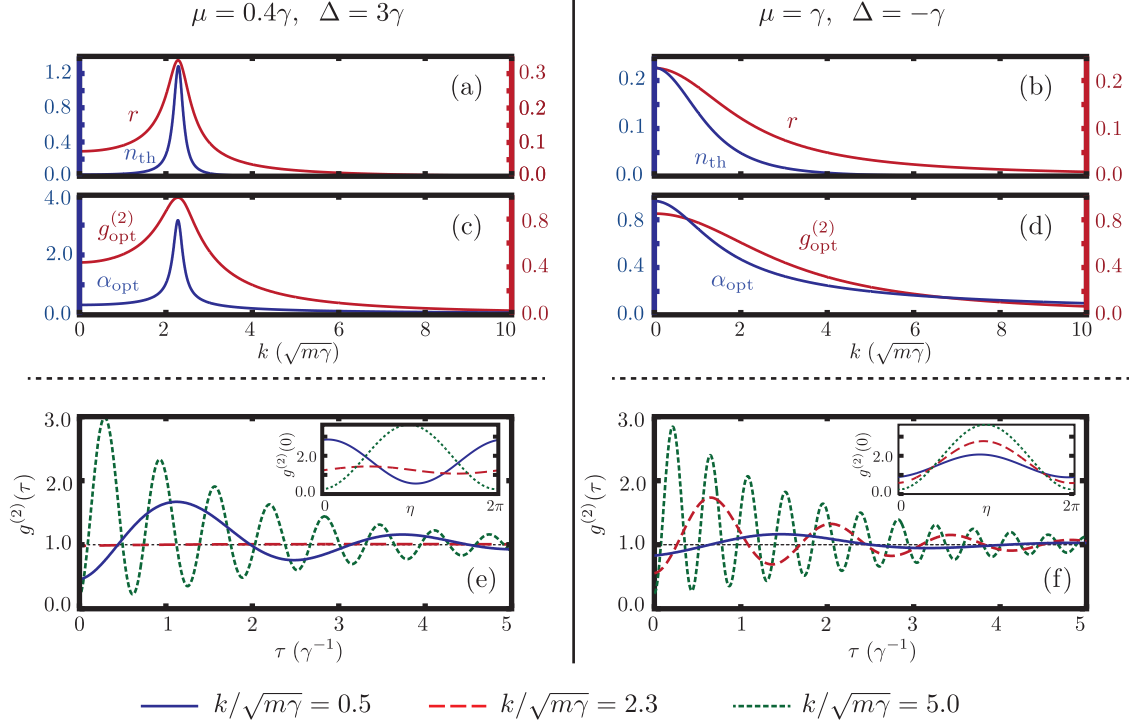


Figure 6.3: (a,b) The squeezing parameter r and the thermal occupation n_{th} as a function of momentum k for a steady state with a positive (a) and a negative (b) interaction-renormalized detuning (8). (c,d) The optimal displacement amplitude α_{opt} (21) and corresponding $g_{\text{opt}}^{(2)} = g^{(2)}(0)|_{\text{min}}$ (6.9) as a function of momentum for the same parameters as above. (e,f) The temporal profile of $g^{(2)}(\tau)$ after selecting various momenta as indicated below. The displacement amplitude $\bar{\alpha}$ and phase η have been chosen to fulfil the optimal antibunching conditions (as derived from (c,d)) at $\tau = 0$. The insets show $g^{(2)}(0)$ upon varying the total phase between squeezing and displacement (corresponding to rotating the ellipse in Fig. 6.2c) for the showed momenta.

6.2. Engineering squeezed coherent output states from a microcavity

squeezing parameter r_k , which quantifies somehow the mixing of particles and holes, drops to zero in this limit as well. Additionally, we also expect the thermal population $n_{\text{th},k}$ of high-momentum modes to go to zero because it is generally less likely to excite fluctuations with higher momenta.

In the case $\Delta < 0$, shown in Fig. 6.3(b), both n_{th} and r drop to zero monotonously for higher selected momenta k . Remember that in this case the spectrum of quasiparticles is gapped and has no nontrivial imaginary contributions. When $\Delta > 0$, shown in 6.3(a), we see that both n_{th} and r show a more versatile behavior as function of k . As we have explained in Sec. 5.4, this regime is characterized by a set of diffusive-like modes, which have quasiparticle frequencies that are purely imaginary. On Fig. 5.3(c) we show the quasiparticle spectrum of a polariton field with the same mean-field parameters as in Fig. 6.3(a) and we see that the diffusive modes are found on a ring of nonzero momentum. Exactly at these momenta, we notice a strong peak in n_{th} , which signals that these modes are parametrically amplified. Additionally, we observe a strong squeezing of these modes, as we conclude from the strongly enhanced squeezing parameter r at the same momenta as the peak in n_{th} .

6.2.3 Optimizing the antibunched emission

The setup that we propose in Fig. 6.2(b) has the built-in freedom to shape the coherent field $\alpha = \bar{\alpha}e^{i\zeta}$ before it is interfered with the single-mode squeezed state engineered by selecting the emitted light from the quantum fluctuations. More precisely, the coherent field passes through an attenuator, which allows to vary the displacement amplitude $\bar{\alpha}$, and a phase shifter to tune the phase ζ .

In the Hanbury Brown-Twiss (HBT) scheme from Fig. 6.2(d) the *delayed* intensity correlations of the output state σ_k (6.10) are measured, which gives access to the quantity

$$g^{(2)}(\tau) = \frac{\langle \hat{\sigma}_k^\dagger(0)\hat{\sigma}_k^\dagger(\tau)\hat{\sigma}_k(\tau)\hat{\sigma}_k(0) \rangle}{\langle \hat{\sigma}_k^\dagger\hat{\sigma}_k \rangle^2} = 1 + \frac{2\bar{\alpha}^2\Re\{n_k(\tau) + c_k(\tau)e^{i\eta}\} + n_k^2(\tau) + c_k^2(\tau)}{(\bar{\alpha}^2 + n_k(0))^2}, \quad (6.14)$$

where $n_k(\tau)$ and $c_k(\tau)$ are given in (5.32) and we have defined the overall phase

$$\eta = \varphi_+ + \varphi_- - 2\zeta. \quad (6.15)$$

The motivation to introduce the setup from Fig. 6.2(b) is that it permits us to tune the displacement field to approach the optimal condition (6.8). Let us first start by analyzing $g^{(2)}(0)$, that is, the case of zero time delay between photon clicks on the two detectors. To reach optimal antibunching, which corresponds to minimal $g^{(2)}(0)$, we immediately see from (6.14) that we need to tune the overall phase η such that

$$\eta \rightarrow \eta_{\text{opt}} = \pi - \arg c_k(0). \quad (6.16)$$

With this condition, the squeezing of the mode is exactly situated in the amplitude quadrature, such as we had already seen from (6.7). This regime is characterized by severely

reduced fluctuations in the photon number, at the cost of having a strongly fluctuating phase (see the example on the middle panel of Fig. 6.1). In Fig. 6.2(c), this is nicely visualized as having the squeezing ellipse rotated such that its major axis is exactly perpendicular to the direction of the displacement vector.

When the phases are tuned to match condition (6.16), we can obtain the optimal displacement amplitude $\bar{\alpha}_{\text{opt}}$, shaped with the attenuator in Fig. 6.2(b), to achieve optimally antibunched photon statistics in the output state, given the selection of two modes $\pm\mathbf{k}$. In Fig. 6.3(c)–(d) we illustrate how the optimal displacement field $\bar{\alpha}_{\text{opt}}$ varies with selected momentum. Additionally, we show the value of $g^{(2)}(0)|_{\text{min}}$, the minimum of density fluctuations at zero time delay, which the output state with $\bar{\alpha}_{\text{opt}}$ is expected to produce.

An important observation is that $g^{(2)}(0)|_{\text{min}}$ drops to zero if we select higher momentum modes in the setup, suggesting that we can, at least in principle, approach the genuine *photon blockade* regime asymptotically by isolating higher momenta. Unfortunately, we also conclude that $\bar{\alpha}_{\text{opt}}$ drops to zero in the same limit, meaning that the photon flux of the output state σ_k is expected to become vanishingly small.

For intermediate values of k , the behavior is different according to the sign of Δ . When $\Delta < 0$, shown in Fig 6.3(d), we notice a monotonously decay for both α_{opt} and $g^{(2)}(0)|_{\text{min}}$ as a function of isolated momentum \mathbf{k} . We have seen before that the presence of a set of parametrically amplified modes, present in the regime $\Delta > 0$, results in a strong increase of $n_{\text{th},k}$ and r_k . As is shown in Fig 6.3(c), the overall effect on $g^{(2)}(0)|_{\text{min}}$ is, however, detrimental. When momenta are selected that correspond to diffusive-like modes, $g^{(2)}(0)|_{\text{min}}$ is pushed back towards the value of a classical coherent field; $g^{(2)}(0)|_{\text{min}} \approx 1$.

The following step consists of analyzing the full temporal dependence of the function $g^{(2)}(\tau)$ (6.14). At long time delays τ , we expect $g^{(2)}(\tau)$ to return to 1, reflecting the coherence of the laser drive. The excitations that we employ to engineer non-trivial photon statistics at short delay times are limited by their finite lifetime, as signaled by the exponentially decaying envelope in the expression of their time evolution (5.28).

In Fig. 6.3(e)–(f) we analyze the delayed second-order correlations $g^{(2)}(\tau)$ for the displacement amplitude $\tilde{\alpha} = \tilde{\alpha}_{\text{opt}}$ that optimizes $g^{(2)}(0)$ via expression (6.8)) for different values of $k/\sqrt{m\gamma}$. Generally speaking, we see from Fig. 6.3(e)–(f) that $g^{(2)}(\tau)$ can be regarded as a damped oscillatory function with an oscillation frequency set by $\Re\omega_k$, the Bogoliubov frequency of the selected Fourier component, and a damping equal to $\gamma/2 - \Im\omega_k$, which is the dissipation rate of the associated Bogoliubov mode.

The offset of the oscillation from $g^{(2)}(\tau)$ can be set by tuning the overall phase η with the phase shifters from the setup in Fig. 6.2(b) through expression (6.15); this is illustrated on the insets of Fig. 6.3(e)–(f). Choosing optimal antibunching at $\tau = 0$, the case that is shown in the main panels (a)–(b), can then be pictured as tuning the offset of the oscillation in $g^{(2)}(\tau)$ such that a minimum is found at $\tau = 0$, as given by condition (6.16). By merely changing the phase η , we can switch from amplitude squeezing, with associated reduced density fluctuations, to phase squeezing, with largely enhanced density fluctuations. In the

6.3. Manipulating and probing photon statistics with a wide-aperture lens

schematic image of a squeezed coherent state from Fig. 6.2(c), this is easily understood as a rotation of the squeezing ellipse, while leaving its shape unaltered.

We have concluded previously that, in theory, perfect antibunching in the output state $\hat{\sigma}_k$ (6.10) can be approached asymptotically by isolating higher momentum modes with the setup from Fig. 6.2(b). Yet, we now see in Fig. 6.3(e)–(f) that the oscillation frequency of $g^{(2)}(\tau)$ increases as well upon selecting higher momenta. In fact, this should be no surprise, since we had seen before that the oscillation frequency is typically set by ω_k , the Bogoliubov frequency of the isolated mode, which scales as $k^2/2m$ at high momenta. Unfortunately, the rapid fluctuation of $g^{(2)}(\tau)$ between low and high values implies that the initial antibunched photon statistics can be easily washed away in the detection scheme from Fig. 6.2(d) when realistic photon detectors are employed. The response time of photon detectors is typically of the same order or even longer than the photon lifetime of the cavity.

Another experimental difficulty may arise from the requirement of an approximately spatially homogeneous fluid inside the microcavity, which we needed for the initial ansatz (5.22). Disorder along the cavity plane, possibly originating from imperfections during the growth process of the sample, may lead to unwanted scattering that could spoil the signal of the coherent pair-creation processes, forming the premise of our engineered scheme. See Appendix B.4 for a detailed study of various noise sources in the setup.

6.3 Manipulating and probing photon statistics with a wide-aperture lens

In the previous section, we have theoretically developed an optical scheme that relied on the isolation and subsequent interference of single Fourier modes to engineer strongly antibunched photon statistics. The main idea was to utilize the inherent two-mode squeezing of quantum fluctuations inside the microcavity as a source to engineer a state of form (6.5) with a series of linear optical elements.

We now continue with illustrating how we can exploit the in-cavity interference between *all* \mathbf{k} modes in real space to amplify the nontrivial photon statistics originating from the quasiparticles, while retaining the qualitative spatio-temporal profile of correlations. In Fig. 6.4(a) we depict the proposed optical scheme to achieve this. A spatial image of the cavity field can be reconstructed by placing a system of two wide-aperture lenses in a confocal configuration after the microcavity. In the focal plane between the two lenses, a space-dependent attenuation element, e.g. based on a Spatial Light Modulator (SLM) (see Fig. 6.4b)), provides the required shaping for this analysis. Again, we want to reduce the amplitude of the $\mathbf{k} = 0$ mode, which encompasses the coherent field, to manipulate the displacement amplitude before interference with the other $\mathbf{k} \neq 0$ modes that originate from the pair-creation processes of quantum fluctuations.

6.3.1 Intensity correlations in position space

By looking back at ansatz (5.22), it is immediate to see that the delayed two-point correlation function of the quantum fluctuations in position space can be obtained from (5.32) by merely Fourier transforming the quantities $n_k(\tau)$ and $c_k(\tau)$

$$n(x, \tau) = \langle \hat{\phi}^\dagger(\mathbf{r}, t) \hat{\phi}(\mathbf{r}', t') \rangle = \frac{1}{V} \sum_{\mathbf{k}} n_k(\tau) e^{i\mathbf{k} \cdot (\mathbf{r} - \mathbf{r}')}, \quad (6.17)$$

$$c(x, \tau) = \langle \hat{\phi}(\mathbf{r}, t) \hat{\phi}(\mathbf{r}', t') \rangle = \frac{1}{V} \sum_{\mathbf{k}} c_k(\tau) e^{i\mathbf{k} \cdot (\mathbf{r} - \mathbf{r}')}. \quad (6.18)$$

Here, we have introduced the relative distance $x = |\mathbf{r} - \mathbf{r}'|$ in the cavity plane to reflect the presumed spatial homogeneity of the fluid inside the microcavity.

Optically, a Fourier transform is easily performed by placing a lens at a distance from the sample that corresponds to its focal length. The Fourier image of the output field of the cavity is then found in the plane at a focal length from the lens, on the other side than the cavity. In Fig. 6.4(a), the first lens after the sample is employed to construct the Fourier image of the sample in this scheme, while the second projects the Fourier image back onto position space, where the photon detection takes place.

An important thing to note is that the quadratic correlation functions in momentum space generally behave as $n_k \sim k^{-4}$ and $c_k \sim k^{-2}$ at large k , which are universal scaling laws for gases that interact with a contact interaction [99]. While this poses no issues for the first-order correlation function $n(x, \tau)$, the pair correlation $c(x, \tau)$ suffers from an ultraviolet divergence in two or more spatial dimensions in the limit of vanishing separation x . In other words, the convenient introduction of a zero-ranged contact interaction has the inconvenient consequence that pair correlations are only reproduced correctly for separations x much larger than the true range of the interaction potential.

6.3.2 The density-density correlation function

For the purposes of this analysis, our interest lies in the spatial and temporal properties of the fluid of light inside the quantum well. An important quantity in this context is the *density-density correlation function*,

$$g^{(2)}(\mathbf{r}, t; \mathbf{r}', t') = \frac{\langle \hat{\Psi}^\dagger(\mathbf{r}, t) \hat{\Psi}^\dagger(\mathbf{r}', t') \hat{\Psi}(\mathbf{r}', t') \hat{\Psi}(\mathbf{r}, t) \rangle}{\langle \hat{\Psi}^\dagger(\mathbf{r}, t) \hat{\Psi}(\mathbf{r}, t) \rangle \langle \hat{\Psi}^\dagger(\mathbf{r}', t') \hat{\Psi}(\mathbf{r}', t') \rangle}, \quad (6.19)$$

which relates fluctuations in fluid density at two spatio-temporal points (\mathbf{r}, t) and (\mathbf{r}', t') .

Within the linearized approximation introduced in Sec. 5.4, we found an approximate representation of the full quantum state in terms of a coherent displacement field and quadratic fluctuations on top. Under the assumption of Gaussian fluctuations, the expression of the density-density correlation function (6.19) can be expanded with Wick's theorem in products of two-point correlation functions and a coherent displacement field. By shaping

6.3. Manipulating and probing photon statistics with a wide-aperture lens

the beam with the Spatial Light Modulator (SLM) from the scheme in Fig. 6.4(a)–(b), we can attenuate a fraction of the coherent field before all modes are interfered again on the second lens for the optical Fourier transform to real space. With $\psi_f = \mathcal{F}\psi_0$, the attenuated coherent field, we then obtain the expression for the density correlations with delay τ between two points situated at a distance x from each other on the Gaussian level,

$$g^{(2)}(x, \tau) = 1 + \frac{\Re(|\psi_f|^2 n(x, \tau) + \psi_f^{*2} c(x, \tau)) + |n(x, \tau)|^2 + |c(x, \tau)|^2}{(|\psi_f|^2 + \delta n)^2}, \quad (6.20)$$

where $\delta n = n(0, 0)$ is the density of noncondensed particles or the *depletion*.

The density correlation function (6.20) suffers from exactly the same ultraviolet divergence as the pair-correlations from (6.18) when interactions are modeled with a zero-ranged contact interaction. Yet, whenever there is a nonzero separation x between two correlated points, the function is well-behaved and there is no divergence. We therefore focus on separations x significantly larger than the true potential range for the upcoming analysis, ensuring that our results do not suffer from divergences. In practice, we see that for each non-zero point (x, τ) , the spatial-temporal profile of $g^{(2)}(x, \tau)$ converges to a well-defined value when choosing a larger cutoff; solely the point $(0, 0)$ suffers from the ultraviolet divergence. For the upcoming analysis, we choose the cutoff high enough such that the profiles are converged. In any practical experiment, the imaging system inevitably introduces an effective cutoff that comes from the finite aperture of the lenses.

We next discuss the spatio-temporal profiles of the density-density correlation function (6.20) for two different mean-field regimes that exhibit interesting features. For the results, we will apply a dimensionless interaction constant $mg = 10^{-4}$, which is typically found in state-of-the-art microcavity polariton experiments. Nevertheless, we want to highlight that our discussion holds regardless of the exact value of the interaction constant g . When the mean-field interaction energy $\mu = gn_0$ is kept constant, which is the relevant parameter for the Bogoliubov analysis (see Sec. 5.4), having a lower interaction constant merely requires a higher mean-field polariton density n_0 . In order to obtain the same spatio-temporal correlation profile, the coherent field ψ_0 then simply needs a stronger attenuation \mathcal{F} with the SLM from Fig. 6.4(b) to attain the same displacement field ψ_f for interference.

6.3.3 Lightcone-like correlations in the high-density regime

When a fluid of light with mean field having $\Delta < 0$ is established (a case found in the optical-limiter regime discussed in Sec. 5.4.1) and $\mu > \gamma, |\Delta|$, we have a scenario where interactions dominate over losses and other relevant energy scales in the fluid. The quasiparticles that arise in this case are characterized by a dispersion that exhibits a gap for small momenta, as we show in Fig. 5.3(a). When a quasiparticle is generated in this case, we expect that it starts traveling through the fluid with a velocity set by its quasiparticle group velocity, during a time roughly corresponding to the photon lifetime $\tau = \gamma^{-1}$ before it decays. Since mostly low momentum modes, with a bound group velocity, are occupied by the

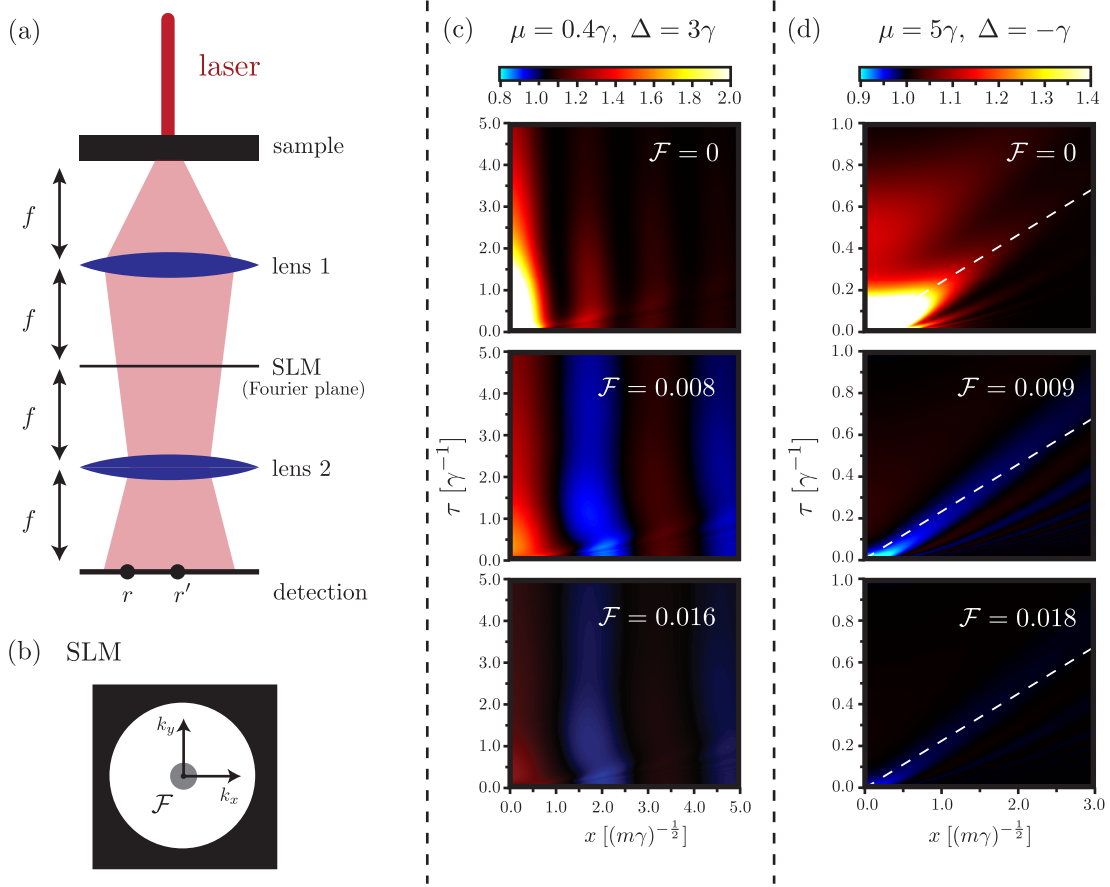


Figure 6.4: (a) The confocal two-lens setup to measure density-density correlations of a fluid of light. A spatial light modulator (SLM) is placed in the common Fourier plane of the two lenses to perform the desired \mathbf{k} -space selection. Delayed correlations between photon detections separated by a time interval τ allow to measure the $g^{(2)}(x, \tau)$ intensity correlation function defined in (6.19). (b) The spatial profile of the SLM used for the shaping of the beam. All modes in the 2D plane are transmitted, except a small disk centered around $\mathbf{k} = 0$, where the coherent field is situated. White corresponds to transmission, black to full blocking and gray to attenuating with a factor \mathcal{F} , so as to transmit a coherent field $\psi_f = \mathcal{F}\psi_0$. (c)–(d) Spatial-temporal profiles of the density-density correlation function $g^{(2)}(x, \tau)$ for varying (top to bottom) filtering fraction \mathcal{F} (see (6.20)) and different (left/right) pumping parameters. Red shades correspond to bunching and blue to antibunching. (c) Parametrically amplified modes give rise to a steady spatial pattern of alternating bunching and antibunching, which turns into complete bunching for $\mathcal{F} \rightarrow 0$. The quasiparticle dispersion of this mean-field configuration is plotted in Fig. 5.3(c). (d) We notice the appearance of an approximate sound cone $x = \tau/2c$ (white dashed lines) of antibunched correlations. Also here, when $\mathcal{F} \rightarrow 0$, the antibunching turns into bunching. The quasiparticle dispersion for this case is plotted in Fig. 5.3(a).

6.3. Manipulating and probing photon statistics with a wide-aperture lens

previously discussed coherent pair-creation processes, we expect to observe features that we can relate back to the lightcone-like propagation of quasiparticles, much like the discussion from Chapter 3. In Fig. 6.4(d) we show the profiles of a fluid pumped with $\mu = 5\gamma$ and $\Delta = -\gamma$ for different attenuation levels \mathcal{F} of the $\mathbf{k} \approx 0$ modes, which give different amplitudes of the displacement fields ψ_f .

The case where the coherent field is entirely blocked, found by setting $\mathcal{F} = 0$, shows some illuminating features; we are now solely looking at the photon statistics originating from the quantum fluctuations, without interference of the coherent field. Since quasiparticles are created in pairs that travel with opposite momenta, we observe only bunched photon statistics in the spatial-temporal profile of $g^{(2)}(x, \tau)$ plotted in Fig. 6.4(b) for $\mathcal{F} = 0$. The regions with stronger illumination reveal the spatio-temporal points with a higher probability of detecting the partner particle of the pair created at $(0, 0)$. Most notably, an oscillation with a frequency of the spectral gap $\sqrt{|\Delta|(|\Delta| + \gamma)}$ in time is seen, which is the frequency at which low-momentum quasiparticles oscillate.

As a next step we can interfere a fraction of the coherent field ψ_0 in the scheme of Fig. 6.4(a) by varying the transmittance \mathcal{F} of the SLM (see Fig. 6.4(b)). Adding a nonzero displacement $\psi_f = \mathcal{F}\psi_0$ to expression (6.20) leads to a spatio-temporal profile of $g^{(2)}(x, \tau)$ that is drastically changed in appearance: we observe how the bunching of the quasiparticle pairs turns into antibunching in a *sound-like* band. (see the middle panel of Fig. 6.4(d) with $\mathcal{F} = 0.009$). The quantum fluctuations inside the microcavity stem from interactions and the antibunched signal actually reflects the fact that photons inside are slightly pushed apart from each other at short distances. At nonzero delay times, this is then perceived as a propagating band of antibunched statistics. For a larger fraction of ψ_f (see panel in (d) with $\mathcal{F} = 0.018$) the profile of $g^{(2)}(x, \tau)$ remains largely the same in shape, but the variation from $g^{(2)} = 1$, the statistics of a coherent state, diminishes.

At this point, we halt to make a connection with the previous part of this thesis, where we studied quenches in conservative quantum systems and analyzed the few-body correlation functions that are generated with the unitary time evolution of the full many-body wave function. A possible interpretation – perhaps somewhat hand-waving – of the results from Fig. 6.4(d) can be given in terms of the celebrated Lieb-Robinson bound that we have reviewed in Sec. 3.3.1. When we detect a photon at a spatio-temporal point $(0, 0)$ in the profiles from Fig. 6.4(d), there is *Bogoliubov* quasiparticle created in the photon fluid. At that point, the Bogoliubov particle propagates away and modifies the probability to detect another photon at space-time points that are situated along its world line, thereby giving rise to an effective ‘light cone’. Notice that an important difference comes with the nature of the group velocities. For equilibrium lattice models – at least for short-range interactions – the set of group velocities that quasiparticles can attain is bounded from above, while the group velocity in a continuum model keeps on growing linearly for higher momenta. Nevertheless, mostly low-momentum quasiparticles are excited in the quantum fluid, making that some lightcone-like features are still visible in Fig. 6.4(d), while there

are also oscillations leaking out due to the small occupation fast-propagating modes.

6.3.4 Spatial pattern formation with diffusive modes

We have illustrated how we can retrieve some of the familiar features from equilibrium models in a driven-dissipative quantum fluid with sufficiently high mean-field interaction energy μ . We now continue with discussing how the explicit nonequilibrium nature of the system may lead to completely novel features, unseen in a system at equilibrium.

When the fluid is pumped on the lower-density branch of the bistable regime, the quasiparticle spectrum is characterized by a set of diffusive-like modes with zero group velocity and an altered decay rate. Provided losses still dominate over interactions ($2\mu < \gamma$), the homogeneous state remains dynamically stable and quasiparticles generated by quantum fluctuations eventually decay, albeit on a modified time scale $\tau_k = 1/(\gamma - \Gamma_k)$ (with $\Gamma_k = \Im\omega_k$) that may be substantially longer than the photon lifetime. In the most interesting mean-field case $2\mu < \Delta$, for which the spectrum is shown in Fig. 5.3(c), a set of diffusive modes (indicated by the blue band) is found on a ring with nonzero radius in momentum space. Due to their potentially longer lifetimes, we expect that these modes may leave a distinctive footprint on the pattern of density-density correlations.

In Fig. 6.4(c), we show the spatio-temporal profiles of $g^{(2)}(x, \tau)$ for a fluid pumped with mean-field parameters $\mu = 0.4\gamma$ and $\Delta = 3\gamma$ and for varying displacement field ψ_f , which we engineer again from the condensate mode with the SLM (see Fig. 6.4(a)–(b)). The quasiparticle spectrum for these modes is plotted in Fig. 5.3(c), where we see that a diffusive-like band is found centered around nonzero momentum $k_c \approx 2.3\sqrt{m\gamma}$. The parametric amplification of these modes generates a standing-wave-like pattern in $g^{(2)}(x, t)$, with a wavelength corresponding to the parametrically amplified wave vectors. Moreover, the vanishing real part of the frequency of these modes implies a zero group velocity $v_k^g = \partial_k\omega_k$, leading to a spatial pattern that persists in time, practically without moving.

Upon varying \mathcal{F} , we can again switch from a profile with alternating bunching and antibunching stripes in space (lower panels of Fig. 6.4(c), with $\mathcal{F} = 0.008, 0.016$) to a profile with only bunching when the condensate mode is completely attenuated (panel with $\mathcal{F} = 0$). There is an optimum at about $\mathcal{F} \approx 0.008$, which stabilizes a temporal band with minimum density correlations $g^{(2)}(x, \tau)$ at a separation $x \approx 2(m\gamma)^{-1/2}$. In all cases, we see that the spatial structure, as imprinted by the parametrically amplified modes, is remarkably well preserved in time. Also the temporal sustain of the nontrivial correlations is now substantially longer than the photon lifetime, which would facilitate a measurement of correlations when realistic photo-detectors, with nonzero photon-collection time, are employed to detect photon clicks. Unfortunately, the strong suppression of $g^{(2)}(x, \tau)$ at nonzero separation x cannot be utilized to produce strongly antibunched photon statistics, since it relates to correlations between two spatially separated points.

Finally, in Fig. 6.4(c) we also notice small ripples that appear at short times on top

6.4. Conclusive remarks

of the otherwise remarkably stable space-time structure generated with the parametrically amplified modes. Similar to the correlations that we saw leaking out of the effective light cone in Fig. 6.4(d), we attribute these oscillations to the presence of modes with a large group velocity. Right outside the parametrically amplified disk, we can even verify that modes exhibit a diverging group velocity, as can be seen in Fig. 5.3(b)–(c).

6.4 Conclusive remarks

We have first established the general model of exciton-polaritons inside a planar microcavity device in Chapter 5. The explicit openness of the setup was treated on the level of a stochastic operator equation for the lower-polariton field; the *quantum Langevin equation* (5.21). Within a linear approximation, we concluded that the full quantum state of the polariton field inside the microcavity in the steady-state regime is well parametrized in terms of a *Gaussian state*, with delayed quadratic correlation from (5.32).

We then continued in Chapter 6 with illustrating how the approximate Gaussian output state of the microcavity can be utilized as input in a selection and interference scheme to render the resulting light strongly nonclassical (see Fig. 4.4). The scheme, composed of linear optical building blocks, relies on the momentum-dependent *two-mode squeezing* of quantum fluctuations in the microcavity to construct a squeezed coherent state of light (6.5) by means of selecting and interfering \mathbf{k} -components *after* the cavity. This way, we separate the squeezing and interference stage, resulting in a larger control as compared to previous proposals based on two coupled cavities.

The nonclassical nature of the output light was characterized by its *antibunching* features. In the spirit of the *unconventional photon blockade* with Gaussian states, it was then explained in Sec. 6.2 how the scheme can be tuned to produce a train of strongly antibunched photons as output (see Fig. 6.3). The main limitation turned out to be the *quasiparticle* oscillation frequency of the selected modes; this can be detrimental if it is substantially faster than the photon collection time of photon detectors.

Finally, we demonstrated in Sec. 6.3 how we can image the density-density correlation function of the fluid of light inside the cavity with a free-space optics scheme (see Fig. 6.4). A Spatial Light Modulator (SLM) offers the freedom to shape the passing beam of light before transforming the image from Fourier space back to real space. When the fluid of light is excited in the optical limiter regime, we recognized qualitative features from nonequilibrium dynamics of conservative quantum systems in terms of a light-cone-like propagation of correlations. In the other scenario, the bistable regime, a spatial pattern can be generated from parametrically amplified modes. Interestingly, these patterns can be stabilized for delay times substantially longer than the photon lifetime inside the cavity. We relate these intriguing features, having no analog at equilibrium, to the intrinsic driven-dissipative nature of the system.

The results of this work can be found in the manuscript [106], which is currently under

review for publication in the journal SciPost.

Part III

Interacting quasiparticles: Beliaev-Landau scattering

Chapter 7

Beliaev-Landau scattering

As for now, one of the key assumptions of this work was that we could treat a quantum field as (approximately) Gaussian. In Chapter 3, we had put forward a quadratic fermionic model (3.7), making this assumption somehow trivial. However, the photon field coming from a semiconductor microcavity was only found to be *approximately* Gaussian in Chapter 5, after neglecting higher-order corrections. The approximation was justified by the weakness of particle interactions.

In this chapter, however, we explicitly aim to study improvements upon an approximate Gaussian quantum state. From a physical point of view, these corrections have a very natural interpretation in terms of effective interactions among the quasiparticles of the system: *Beliaev-Landau scattering*.

7.1 The decay of a phonon

In another seminal paper [107], published in 1957, S. Beliaev considered the problem of determining the energy spectrum of a *non-ideal* gas of bosonic particles. He concluded

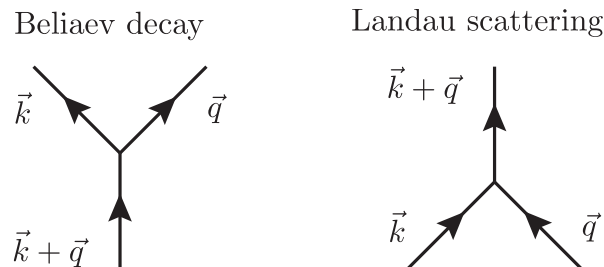


Figure 7.1: A diagrammatic representation of Beliaev-Landau scattering processes. Left: a quasiparticle with momentum \mathbf{k} decays into two lower momenta \mathbf{q} and $\mathbf{k} - \mathbf{q}$. Right: the inverse process, two quasiparticles with momenta \mathbf{q} and $\mathbf{k} - \mathbf{q}$ collide and scatter into a momentum \mathbf{k} . Notice that there is also one condensate mode with zero momentum involved in the collisions; this is not drawn on the figure.

that a phonon, once it is created, has a few mechanisms to decay through interactions with the atoms or with other phonons. Also Landau considered the problem and the collisions now bear both their names; Beliaev damping is the decay of a phonon through interaction with *condensate* particles while Landau scattering describes the interaction of one phonon with another to leave a high-momentum phonon and a condensate mode (see Fig. 7.1). However, on the level of the Hamiltonian both processes are of the same order and result from truncating the Hamiltonian at *third* order in quantum fluctuations. Recall that Bogoliubov theory requires a truncation at *second* order, giving an approximate quadratic theory that we can treat on a Gaussian footing.

In this part, we therefore explicitly seek to investigate corrections beyond the standard Gaussian approximation of a weakly interacting theory. Phonons, essentially the product of a quadratic approximation, are then expected to decay through the Beliaev-Landau scattering processes. As such, phonons are actually expected to have only a finite lifetime¹, while they are conserved on the level of a quadratic approximation of the Hamiltonian. As a preferred method to study these mechanisms, we will in this part develop a *hierarchy of correlation functions* with explicit inclusion of third-order correlators, so as to describe these higher-order collisions.

Quasiparticle scatterings were originally predicted in the many-body theory of quantum fluids [109] to be responsible for the finite lifetime of phonons in systems of either bosonic [110, 111, 112] or fermionic particles [113]. In the context of Beliaev-Landau scattering, important cold-atom experiments were carried out in [108] and [114]. By applying a periodic potential to a trapped bosonic atomic condensate, it is possible to excite a population of phonons with a certain momentum \mathbf{k} in the gas through Bragg scattering of particles off the potential. It was then observed in [108] how these injected phonons subsequently decay through collisions with the condensate particles; Beliaev decay. As a final result of their experiment, they presented a curve representing the cross section of phonon decay as a function of momentum \mathbf{k} , which we show here in Fig. 7.2. Their observations agreed very well with the original theoretical predictions from [110] and [111].

It was also soon realized, from relatively simple geometrical considerations, that Beliaev-Landau scattering can only occur *on-shell* (with energy conservation) if there is a nonzero angle between the in and out-states of a collision (see Fig. 7.2). As a consequence, there can be no such scatterings in a one-dimensional condensate, so that even higher collisions need to be considered [115]. However, a gas of atoms in a lattice, so not in the continuum, may have a (restricted) phase space for scattering again, even in one dimension [116].

The decay of a phonon through Beliaev decay requires a collision with a condensate mode and will generally be the predominant process of decay. The mean free path length of a phonon is the relevant quantity to be compared with the full dimensions of the condensate; $x_{\text{MF}} \sim 1/(\sigma n)$, with n the density of scatterers (here the condensate density) and σ the

¹That is, of course, at equilibrium. Out-of-equilibrium the photon lifetime sets another decay rate for the phonons.

7.1. The decay of a phonon

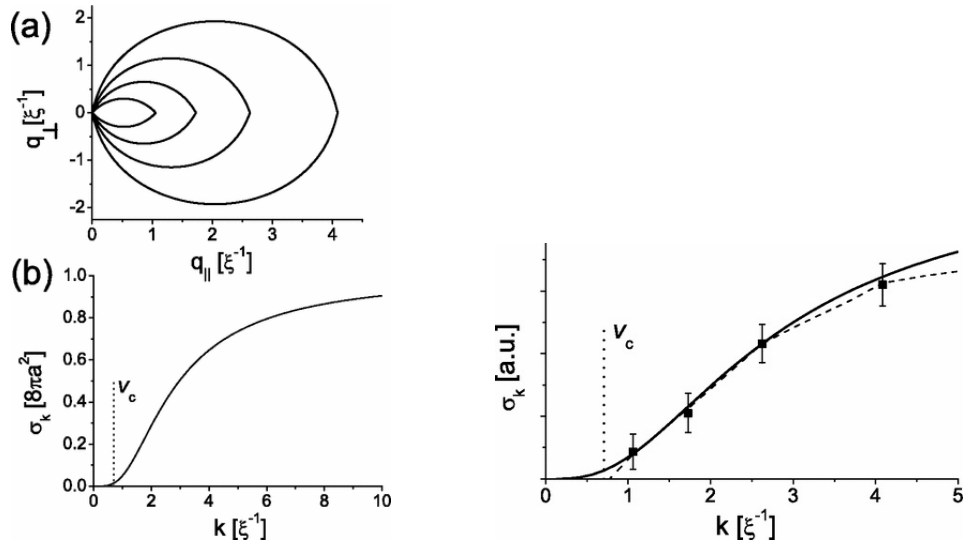


Figure 7.2: The decay of a phonon. (up) A phonon with momentum \mathbf{k} always decays to end states \mathbf{q} and $\mathbf{k} - \mathbf{q}$ with a well-specified angle. The \mathbf{k} -vector is oriented along the x -axis and the possible end state lie on the contours. (down) The scattering cross section of a phonon injected with momentum \mathbf{k} , for the theoretical prediction (left) and the experiment (right). When a photon has a higher momentum, it is expected to decay faster. This can be understood by noticing that the scattering contours (up) are larger for higher input momentum, making that the accessible scattering phase space grows as function of k . From [108].

cross section of a collision ($\sigma \sim a_s^2$, with a_s the scattering length for a contact potential, see Sec. 9.1). Whenever $x_{\text{MF}} > L$, with L a length scale associated with the total dimensions of the gas, a phonon's chance to scatter as it propagates is small; the gas is said to be in the *collisionless regime*. In the other case $x_{\text{MF}} < L$, there is high chance for a collision; the gas is then in the *hydrodynamic regime* [99]. For the decay of a photon through Landau damping, there must be a cloud of quasiparticles already present in the condensate, which can only be the case at nonzero temperatures [111].

7.2 Equilibrium vs. out-of-equilibrium

Given a closed quantum system (e.g. a gas of ultracold atoms or a superfluid liquid Helium sample), the assumption of detailed balance and ergodicity inevitably restricts the possible effect of Beliaev-Landau collisions to driving the system back towards a thermal ensemble once it is brought out of equilibrium. As was explained, one possibility is to inject a population of phonons through Bragg scattering and study the subsequent damping through the collisions, bringing the system back to its steady state; a thermal equilibrium. In Chapter 9 we illustrate this, when we consider the thermalization of a gas of bosonic atoms following a sudden quench of the interaction constant.

Nevertheless, an intriguing question is how Beliaev-Landau scattering manifests itself in an explicit out-of-equilibrium context, where *out-of-equilibrium* here means *driven-dissipative*. In such systems, many of the convenient assumptions from equilibrium quantum dynamics cease to hold [117]. For example, there are many-body systems known that are driven and dissipate and eventually find an equilibrium as a *pure quantum state*, characterized by having *zero entropy* [118, 119]. This suggests that the route toward equilibration must have occurred in such a way that it violated the *second law of thermodynamics*, stating that entropy is an ever-growing quantity. Clearly, the excess entropy has been dissipated somehow into the environment, but considering only the system dynamics, there is an apparent violation of one of the fundamental laws of equilibrium thermodynamics.

For the following chapter, we are motivated by the absence of *detailed balance* in an out-of-equilibrium scenario to study the effects of Beliaev-Landau collisions in the steady-state of an array of nonlinear cavities. At equilibrium, detailed balance states that any microscopic process is balanced by its reverse process, thereby severely restricting the possible effects of the collisions. Out of equilibrium, there is no analog statement, suggesting that steady-state quantities may be substantially more sensitive to the exact underlying microscopic processes.

Chapter 8

Interacting quasiparticles in a cavity array

Previously, we have focused on the light that escapes from a *planar* microcavity device. Now, the setup is slightly different from the one used in the previous part. Rather than considering a continuous planar microcavity, we will now look into an *array* of cavities that are coupled to one another. When the spatial confinement of these cavities is strong enough, they can be treated as effectively 0D, suggesting that we merely have a single bosonic degree of freedom in each cavity to characterize the entire quantum state.

8.1 Cavity arrays

Today, cavity arrays can be engineered with a variety of different platforms. For the purposes of this analysis, we will primarily focus on semiconductor devices, the same platform as the planar microcavities discussed in Chapter 5. Alternatively, coupled arrays of microwave photons can be integrated in a superconducting circuit on a chip. Contrary to the semiconductor devices, where the nonlinearity of the cavities is mediated by the quantum-well excitons, photon-photon interactions on the circuit are here generated by *superconducting qubits*. While the energy scales on which both platforms operate are vastly different – one at optical and the other at microwave frequencies – the description of the effective degrees of freedom is largely analogous and very similar Hamiltonians come about in both systems.

As the photons inside the array can be treated effectively as interacting particles and the systems are largely scalable and controllable, the platforms of cavity and circuit QED provide a promising platform for the quantum simulation of a large variety complicated Hamiltonians. In this context, a detailed overview of the possibilities of quantum simulation with light can be found in the review articles [80, 79].

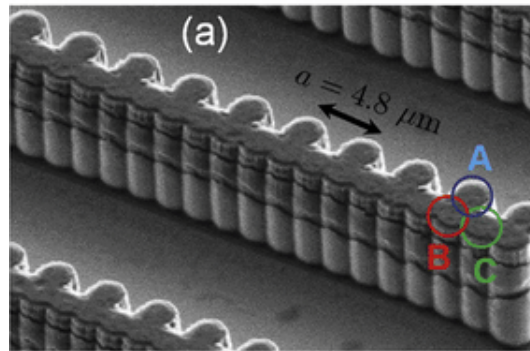


Figure 8.1: A Scanning Electron Microscopy image of a cavity array etched from a 2D semiconductor microcavity sample. The cavities are pillars, placed adjacent to one another, and are pumped with a laser from the top. Photons can hop from one cavity to the next and a nonlinear optical material mediates photon-photon interactions inside the cavities. This particular configuration constitutes a *Lieb lattice*, where every other pillar has an extra neighbor. Figure taken from [120].

8.1.1 Semiconductor microcavities

The analysis of this part is primarily situated in the context of cavity arrays engineered from semiconductor microcavities, which were already introduced in the previous part. When a 2D microcavity is made sufficiently narrow in the planar dimension, that is when confinement energy exceeds all other relevant energy scales, it can be approximated as an effective 0D cavity. The in-plane spatial dimensions become largely irrelevant as photons are now confined in any direction in space.

In Fig. 8.1 an image is shown of a microcavity array structure. Each pillar consists of two distributed Bragg mirrors with a nonlinear material between them that mediates effective photon-photon interactions. The configuration is pumped from the top with a laser beam, creating an approximately homogeneous polariton population throughout the chain of cavities. Photons in the chain can tunnel from one cavity to the next and hop through the chain. When more than one photon is contained inside the same pillar, they feel an interaction that is mediated by the excitons from the quantum well. The photons are also expected to leak out of the chain at a rate that corresponds to their inverse lifetime, analogous to photons inside a planar microcavity.

Photonic structures like the one shown in Fig. 8.1 are generally engineered with sophisticated etching techniques from a full 2D sample. Starting from a planar microcavity, the desired structure is imprinted on the sample and other regions are etched away to create an entire ‘photon landscape’. Usually, the full dimensions of the sample (order millimeters) are much larger than the wanted photonic structure (micrometer scale), so that a few copies of the system of interest and many different structures for other experiments fit within one

8.1. Cavity arrays

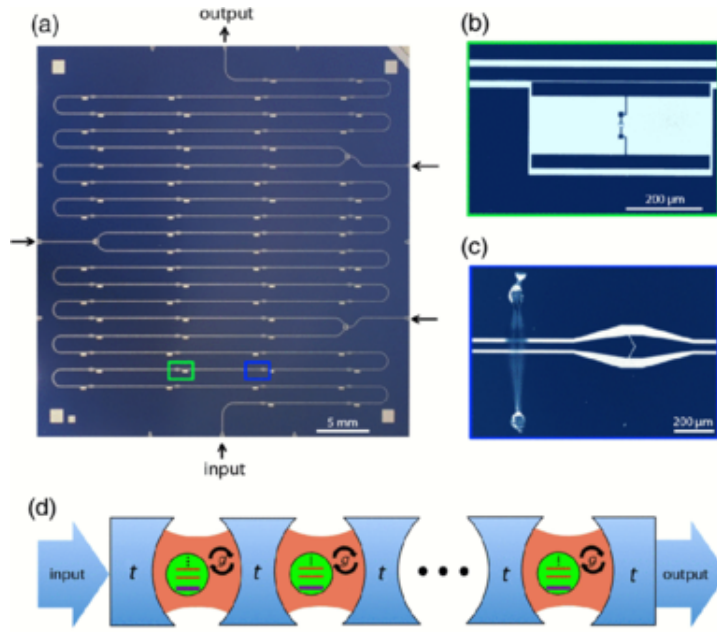


Figure 8.2: A 72-site superconducting circuit on a $35\text{mm} \times 35\text{mm}$ chip, taken from Ref. [121]. (a) The circuit consists of a number of qubits, transmon qubits in this case (blue square), coupled with microwave resonators (white lines) that are coupled with capacitances (green square). The system is driven at the input gate and read out at the gates indicated with an arrow. (b)–(c) an image of the circuit configuration of the capacitive coupling of microwave resonators and the transmon qubit, respectively. (d) The system can be modeled as a linear chain of coupled cavity-qubit systems that is driven at one end.

sample.

8.1.2 Superconducting circuits

Superconducting circuits provide an alternative platform to implement nonlinear cavities that are chained to one another. While the semiconductor microcavities typically operate at visual or near-infrared frequencies, corresponding to characteristic length scales of micrometers, superconducting circuits are driven at microwave frequencies, leading to structures on the millimeter scale. This also has important consequences for the sensitivity of these systems to the residual temperature in the sample. When we assume the noise in the system to attain zero-temperature statistics, as formulated previously in (5.20), it is usually sufficient to cool a semiconductor sample down to a few Kelvin. For a system operating at microwave frequencies, in turn, sufficient noise reduction may require cooling down to a few mK, which poses more stringent experimental conditions.

The superconducting circuit generally consists of numerous microwave resonators and nonlinear superconducting building blocks that are chained to each other on a chip. Various

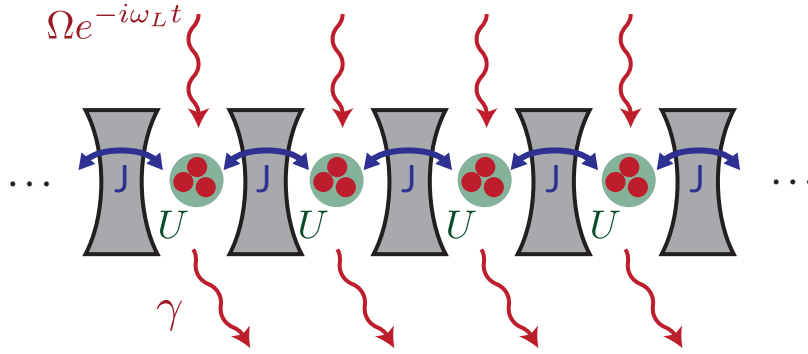


Figure 8.3: A schematic image of the model of a cavity array. Each cavity contains a nonlinearity to mediate effective photon-photon interactions, parametrized by U . Photons inside the chain can hop from one cavity to the next with a tunneling rate J . The entire chain is – in our case – uniformly pumped with a laser beam of frequency ω_L and amplitude Ω . Photons leak out of the cavities with a dissipation rate $\gamma = 1/\tau$, with τ the photon lifetime inside the cavities.

configurations exists for the realization of the nonlinear circuit elements, but they each have in common that they are engineered with a simple electronic circuit, which contains standard electronic elements like conductances, inductances and resistors, but also a *Josephson junction*, which introduces a strongly nonlinear spectrum for the states of the circuit. If the effective nonlinearity is large enough, we can then regard these elementary building blocks as *superconducting qubits* when only two of their internal states are practically accessible. Today, a large variety of such qubits have been theoretically described and implemented. Examples are the *charge qubit* [122], the *flux qubit* [123], the *phase qubit* [124] and the *transmon qubit* [125].

The qubits are then integrated on a chip and coupled to the microwave resonators that store the photons and act as cavities. Analogous to semiconductor cavities, the spectrum of such a microwave cavity is linear in the number of photons and constitutes an harmonic oscillator. In the strong coupling regime, the linear ladder of states from the cavity converts into the strongly nonlinear spectrum of the *Jaynes-Cummings model* when it is dressed with the qubit degree of freedom. When many of those cavity-qubit systems are chained together, allowing photons to hop from one cavity to the other, this realizes the *Jaynes-Cummings-Hubbard model*, as illustrated in Fig. 8.2. We refer the interested reader to the excellent reviews [126, 127] for a broad overview of the topic of superconducting circuits.

8.2 The model

When a cavity array is modeled, the internal structure of each of the cavities separately is neglected and they are treated as 0D. In practice, this means that we merely need a

8.2. The model

handful of parameters to characterize a single cavity, while an effective *tight-binding* (or lattice) model is then formulated to describe the physics of the coupled chain of cavities.

8.2.1 The Hamiltonian of a cavity array

We couple L nonlinear cavities, assumed to contain only a single photonic mode, into a 1D configuration, as illustrated in Fig. 8.3. The resonator frequencies ω_c of the microcavities are taken to be uniform throughout the whole chain. We consider the case of a uniform drive with a laser field that is characterized by a frequency ω_L and an amplitude Ω . After a unitary transform, which is employed to remove the time-dependence of the drive, exactly in the same spirit as in Sec. 5.2, we find the driven *Bose-Hubbard* Hamiltonian to describe the physics of photons inside the cavity chain,

$$\begin{aligned} \hat{H} = & -J \sum_{\langle j,l \rangle} \left(\hat{a}_j^\dagger \hat{a}_l + \hat{a}_l^\dagger \hat{a}_j \right) - \delta \sum_{j=1}^L \hat{n}_j + \frac{U}{2} \sum_{j=1}^L \hat{n}_j (\hat{n}_j - 1) \\ & + \sum_{j=1}^L \Omega_j (\hat{a}_j + \hat{a}_j^\dagger). \end{aligned} \quad (8.1)$$

The first term describes the hopping of photons from one cavity to neighboring cavities with a tunneling rate J . In the second term we introduce the detuning of the laser frequency from the cavity resonance, defined as $\delta = \omega_c - \omega_L$. Photon-photon interactions with a typical on-site interaction strength U are described with the third term. In the tight-binding approximation, the interaction constant is easily derived from the polaritonic interaction constant in 2D as $U = g/\Delta S$, with ΔS the surface of a single cavity. Practically, this means that we can increase on-site interactions by reducing the cavity size, rather than modifying the interaction constant g directly. The injection of photons into the cavity array is a coherent process when it is done with a laser. The last term is a driving term to describe the continuous replenishment of photons in the array.

8.2.2 Dissipative photon losses

Photons have a finite lifetime inside the cavities before they escape again. The losses of photons from the systems are not coherent and are therefore described in the Born-Markov approximation with a dissipator of the Lindblad form (see Chapter 4)

$$\mathcal{D}[\hat{\rho}] = \frac{\gamma}{2} \sum_j (2\hat{a}_j \hat{\rho} \hat{a}_j^\dagger - \hat{\rho} \hat{n}_j - \hat{n}_j \hat{\rho}). \quad (8.2)$$

The full dynamics of the density matrix $\hat{\rho}$ is then governed by a master equation, which includes both the unitary evolution under \hat{H} and the photonic losses

$$\partial_t \hat{\rho} = -i[\hat{H}, \hat{\rho}] + \mathcal{D}[\hat{\rho}] \quad (8.3)$$

We, however, prefer to work again in the framework of the quantum Langevin equation, in this case for the operators \hat{a}_j , which annihilate a photon at site j . The derivation of the stochastic operator equation is analogous to the one given in Sec. 5.3.2 and leads to the equation of motion [87],

$$i\partial_t \hat{a}_j = -\left(\delta - i\frac{\gamma}{2}\right) \hat{a}_j - J(\hat{a}_{j-1} + \hat{a}_{j+1}) + U\hat{a}_j^\dagger \hat{a}_j \hat{a}_j + \Omega_j + \sqrt{\gamma} \hat{\xi}_j. \quad (8.4)$$

The first terms on the right-hand side of this equation are readily derived from Heisenberg's equations of motion $i\partial_t \hat{a}_j = [\hat{a}_j, \hat{H}]$, while the last term originates from the coupling of the cavities to an external reservoir. The noise operators $\hat{\xi}_j$ therefore satisfy the statistics of a bath of harmonic oscillators at zero-temperature

$$\begin{aligned} \langle \hat{\xi}_k(t) \hat{\xi}_{k'}(t') \rangle &= \langle \hat{\xi}_k^\dagger(t) \hat{\xi}_{k'}(t') \rangle = 0, \\ \langle \hat{\xi}_k(t) \hat{\xi}_{k'}^\dagger(t') \rangle &= \delta_{j,j'} \delta(t-t') \end{aligned}$$

For the analysis of this chapter, Eq. (8.4) will provide the starting point.

8.2.3 Expanding the photon field operator

When the cavity array is pumped coherently in the $k = 0$ mode, we can again conveniently decompose the photon field into a classical mean field ψ_0 and quantum fluctuations $\hat{\phi}_k$ with nonzero momentum on top,

$$\hat{a}_j = \psi_0 + \frac{1}{\sqrt{L}} \sum_k e^{ikj} \hat{\phi}_k. \quad (8.5)$$

Notice that the fields in this chapter are defined in a dimensionless way, while the 2D structure of the microcavity in the previous chapter was accompanied by fields of dimension $\sim 1/\sqrt{V}$, where V was the 2D volume of the microcavity. This is reminiscent of the underlying lattice structure, where we absorb all the effects of lattice dimensions into the parameters of the model. We will come back to this in Sec. 8.6, when we translate our results to a realistic experimental implementation with semiconductor micropillars.

By substituting ansatz (5.22) into the quantum Langevin equation, we derive the equation of motion for the quantum fluctuations

$$\begin{aligned} i\partial_t \hat{\phi}_k &= (\epsilon_k + Un_0 - i\gamma/2) \hat{\phi}_k + U\psi_0^2 \hat{\phi}_{-k}^\dagger + \hat{\xi}_k \\ &+ \frac{2U\psi_0}{\sqrt{L}} \sum_q \hat{\phi}_q^\dagger \hat{\phi}_{k+q} + \frac{U\psi_0^*}{\sqrt{L}} \sum_q \hat{\phi}_q \hat{\phi}_{k-q} \\ &+ \frac{U}{L} \sum_{q,l} \hat{\phi}_q^\dagger \hat{\phi}_l \hat{\phi}_{k+q-l}, \end{aligned} \quad (8.6)$$

with the lattice dispersion in the tight-binding approximation

$$\epsilon_k = -\delta + Un_0 - 2J \cos k. \quad (8.7)$$

8.2. The model

Importantly, contrary to Eq. (5.25), we insist here on retaining higher-order terms of interactions as well. Clearly, the reason is that they encode the physics of interactions between the quantum fluctuations, which we explicitly seek to describe in this part.

Likewise, we derive the equation of motion for the homogeneous mean field ψ_0 , which now couples back to the quantum fluctuations $\hat{\phi}_k$,

$$i\partial_t\psi_0 = \left(-\Delta - i\frac{\gamma}{2}\right)\psi_0 + \Omega + \frac{2U\psi_0}{L} \sum_k \langle \hat{\phi}_k^\dagger \hat{\phi}_k \rangle + \frac{U\psi_0^*}{L} \sum_k \langle \hat{\phi}_k \phi_{-k} \rangle + \frac{U}{\sqrt{L^3}} \sum_{k,q} \langle \hat{\phi}_k^\dagger \hat{\phi}_q \hat{\phi}_{k-q} \rangle, \quad (8.8)$$

where Δ is again the interaction-renormalized detuning

$$\Delta = \delta - Un_0 + 2J. \quad (8.9)$$

For this analysis, we will focus on the case $\Delta < 0$, which corresponds to a fluid in the optical-limiter regime or the upper-density branch of the bistable regime. At this stage, no additional approximations were made, meaning that Eqs. (8.6)–(8.9) provide, in principle, a solution to the full quantum problem, exactly as it is expressed in (8.3) or (8.4).

8.2.4 Free quasiparticles: the Bogoliubov approximation

As a first analysis, we can treat the quantum Langevin equation for the fluctuations (8.6) only in the linear regime by neglecting any effects from higher-order interaction terms. This approximation gives the same expressions as (5.31), which we repeat here for clarity,

$$n_k = \frac{1}{2} \frac{(gn_0)^2}{\omega_k^2 + \gamma^2/4}, \quad c_k = -\frac{g\psi_0^2}{2} \frac{\epsilon_k + gn_0 + i\gamma/2}{\omega_k^2 + \gamma^2/4}, \quad (8.10)$$

with $n_k = \langle \hat{\phi}_k \hat{\phi}_{-k} \rangle$ and $c_k = \langle \hat{\phi}_k^\dagger \hat{\phi}_{-k} \rangle$. The only difference comes with the Bogoliubov dispersion relation

$$\omega_k = \sqrt{\epsilon_k(\epsilon_k + 2Un_0)}, \quad (8.11)$$

where ϵ_k is now given by the lattice result in the tight-binding approximation from (8.7). We plot the quasiparticle spectrum of a cavity array in Fig. 8.4(a).

When the set of equations is linear, we can introduce new operators $\hat{\chi}_k$, defined as

$$\hat{\phi}_k = u_k \hat{\chi}_k + v_k \hat{\chi}_{-k}^\dagger, \quad (8.12)$$

which diagonalize the set of equations of motion. This leads to the equation of motion for the *quasiparticle* operator

$$i(\partial_t + \gamma/2)\hat{\chi}_k = \omega_k \hat{\chi}_k + u_k \hat{\xi}_k - v_k \hat{\xi}_{-k}^\dagger, \quad (8.13)$$

where the transformation coefficients are found as

$$u_k, v_k = \frac{\sqrt{\epsilon_k + 2Un_0} \pm \sqrt{\epsilon_k}}{2\sqrt{\omega_k}}. \quad (8.14)$$

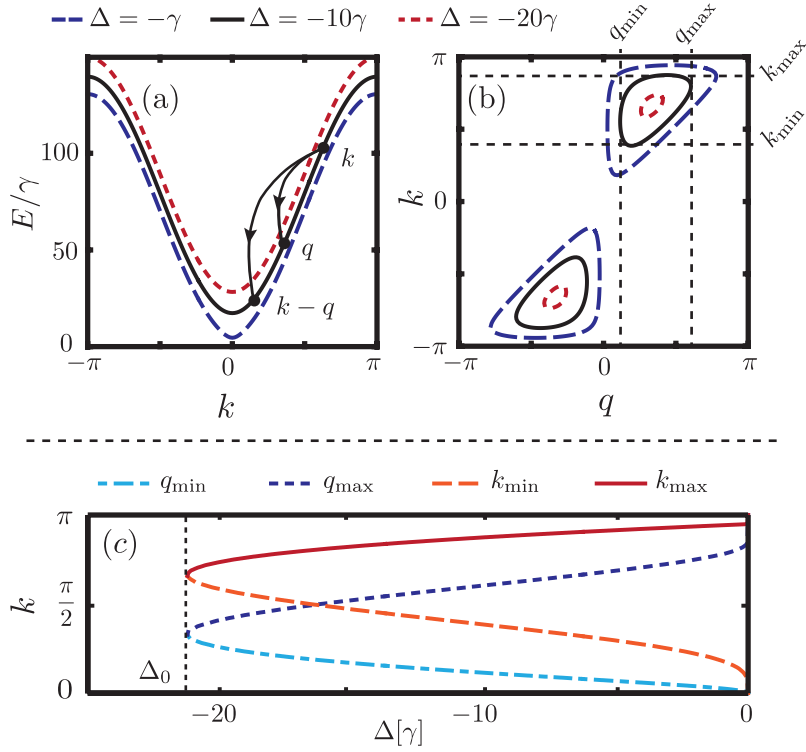


Figure 8.4: (a) The spectrum of excitations (8.14) for $(J, Un_0) = (30\gamma, 10\gamma)$ and for different values of the renormalized detuning Δ (8.9). If the drive is exactly on resonance, obtained by $\Delta \rightarrow 0^-$, the gap in the quasiparticle spectrum closes. Beliaev decay is sketched in the figure as an excitation at momentum k that decays to q and $k - q$ with conservation of energy. (b) The contours of energy conservation from (8.28) for the same parameters as panel (a). The extremal momenta are found from the contours and are indicated for $\Delta = -10\gamma$ (full black line), the case we have considered for the rest of the analysis. (c) The shift of the extremal momenta as a function of Δ for the positive contour. At $\Delta < \Delta_0 < 0$ the spectral gap becomes too large as compared to the bandwidth and no resonant scattering channels exist.

8.3. The truncated Wigner approximation

The equation of motion from (8.13) describes the *quasifree* degrees of freedom of the model in the linearized approximation. Again, quasiparticles are introduced that propagate through the chain with a lattice momentum k . Similar to the fermions from Chapter 3, they oscillate at a frequency ω_k , but they are now also damped at a rate γ .

The noise operators $\hat{\xi}_k$ enter as a drive term in (8.13) and therefore trigger the creation of quasiparticles. Their presence ensures that quasiparticle modes have a nonzero occupation, accompanied by non-trivial anomalous correlations in the stationary regime,

$$n_k^{(\chi)} = \langle \hat{\chi}_k^\dagger \hat{\chi}_k \rangle = v_k^2, \quad c_k^{(\chi)} = \langle \hat{\chi}_k \hat{\chi}_k \rangle = \frac{u_k v_k \gamma}{\gamma + 2i\omega_k}. \quad (8.15)$$

The nonequilibrium nature of the system is here neatly reflected by the fact that the occupation of the quasiparticle modes is not at all given by a finite-temperature Boltzmann-Gibbs distribution, as we would expect for an equilibrium condensate (see Chapter 9). Instead, it is set by a genuine interplay of interactions, hopping, driving and dissipation. This different origin is apparent in the slow, power-law-like decay of the occupation of high momentum modes, much slower than the usual exponential $n_k \propto \exp[-\omega_k/k_B T]$ of equilibrium systems.

8.3 The truncated Wigner approximation

While we have, up to now, always worked on the level of the density matrix or a stochastic operator equation to simulate quantum dynamics, the problem can also be translated to *phase space*, where the quantum fields are replaced by semiclassical phase-space variables. In principle entirely equivalent, this formulation has the advantage that a (quasi)probability distribution can be assigned to the phase-space variables, which – under certain approximations – can be sampled with semiclassical trajectories.

The mapping of a quantum problem onto a semiclassical problem is not unique, as can be understood from the fact that a phase-space representation always assumes a specific *operator ordering* for the quantum fields; classical variables can never account for non-commuting quantum mechanical fields. The three most common phase-space representations are the (positive or complex) P (normal ordering), the Q (antinormal ordering) and the Wigner representation (symmetric ordering). For this work, we will briefly review the latter, but a general overview of phase-space methods, with the advantages and difficulties of each representation, can be found in Ref. [69].

8.3.1 The Wigner quasiprobability distribution

The Wigner function or quasiprobability distribution was first proposed by Eugene Wigner in 1932 [128] and bears a rich history of applications in quantum optics and cold-atom physics [129]. Although it was first introduced in terms of the operators \hat{x} and \hat{p} , we prefer here to work in the basis of ladder operators $\hat{a}^{(\dagger)}$. For clarity, we start by defining the

Wigner function for a single mode, but the results generalize straightforwardly to a system that encompasses many independent modes, such as the array of cavities.

The first step is to introduce the characteristic function of a density matrix

$$\chi(\lambda, \lambda^*) = \text{tr} \left\{ \hat{\rho} e^{\lambda \hat{a}^\dagger - \lambda^* \hat{a}} \right\}. \quad (8.16)$$

The Wigner quasiprobability distribution is then defined as the Fourier transform of the characteristic function.

$$W(\alpha, \alpha^*) = \frac{1}{\pi^2} \int e^{-\lambda \alpha^* + \lambda^* \alpha} \chi(\lambda, \lambda^*) d^2 \lambda. \quad (8.17)$$

First of all, it always holds that

$$1 = \int W(\alpha, \alpha^*) d^2 \alpha, \quad (8.18)$$

making it tempting to treat the Wigner distribution directly as a probability distribution.

Furthermore, the moments of the Wigner distribution give the *symmetrically ordered* expectation values of the quantum operators

$$\langle \hat{a}^r \hat{a}^s \rangle_{\text{sym}} = \langle \alpha^r \alpha^{*s} \rangle_W = \int \alpha^r \alpha^{*s} W(\alpha, \alpha^*) d^2 \alpha, \quad (8.19)$$

where symmetrical ordering means that the expectation value is averaged over *all* possible operator orderings. In particular, for the density we then find

$$\langle |\alpha|^2 \rangle_W = \frac{1}{2} \left(\langle \hat{a} \hat{a}^\dagger \rangle + \langle \hat{a}^\dagger \hat{a} \rangle \right) = n + \frac{1}{2}, \quad (8.20)$$

with $n = \langle \hat{a}^\dagger \hat{a} \rangle$ the density of the quantum fields. We can anticipate at this point that the $1/2$ density as representation of the vacuum can be detrimental when it is not treated properly.

A very important result is that a unique Wigner function $W(\alpha, \alpha^*)$ can be assigned to any density matrix $\hat{\rho}$ and viceversa, making it a *one-to-one* correspondence. However, the downside of the Wigner representation is that a Wigner function is not necessarily positive-valued over its entire domain – hence the name *quasiprobability* distribution. For example, the Wigner function of a number (or Fock) state is a highly oscillatory function (certainly for higher photon numbers) with large positive and negative values on its domain, which eventually all add up to one after integration with (8.18).

Yet, when the quantum state is – loosely speaking – sufficiently close to Gaussian, the Wigner function is generally well-behaved and we can regard it (approximately) as a true probability distribution that does not suffer from these troublesome negative function values [130].

8.3.2 Truncating the equation of motion

The key observation to appreciate the value of phase-space methods, is that a partial differential equation for the evolution of the Wigner distribution can be derived from the master equation (8.3). In Ref. [69] it is explained how *operator correspondences* can be exploited to establish this mapping, but the final result is that the evolution of the Wigner distribution of the cavity array (8.1) is governed by [87]

$$\frac{\partial}{\partial t} W(\bar{\alpha}, \bar{\alpha}^*; t) = \sum_j \left\{ -i \left(\frac{\partial}{\partial \alpha_j} \mathcal{F}_j^{\text{MF}} + \frac{\partial}{\partial \alpha_j^*} \mathcal{F}_j^{\text{MF}*} \right) \right. \quad (8.21)$$

$$\left. + \gamma \frac{\partial^2}{\partial \alpha_j \partial \alpha_j^*} \right. \quad (8.22)$$

$$\left. + i \frac{U}{2} \frac{\partial^2}{\partial \alpha_j \partial \alpha_j^*} \left[\frac{\partial}{\partial \alpha_j^*} \alpha_j^* - \frac{\partial}{\partial \alpha_j} \alpha_j \right] \right\} W(\bar{\alpha}, \bar{\alpha}^*; t), \quad (8.23)$$

where we have denoted $\bar{\alpha} = \{\alpha_1, \dots, \alpha_L\}$ as the collection of semiclassical modes (one per cavity in the chain). The mean-field force in the Wigner representation then reads

$$\mathcal{F}_j^{\text{MF}} = \left(-\delta + |\alpha_j|^2 - i \frac{\gamma}{2} \right) \alpha_j - J(\alpha_{j-1} + \alpha_{j+1}) + \Omega_j. \quad (8.24)$$

Importantly, three different contributions to the dynamics of the Wigner distribution can be distinguished and they can be ordered according to the number of derivatives to the field α_j they contain. In the context of a Fokker-Planck-like equation for the evolution of a probability distribution, some have a natural interpretation [69].

1. The first line (8.21) only contains first derivatives to the field. This constitutes a drift of the probability distribution, which can be captured by deterministic dynamics under the effective mean-field force (8.24).
2. The second line (8.22) has a second derivative and corresponds to a diffusion term. The diffusion constant is here given by γ , the dissipation rate of the cavities.
3. On the third line (8.23) terms are collected that have a third-order derivative to the fields α_j . Unfortunately, there is no known analog of these terms in the context of a Fokker-Planck equation. As one may notice, though, they scale with the on-site interaction constant U . Generally one can say that these terms describe the genuine *quantum corrections* from interactions in the evolution of the Wigner distribution. Also, whenever we start with a positive-valued Wigner function, it is exactly this third-order term that is responsible for generating negative function values under time evolution.

While the dynamics of the Wigner distribution is close to being simulable with a (classical) Langevin equation, the third-order derivative-terms from (8.23) hinder the exact correspondence. However, whenever $U \ll \gamma$ we are led to assume that these third-order terms can be

neglected with respect to the second-order, the diffusion. This approximation comes down to truncating the equations of motion (8.21)–(8.23) – hence the name *truncated* Wigner approximation.

After truncation, the evolution of the Wigner distribution is essentially governed by a *Fokker-Planck equation*, for which we know from classical statistics that it has an equivalent *Langevin equation* for the Brownian motion of the phase-space variables [69],

$$id\alpha_j(t) = \mathcal{F}_j^{\text{MF}}(t)dt + \sqrt{\frac{\gamma}{2}}dW_j(t) \quad (8.25)$$

$$= \left[- \left(\delta + i\frac{\gamma}{2} \right) \alpha_j(t) - J(\alpha_{j+1}(t) + \alpha_{j-1}(t)) \right. \quad (8.26)$$

$$\left. + U(|\alpha_j(t)|^2 - 1)\alpha_j(t) + \Omega_j(t) \right] dt + \sqrt{\frac{\gamma}{2}}dW_j(t), \quad (8.27)$$

where the stochastic Wiener increment $dW_j(t)$ is white Gaussian noise with variance $\langle dW_j^*(t)dW_{j'}(t) \rangle = \delta_{j,j'}dt$ and a random phase.

In conclusion, by neglecting the third-order derivative terms from (8.23), we have established a stochastic differential equation for the semiclassical phase-space variables α_j . The Brownian motion of the fields α_j in phase space would then allow to sample from the Wigner distribution $W(\bar{\alpha}, \bar{\alpha}^*; t)$ by taking statistical ensemble averages over the generated fields. We merely need to bear in mind that averages over the semiclassical fields α_j give access to *symmetrically ordered* expectation values of the corresponding quantum fields \hat{a}_j , as we explained in (8.19).

8.3.3 A TWA simulation of the cavity array

Having reviewed the essentials of the truncated Wigner approach to establish the Langevin equation (8.25) that approximately samples the Wigner distribution, we can now continue with a simulation of the cavity array by means of semiclassical phase-space variables. The truncated Wigner approach is supposed to be valid in a regime of relatively weak interactions, characterized by $U \ll \gamma$, which motivated us to neglect the third-order derivative from (8.23) in the Fokker-Planck-like equation for the Wigner distribution. The linearized treatment presented in Sec. 8.2.4 would be valid in the same regime, provided the density is sufficiently large – sending U to zero whilst keeping Un_0 constant is the mean-field limit. Consequently, we would expect that both the truncated Wigner approach and the Bogoliubov analysis produce the same expectation values for a system with sufficiently small U and $n_0 \gg 1$, i.e. many more than one photon per cavity on average.

Nevertheless, when we compare in Fig. 8.5(a) the result of both methods for the density distribution n_k , with Bogoliubov prediction given in (8.15), we see that they yield largely different predictions. The worst of it all, however, is that we even see that the TWA produces *negative* occupation numbers for certain momenta. Note that this can in principle occur, as the semiclassical field ϕ_k contains 1/2 more density than the quantum field $\hat{\phi}_k$ through relation (8.20), which we have to subtract at the end of the simulation.

8.3. The truncated Wigner approximation

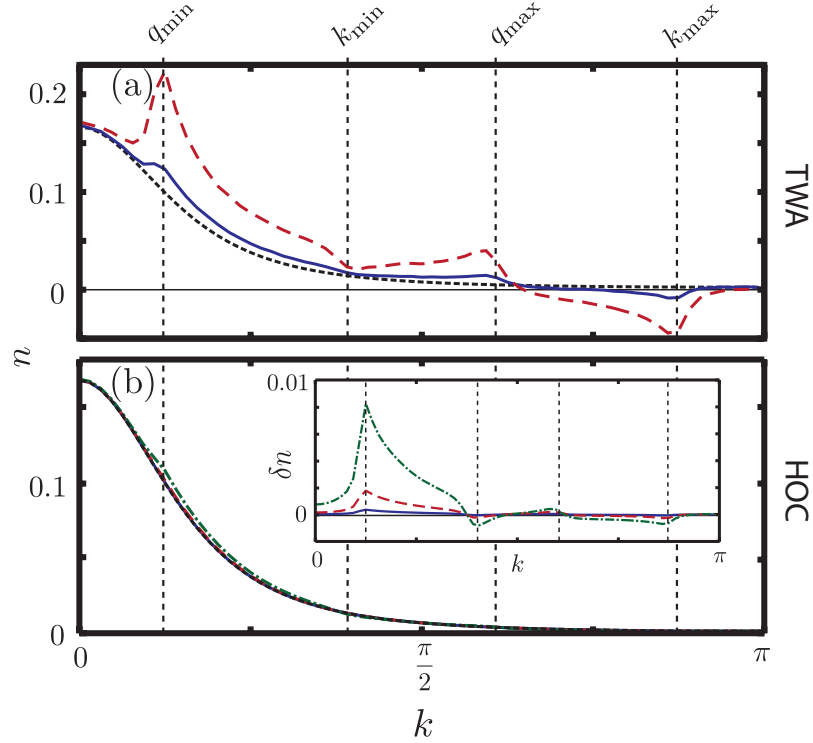


Figure 8.5: The momentum distribution of photons (in units of number of photons per mode) as obtained (a) from the truncated Wigner approximation (TWA) and (b) by truncating the hierarchy of correlation functions (HOC) at the third-order as discussed in the text. The parameters are $(J, \Delta, Un_0) = (30\gamma, -10\gamma, 10\gamma)$, $L = 128$ and three different interaction strengths $U = 0.02\gamma$ (blue full lines), $U = 0.1\gamma$ (red dashed lines) and $U = 0.5\gamma$ (green dash-dotted lines), such that the average number of photons per cavity is 500, 100 and 20 respectively. The latter case is not shown for the TWA computation, because it is outside of its regime of validity anyway. The Bogoliubov result (5.29) is also indicated (black dotted line). For clarity, we show the difference of the HOC with Bogoliubov $\delta n = n - n_{bog}$ in the inset of (b). The redistribution of particles is in both cases the strongest around the extremal values q_{min} , k_{min} , q_{max} and k_{max} (vertical dotted lines) of the contour from Fig. 8.4b). The inaccurate TWA result tremendously overestimates the corrections stemming from Beliaev-Landau decay, with a negative density for certain k modes, while the HOC result predicts only a small deviation from the Bogoliubov distribution. This is a direct consequence of the unphysical decay of the quantum vacuum in the Wigner representation.

Obviously, something is seriously going wrong within the TWA simulation. We come back to this breakdown in Sec. 8.4.2 after analyzing in detail what is happening.

8.4 Quasiparticle interactions: Beliaev-Landau channels

The Bogoliubov approximation provides an approximate description of the quantum state of the cavity array by including coherent pair-creation processes. These are of second order in the quantum fluctuations $\hat{\phi}_k$ in the interaction Hamiltonian and involve two condensate modes ψ_0 . The next order describes collisions that involve *three* quasiparticles and only one condensate mode. In the literature on superfluidity, these corrections are commonly known as Beliaev decay and Landau scattering (see Fig. 7.1 for the schematic representation). The former deals with a propagating quasiparticle that interacts with a condensate mode and gets converted into two new quasiparticles with lower momentum, while the latter describes the collision of two low-momentum quasiparticles into one with high momentum and a zero-momentum condensate mode. In Chapter 9 we will study how these collisions may drive the system to thermalization after an abrupt ramp of the interaction constant in an ultracold atomic gas.

Here, however, we are dealing with an inherent out-of-equilibrium setup and many of the convenient assumptions from equilibrium quantum dynamics are not expected to hold. While very general arguments at equilibrium, such as the second law of thermodynamics and detailed balance, assure us that higher-order scatterings will always guide the system to maximal entropy for a given conserved energy, the out-of-equilibrium scenario is much more ambiguous and may lead to surprises when these interactions turn out to be important.

8.4.1 Resonant scattering channels

If we take a few steps back to investigate the quasiparticle spectrum from the cavity array, which we showed in Fig. 8.4, we see from simple geometrical considerations that resonant scattering channels for third-order collision processes are possible in specific mean-field regimes. These are characterized by the general relation

$$\omega_{\mathbf{k}} = \omega_{\mathbf{q}} + \omega_{\mathbf{k}-\mathbf{q}}, \quad (8.28)$$

with $\omega_{\mathbf{k}}$ the quasiparticle oscillation frequency from (8.11). While there is no strict requirement of energy conservation out of equilibrium, the presence of these collision may show its importance when the linewidth, set by the photon decay rate γ , is significantly smaller than the interaction energy Un_0 , ensuring that scatterings take place mostly on-shell.

Recall that we needed at least two spatial dimensions to have resonant channels for Beliaev-Landau scatterings in a continuum setup at equilibrium. In other words, the convexity of the quasiparticle spectrum and the absence of a spectral gap in an equilibrium scenario implied that third-order scatterings always require a nonzero angle between the

8.4. Quasiparticle interactions: Beliaev-Landau channels

incoming and outgoing states, as is illustrated in Fig. 7.2. For lattice models, however, resonant scattering channels can also be found in one spatial dimension because the quasiparticle spectrum follows the shape of the tight-binding lattice dispersion, which is concave at momenta close to the edge of the Brillouin zone [116].

In our model, the allowed wavevectors k and q that *exactly* satisfy the energy and momentum conservation condition (8.28) in a one-dimensional chain of cavities, for which the quasiparticle dispersion is given in (8.11), are drawn in Fig. 8.4(b). From the contours we can derive maximal and minimal values for the allowed k and q lattice vectors that can scatter, as is indicated on the contour plot. More precisely, only excitations with a wavevector k for which $k_{\min} < k < k_{\max}$ can scatter resonantly to excitations with wavevectors q and $k - q$ through Beliaev decay. Likewise, only excitations with a wavevector q for which $q_{\min} < q < q_{\max}$ can combine with an excitation at $k - q$ to form one at k . Notice that the momentum distribution from TWA, drawn in Fig. 8.5, shows pronounced peaks at *exactly* the minimal and maximal q value and dips at the k value. Clearly, this is a compelling suggestion that Beliaev-Landau processes lie at the heart of the erroneous TWA prediction.

When we change the parameters that characterize the mean-field, we also modify the dispersion relation for quasiparticles in the array. In turn, this will deform the shape of the resonant scattering contours from Fig. 8.4(b) and therefore also shifts the peaks and dips that we encountered in the momentum distribution from the TWA simulation¹. In particular, we illustrate in Fig. 8.4(c) how the four extremal momenta k_{\min} , k_{\max} , q_{\min} and q_{\max} shift when we vary the interaction-renormalized pump detuning Δ ; this is conveniently done in experiment by changing the laser frequency ω_L (see relation (8.9)). When the drive is too far below resonance, i.e. when $\Delta < \Delta_0$, with $\Delta_0 < 0$ a critical value that can be derived from the dispersion relation, the spectral gap is too large in energy as compared to the spectral bandwidth and no resonant Beliaev-Landau scattering channels exist. In the limit of $\Delta \rightarrow 0$, for which the dispersion relation becomes linear at low momenta, we retrieve the contour of an equilibrium condensate in a one-dimensional lattice, which was studied in Ref. [116].

8.4.2 The origin of the breakdown of TWA

Ironically, while a simulation of the cavity array within the TWA formalism produced largely unphysical results, it presented at the same time an invaluable hint regarding the possible importance of Beliaev-Landau collisions in the array – which might have gone unnoticed otherwise. The reason is that the impact of the scatterings is severely overestimated within this approach, rendering their footprints far more pronounced.

To understand this, we need to take a step back and recall that within the Wigner representation of a quantum problem, we actually sample the expectation values of *symmetrically*

¹This is actually how we found out what was going wrong with the TWA.

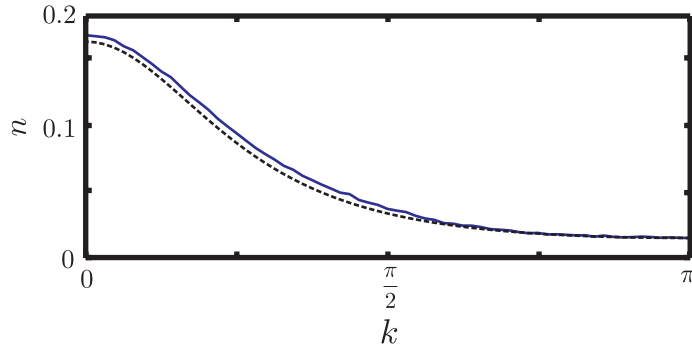


Figure 8.6: The momentum distribution (full blue line) obtained from a TWA simulation with $(J, \Delta, Un_0) = (10\gamma, -10\gamma, 10\gamma)$ and an interaction constant $U = 0.1\gamma$. The result lies very close to the Bogoliubov prediction (dotted black line) when the quasiparticle spectrum does not contain resonant Beliaev-Landau channels.

ordered operator products, as explained in (8.19). For the density of the semiclassical phase-space fields, this means that we do not directly sample the density of the corresponding quantum fields, but the density plus a half-quantum, as illustrated in (8.20). Nevertheless, the density of the quantum fields that we found within the Bogoliubov formalism, shown in Fig. 8.5, does not exceed ~ 0.2 which is even significantly smaller than the $1/2$ density from the representation of the vacuum. Upon truncating the equation of motion for the evolution of Wigner distribution, explained in Sec. 8.3, we directly neglected a fraction of interactions that can be attributed to quantum corrections. Consequently, in the *truncated* Wigner approach this $1/2$ density of the quantum vacuum also participates in the scattering and entirely spoils the actual corrections coming from the true quantum density of fluctuations. At high momenta, we expect the Bogoliubov distribution to approach zero, such that in reality only a restricted fraction of quantum fluctuations can actively participate in the true scattering.

Our conclusion that the breakdown of the TWA can be attributed to quasis resonant third-order scattering of quantum fluctuations is confirmed by running another simulation with mean-field parameters with a quasiparticle spectrum without resonant Beliaev-Landau channels. By modifying the parameters Un_0 , J and/or δ we can enter into a regime where no resonant third-order scattering exists. Here, we simply choose to replace the value $J = 30\gamma$, used in the previously presented simulations, with $J = 10\gamma$, in order to have $\Delta < \Delta_0$ (see Fig. 8.4c)). As can be seen in Fig. 8.6, the absence of on-shell Beliaev-Landau channels leads to a much better agreement with the prediction of the Bogoliubov approximation and, most of all, no unphysical negative densities are found. The small deviation from the Bogoliubov distribution can probably be attributed to the nonresonant scattering of the $1/2$ vacuum noise.

As far as we are aware, these problems are related to an intrinsic shortcoming of the *truncated* Wigner approach. Supposedly, when the third-order derivative term from (8.23)

8.5. Constructing a hierarchy of correlation functions

is properly dealt with – rather than simply neglected – the problems that we have stumbled upon should be remedied. As for now, we believe that determining reliably the domain of validity for the truncated Wigner approach is an open question, as is the possibility to improve upon the method.

8.5 Constructing a hierarchy of correlation functions

Before continuing with the analysis, we would like to highlight an important consideration again. It is exactly the *absence* of detailed balance in a driven-dissipative context which motivates us to study the effects of spontaneous Beliaev-Landau processes in the steady-state regime of the cavity array (see Chapter. 7). In the previous section, we have illustrated that two crucial ingredients for these scatterings to be possibly relevant are indeed present: 1) there is finite occupation of Bogoliubov modes over the entire Brillouin zone, as given in (8.15), and 2) there are regions in phase space for which energy and momentum are conserved according to (8.28), which allows the Bogoliubov modes to scatter and redistribute (quasi)resonantly.

Although the TWA gave us a strong hint of the possible importance of Beliaev-Landau scatterings, it produced highly unphysical results. This section deals with the construction of a method, physically sound in nature, in terms of a truncated hierarchy of correlation functions to predict the true corrections attributed to Beliaev-Landau scattering in the cavity array.

8.5.1 Deriving the hierarchy

For the Bogoliubov formalism, presented in Sec. 8.2.4, we introduced a linearized form of Eq. (8.6) to reproduce the quadratic correlation functions (8.15), describing the effect of a nonzero quasiparticle occupation due to coherent pair-creation processes. Straightforwardly, we can expect the *third-order* correlation functions of Bogoliubov modes to represent *third-order* scattering processes. More precisely, the matrix $M_{k,q}^{(\chi)} = \langle \hat{\chi}_{k-q}^\dagger \hat{\chi}_q^\dagger \hat{\chi}_k \rangle$, with $\hat{\chi}_k$ the diagonalized Bogoliubov modes, would capture the physics of scatterings that turn a quasiparticle with momentum k into two quasiparticles with momenta q and $k - q$ and vice versa: the Beliaev-Landau scatterings (see Fig. 7.1).

To facilitate our discussion, we now go back from the Bogoliubov basis to the original basis of the quantum fluctuations, represented by the $\hat{\phi}_k$ operators, such that we need to include two distinct third-order correlators in the dynamics², namely

$$M_{k,q} = \langle \hat{\phi}_{k-q}^\dagger \hat{\phi}_q^\dagger \hat{\phi}_k \rangle, \quad R_{k,q} = \langle \hat{\phi}_{-k-q} \hat{\phi}_q \hat{\phi}_k \rangle. \quad (8.29)$$

In Appendix C.1 we explain how we can derive the equations of motion for correlators up to third order from the time evolution of a quantum fluctuation (8.6).

²This is only a choice. In fact, for the analysis of the next chapter we prefer to work in the Bogoliubov basis.

If we fix ψ_0 to the mean-field value, we find a finite value for the first-order correlator $\phi_0 = \langle \hat{\phi}_0 \rangle$ from the back-reaction of the second and third-order correlator in (8.9). It turns out to be much more convenient to choose $\phi_0 = 0$ by definition and absorb any variations of the condensate wavefunction directly in the mean field ψ_0 through the Gross-Pitaevskii-like equation with back-reaction terms from (8.9). Setting $\phi_0 = 0$ also has the convenient implication that all correlators employed in the hierarchy are of *connected* nature because the factorizable part vanishes. This is easily understood by noticing that the factorization of correlators up to third order always contains a first order in the products, making these terms drop. Generally, the convergence of a scheme composed only of connected correlators is much better [131].

The *truncation* of a hierarchy of correlation functions is tricky in general and one must always try to compare with higher-order truncations to verify the convergence of the observables of interest. In our case, though, we have the additional benefit that we can expand the quantum field via ansatz (8.5) by means of a condensate mode ψ_0 and quantum fluctuations $\hat{\phi}_k$ on top. In terms of the connected correlators of the quantum fluctuations $\hat{\phi}_k$, this permits us to show that the magnitude of the correlators goes down to zero for higher truncation order.

Correlation functions of order four, which enter into the equations of motion of the second and third-order correlators, are then factorized into all different products of second-order correlation functions³. Within this approximation, we explicitly neglect the *connected* part of the fourth-order correlation function, but we retain the main contribution attributed to factorizable correlations.

The fifth-order correlator, which enters in the equation of motion for the third-order correlation functions, can be neglected on this level of approximation. Already in factorized form it would be decomposed into various products of second and third order, which are higher-order corrections to other dominant terms in the equations of motion. In Appendix C.1 we give more details on the truncation of the equations of motion and the implications. Also, to ensure that our method is physically sound, we present a comparison with higher-order truncation schemes for an array composed of only 10 sites in Appendix C.2.

Using the notation from (8.29) we can then present the different equations of motion that build up the constructed truncated hierarchy of correlation functions:

- With the introduced notation for the third-order correlators, the Gross-Pitaevskii equation from (8.9) for the homogeneous condensate background ψ_0 , extended with the back-reaction terms reads

$$\begin{aligned} i\partial_t\psi_0 &= \left(-\Delta - i\frac{\gamma}{2}\right)\psi_0 + \Omega \\ &+ \frac{2U\psi_0}{L} \sum_k n_k + \frac{U\psi_0^*}{L} \sum_k c_k + \frac{U}{\sqrt{L^3}} \sum_{k,q} M_{k,q}^*. \end{aligned} \quad (8.30)$$

³In principle, also factorizations of third and first order should be included, but these cancel with our choice of variables, namely $\phi_0 = 0$.

8.5. Constructing a hierarchy of correlation functions

- The second-order correlation functions that we found within the Bogoliubov formalism (5.29) are now coupled to the third-order correlation functions (8.29). For the density distribution we then find

$$i\partial_t n_k = -i\gamma n_k + 2i\Im \left[U \left(\psi_0^2 + \frac{1}{L} \sum_q c_q \right) c_k^* + \frac{2U\psi_0}{\sqrt{L}} \sum_q M_{q,k} + \frac{U\psi_0^*}{\sqrt{L}} \sum_q M_{k,q}^* \right], \quad (8.31)$$

and for the pair correlations,

$$\begin{aligned} i\partial_t c_k &= \left(2\epsilon_k + 2U \left(|\psi_0|^2 + \frac{1}{L} \sum_q n_q \right) - i\gamma \right) c_k + U \left(\psi_0^2 + \frac{1}{L} \sum_q c_q \right) (2n_k + 1) \\ &\quad + \frac{2U\psi_0}{\sqrt{L}} \sum_q (M_{q,-k}^* + M_{q,k}^*) + \frac{U\psi_0^*}{\sqrt{L}} \sum_q (R_{-k,q} + R_{k,q}). \end{aligned} \quad (8.32)$$

Note that the factorized contribution of the fourth-order correlator enters here in the equations of motion as a small correction to the couplings ψ_0^2 and $|\psi_0|^2$. At equilibrium these corrections are well-studied in the Hartree-Fock-Bogoliubov method [132].

- Finally, we also derive the equation of motion for the third-order correlations (8.29)

$$\begin{aligned} i\partial_t M_{k,q} &= \left(\epsilon_k - \epsilon_q - \epsilon_{k-q} - U|\psi_0|^2 - \frac{3i}{2}\gamma \right) M_{k,q} \\ &\quad - U(\psi_0^*)^2 (M_{q,k}^* + M_{k-q,k}^*) + U\psi_0^2 R_{-k,q}^* + F_{k,q}^{(M)}, \end{aligned} \quad (8.33)$$

and

$$i\partial_t R_{k,q} = \left(\epsilon_k + \epsilon_q + \epsilon_{k+q} + 3U|\psi_0|^2 - \frac{3i}{2}\gamma \right) R_{k,q} \quad (8.34)$$

$$+ U\psi_0^2 (M_{-k,q}^* + M_{-q,k}^* + M_{k+q,k}^*) + F_{k,q}^{(R)}. \quad (8.35)$$

Here, the $F_{k,q}^{(M,R)}$ are drive terms containing the coupling to fourth-order correlation functions. In our scheme, this is the level where we truncate to decompose the fourth-order correlators into all possible products of second order. In Appendix C.1 we provide more details, but the final result is

$$\begin{aligned} F_{k,q}^{(M)} &= \frac{2U\psi_0}{\sqrt{L}} \left(c_{k-q}^* n_q + n_{k-q} c_q^* - n_k (c_q^* + c_{k-q}^*) \right) \\ &\quad + \frac{2U\psi_0^*}{\sqrt{L}} \left(n_{k-q} n_q - n_k (1 + n_q + n_{k-q}) - c_k (c_q^* + c_{k-q}^*) \right) \end{aligned} \quad (8.36)$$

$$\begin{aligned} F_{k,q}^{(R)} &= \frac{2U\psi_0}{\sqrt{L}} \left(c_k + c_q + c_{k+q} + n_{k+q} c_q + c_{k+q} n_q + n_k c_q + n_k c_{k+q} + c_k n_q + c_k n_{k+q} \right) \\ &\quad + \frac{2U\psi_0^*}{\sqrt{L}} \left(c_k c_q + c_k c_{k+q} + c_q c_{k+q} \right) \end{aligned} \quad (8.37)$$

Equations (8.31)–(8.35) provide a truncated solution to the full time-dependent problem when appropriate initial conditions are inserted for all the variables. We, however, intend

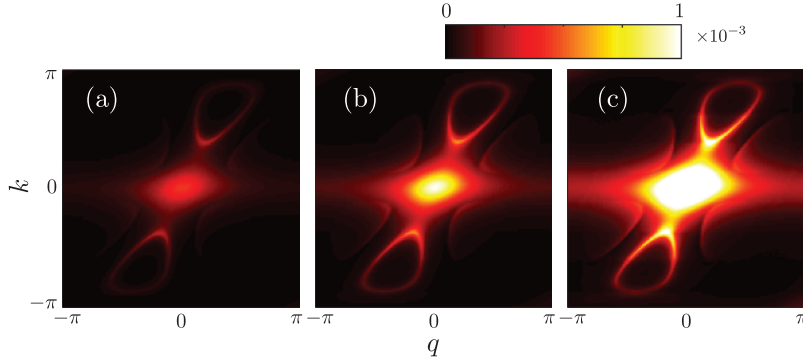


Figure 8.7: The absolute value of the third-order correlation matrix $M_{k,q}$ for $U = 0.02\gamma$ (a), $U = 0.1\gamma$ (b) and $U = 0.5\gamma$ (c) for the same parameters as Fig. 8.5. The curve representing energy and momentum conservation shown as a full black line in Fig. 8.4b) corresponds here to a line of enhanced scattering.

to focus only on the convergence of the scheme to the steady-state solution. To obtain this, we initialize the system with the mean-field condensate amplitude ψ_0 and the Bogoliubov solution (8.10) for n_k and c_k , and we initially set $M_{k,q}$ and $R_{k,q}$ to zero. We then let the system evolve in time until it converges and reaches a steady state.

For the time evolution we have implemented a Runge-Kutta-based routine with adaptive time step to integrate the hierarchy (8.31)–(8.35) in time. We can follow a quantity such as $\delta(t) = 1/(L\Delta t) \sum_k |n_k^{t+\Delta t} - n_k^t|/n_k^t$ as a function of t for fixed Δt to monitor the convergence of the equations. We then set a criterion $\delta(t) < \epsilon$, with ϵ a chosen small number, to stop the evolution of the system of equations. Typically, $\delta(t) \sim \exp(-\kappa t)$ and therefore convergence is rapidly achieved. For a system with 128 cavities we need about 2 minutes of CPU time on a standard computer, without any optimization, to obtain an accuracy $\delta < 10^{-6}$.

8.5.2 The momentum distribution in the HOC scheme

In Fig. 8.5 we show the comparison between the erroneous results that were found within the truncated Wigner approach and the ones obtained with the presented truncated hierarchy of correlation functions (HOC). We again see that the corrections from Bogoliubov theory scale with the single-photon interaction constant U when interaction energy Un_0 , the relevant parameter for the Bogoliubov analysis is kept fixed. Importantly, the predictions from the HOC do *not* suffer from unphysical negative occupation numbers, such as they were found in TWA. Quantitatively, we find that the corrections upon Bogoliubov theory are much smaller than the ones found in TWA. From a qualitative point of view, however, we note the similarity in shape with the exaggerated corrections from TWA, but far less pronounced. As we had presumed before, we can now safely conclude that the physical scattering processes between quasiparticles within the TWA are severely overwhelmed by

8.5. Constructing a hierarchy of correlation functions

the unphysical Beliaev-like decay of the 1/2 vacuum noise; the magnitude of this noise is substantially larger than the true occupation number of excitations on the Bogoliubov level.

We conclude from Fig. 8.5(b) that there is a small redistribution of particles from high to low momenta, meaning that Beliaev decay of high-momentum quasiparticles is the predominant mechanism for the redistribution. Similar to what we found with the TWA method, this is reflected by two peaks in the momentum distribution around the extremal values of the output states from this process, the q_{\min} and q_{\max} , while there are small dips at the extremal input momenta k_{\min} and k_{\max} . As can be seen on Fig. 8.4, this is attributed to the larger density of states for possible output (input) states for scatterings with input (output) momenta around k_{\min} or k_{\max} (q_{\min} or q_{\max}). Recall that energy does not need to be exactly conserved in an open system, which implies that scatterings can also occur slightly outside the interval $[q_{\min}, k_{\max}]$ with a width set by the linewidth γ . We can anticipate at this point that the characteristic series of peaks and dips in the steady-state momentum distribution may provide a promising experimental signature of Beliaev-Landau scattering in nonequilibrium quantum fluids. In the next section, we investigate in more detail which footprint these scatterings may leave in a realistic semiconductor microcavity array.

8.5.3 The third-order correlation functions

Now that we have identified a possible imprint of Beliaev-Landau scattering on the momentum distribution of the cavity array, we can try to gain insight into the nature of these scatterings by studying the scattering matrix $M_{k,q}$, shown in Fig. 8.7. Besides a central peak that we attribute to nonresonant decay, the contour that represents energy and momentum conservation from Fig. 8.4(b) is apparent as a band of enhanced magnitude in the matrix $M_{k,q}$. To understand this better, we can take a step back and consider the third-order correlator in terms of the Bogoliubov operators $\hat{\chi}_k$; the modes that diagonalize the quadratic equations of motion. While both are in principle equivalent and merely require a number of linear transformations with the u_k and v_k Bogoliubov functions, we had preferred to work in the basis of quantum fluctuations $\hat{\phi}_k$ for the purposes of this analysis. In Chapter 9 we will develop a hierarchy of correlation functions in terms of the diagonalized Bogoliubov operators $\hat{\chi}_{\mathbf{k}}$.

In any case, it is not difficult to see that the corresponding third-order correlator of the $\hat{\chi}_k$ assumes the form

$$\langle \hat{\chi}_{k-q}^\dagger \hat{\chi}_q^\dagger \hat{\chi}_k \rangle = \frac{2U}{\sqrt{L}} \frac{\psi_0 A_{k,q} + \psi_0^* B_{k,q}}{\omega_k - \omega_q - \omega_{k-q} - \frac{3i}{2}\gamma}, \quad (8.38)$$

where the $A_{k,q}$ and $B_{k,q}$ are coefficients of order one that would result from the various combinations of the Bogoliubov u_k and v_k factors when the different terms from the factorization of the fourth-order correlation functions, presented in (8.36)–(8.37) are transformed

to the $\hat{\chi}_k$ basis⁴.

Written in form (8.38), it is now immediate to see that Beliaev-Landau scatterings are concentrated about the energy-conserving contours from (8.28) with a linewidth set by the photon decay rate γ . Since we have opted to work out the hierarchy in terms of the $\hat{\phi}_k$ operators, which are a linear transform of $\hat{\chi}_k$ and $\hat{\chi}_{-k}^\dagger$ with oscillation frequencies $\pm\omega_k$ (see (8.12)), also scatterings to negative energy states must be included. The contours characterizing these scatterings can be simply found by setting $\omega_k \rightarrow -\omega_{-k}$ and/or $\omega_q \rightarrow -\omega_{-q}$ in (8.28) and in Fig. 8.7 they appear as less pronounced bands of enhanced matrix elements.

As a final remark, we want to emphasize that the hierarchy of correlation functions, presented in (8.31)–(8.35), constitutes a consistent expansion of one order beyond standard Bogoliubov theory. More precisely, while the Bogoliubov approximation is an expansion upon mean-field that captures corrections scaling as $\sim Un_0$, we now conclude from (8.38) that terms scaling as $\sim U\sqrt{n_0/L}$, the next order in the expansion, are also represented in the introduced method. Exactly these terms were vital for illustrating that the occupation numbers of quasiparticles in the array are slightly redistributed due to quairesonant Beliaev-Landau scattering. In our framework, this effect is accounted for in (8.31)–(8.32) by the back-reaction of the third-order correlation matrices, which capture the scatterings, upon the momentum distribution and anomalous correlation.

8.6 The footprint of spontaneous Beliaev-Landau scattering in an array of semiconductor micropillars

In the previous section, we have presented the analysis of a generic cavity array characterized by Hamiltonian (8.1). Recall that we merely needed a number of dimensionless couplings to quantify the interplay of photon hopping, interactions, detuning and losses. In this section, we aim to concretize the theoretical results and to estimate the expected experimental signal for a realistic cavity array composed of semiconductor micropillars, inspired by the experimental results from Ref. [120].

For our estimations, the cavities, L in total, are positioned at a distance $\Delta x = 1 \mu\text{m}$ from each other and are irradiated by a laser with frequency $\hbar\omega_L = 1.6 \text{ eV}$. Photons inside the cavities have an average lifetime of 20 ps, giving a linewidth of $\hbar\gamma = 33 \mu\text{eV}$, and display a single-photon nonlinearity of $U = 3.3 \mu\text{eV}$, so that $U \approx 0.1\gamma$. Furthermore, we set $J = 30\hbar\gamma \approx 1\text{meV}$, $\Delta = -10\hbar\gamma \approx -330\mu\text{eV}$ and assume an average number of photons per cavity of $n_0 = 100$, corresponding to $Un_0 \approx 10\gamma \approx 330\mu\text{eV}$. With this choice of parameters, we can rely on the theoretical results that were discussed previously in Sec. 8.5 (see Fig. 8.5(b) red dashed line and Fig. 8.7(b)).

⁴After elaboration, the result would be similar to equations (9.33)–(9.34) from the next chapter.

8.6. The footprint of spontaneous Beliaev-Landau scattering in an array of semiconductor micropillars

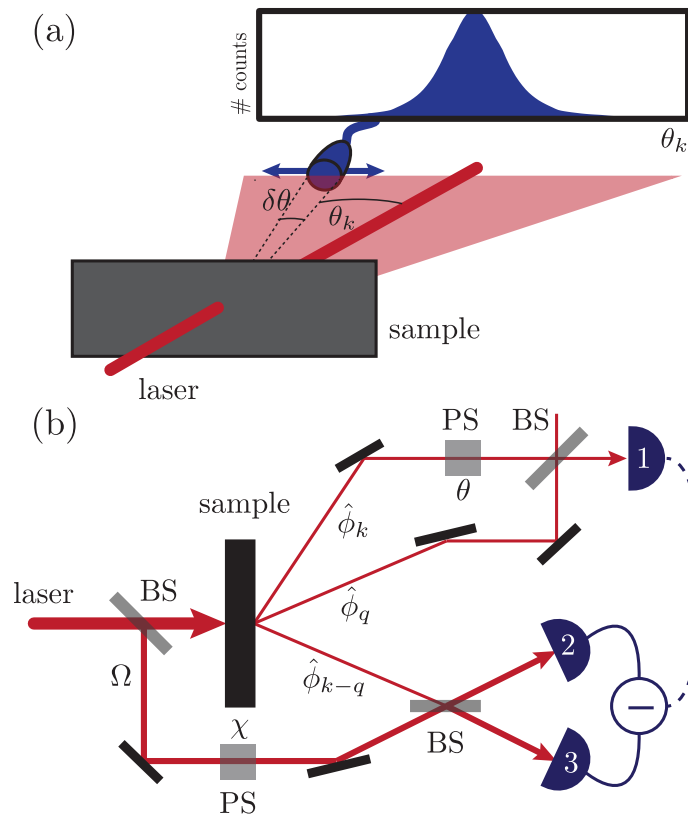


Figure 8.8: (a) A sketch of the standard setup for an angle-resolved measurement. While the cavity array is pumped in $k = 0$ mode with a perpendicularly incident laser beam, quantum fluctuations are expected to leak out at a nonzero angle $\sin \theta_k = ck/(\omega_L \Delta x)$. In the setup discussed in the text, all photons are expected to leak out within an angle of about 23° . Measuring the intensity at an angle θ_k with width $\delta\theta$ then leads to the measurement of n_k , for which the theoretical prediction is given in Fig. 8.5(b). (b) A possible selection and interference scheme to detect the non-Gaussianities in the cavity output field through the third-order correlator (8.29). Simultaneous clicks between detector 1 and the difference signal of detectors 2 and 3 allows for the measurement of the quantity from expression (8.44). 'PS' stands for phase shifter and 'BS' for a (50:50) beam splitter.

8.6.1 Measuring the momentum distribution

In the theoretical analysis from Sec. 8.5, we suggested that the momentum distribution would be a good candidate to witness signatures of Beliaev-Landau scattering in the cavity array. The scatterings slightly redistribute the occupation numbers of the quantum fluctuations as they are found within the Bogoliubov formalism, leaving a series of peaks and dips as characteristic imprint. From Fig. 8.5(b) (red dashed line) we predict a deviation of about 2% from the Bogoliubov result (8.10) around the minimal final-state momentum of Beliaev decay q_{\min} with the proposed parameters for the microcavity array.

The momentum distribution can be detected with an angle-resolved measurement of the far-field emission, as is sketched in Fig. 8.8(a); a photon with in-plane momentum k , flies out of the cavity array at an angle given by $\sin \theta_k = ck/(\omega_L \Delta x)$, with c the speed of light in vacuum [87]. With the parameters of this particular microcavity array, we find that all quantum fluctuations can be detected by restricting the field of view to a cone of aperture $\theta_{\max} \approx 23^\circ$. Importantly, the dominant signal of the condensate mode at $k = 0$ is concentrated about the perpendicular axis and can be filtered out in space after the microcavity. Recall that we have exploited this property intensely in Chapter 6 to shape the coherent field before interference in order to engineer photon statistics.

The momentum-space density of photons that escape from the cavity array (i.e the flux of photons escaping per momentum mode) is approximately given by $\frac{d\Phi}{dk} = L n_k \gamma / (2\pi)$ where $2\pi/L$ is the momentum-space separation between adjacent modes for an array of L cavities. If we assume an angular resolution of $\delta k = 0.025 \times 2\pi$, which is larger than the k -space mode separation but smaller than the width of the Beliaev peaks, we find a photon flux of about $\Phi = 1.5 \cdot 10^{10} \text{ s}^{-1}$ around q_{\min} , where $n_k \approx 0.1$. Unfortunately, detectors usually have a limited efficiency, such that we can estimate the number of photon clicks as $N = \varepsilon_{\text{eff}} \Phi$, where ε_{eff} is some overall efficiency factor that incorporates uncontrolled photon losses and detection efficiency. A huge advantage is that the signal can be integrated in time until a sufficient amount of photons is collected; at least during the time the whole setup can be held under stable conditions.

Obviously, when a stronger single-photon nonlinearity U can be realized, we expect an even stronger signal of Beliaev-Landau processes, as we see in Fig. 8.5(b). While this poses some experimental challenges, a stronger nonlinearity can in principle be obtained by reducing the dimensions of the microcavities or by increasing the excitonic fraction of polaritons [98], and does not necessarily require a different mechanism to mediate photon interactions. Alternatively, a more speculative possibility is to use the platform of superconducting circuits, explained in Sec. 8.1.2, where strong nonlinearities are naturally achieved [121].

8.6.2 The role of disorder

A crucial point of concern is that the Beliaev-Landau peaks, being rather small in magnitude, can be washed away when a large amount of disorder is present in the cavity array. For example, when the cavity resonance ω_c slightly varies from site to site, this can be modeled as a random potential V_j that is applied to the photon field in each pillar. This is particularly easy to see from the Hamiltonian (8.1), where this would modify the detuning δ differently for each cavity in the chain.

We may give an estimate for the effects of disorder by considering the Fourier transform V_k of a random potential, $V_j = \frac{1}{\sqrt{L}} \sum_k V_k e^{ikj}$, which is applied to the cavity array. Following (8.9), we then find that the random potential enters into the equation of the mean field as

$$i\dot{\psi}_j = \left(V_j - \delta - i\frac{\gamma}{2} \right) \psi_j - J(\psi_{j+1} + \psi_{j-1}) + U|\psi_j|^2 \psi_j + \Omega_j. \quad (8.39)$$

When we restrict to evaluating the linear response of the mean field to disorder, we find that the non-uniform polariton field can be formulated as $\psi_j = \psi_0 + \frac{1}{\sqrt{L}} \sum_k \delta\psi_k e^{ikj}$. After substitution in (8.39) and collecting terms up to linear order in $\delta\psi_k$ and V_k , we find a set of linear equations for each mode

$$\mathcal{L}_k \begin{pmatrix} \delta\psi_k \\ \delta\psi_{-k}^* \end{pmatrix} = \begin{pmatrix} -V_k \psi_0 \\ V_k \psi_0^* \end{pmatrix} \quad (8.40)$$

with the response matrix

$$\mathcal{L}_k = \begin{pmatrix} \epsilon_k + Un_0 - i\frac{\gamma}{2} & U\psi_0^2 \\ -U\psi_0^{*2} & -\epsilon_k - Un_0 - i\frac{\gamma}{2} \end{pmatrix} \quad (8.41)$$

and ϵ_k given in (8.7). By solving (8.40) we derive the response of the density distribution to the disorder potential in the linear regime

$$\delta n_k = |\delta\psi_k|^2 = |V_k \psi_0|^2 \frac{\epsilon_k^2 + \gamma^2/4}{(\omega_k^2 + \gamma^2/4)^2} \quad (8.42)$$

with ω_k given in (8.14).

Since all relevant energy scales are larger than γ and $\omega_k \approx \epsilon_k$ for the purposes of this (very qualitative) analysis, we can further approximate $\delta n_k \sim n_0 (V_k/\omega_k)^2$. Provided the disorder noise is white and uncorrelated, we then find that the disorder potential is required to satisfy

$$\sqrt{\langle V_j^2 \rangle} \lesssim \omega_k^{\text{peak}} \sqrt{\frac{\delta n_k^{\text{peak}}}{n_0}}, \quad (8.43)$$

in order to have peaks from disorder that are smaller than the peaks of Beliaev-Landau scattering. Here, ω_k^{peak} is the frequency of the mode at the Beliaev-Landau peak and δn_k^{peak} is the height of the peak (on the order of $2 \cdot 10^{-3}$, see the red line in the inset of Fig. 8.5(b)). Unfortunately, a recent experiment with a setup similar to ours reported a

standard deviation of about $30\mu\text{eV}$ for the disorder potential [133], about a factor 10 larger than required for our estimations.

Nevertheless, the origin of the Beliaev-Landau peaks is fundamentally different in nature than the ones attributed to disorder. For each realization of a cavity array, the disorder peaks should be different, while the Beliaev-Landau signal is not expected to depend on this. With modern etching techniques entire 2D landscapes for the photons are usually created on a single microcavity sample (see Sec. 8.1.1). If many copies of the cavity array are etched on the same sample, it is expected that averaging out over the different realizations will cancel out effects from disorder, while the Beliaev-Landau peaks are left in place. If the different copies are positioned adjacent to one another, this merely requires displacing the incident laser beam from one array to the next.

Another possibility to distinguish the peaks from Beliaev-Landau scatterings in cavity array from disorder is as follows. Recall that the exact position of the Beliaev-Landau peaks strongly depends on the mean-field parameters Un_0 , Δ and J . In Fig. 8.4(c) we show how the peaks are expected to shift when the interaction-renormalized detuning Δ is varied. Consequently, by simply varying the laser frequency ω_L as the sample is shone, the detuning Δ is modified according to (8.9) and the Beliaev-Landau peaks in the momentum distribution are expected to experience a well-defined shift, such as the one illustrated in 8.4(c).

8.6.3 Measuring the third-order correlator

Rather than searching for the small peaks predicted as genuine signatures of Beliaev-Landau scattering, an alternative method is the direct measurement of the third-order correlation function. Admittedly, this strategy is somewhat more sophisticated and requires an involved selection and interference scheme of the modes with wavevector k , q and $k - q$.

In Fig. 8.8(b) we present a sketch of the scheme that would allow to measure the quantity

$$\begin{aligned} & \left\langle (\hat{\phi}_q^\dagger + e^{-i\theta}\hat{\phi}_k^\dagger)(\hat{\phi}_q + e^{i\theta}\hat{\phi}_k)(e^{i\chi}\Omega\hat{\phi}_{k-q}^\dagger + e^{-i\chi}\Omega^*\hat{\phi}_{k-q}) \right\rangle \\ & = 2\Re\left\{ \Omega e^{i(\theta+\chi)} \langle \hat{\phi}_{k-q}^\dagger \hat{\phi}_q^\dagger \hat{\phi}_k \rangle \right\} = 2\Re\left\{ \Omega e^{i(\theta+\chi)} M_{k,q} \right\}. \end{aligned} \quad (8.44)$$

Here, the second step is obtained after omitting all correlations that are not momentum-conserving, since they must vanish in a spatially uniform sample. One needs to detect simultaneous clicks between detector 1 and the difference signal of detectors 2 and 3 from Fig. 8.8 to get an estimate for the third-order correlator. The benefit of this more complicated approach is that any deviation from zero of the quantity (8.44) at non-vanishing angles $k, q, k - q \neq 0$ would be a manifest indication of the non-Gaussian nature of the cavity output field and would provide a direct suggestion of quairesonant Beliaev-Landau scattering in the cavity array.

Chapter 9

Prethermalization to thermalization crossover following a quench in a weakly interacting Bose gas

Belieav decay manifests itself highly unexpectedly in the steady state of a driven-dissipative chain of nonlinear cavities due to the strong nonequilibrium nature of the setup. In this last chapter, we move our attention back to a system that is entirely isolated from its environment, ensuring that detailed balance plays a significant role. To make the circle complete, we return to the study of the nonequilibrium dynamics of a quantum system after an abrupt global quench – as we had considered in Chapter 3 for a chain of spinless fermions. This time, the system consists of a gas of weakly interacting *bosonic* atoms and we seek to reconstruct the many-body dynamics after a sudden ramp of the interparticle interaction strength. While the chain of long-range interacting fermions merely constituted a toy model, this system has an exceedingly experimental relevance today in the context of *cold-atom experiments*. Consequently, our ultimate focus will be on the evolution of a local quantity that can be realistically measured in experiment: the density-density correlation function. Via a phenomenon called a *Feshbach resonance* the interparticle interaction strength of the bosons is sensitive to an external magnetic field; this provides the perfect playground for generating an abrupt global ramp of the interaction strength.

9.1 The weakly interacting Bose gas

In this section, we start from the Hamiltonian of a trapped gas of bosonic particles that interact with contact interactions. Below a critical temperature, the system undergoes a phase transition where a macroscopic fraction of the atoms occupy the lowest energy

state: *Bose-Einstein condensation* [99]. In this regime, we can expand the full quantum field around a classical field ψ_0 , which represents the condensate, and a small population of atoms that are not condensed, the *depletion*. Then, we aim to establish an effective Hamiltonian in terms of these fluctuations only. We study the gas in the *hydrodynamic* regime, which means that the mean free path of an excitation is short as compared to the total dimensions of the system (see Sec. 7.1).

9.1.1 The full Hamiltonian

The bosonic particles are represented by a continuous quantum field $\hat{\Psi}(\mathbf{r})$ that is defined on each point \mathbf{r} in a D -dimensional space. The quantum field satisfies the usual bosonic canonical commutation relations

$$[\hat{\Psi}(\mathbf{r}), \hat{\Psi}(\mathbf{r}')] = [\hat{\Psi}^\dagger(\mathbf{r}), \hat{\Psi}^\dagger(\mathbf{r}')] = 0, \quad [\hat{\Psi}(\mathbf{r}), \hat{\Psi}^\dagger(\mathbf{r}')] = \delta(\mathbf{r} - \mathbf{r}'). \quad (9.1)$$

The full Hamiltonian of the gas of trapped bosonic atoms can then be formulated as

$$\hat{H} = \int \hat{\Psi}^\dagger(\mathbf{r}) \left(-\frac{\hbar^2}{2m} \nabla^2 + U(\mathbf{r}) \right) \hat{\Psi}(\mathbf{r}) d^D r + \int \int \hat{\Psi}^\dagger(\mathbf{r}) \hat{\Psi}^\dagger(\mathbf{r}') V(\mathbf{r} - \mathbf{r}') \hat{\Psi}(\mathbf{r}') \hat{\Psi}(\mathbf{r}) d^D r d^D r'. \quad (9.2)$$

In our case, we take a gas of atoms that is trapped in three spatial dimensions, corresponding to setting $D = 3$ in the Hamiltonian. However, with appropriate trapping configurations gases can be realized in one or two effective dimension [58].

Written in form (9.2), we distinguish two contributions in the many-body Hamiltonian. The first one is quadratic in the field $\hat{\Psi}(\mathbf{r})$ and contains the kinetic energy of (nonrelativistic) particles with mass m that reside in a spatial potential $U(\mathbf{r})$. The second part is quartic in the operator $\hat{\Psi}(\mathbf{r})$ and describes the effect of an interaction potential $V(\mathbf{r} - \mathbf{r}')$ upon two particles sitting a distance $x = |\mathbf{r} - \mathbf{r}'|$ apart from each other.

We start by making the assumption that the gas is *dilute*. We take a gas that consists of N particles and is contained inside a volume V . Provided the density does not vary too much within this volume, it makes sense to define an average density $n = N/V$, such that, on average, particles are a distance $r_0 = n^{-1/3}$ separated from each other. On the other hand, we can associate a typical length scale r_V with the interparticle interaction potential $V(\mathbf{r} - \mathbf{r}')$. Consequently, when $r_V \ll r_0$, the gas is called dilute since the chance is small that one particle sits within the interaction volume r_V^3 of another. A second length scale in the problem is the *de Broglie* or *thermal* wavelength $\lambda_{dB} = \hbar\sqrt{2\pi/mk_B T}$ of the atoms and relates to the temperature of the gas. In the low-temperature regime, where the gas is well condensed, one has $\lambda_{dB} > r_0 \gg r_V$. If this is the case, we know that any scattering process is largely dominated by its low-energy properties and we can model the potential with a *contact* interaction [99]: $V(\mathbf{r} - \mathbf{r}') \approx g \delta(\mathbf{r} - \mathbf{r}')$.

The interaction constant g can be derived from the s-wave scattering length a_s of the

9.1. The weakly interacting Bose gas

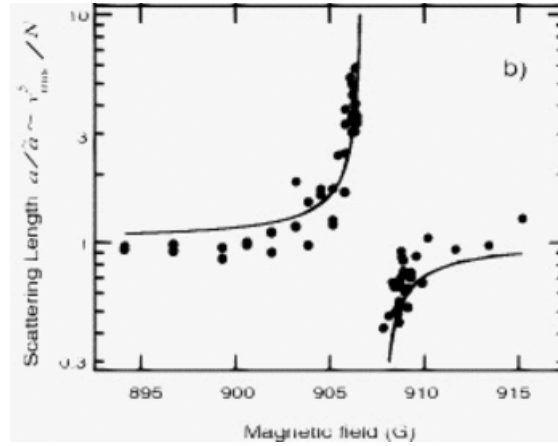


Figure 9.1: The scattering length a_s of the interatomic scattering potential is sensitive to an external magnetic field via a *Feshbach resonance*. The image shows the data from an experiment with sodium atoms [134], where they succeeded in varying the scattering length with a factor of 10. Through relation (9.3) this allows for the tuning of the interaction constant g from (9.4).

true potential $V(\mathbf{r} - \mathbf{r}')$ through the relation

$$g = \frac{4\pi\hbar^2 a_s}{m}. \quad (9.3)$$

Within this approximation we see that (9.2) simplifies to

$$\hat{H} = \int \hat{\Psi}^\dagger(\mathbf{r}) \left(-\frac{\hbar^2}{2m} \nabla^2 + U(\mathbf{r}) \right) \hat{\Psi}(\mathbf{r}) d\mathbf{r} + g \int \hat{\Psi}^\dagger(\mathbf{r}) \hat{\Psi}^\dagger(\mathbf{r}) \hat{\Psi}(\mathbf{r}) \hat{\Psi}(\mathbf{r}) d\mathbf{r}. \quad (9.4)$$

Furthermore, if we set $U(\mathbf{r}) = cte$ everywhere, the gas is expected to be homogeneously distributed throughout the trapping region.

The reason why we concentrate on a system with Hamiltonian (9.4) in this chapter is that the interaction constant g can be modified in experiment. Via a phenomenon called a *Feshbach resonance* [135] the scattering length a_s of the two-body interaction potential can be manipulated. The principle relies on the fact that the energy of a bound molecular-like state of the two scattering atoms is sensitive to an external magnetic field. When this energy is brought close to the typical energy of two colliding atoms, a resonance effect occurs that results in an enhanced scattering length a_s and therefore, through relation (9.3), in a higher interaction constant g (see Fig. 9.1).

Previously, this phenomenon was considered theoretically to study the relaxation dynamics of an atomic condensate after an interaction quench [136, 137]. In experiment, it was used as an analog model for simulating *Sakharov oscillations* in the cosmic microwave background [138]. The central purpose of this chapter, however, is the study of the time evolution of the gas of atoms, initially equilibrated at zero temperature, following an abrupt change $g_i \rightarrow g_f$, as can be realized by suddenly ramping up an external magnetic field.

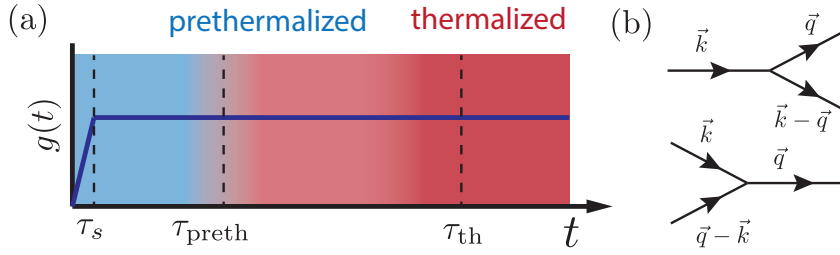


Figure 9.2: An illustration of the different time scales of this chapter. The interaction constant g is suddenly ramped up in a switching time τ_s to bring the system out of equilibrium. The quadratic part of Hamiltonian (9.12) leads the system through a dephasing stage on a time scale τ_{preth} , after which it relaxes to reach a quasisteady *prethermal* state when the lightcone-like peak of correlations has passed. At much later times, the higher-order (nonintegrable) interactions from (b) come into play and convey the final relaxation of the system, which ends in a thermal equilibrium, on a much slower time scale τ_{th} .

9.1.2 Hamiltonian in Bogoliubov basis

For the purposes of this analysis, we again prefer to formulate Hamiltonian (9.4) in momentum space, which is particularly convenient in the case of a homogeneous gas. By introducing the momentum-space operator $\Psi(\mathbf{r}) = 1/\sqrt{V} \sum_{\mathbf{k}} e^{i\mathbf{k}\cdot\mathbf{r}} \hat{a}_{\mathbf{k}}$, we conclude that (9.4) can be written as (we return to units of $\hbar = 1$)

$$\hat{H} = \sum_{\mathbf{k}} \frac{k^2}{2m} \hat{a}_{\mathbf{k}}^\dagger \hat{a}_{\mathbf{k}} + \frac{g}{2V} \sum_{\mathbf{p}, \mathbf{k}, \mathbf{q}} \hat{a}_{\mathbf{p}+\mathbf{q}}^\dagger \hat{a}_{\mathbf{k}-\mathbf{q}}^\dagger \hat{a}_{\mathbf{k}} \hat{a}_{\mathbf{p}}, \quad (9.5)$$

where the summations over \mathbf{k}, \mathbf{p} and \mathbf{q} run in three spatial dimensions. When there is some length scale L that we can associate to the size of the condensate, the summation runs over $k_x = 0, \pi/L, 2\pi/L, \dots$ and likewise for k_y and k_z .

Below a critical temperature and when interactions are weak, almost all particles are found in the zero-momentum state, with only a small population at $\mathbf{k} \neq \mathbf{0}$. In that case, we can conveniently separate the terms from (9.5) according to the number of $\hat{a}_{\mathbf{0}}$ operators they contain. When the number of particles in the condensate is large, we can neglect the quantum commutator and replace the quantum field $\hat{a}_{\mathbf{0}}$ of the condensate mode with a classical field $\psi_0 = \langle \hat{a}_{\mathbf{0}} \rangle / \sqrt{V}$, with $V = L^3$ the 3D volume [99]. This permits us to write (9.5) as

$$\hat{H} = E_0 + \sum_{\mathbf{k} \neq \mathbf{0}} \frac{k^2}{2m} \hat{a}_{\mathbf{k}}^\dagger \hat{a}_{\mathbf{k}} + \frac{gn_0}{2} \sum_{\mathbf{k} \neq \mathbf{0}} \left(2\hat{a}_{\mathbf{k}}^\dagger \hat{a}_{\mathbf{k}} + \hat{a}_{\mathbf{k}} \hat{a}_{-\mathbf{k}} + \hat{a}_{\mathbf{k}}^\dagger \hat{a}_{-\mathbf{k}}^\dagger \right) \quad (9.6)$$

$$+ \frac{g\sqrt{n_0}}{\sqrt{V}} \sum_{\mathbf{k}, \mathbf{q} \neq \mathbf{0}} \left(\hat{a}_{\mathbf{k}+\mathbf{q}}^\dagger \hat{a}_{\mathbf{k}} \hat{a}_{\mathbf{q}} + \hat{a}_{\mathbf{k}}^\dagger \hat{a}_{\mathbf{q}}^\dagger \hat{a}_{\mathbf{k}+\mathbf{q}} \right) \quad (9.7)$$

$$+ \frac{g}{2V} \sum_{\mathbf{p}, \mathbf{k}, \mathbf{q} \neq \mathbf{0}} \hat{a}_{\mathbf{p}+\mathbf{q}}^\dagger \hat{a}_{\mathbf{k}-\mathbf{q}}^\dagger \hat{a}_{\mathbf{k}} \hat{a}_{\mathbf{p}}, \quad (9.8)$$

9.1. The weakly interacting Bose gas

where $n_0 = |\psi_0|^2$ is the density of condensate particles and $E_0 = gn_0^2V/2$ is the total mean-field interaction energy.

The first line of (9.6) is quadratic in the operators $\hat{a}_{\mathbf{k}}$ and can be diagonalized. We again introduce the quasiparticle operators $\hat{a}_{\mathbf{k}} = u_k \hat{\chi}_{\mathbf{k}} + v_k \hat{\chi}_{-\mathbf{k}}^\dagger$, which will diagonalize the quadratic part of \hat{H} if we choose [99]

$$u_k, v_k = \pm \sqrt{\frac{k^2/2m + gn_0}{2\omega_k}} \pm \frac{1}{2}, \quad (9.9)$$

with the quasiparticle dispersion

$$\omega_k = \sqrt{\frac{k^2}{2m} \left(\frac{k^2}{2m} + 2gn_0 \right)}. \quad (9.10)$$

Furthermore, the second line collects all terms that contain three operators $\hat{a}_{\mathbf{k}}$, represented by the diagrams on Fig. 9.2(b). We have seen in the previous chapter that these describe interactions between quasiparticles, the Beliaev-Landau scatterings. Finally, the third line contains terms that have four excitation operators $\hat{a}_{\mathbf{k}}$ and no condensate mode. When the number of particles in the condensate is substantially larger than the number of excitations, i.e.

$$n_0 \gg n_{\text{ex}} = \frac{1}{V} \sum_{\mathbf{k}} \langle \hat{a}_{\mathbf{k}}^\dagger \hat{a}_{\mathbf{k}} \rangle, \quad (9.11)$$

with n_{ex} the *depletion*, scattering events will become less important if they involve less condensate particles. Standard Bogoliubov theory then truncates Hamiltonian (9.6)–(9.8) at the quadratic level (the first line). We, however, opt to explicitly retain the third order as well, with the aim of studying the effect of Beliaev-Landau collisions in the atomic gas.

For the analysis of the cavity array in Chapter 8, we preferred to work in the basis of the fluctuation operators, which would be the $\hat{a}_{\mathbf{k}}$ in this case. We had emphasized, though, that this was merely a choice and that the same analysis could have been done in the quasiparticle basis, here the $\hat{\chi}_{\mathbf{k}}$. For this part, it turned out to be more convenient to expand Hamiltonian (9.6)–(9.8) in the quasiparticle basis. The reason is that, as long as the gas is completely isolated from its environment, the total energy of the system is a constant in time. In a kinetic view, this then implies that quasiparticle collisions always occur *on-shell*, meaning that the energy of the incoming quasiparticles in a collision is redistributed over the outgoing quasiparticles.

Upon truncating the Hamiltonian (9.6)–(9.8) at third order in the fluctuation operator $\hat{a}_{\mathbf{k}}$ and performing a Bogoliubov rotation with (9.9), we then find that the full Hamiltonian can be approximately expanded into a quadratic and a cubic part

$$\hat{H} \approx E'_0 + \hat{H}_2 + \hat{H}_3, \quad (9.12)$$

with

$$\hat{H}_2 = \sum_{\mathbf{k}} \omega_k \hat{\chi}_{\mathbf{k}}^\dagger \hat{\chi}_{\mathbf{k}}, \quad (9.13)$$

$$\hat{H}_3 = g \sqrt{\frac{n_0}{V}} \sum_{\mathbf{k}, \mathbf{q}} \left(A_{\mathbf{k}, \mathbf{q}} \hat{\chi}_{\mathbf{k}}^\dagger \hat{\chi}_{\mathbf{q}}^\dagger \hat{\chi}_{\mathbf{k}+\mathbf{q}} + B_{\mathbf{k}, \mathbf{q}} \hat{\chi}_{\mathbf{k}} \hat{\chi}_{\mathbf{q}} \hat{\chi}_{-\mathbf{k}-\mathbf{q}} + \text{h.c.} \right). \quad (9.14)$$

The energies ω_k of \hat{H}_2 are found as the standard Bogoliubov spectrum from (9.10), while the scattering coefficients in \hat{H}_3 are derived as [139]

$$A_{\mathbf{k}, \mathbf{q}} = u_{\mathbf{k}} u_{\mathbf{q}} u_{\mathbf{k}+\mathbf{q}} + v_{\mathbf{k}} v_{\mathbf{q}} v_{\mathbf{k}+\mathbf{q}} + (u_{\mathbf{k}+\mathbf{q}} + v_{\mathbf{k}+\mathbf{q}})(u_{\mathbf{k}} v_{\mathbf{q}} + u_{\mathbf{q}} v_{\mathbf{k}}), \quad (9.15)$$

$$B_{\mathbf{k}, \mathbf{q}} = u_{\mathbf{k}} u_{\mathbf{q}} v_{-\mathbf{k}-\mathbf{q}} + v_{\mathbf{k}} v_{\mathbf{q}} u_{-\mathbf{k}-\mathbf{q}}, \quad (9.16)$$

with $u_{\mathbf{k}}, v_{\mathbf{k}}$ given in (9.9).

The cubic Hamiltonian \hat{H}_3 is expected to represent the energy fraction corresponding with interactions between quasiparticles, the Beliaev-Landau scattering. Important to realize is that \hat{H} , expressed in the truncated form (9.12), does conserve total energy (it is Hermitian), but it does not conserve the total quasiparticle number. Recall that in Beliaev decay one high-momentum quasiparticle is converted into two low-momentum quasiparticles by absorption of a condensate mode. Conversely, Landau scattering is the collision of two low-momentum quasiparticles into a single high-momentum quasiparticle, leaving also a condensate mode. Moreover, note that the first term from \hat{H}_3 describes these collisions, sketched in Fig. 7.1, while the second is an anomalous interaction term that creates or annihilates *three* quasiparticles at a time.

When we take the thermodynamic limit of (9.12) to turn the summations into integrals and we rescale the wave vectors with the healing length $\xi = \sqrt{1/m\mu}$, $k \rightarrow \tilde{k} = k\xi$, we conclude that the density of states times the matrix elements of \hat{H}_3 squared scale as $1/(n\xi^3) = \sqrt{(4\pi)^3 n a_s^3}$; this is exactly like the condensate depletion $n - n_0$ (9.11). Consequently, when the number of depleted particles is sufficiently small, the dynamics under the integrable Hamiltonian \hat{H}_2 occurs on a substantially faster time scale than the ergodic dynamics of \hat{H}_3 ¹. When the system is initiated in a highly nonequilibrium state, the fast dynamics under \hat{H}_2 results in a first ‘dephasing’ stage that leads the system to a quasisteady *prethermal* state. From there on, quasiparticle interactions will come into play and bring the system to its final state, which is again a thermal equilibrium. We illustrate this pictorially in Fig. 9.2(a).

Though, care must be taken at low momenta, for which $\omega_k \rightarrow 0$, thus leading to a diverging prethermalization time scale. In part for this reason, our main focus will be on higher momenta, of the order of the healing or thermal length, which are expected to be roughly independent of the trap configuration in the hydrodynamic regime.

¹We perform a simplified approach, where the total number of particles in the gas is not conserved, but number-conserving approaches [140] would result in exactly the same Hamiltonians \hat{H}_2 and \hat{H}_3 [139]

9.2 The approximately integrable dynamics

At short times, the dynamics is largely dominated by \hat{H}_2 , the quadratic Hamiltonian. In particular, to bring the bosonic gas from (9.4) out of equilibrium, we will consider abrupt changes of the interaction strength g , such as illustrated in Fig. 9.2(a). Through relation (9.3), it is seen that this can be achieved by modifying the s -wave scattering length a_s of the two-body interaction potential. Interestingly, this quantity is sensitive to an external magnetic field, due to a phenomenon called a *Feshbach resonance* (see Fig. 9.1).

Subsequently, \hat{H}_2 will guide the system through a first dephasing stage, eventually leaving the system in a quasisteady prethermal state. Again, we can formulate a generalized Gibbs ensemble (see Sec. 3.6) that embraces all the conserved quantities of \hat{H}_2 , which are now only approximately conserved on the level of the full Hamiltonian (9.12). The quadratic problem and its expected dephasing has been studied previously in Refs. [141] and [142].

9.2.1 An interaction ramp: the dynamical Casimir effect

Traditionally, the protocol for a quench in a quantum system is considered *instantaneous*, meaning that a parameter in the Hamiltonian is varied on a time scale substantially faster than any relevant time scale in the system. With this assumption it is ensured that the quench is highly non-adiabatic and that the system does not have sufficient time to respond to the applied changes, leaving it typically in a strongly nonequilibrium state. For the fermionic Kitaev chain in Chapter 3 it was sufficient to assume a switching time substantially faster than $1/\epsilon_k^{\max}$, with ϵ_k^{\max} the largest energy present in the quasiparticle spectrum².

For this problem, we will consider a quench $g_i \rightarrow g_f$, with $g_i = 0 < g_f$, explicitly within a nonzero switching time τ_s . The quasiparticle spectrum (9.10) behaves asymptotically as $\omega_k \approx k^2/2m$ for high momenta and it is not bound, unless some UV cutoff is introduced³. When the system is now quenched, the switching time scale τ_s will determine what the initial state after the quench is. In the view of quasiparticles, modes with an oscillation frequency $\omega_k \ll \tau_s^{-1}$ will perceive the quench as instantaneous, while the ones with $\omega_k \gg \tau_s^{-1}$ can follow adiabatically and maintain their occupation from before the quench.

Since the time scale on which quasiparticle interactions typically take place is substantially slower than the switching time, we can neglect any effects of Beliaev-Landau scattering between the modes during the switch and treat the problem fully on the level of the quadratic Hamiltonian \hat{H}_2 . The evolution of the fluctuation operator $\hat{a}_{\mathbf{k}}$ under a changing interaction strength $g(t)$ is then formulated as the evolution under a time-dependent

²Remember that we found a divergence in the spectrum for long-range interactions $\alpha < 1$. Although we did not go into it, one should in principle consider a cutoff at a quasiparticle energy that roughly corresponds to the inverse switching time.

³In principle, a cutoff is naturally introduced at the length scale of the scattering length a_s , where the approximation of a contact interaction breaks down. However, we concentrate on length scales much larger than this.

Bogoliubov Hamiltonian [143]

$$i\partial_t \begin{pmatrix} \hat{a}_{\mathbf{k}} \\ \hat{a}_{-\mathbf{k}}^\dagger \end{pmatrix} = B_{\mathbf{k}}(t) \begin{pmatrix} \hat{a}_{\mathbf{k}} \\ \hat{a}_{-\mathbf{k}}^\dagger \end{pmatrix}, \quad B_{\mathbf{k}}(t) = \begin{pmatrix} \frac{k^2}{2m} + g(t)n_0 & g(t)n_0 \\ -g(t)n_0 & -\frac{k^2}{2m} - g(t)n_0 \end{pmatrix}, \quad (9.17)$$

where we assume the density of the condensate n_0 to remain roughly invariant under the change. Note that this expression is reminiscent of (5.25), where the propagation of fluctuations through a 2D planar microcavity was studied.

From the equation of motion for the quasiparticles, we can derive how the quadratic correlation functions evolve under the change. With $n_k^{(a)} = \langle \hat{a}_{\mathbf{k}}^\dagger \hat{a}_{\mathbf{k}} \rangle$ and $c_k^{(a)} = \langle \hat{a}_{\mathbf{k}} \hat{a}_{-\mathbf{k}} \rangle$, we then find that they follow

$$\partial_t n_k^{(a)} = -2\Im[g(t)n_0 c_k^{(a)}], \quad (9.18)$$

$$i\partial_t c_k^{(a)} = 2\left(\frac{k^2}{2m} + g(t)n_0\right)c_k^{(a)} + g(t)n_0(2n_k^{(a)} + 1). \quad (9.19)$$

For given initial conditions $n_k^{(a)}(t=0)$ and $c_k^{(a)}(t=0)$, this system of equations is readily integrated in time with standard numerical methods for a given temporal profile $g(t)$.

We assume that the transition $g_i \rightarrow g_f$ takes place within a finite time window τ_s , after which the interaction constant is fixed to $g = g_f$ during the subsequent (unitary) time evolution under the time-independent Hamiltonian $\hat{H}(g_f)$ from (9.4), see Fig. 9.2(a). For the final Hamiltonian, we can then evaluate the quadratic correlations of the quasiparticle modes $\hat{\chi}_{\mathbf{k}} = u_k \hat{a}_{\mathbf{k}} - v_k \hat{a}_{-\mathbf{k}}^\dagger$ as

$$n_k^{(\chi)} = \left(u_k^2 + v_k^2\right)n_k^{(a)} - 2u_k v_k \Re\{c_k^{(a)}\} + v_k^2, \quad (9.20)$$

$$c_k^{(\chi)} = u_k^2 c_k^{(a)} + v_k^2 c_k^{(a)*} - 2u_k v_k n_k^{(a)} - u_k v_k, \quad (9.21)$$

with u_k, v_k given in (9.9) and $n_k^{(a)}$ and $c_k^{(a)}$ come out of the numerical integration of (9.18) over the time window during which $g(t)$ varies.

In the absence of interactions, the Bogoliubov modes $\chi_{\mathbf{k}}$ coincide with the fluctuation modes $\hat{a}_{\mathbf{k}}$, such that they all have $n_{\mathbf{k}}^{(a)} = 0$ initially, at zero temperature. Let us first consider the limiting case of instantaneous switching, obtained by sending $\tau_s \rightarrow 0$. After the sudden ramp, the population will be largely unaltered, but the transformation (9.20) is different for the Hamiltonian $\hat{H}(g_f)$. After evaluation, we find that

$$n_{\mathbf{k}}^{(\chi)} = v_k^2, \quad c_{\mathbf{k}}^{(\chi)} = -u_k v_k, \quad (9.22)$$

and we are left with a nonzero population of Bogoliubov modes with nontrivial anomalous correlations. In Fig 9.3(a) we confirm that this is indeed the value to which the momentum distribution converges for decreasing τ_s .

The quantities $n_k^{(\chi)}$ and $c_k^{(\chi)}$ are particularly interesting to study the dynamics because they evolve trivially under the quadratic part of \hat{H} as $n_k^{(\chi)}(t) = n_k^{(\chi)}$ and $c_k^{(\chi)}(t) = \tilde{c}_k^{(\chi)} e^{-2i\omega_k t}$,

9.2. The approximately integrable dynamics

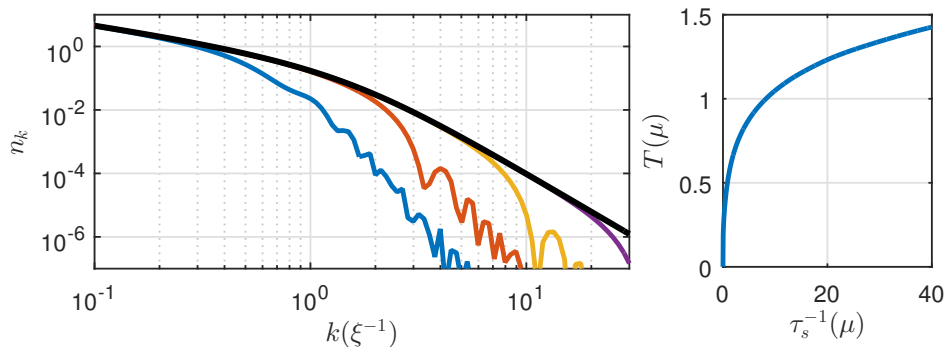


Figure 9.3: In the view of the *dynamical Casimir effect* the vacuum of Bogoliubov excitations is changed when the interaction constant $g(t)$ is varied over time. (a) The momentum distribution of quasiparticles after suddenly ramping up interactions from zero (universal) within a time window $\tau_s = \{5, 0.5, 0.05, 0.005\} \times \mu^{-1}$. The thick black line shows the prediction for an *instantaneous* quench ($\tau_s \rightarrow 0$). Another way to see this, is that a nonzero switching time τ_s introduces an effective cutoff in momentum space for the initial state. (b) Upon decreasing switching time τ_s more energy is injected into the system, which then translates into a higher equilibrium temperature T . For $\tau_s \rightarrow 0$, we derive the asymptotic scaling $T \propto \tau_s^{-1/5}$.

where $\tilde{c}_k^{(x)}$ is independent of time. Consequently, all the $n_k^{(x)}$ and $\tilde{c}_k^{(x)}$ are conserved quantities under \hat{H}_2 and their dynamics is solely governed by \hat{H}_3 .

The set of equations from (9.17) has been studied intensely in the context of the *dynamical Casimir effect* [144]. A condensate at zero temperature is characterized by having all $n_k^{(x)} = 0$ and $c_k^{(x)} = 0$, while there is a nonzero quantum depletion $n_k^{(a)} = v_k^2$ [99]. By modifying interactions (or condensate density), it is as if the vacuum of quasiparticles has changed over time [143]. Following the prediction of quantum field theory [145], this change of vacuum then creates a nonzero population of quasiparticles in the condensate. Also in the context of polariton fluids this phenomenon was studied, where the change of vacuum comes from the spontaneous decay of a coherently injected polariton condensate [146]. Recently, dynamical Casimir emission was observed in an experiment on a superconducting circuit [147].

9.2.2 Prethermalization

On the level of \hat{H}_2 , the system is approximately integrable and the relevant conserved quantities are identified as the $n_{\mathbf{k}}^{(x)}$, the occupation numbers of Bogoliubov modes from (9.12). At late times (within the short-time approximation), the integrable dynamics leads the system through a dephasing stage, after which it is left in a quasisteady or *prethermal* state. To obtain expectation values of observables in the prethermalized state, it is then

sufficient to compute them with respect to the *time-averaged* quantities

$$\bar{n}_k^{(a)} = (u_k^2 + v_k^2)n_k^{(\chi)} + v_k^2, \quad \bar{c}_k^{(a)} = u_k v_k (2n_k^{(\chi)} + 1). \quad (9.23)$$

The relevant ensemble for this quasisteady state is then again found as the *generalized Gibbs ensemble*, introduced in Sec. 3.6. For this problem, the conserved quantities that enter the ensemble are the occupation number of quasiparticles. In the thermodynamic limit, we then expect to hold that

$$\lim_{t \rightarrow \infty} \lim_{V \rightarrow \infty} \langle \hat{O} \rangle_t = \text{tr} \{ \rho_{\text{GGE}} \hat{O} \}, \quad \hat{\rho}_{\text{GGE}} = \frac{1}{\mathcal{Z}} \exp \left\{ - \sum_{\mathbf{k}} \lambda_{\mathbf{k}} \hat{n}_{\mathbf{k}}^{(\chi)} \right\}, \quad (9.24)$$

for any *local* operator $\langle \hat{O} \rangle$. The $\lambda_{\mathbf{k}}$ are again Lagrange multipliers that have to be fixed by means of the expectation values of the constants of motion in the initial state (see Sec. 3.6). They can be regarded as different effective temperatures for each conserved quantity $\hat{n}_{\mathbf{k}}^{(\chi)}$ on the level of the quadratic Hamiltonian \hat{H}_2 . Obviously, the requirement of a separate effective temperature for each constant of motion implies that this ensemble, in general, does not coincide with a thermal one. This is an immediate consequence of the approximate integrable dynamics of the Bose gas at short times. Therefore, the limit $t \rightarrow \infty$ in (9.24) is to be taken only for times long enough for the dephasing process. We will next see that this constitutes a *quasisteady* state and that further evolution generally breaks integrability and brings the system back to a thermal equilibrium on a vastly longer time scale, such as illustrated in Fig. 9.2(a).

9.3 Constructing a hierarchy of correlation functions

We were able to identify a number of quantities, conserved under evolution with the quadratic Hamiltonian \hat{H}_2 from (9.12), which prevent the system from approaching thermalization. However, this integrable dynamics is only approximate and higher-order corrections usually break integrability. In this part, we seek to investigate how the conserved quantities from \hat{H}_2 do experience a variation under \hat{H}_3 , albeit on a much slower characteristic time scale. The clear separation of time scales will permit us to derive effective *kinetic equations* that we can relate back to quasiparticle collisions. Supposedly, this kinetic formulation of the problem should become valid at sufficiently late times, as we explicitly numerically verify in Appendix C.4.

9.3.1 Equation of motion of the quasiparticle operator

We start by deriving the equations of motion for the quasiparticle operators under the Hamiltonian (9.12). By evaluating Heisenberg's equation of motion $i\partial_t \hat{\chi}_{\mathbf{k}} = [\hat{\chi}_{\mathbf{k}}, \hat{H}]$, we find that they evolve as

$$i\partial_t \hat{\chi}_{\mathbf{k}} = \omega_{\mathbf{k}} \hat{\chi}_{\mathbf{k}} + g \sqrt{\frac{n_0}{V}} \sum_{\mathbf{q}} \left\{ 2A_{\mathbf{k},\mathbf{q}} \hat{\chi}_{\mathbf{q}}^\dagger \hat{\chi}_{\mathbf{q}+\mathbf{k}} + A_{\mathbf{q},\mathbf{k}-\mathbf{q}} \hat{\chi}_{\mathbf{q}} \hat{\chi}_{\mathbf{k}-\mathbf{q}} + 3B_{\mathbf{k},\mathbf{q}} \hat{\chi}_{\mathbf{q}}^\dagger \hat{\chi}_{-\mathbf{k}-\mathbf{q}}^\dagger \right\}. \quad (9.25)$$

9.3. Constructing a hierarchy of correlation functions

Here, the first term on the right-hand side represents the evolution under \hat{H}_2 , generating the integrable part of the dynamics by means of coherent oscillations of the $\hat{\chi}_{\mathbf{k}}$ modes, as was discussed in the previous section. The last terms, generated by \hat{H}_3 , describe interferences of the mode \mathbf{k} with other modes $\pm\mathbf{q}$ and $\pm\mathbf{k}\pm\mathbf{q}$. We will next see how these couplings can be interpreted as effective collisions between quasiparticles.

9.3.2 The hierarchy of correlations

Starting from (9.25) we can again construct a hierarchy of correlation functions, in the same spirit as in Sec. 8.5. For this analysis, however, we opt to work in the basis $\hat{\chi}_{\mathbf{k}}$ of the quasiparticle modes and not of the fluctuation operators $\hat{a}_{\mathbf{k}}$. The reason is that, when the dynamics is unitary and not dissipative, the collisions occur strictly *on-shell* in the long-time limit; with exact energy conservation for the quasiparticles.

We can again derive the equations of motion for different correlators via the product rule for derivatives and then using (9.25). This way, we find that the occupation number of quasiparticle modes $n_k^{(\chi)} = \langle \hat{\chi}_{\mathbf{k}}^\dagger \hat{\chi}_{\mathbf{k}} \rangle$ evolves in time as

$$\begin{aligned} \partial_t n_{\mathbf{k}}^{(\chi)} &= 2g\sqrt{\frac{n_0}{V}} \Im \left\{ \sum_{\mathbf{q}} 3B_{\mathbf{k},\mathbf{q}} \langle \hat{\chi}_{\mathbf{k}}^\dagger \hat{\chi}_{\mathbf{q}}^\dagger \hat{\chi}_{-\mathbf{k}-\mathbf{q}}^\dagger \right. \\ &\quad \left. + \left(2A_{\mathbf{k},\mathbf{q}} \langle \hat{\chi}_{\mathbf{k}}^\dagger \hat{\chi}_{\mathbf{q}}^\dagger \hat{\chi}_{\mathbf{k}+\mathbf{q}} \rangle + A_{\mathbf{q},\mathbf{k}-\mathbf{q}} \langle \hat{\chi}_{\mathbf{k}}^\dagger \hat{\chi}_{\mathbf{k}-\mathbf{q}} \hat{\chi}_{\mathbf{q}} \rangle \right) \right\}. \end{aligned} \quad (9.26)$$

Here, we see that *all* the dynamics is generated by \hat{H}_3 , with characteristic coupling $g\sqrt{n_0/V}$, since n_k is a constant of motion of \hat{H}_2 . Likewise, we find that the anomalous correlation function of quasiparticles $c_k = \langle \hat{\chi}_{\mathbf{k}} \hat{\chi}_{-\mathbf{k}} \rangle$ follows

$$\begin{aligned} i\partial_t c_{\mathbf{k}}^{(\chi)} &= 2\omega_k c_{\mathbf{k}}^{(\chi)} + g\sqrt{\frac{n_0}{V}} \sum_{\mathbf{q}} \left\{ 3 \left(B_{-\mathbf{k},\mathbf{q}} \langle \hat{\chi}_{\mathbf{q}}^\dagger \hat{\chi}_{\mathbf{k}-\mathbf{q}}^\dagger \hat{\chi}_{\mathbf{k}} \rangle + B_{\mathbf{k},\mathbf{q}} \langle \hat{\chi}_{\mathbf{q}}^\dagger \hat{\chi}_{-\mathbf{k}-\mathbf{q}}^\dagger \hat{\chi}_{-\mathbf{k}} \rangle \right) \right. \\ &\quad + 2 \left(A_{-\mathbf{k},\mathbf{q}+\mathbf{k}} \langle \hat{\chi}_{\mathbf{q}+\mathbf{k}}^\dagger \hat{\chi}_{\mathbf{q}} \hat{\chi}_{\mathbf{k}} \rangle + A_{\mathbf{k},\mathbf{q}-\mathbf{k}} \langle \hat{\chi}_{\mathbf{q}-\mathbf{k}}^\dagger \hat{\chi}_{\mathbf{q}} \hat{\chi}_{-\mathbf{k}} \rangle \right) \\ &\quad \left. + A_{\mathbf{q},-\mathbf{k}-\mathbf{q}} \langle \hat{\chi}_{\mathbf{k}} \hat{\chi}_{\mathbf{q}} \hat{\chi}_{-\mathbf{k}-\mathbf{q}} \rangle + A_{\mathbf{q},\mathbf{k}-\mathbf{q}} \langle \hat{\chi}_{-\mathbf{k}} \hat{\chi}_{\mathbf{q}} \hat{\chi}_{\mathbf{k}-\mathbf{q}} \rangle \right\}. \end{aligned} \quad (9.27)$$

The evolution with \hat{H}_2 generates the first term, an oscillation of $c_{\mathbf{k}}$ with frequency $2\omega_k$, while \hat{H}_3 causes $c_{\mathbf{k}}$ to couple to the third-order correlators. By introducing the notation

$$M_{\mathbf{k},\mathbf{q}} = \langle \hat{\chi}_{\mathbf{k}-\mathbf{q}}^\dagger \hat{\chi}_{\mathbf{q}}^\dagger \hat{\chi}_{\mathbf{k}} \rangle, \quad R_{\mathbf{k},\mathbf{q}} = \langle \hat{\chi}_{\mathbf{q}-\mathbf{k}} \hat{\chi}_{-\mathbf{q}} \hat{\chi}_{\mathbf{k}} \rangle, \quad (9.28)$$

we find that these equations can be expressed in the rotating frame $c_k = \tilde{c}_k e^{-2i\omega_k t}$ after a shift of summation indices as

$$\partial_t n_{\mathbf{k}}^{(\chi)} = 2g\sqrt{\frac{n_0}{V}} \Im \left\{ \sum_{\mathbf{q}} 3B_{\mathbf{k},-\mathbf{q}} R_{\mathbf{k},\mathbf{q}}^* + 2A_{\mathbf{k},\mathbf{q}-\mathbf{k}} M_{\mathbf{q},\mathbf{k}} + A_{\mathbf{q},\mathbf{k}-\mathbf{q}} M_{\mathbf{k},\mathbf{q}}^* \right\}, \quad (9.29)$$

$$i\partial_t \tilde{c}_{\mathbf{k}}^{(\chi)} = 2g\sqrt{\frac{n_0}{V}} \sum_{\mathbf{q}} \left\{ 3B_{-\mathbf{k},\mathbf{q}} M_{\mathbf{k},\mathbf{q}} + 2A_{\mathbf{k},-\mathbf{q}} M_{\mathbf{q},\mathbf{k}}^* + A_{\mathbf{q},\mathbf{k}-\mathbf{q}} R_{\mathbf{k},\mathbf{q}} \right\} e^{2i\omega_k t}. \quad (9.30)$$

Equations (9.29)–(9.30) are now completely decoupled from the integrable dynamics generated with \hat{H}_2 , apart from the trivial oscillation with frequency $2\omega_k$ in the time evolution of the \tilde{c}_k .

We next evaluate the time evolution of the third-order correlation functions $M_{\mathbf{k},\mathbf{q}}$ and $R_{\mathbf{k},\mathbf{q}}$ in the same spirit as above,

$$i\partial_t M_{\mathbf{k},\mathbf{q}} = (\omega_{\mathbf{k}} - \omega_{\mathbf{q}} - \omega_{\mathbf{k}-\mathbf{q}})M_{\mathbf{k},\mathbf{q}} + g\sqrt{\frac{n_0}{V}}F_{\mathbf{k},\mathbf{q}}^{(M)}, \quad (9.31)$$

$$i\partial_t R_{\mathbf{k},\mathbf{q}} = (\omega_{\mathbf{k}} + \omega_{\mathbf{q}} + \omega_{\mathbf{q}-\mathbf{k}})R_{\mathbf{k},\mathbf{q}} + g\sqrt{\frac{n_0}{V}}F_{\mathbf{k},\mathbf{q}}^{(R)}. \quad (9.32)$$

The first terms on the right-hand side are again found from the evolution of \hat{H}_2 and constitute coherent oscillations characterized by the Bogoliubov frequencies $\omega_{\mathbf{k}}$ of the modes enclosed in the correlator. The last term, in turn, acts as a drive and is found from evaluating the time evolution with \hat{H}_3 . In principle, the $F_{\mathbf{k},\mathbf{q}}^{(M,R)}$ consists of fourth-order correlation functions, but we opt here to factorize again the fourth-order into lower-order correlation functions (exactly as in Chapter 8). We take again $\langle \hat{\chi}_{\mathbf{k}} \rangle = 0$, such that the factorization of a fourth-order correlator restricts to splitting into various products of second order (see Appendix C.1).

After evaluation, we find the drive term of (9.31) as (we omit the superscript $\cdot^{(x)}$ for ease of notation)

$$\begin{aligned} F_{\mathbf{k},\mathbf{q}}^{(M)} &= 2A_{\mathbf{k},-\mathbf{q}} \left(c_{\mathbf{q}}^* (n_{\mathbf{k}-\mathbf{q}} - n_{\mathbf{k}}) - c_{\mathbf{k}-\mathbf{q}}^* c_{\mathbf{k}} \right) \\ &+ 2A_{\mathbf{k},\mathbf{q}-\mathbf{k}} \left(c_{\mathbf{k}-\mathbf{q}}^* (n_{\mathbf{q}} - n_{\mathbf{k}}) - c_{\mathbf{k}} c_{\mathbf{q}}^* \right) \\ &+ 2A_{\mathbf{q},\mathbf{k}-\mathbf{q}} \left(n_{\mathbf{k}-\mathbf{q}} (n_{\mathbf{q}} - n_{\mathbf{k}}) - n_{\mathbf{k}} (n_{\mathbf{q}} + 1) \right) \\ &+ 3B_{\mathbf{k},-\mathbf{q}} \left(c_{\mathbf{k}-\mathbf{q}}^* c_{\mathbf{q}}^* - c_{\mathbf{k}} n_{\mathbf{k}-\mathbf{q}} \right) \\ &+ 3B_{\mathbf{k},\mathbf{q}-\mathbf{k}} \left(c_{\mathbf{k}-\mathbf{q}}^* c_{\mathbf{q}}^* - c_{\mathbf{k}} (n_{\mathbf{q}} + 1) \right) \\ &- 3B_{\mathbf{q},\mathbf{k}-\mathbf{q}} c_{\mathbf{k}} \left(n_{\mathbf{q}} + n_{\mathbf{k}-\mathbf{q}} + 1 \right), \end{aligned} \quad (9.33)$$

and the one from (9.32) as

$$\begin{aligned} F_{\mathbf{k},\mathbf{q}}^{(R)} &= 2A_{\mathbf{k},-\mathbf{q}} \left(c_{\mathbf{k}-\mathbf{q}} (n_{\mathbf{k}} + n_{\mathbf{q}} + 1) + c_{\mathbf{k}} c_{\mathbf{q}} \right) \\ &+ 2A_{\mathbf{k},\mathbf{q}-\mathbf{k}} \left(c_{\mathbf{q}} (n_{\mathbf{k}} + n_{\mathbf{k}-\mathbf{q}} + 1) + c_{\mathbf{k}-\mathbf{q}} c_{\mathbf{k}} \right) \\ &+ 2A_{\mathbf{q},\mathbf{k}-\mathbf{q}} \left(c_{\mathbf{k}} (n_{\mathbf{q}} + n_{\mathbf{k}-\mathbf{q}} + 1) + c_{\mathbf{q}} c_{\mathbf{k}-\mathbf{q}} \right) \\ &+ 3B_{\mathbf{k},-\mathbf{q}} \left((n_{\mathbf{k}-\mathbf{q}} + 1) (n_{\mathbf{k}} + n_{\mathbf{q}} + 1) \right) \\ &+ 3B_{\mathbf{k},\mathbf{q}-\mathbf{k}} \left(n_{\mathbf{q}} (n_{\mathbf{k}} + n_{\mathbf{k}-\mathbf{q}} + 1) + n_{\mathbf{k}-\mathbf{q}} + 1 \right) \\ &+ 3B_{\mathbf{q},\mathbf{k}-\mathbf{q}} \left(n_{\mathbf{k}} (n_{\mathbf{q}} + n_{\mathbf{k}-\mathbf{q}} + 1) \right). \end{aligned} \quad (9.34)$$

9.4. The kinetic description of the problem

With expressions (9.29)–(9.32) we present a closed set of differential equations that describes the dynamics of the gas of atoms after the abrupt interaction ramp. The equations of motion are now explicitly expanded up to one order higher than the standard Bogoliubov approach. Again, we capture all terms that scale as $\sim g\sqrt{n_0/V}$, while the Bogoliubov approximation truncates at $\sim gn_0$, the level of \hat{H}_2 from (9.12).

Numerical integration of the set of equations provides a full solution to the time-dependent problem of the gas after the quench on the level of approximation of (9.12), where the Hamiltonian was truncated at third order in the fluctuation operators $\hat{\chi}_{\mathbf{k}}$. With the inverse of transformation (9.20) we can move from the basis of Bogoliubov modes, in which the problem (9.29)–(9.32) is expressed, to the basis of the fluctuation operators $\hat{a}_{\mathbf{k}}$, which represent the noncondensed atoms in the gas and are needed to obtain relevant observables.

9.4 The kinetic description of the problem

Recall that the dynamics of the quantities $n_{\mathbf{k}}^{(\chi)}$ and $c_{\mathbf{k}}^{(\chi)}$, presented in Eqs. (9.29)–(9.30), is solely generated by the coupling to the third-order correlators $M_{\mathbf{k},\mathbf{q}}$ and $R_{\mathbf{k},\mathbf{q}}$. In turn, from (9.31)–(9.32) we conclude that the dynamics of $M_{\mathbf{k},\mathbf{q}}$ and $R_{\mathbf{k},\mathbf{q}}$ consists of an oscillatory part (first term) and a drive (last term). We can now anticipate that any fast oscillations in the summations of (9.29)–(9.30) will generally cancel out on the time scales resolved by the slow dynamics of \hat{H}_3 .

9.4.1 Deriving the kinetic equations for the quasiparticles

We aim to establish an effective description in terms of the conserved quantities of $n_k^{(\chi)}$ and $c_k^{(\chi)}$ only. To this end, we start by formally solving the equations of motion of the third-order correlators, leading to

$$M_{\mathbf{k},\mathbf{q}}(t) = -ig\sqrt{\frac{n_0}{V}} \int_0^t ds F_{\mathbf{k},\mathbf{q}}^{(M)}(s) e^{i(\omega_{\mathbf{k}} - \omega_{\mathbf{q}} - \omega_{\mathbf{k}-\mathbf{q}})(s-t)}, \quad (9.35)$$

and similar for $R_{\mathbf{k},\mathbf{q}}(t)$ in (9.32).

We can now plug these expressions into the equations of motion (9.29)–(9.30) to obtain closed differential equations for the $n_k^{(\chi)}$ and $c_k^{(\chi)}$. Yet, these equations still contain a memory kernel, coming from the integration over the time variable s in (9.35). By sending the integration boundary to infinity, we conclude that this integral actually singles out terms that do not oscillate with the Bogoliubov frequencies ω_k in the integrand. Although the obtained equations are now local in time, we are still left with fast-oscillating terms. By time-averaging over those, we find that the slow dynamics of \hat{H}_3 gives the evolution of

quasiparticle numbers (we omit the superscript $\cdot^{(x)}$ again for ease of notation)

$$\begin{aligned} \partial_t n_{\mathbf{k}} = & 4\pi \frac{g^2 n_0}{V} \left\{ \sum_{\mathbf{q}} A_{\mathbf{q}, \mathbf{k}-\mathbf{q}}^2 \left(n_{\mathbf{k}-\mathbf{q}} n_{\mathbf{q}} - n_{\mathbf{k}} (n_{\mathbf{q}} + n_{\mathbf{k}-\mathbf{q}} + 1) \right) \delta(\omega_{\mathbf{k}} - \omega_{\mathbf{q}} - \omega_{\mathbf{k}-\mathbf{q}}) \right. \\ & \left. + 2 \sum_{\mathbf{q}} A_{\mathbf{k}, \mathbf{q}-\mathbf{k}}^2 \left(n_{\mathbf{q}} (n_{\mathbf{k}} + n_{\mathbf{k}-\mathbf{q}} + 1) - n_{\mathbf{k}} n_{\mathbf{k}-\mathbf{q}} \right) \delta(\omega_{\mathbf{q}} - \omega_{\mathbf{k}} - \omega_{\mathbf{k}-\mathbf{q}}) \right\}. \end{aligned} \quad (9.36)$$

This equation coincides with the well-known *kinetic equation* derived to study phonon decay through Beliaev-Landau scattering in ultracold atomic gases. For example, it was applied in Ref. [139] to study the coherence time of a condensate. Usually, equation (9.36) is derived from *Fermi golden rule*. Then, \hat{H}_3 is considered a perturbation to \hat{H}_2 that causes transitions between the energy level of \hat{H}_2 through the scattering processes and, consequently, also a redistribution of quasiparticle numbers $n_{\mathbf{k}}$. It is therefore a pleasure to recognize the very same equation as a time-averaged result from the hierarchy of correlation functions that we constructed in Sec. 9.3.2.

The first line of (9.36) describes the transition of a quasiparticle mode with momentum \mathbf{k} into two others with momenta \mathbf{q} and $\mathbf{k} - \mathbf{q}$; Beliaev decay. The second line, in turn, represents the transition of a quasiparticle with momentum \mathbf{k} into one with \mathbf{q} by colliding with another mode $\mathbf{k} - \mathbf{q}$; Landau decay (see Fig. 7.1 for a diagrammatic representation of both processes). In the kinetic equation, all these transitions occur on-shell, which is reflected by the δ -function imposing energy conservation. Notice also the extra factor 2 that appears for the Landau scattering (second line): both the modes \mathbf{q} and $\mathbf{k} - \mathbf{q}$ contribute to scattering into the mode \mathbf{k} .

Furthermore, the formal solutions (9.35) can also be substituted into the equation of motion for the anomalous correlations $c_{\mathbf{k}}$ (9.30). We then find an approximate solution for the slow dynamics of $\tilde{c}_{\mathbf{k}}$ in exactly the same way as for $n_{\mathbf{k}}$,

$$\begin{aligned} \partial_t \tilde{c}_{\mathbf{k}} = & -4\pi \frac{g^2 n_0}{V} \left\{ \sum_{\mathbf{q}} A_{\mathbf{q}, \mathbf{k}-\mathbf{q}}^2 \left((n_{\mathbf{q}} + n_{\mathbf{k}-\mathbf{q}} + 1) \tilde{c}_{\mathbf{k}} + \tilde{c}_{\mathbf{q}} \tilde{c}_{\mathbf{k}-\mathbf{q}} \right) \delta(\omega_{\mathbf{k}} - \omega_{\mathbf{q}} - \omega_{\mathbf{k}-\mathbf{q}}) \right. \\ & \left. + 2 \sum_{\mathbf{q}} A_{\mathbf{k}, \mathbf{q}-\mathbf{k}}^2 \left(\tilde{c}_{\mathbf{q}} \tilde{c}_{\mathbf{q}-\mathbf{k}}^* + (n_{\mathbf{k}-\mathbf{q}} - n_{\mathbf{q}}) \tilde{c}_{\mathbf{k}} \right) \delta(\omega_{\mathbf{q}} - \omega_{\mathbf{k}} - \omega_{\mathbf{k}-\mathbf{q}}) \right\}. \end{aligned} \quad (9.37)$$

Also this equation can be related back to well-known results in the literature. It is enlightening to notice that close to equilibrium this equation reduces to

$$\partial_t \tilde{c}_{\mathbf{k}} \approx -2\gamma_{\mathbf{k}}^{\text{B}}(t) \tilde{c}_{\mathbf{k}} - 2\gamma_{\mathbf{k}}^{\text{L}}(t) \tilde{c}_{\mathbf{k}} \quad (9.38)$$

Here, $\gamma_{\mathbf{k}}^{\text{B}}$ and $\gamma_{\mathbf{k}}^{\text{L}}$ are the decay rates through, respectively, Beliaev decay and Landau scattering for a phonon with momentum \mathbf{k} in the condensate, as evaluated from the momentum distribution $n_{\mathbf{k}}$ [111]

$$\gamma_{\mathbf{k}}^{\text{B}} = 2\pi \frac{g^2 n_0}{V} \sum_{\mathbf{q}} A_{\mathbf{q}, \mathbf{k}-\mathbf{q}}^2 \left(n_{\mathbf{q}} + n_{\mathbf{k}-\mathbf{q}} + 1 \right) \delta(\omega_{\mathbf{k}} - \omega_{\mathbf{q}} - \omega_{\mathbf{k}-\mathbf{q}}), \quad (9.39)$$

$$\gamma_{\mathbf{k}}^{\text{L}} = 4\pi \frac{g^2 n_0}{V} \sum_{\mathbf{q}} A_{\mathbf{k}, \mathbf{q}-\mathbf{k}}^2 \left(n_{\mathbf{k}-\mathbf{q}} - n_{\mathbf{q}} \right) \delta(\omega_{\mathbf{q}} - \omega_{\mathbf{k}} - \omega_{\mathbf{k}-\mathbf{q}}). \quad (9.40)$$

9.5. The evolution of the density correlations

Notice again the extra factor 2 for the decay rate of Landau scattering, coming from the two possible scattering channels.

Close to equilibrium, the anomalous correlations $\tilde{c}_{\mathbf{k}}$ therefore decay with *twice* the decay rate of a single phonon. This makes sense, since $\tilde{c}_{\mathbf{k}}$ encloses a $\hat{\chi}_{\mathbf{k}}$ and a $\hat{\chi}_{-\mathbf{k}}$ operator in its definition, which both decay at the same rates $\gamma_{\mathbf{k}}^B$ and $\gamma_{\mathbf{k}}^L$. In fact, (9.37) is more general as it also contains terms proportional to $\tilde{c}_{\mathbf{q}}\tilde{c}_{\mathbf{q}'}^*$. These are expected to accelerate the decay of $\tilde{c}_{\mathbf{k}}$ by incoherent scattering of excitations from the reservoir of modes \mathbf{q} into mode \mathbf{k} .

9.4.2 Approaching a thermal ensemble

The thermodynamic energy of the system, evaluated on the level of the quadratic Hamiltonian,

$$E = \langle \hat{H} \rangle \approx E'_0 + \sum_{\mathbf{k}} \omega_{\mathbf{k}} n_{\mathbf{k}}^{(X)}, \quad (9.41)$$

is conserved under the evolution of the kinetic equations (9.36)–(9.37). One concludes that, since $\omega_{\mathbf{k}} \propto k^2$ and $n_{\mathbf{k}}^{(X)} \propto 1/k^4$ for the initial state, the total integrand scales as $1/k^2$ at large \mathbf{k} right after the quench. Consequently, in three spatial dimensions this gives a UV divergence that scales as $E - E'_0 \propto k_{\text{cut}} \propto \sqrt{\tau_s^{-1}}$.

In the long-time limit, we conclude that the kinetic equation 9.36 approaches a thermal ensemble of atoms, exactly what we expect. In that case, the momentum distribution of quasiparticles assumes the form of the Bose-Einstein distribution

$$n_{\mathbf{k}} = \frac{1}{\exp(\beta\omega_{\mathbf{k}}) - 1}, \quad (9.42)$$

which decays exponentially at large k . This enables us to fix the total injected energy with the switching time τ_s and, consequently, the final equilibrium temperature of the gas by matching this energy with the energy of a thermal ensemble, with momentum distribution (9.42). When $k_B T > \mu$, we have that $E - E'_0 \propto T^{5/2}$, such that we derive the asymptotic scaling $T \propto \tau_s^{-1/5}$. In Fig. 9.3(b), we show the full variation of equilibrium temperature with switching time τ_s .

Furthermore, we see that (9.37) always evolves to $\tilde{c}_{\mathbf{k}} = 0$ at late times. Intuitively, this is also what we expect to happen. The long-time limit corresponds to approaching a thermal ensemble, and in a thermal state there can be no anomalous correlations.

9.5 The evolution of the density correlations

The central idea of this chapter is that we can decompose Hamiltonian \hat{H} from (9.12) into two contributions with different associated time scales. The part that is integrable, \hat{H}_2 , causes a first relaxation of local observables to a quasisteady value, described by a generalized Gibbs ensemble with the relevant conserved charges. Nevertheless, at late times the quasiparticle collisions will come into play and guide the system to the true equilibrium,

the thermal ensemble (see Fig. (9.2)). Local observables, such as the density fluctuations, are therefore expected to exhibit two distinct relaxation stages.

In principle, we can numerically integrate (9.29)–(9.31) to evaluate the full evolution of correlations in the bosonic gas. However, at short enough times we know that the dynamics is well described by the quadratic Hamiltonian \hat{H}_2 . Conversely, at late times we can certainly rely on the kinetic description of the problem, established in the previous section. We also know that this formalism produces the right thermal expectation values in the long-time limit. What about intermediate times? In Appendix C.4, we illustrate that the dephasing mechanism that we relied on to derive the kinetic description of the problem is actually almost instantly valid after the quench for momenta of the order of the inverse healing length. Since the final temperature has $T \sim \mu$ for the quenches that we consider, this also corresponds to the thermal wave vector. In any case, we verify in detail that for local observables, defined within a region of roughly the order of the healing length, the kinetic description is valid from immediately after the quench to compute their time evolution, as we will also apply in the following.

9.5.1 The density correlations

We have come across the density-density correlation function a few times now for this work, but we repeat its definition here for the sake of completeness. First of all, we are interested in quantities in real space, motivating us to return to the position-space operator $\hat{\Psi}(\mathbf{r}) = 1/\sqrt{V} \sum_{\mathbf{k}} \hat{a}_{\mathbf{k}} e^{i\mathbf{k}\cdot\mathbf{r}}$, in terms of which we originally formulated the problem in Sec. 9.1. For a homogeneous density profile, the density-density correlation function is then defined as $\langle : \hat{n}(\mathbf{r}) \hat{n}(\mathbf{r}') : \rangle / \langle \hat{n}(\mathbf{r}) \rangle^2$, with ‘:’ denoting normal ordering and $\hat{n}(\mathbf{r}) = \hat{\Psi}^\dagger(\mathbf{r}) \hat{\Psi}(\mathbf{r})$ the local density operator. Previously, this quantity has been studied intensely in the context of analog gravity, because it encodes a fingerprint of Hawking radiation at a sonic black hole’s horizon [148, 149]. In a recent cold-atom experiment, it was used to witness Hawking radiation and to illustrate that the Hawking particle and its partner inside the sonic black hole are entangled [150].

On the Gaussian level, the density correlation function can be simplified to

$$g^{(2)}(\mathbf{r} - \mathbf{r}'; t) = 1 + \frac{2}{n_0} (\mathbf{n}(\mathbf{r} - \mathbf{r}'; t) + \text{Re}\{\mathbf{m}(\mathbf{r} - \mathbf{r}'; t)\}), \quad (9.43)$$

where we defined

$$\mathbf{n}(\mathbf{r} - \mathbf{r}'; t) = \langle \hat{\Psi}^\dagger(\mathbf{r}) \hat{\Psi}(\mathbf{r}') \rangle_t = \frac{1}{V} \sum_{\mathbf{k} \neq 0} e^{i\mathbf{k}\cdot(\mathbf{r}-\mathbf{r}')} n_{\mathbf{k}}^{(a)}(t), \quad (9.44)$$

and analogous for $\mathbf{m}(\mathbf{r} - \mathbf{r}') = \langle \hat{\Psi}(\mathbf{r}) \hat{\Psi}(\mathbf{r}') \rangle$. The quadratic correlations of fluctuations operators, $n_{\mathbf{k}}^{(a)}$ and $c_{\mathbf{k}}^{(a)}$, can be obtained from the quasiparticle correlations $n_{\mathbf{k}}^{(x)}$ and $c_{\mathbf{k}}^{(x)}$ that we get out of the kinetic equations through the inverse of the transformation (9.20).

We focus on the evolution of the density correlation function in the gas because this quantity can be readily detected in experiment. In particular, by repeatedly performing the

9.6. Conclusive remarks and outlook

same experiment and then doing a *time-of-flight* or *in-situ* measurement at the same time instant, one can get an estimate of (9.43) by correlating the densities found at different points [151].

9.5.2 The two-stage relaxation of local observables

Observables that correlate points separated by a distance $x = |\mathbf{r} - \mathbf{r}'|$ are expected to relax at short times a consequence of a dephasing process under evolution with \hat{H}_2 . This phenomenon relates back to the lightcone-like propagation that we discussed in detail in Sec. 3.3.1. Once the lightcone peak has passed after a characteristic time $t = x/v_{\text{LR}}$, with v_{LR} the Lieb-Robinson velocity⁴, all modes in momentum space generally interfere destructively, thereby causing a relaxation of local observables to a prethermal value. In Fig. 9.4, this is exactly what we see for $g^{(2)}(x; t)$; at short times, of the order of μ^{-1} (when $x \sim \xi$ and after a ramp $\tau_s \sim \mu^{-1}$), we note a first relaxation of the observable. The quasisteady value agrees with the prediction found in a generalized Gibbs ensemble (see 3.6), as indicated in by the first black line in the figures.

Nevertheless, on a much longer time scale, roughly $\tau_{\text{therm}} \sim 10^3 \mu^{-1}$, we see that $g^{(2)}(x; t)$ finds a new steady value. This time, the value corresponds to the one found in a thermal ensemble, as indicated by the second black line. During this relaxation process, the Beliaev-Landau scatterings come into play and break the integrability of \hat{H}_2 . The ergodic dynamics that they convey, much slower than the integrable dynamics, causes the system to fully thermalize. The kinetic description, derived in (9.36)–(9.37), describes this stage, which eventually leads the quasiparticle momentum distribution to its thermal value (9.42) and destroys the pair correlations built up during the ramp. The thermalization time τ_{therm} is in qualitative agreement with the Beliaev-Landau lifetime of the thermal wavenumber $1/\gamma_{k_{\text{th}}}^{BL} \sim 1/\mu \sqrt{n a_s^3}$ for $k_B T \sim \mu$ [139]. Since the correlation function in both the generalized Gibbs ensemble and the thermal ensemble drops to zero at large x , the difference between the prethermal and thermal values vanishes for larger separations.

9.6 Conclusive remarks and outlook

Traditionally, Beliaev-Landau scattering is studied in the context of phonon decay in a superfluid. With this work, however, we have investigated the effects of the scatterings in two radically different scenarios: the steady state of a driven-dissipative array of nonlinear cavities and the thermalization of an ultracold atomic gas of bosonic atoms after a sudden interaction quench. In both cases, the construction of a *hierarchy of correlation functions* was our preferred tool to capture the physics beyond a Gaussian approximation of the model (see Sec. 8.5 and 9.3.2).

⁴In principle the Lieb-Robinson bound holds only strictly for lattice models. However, when the occupation of modes in a continuum is restricted to mostly low-momentum modes, we expect the bound to hold within good approximation.

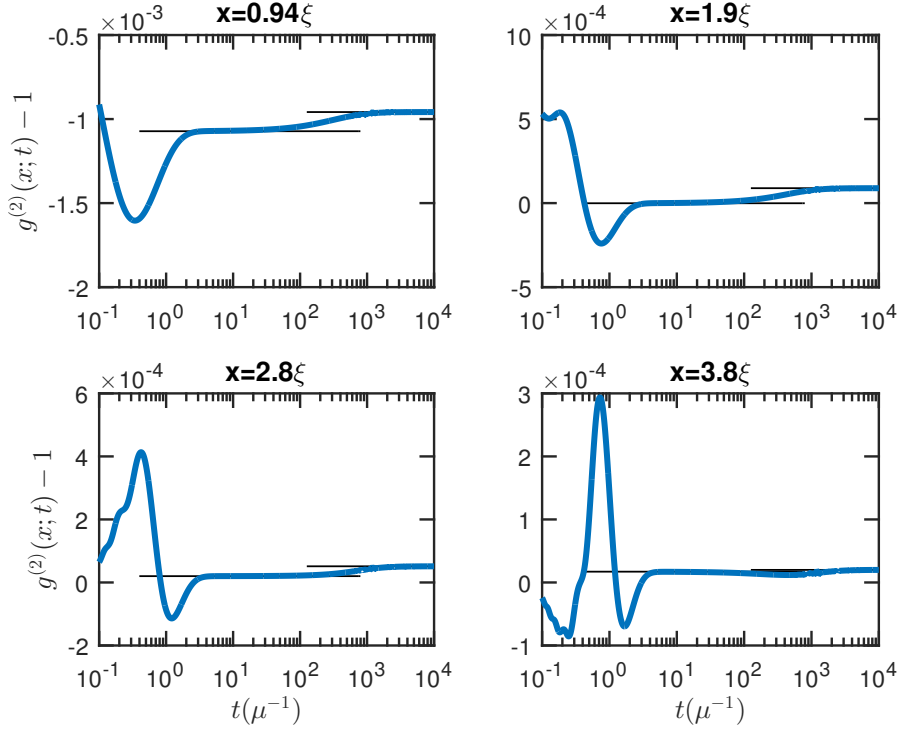


Figure 9.4: The evolution of the density correlation function after the quench $g_i = 0 \rightarrow g_f = 0.05\mu\xi^3$ in a time window $\tau_s = 0.5\mu^{-1}$ (see red line in Fig. 9.3 for initial momentum distribution) for varying separation $x = |\mathbf{r} - \mathbf{r}'|$, with $\xi = 1/\sqrt{m\mu}$ the healing length. The black lines indicate the asymptotic values for the prethermal and thermal (quasi)stationary ensemble; the temperature $T = 0.67\mu$ is found from the initial state. At short distances, we clearly notice a relaxation to a prethermal plateau on a time scale of the order of $\tau_{\text{preth}} = \mu^{-1}$ (for ramps $\tau_s \sim \mu^{-1}$ and $x \sim \xi$), this is due to a dephasing mechanism in \hat{H}_2 . In $g^{(2)}(x; t)$, this is manifested as a fast oscillation at short times, which then diminishes due to a destructive interference between all \mathbf{k} -modes once the light-cone correlation peak has moved away from the considered distance x [143]. Then, at much later times, $\tau_{\text{therm}} \sim 10^3\mu^{-1}$, a new equilibrium value is found that corresponds to the value in the thermal ensemble through the much slower dynamics of \hat{H}_3 . The difference between the prethermal and thermal value vanishes for increasing separation x as the correlation function drops to zero for both ensembles in this limit.

9.6. Conclusive remarks and outlook

In the case of the cavity array, elaborated in Chapter 8, we saw that Beliaev-Landau collisions manifested themselves in a highly unexpected way in the steady state. The absence of detailed balance in a driven-dissipative setting makes that the scatterings are not restricted to driving the system toward thermal equilibrium. In the steady-state momentum distribution of the chain, we therefore see small peaks and dips at specific momenta favored as output or input states for the collisions (see Fig. 8.5). This feature, along with a slight non-Gaussian nature of the output photons, provides a promising experimental signature of Beliaev-Landau scattering in an array of semiconductor micropillars (see Sec. 8.6 and Fig. 8.8).

On the theoretical side, we discovered that our initial attempt to describe Beliaev-Landau collisions within the widely used truncated Wigner approximation dramatically fails, despite being well within the purported domain of validity (see Sec. 8.3). The reason is that the quantum vacuum is represented by $1/2$ artificial classical noise, which also scatters and entirely spoils the signal of the true redistribution of occupation numbers. This raises fundamental questions about the validity of the method and its potential for out-of-equilibrium problems. It would be interesting to reconsider the domain of validity after truncation and, if possible, to formulate higher-order corrections. The results of this work are published in [152].

In Chapter 9, we moved our attention back to the conservative dynamics of isolated quantum many-body systems after an abrupt quench. Here, the system consisted of a dilute gas of trapped atoms, of which the interaction constant can be quenched via a *Feshbach* resonance by suddenly ramping up an external magnetic field. The initial ramp creates a nonequilibrium distribution of quasiparticles through the *dynamical Casimir effect* (see Sec. 9.2), which subsequently relaxes. The switching time of the interaction quench can be used to set the total injected energy and, consequently, the expected final temperature of the condensate. In a first stage, the dynamics is approximately integrable and causes the system to relax to a quasisteady *prethermal* state on a timescale roughly set by the chemical potential (see Sec. 9.2.2).

At later times, the integrability of the Hamiltonian is broken by higher-order interactions in the form of Beliaev-Landau scatterings. This causes a further relaxation of the system to the true final state: a *thermal equilibrium*. By making a dephasing approximation in the constructed hierarchy of correlation functions, we were able to derive an effective *kinetic description* for the quasiparticle dynamics, which in principle holds at sufficiently late times and describes the final thermalization stage (see Sec. 9.4). Nevertheless, as we numerically verify in Appendix C.4, the kinetic description is actually extremely accurate from immediately after the quench, provided distances of the order of the healing length are targeted.

We then focused on a quantity that is realistically measured in experiment; the density correlation function. When a distance of the order of the healing length is considered, this quantity goes through a two-stage relaxation process, as illustrated in Fig. 9.4. The first

relaxation is caused by the approximately integrable dynamics of \hat{H}_2 and corresponds to expectation values found in the generalized Gibbs ensemble. Then, on a much longer time scale the ergodic dynamics from \hat{H}_3 sets in and guide the system away from integrability. This leads to a new relaxation process, on a time scale roughly given by the Beliaev-Landau lifetime of the thermal wave number $1/\gamma_{k_{\text{th}}}^{BL} \sim 1/\mu\sqrt{na_s^3}$ for $k_B T \sim \mu$, and brings the system to its final thermal state. The results of this work are submitted to Phys. Rev. Letters and can be found in the preprint [153].

Chapter 10

Final discussion and open questions

With this work, we have investigated the special role played by quasiparticles in an out-of-equilibrium context. We first illustrated in Part I how they come about in conservative quantum systems after a sudden global quench, as products of an abrupt change of the quantum vacuum. We then continued in Part II with demonstrating how they may render the output light of a planar semiconductor cavity strongly nonclassical. Finally, in Part III we dealt with interactions among the emergent quasiparticles to study Beliaev-Landau collisions as corrections to a quantum field beyond the standard Gaussian approximation.

In Part I, we have seen how an abrupt change of the quantum vacuum by a sudden quench introduces a population of quasiparticles in a long-range interacting chain of fermions. Subsequently, the dynamics of local observables in the chain can be entirely understood by appreciating the particularly simple time evolution of the quasiparticle operators. As such, we were able to demonstrate that the major fraction of information, encoded somehow in the quasiparticles, travels well within an emergent light cone, in spite of the long-ranged nature of interactions that hinders a direct interpretation in terms of a Lieb-Robinson bound. This is in contrast to what has been observed in other long-range interaction quantum systems, such as coupled spin lattices, but confirms the *protected quasilocality* found in long-range bosonic lattices. We would like to emphasize that it is still an open question whether this behavior of protected quasilocality is somehow generic for a certain class of long-range interacting quantum systems and, if so, what the underlying mechanism is that generates it.

For what concerns the equilibration of local observables in the chain, we concluded that the entanglement entropy of a separated subregion grows in time as a power law under the influence of long-range interactions. This observation also contradicts other works, even based on the same model, which generally report a logarithmic growth of entanglement entropy. Contrary to what we intuitively expected, we found that long-range interactions may drastically delay, rather than accelerate, the process of equilibration after the quench.

We attributed this to a scenario where the Hamiltonian spectrum gives rise to a wavefront of quasiparticles with vanishing group velocity.

We then continued in Part II with analyzing how quasiparticles arise inside a quantum fluid of light in a planar microcavity device. The driven-dissipative nature and weak mediated photon interactions in the setup establish a highly nonequilibrium distribution of quasiparticles inside the fluid. Projected onto the resulting output state of the cavity, we then concluded that the output light contains a small signature of nonclassicality that is manifested as slight antibunched statistics.

We next developed a selection and interference scheme, placed after the microcavity, to amplify this nonclassical feature by a few orders of magnitude, thus rendering the resulting light strongly nonclassical. Our results were understood from the *unconventional photon blockade* perspective, which explains how single photons can be generated as an interference result from a device with only weak mediated photon interactions. In a second part, we illustrated how a free-space optics scheme, based on a few lenses and a Spatial Light Modulator (SLM), offers a great flexibility in shaping the spatio-temporal pattern of density-density fluctuations inside the fluid of light.

In the last part of this thesis, Part III, we illustrated how effective interactions among the quasiparticles, *Beliaev-Landau scattering*, may allow for the treatment of weakly interacting quantum many-body systems beyond a standard Gaussian approximation. To this end, we relied on the method of a truncated hierarchy of correlation functions to incorporate the effects of higher-order interactions upon the many-body dynamics.

First, we demonstrated how these quasiparticle collisions manifest themselves highly unexpectedly as a series of peaks and dips in the steady-state momentum distribution of a chain of coupled cavities. We attributed these observations to the absence of detailed balance in a driven-dissipative context, offering a much larger freedom to the kinetics of microscopic processes. Our initial attempt to describe these phenomena within the truncated Wigner formalism dramatically failed and even produced largely unphysical results. Given the discovered inconsistencies, it is now an open question what the true region of validity of the truncated Wigner approximation is. Equally important is the question whether it is possible to (consistently) improve upon the method to overcome the problems that we unveiled.

We finally moved our attention back to the conservative dynamics of quantum many-body systems kicked out of equilibrium. Now, we considered a trapped ultracold gas of bosonic atoms of which the interaction constant is abruptly ramped up. In a first stage, the dynamics is approximately integrable and leads the system to a quasisteady *prethermal* state. On a much longer time scale, quasiparticle interactions come into play and bring the system to its final state, that of a thermal equilibrium. Given the experimental relevance of this setup, our primary focus was on the evolution of the density-density correlations, a quantity that can be directly detected in a time-of-flight or in-situ measurement. In the dynamics of the observable we could distinguish two separate relaxation stages; a first

relaxation to a *prethermal* state followed by a much slower evolution to a thermal ensemble. It would be fascinating to develop these ideas in more detail with an experimental group in the future, as we believe that our proposal lies well within the reach of current experiments.

List of publications by the author

- M. Van Regemortel, M. Wouters, *Negative drag in nonequilibrium polariton quantum fluids*, Phys. Rev. B **89**, 085303 (2014)
- M. Van Regemortel, F. M. Marchetti, M. Wouters, *Probing the collective excitations of a spinor polariton fluid*, Phys. Rev. B **91**, 075308 (2015)
- M. Van Regemortel, D. Sels, M. Wouters, *Information propagation and equilibration in long-range Kitaev chains*, Phys. Rev. A **93**, 032311 (2016)
- M. Van Regemortel, W. Casteels, I. Carusotto, M. Wouters, *Spontaneous Beliaev-Landau scattering out of equilibrium*, Phys. Rev. A **96**, 053854 (2017)
- M. Van Regemortel, S. Ravets, A. Imamoglu, I. Carusotto, M. Wouters, *Engineering photon statistics with quantum fluids of light*, submitted to SciPost (2018)
- M. Van Regemortel, H. Kurkjian, I. Carusotto, M. Wouters, *Prethermalization to thermalization crossover in a weakly interacting Bose gas following an abrupt interaction quench*, submitted to Phys. Rev. Lett. (2018)

Appendix A

Extra info on the long-range Kitaev chain

A.1 Relaxation to the GGE

The generalized Gibbs ensemble is the maximum-entropy ensemble at equilibrium for a system with conserved quantities [19]. It is constructed by inclusion of all conservation laws:

$$\rho_{\text{GGE}} = \mathcal{Z}^{-1} \exp \left(- \sum_k \lambda_k n_k \right), \quad (\text{A.1})$$

with $n_k = v_k^2$, given in the main text, and $\lambda_k = \log(u_k^2/v_k^2)$, as set by the initial state.

The matrix constructed on \mathcal{A} , of which the eigenvalues $\mu_q = (2n_q^{(\gamma)} - 1)^2$ yield $S_{\mathcal{A}}$, reads

$$\Gamma_{\mathcal{A}} = \mathcal{G}_{\mathcal{A}}^{(+)} \times \mathcal{G}_{\mathcal{A}}^{(-)} = \begin{pmatrix} \Gamma_{\mathcal{A}}^{(d)} & \Gamma_{\mathcal{A}}^{(a)} \\ \Gamma_{\mathcal{A}}^{(a)*} & \Gamma_{\mathcal{A}}^{(d)*} \end{pmatrix}. \quad (\text{A.2})$$

We find that $\langle c_k^\dagger c_l \rangle = n^{(c)} \delta_{kl}$ and $\langle c_k c_l \rangle = m^{(c)} \delta_{kl}$, with the density and anomalous correlation

$$\begin{aligned} n_k^{(c)} &= \sin^2 \theta_k \sin^2 \epsilon_k t, \\ m_k^{(c)} &= \sin \theta_k \left(1 - \cos^2 \left(\frac{\theta_k}{2} \right) e^{-i2\epsilon_k t} + \sin^2 \left(\frac{\theta_k}{2} \right) e^{i2\epsilon_k t} \right). \end{aligned}$$

Using these, (A.2) can be written as:

$$\begin{aligned} \Gamma_{mn}^{(d)} &= \delta_{mn} - \frac{4}{L} \sum_k e^{-ik(m-n)} n_k^{(c)} \\ &\quad + \frac{4}{L^2} \sum_{kl} e^{-ikm} e^{iln} W_{kl}^{\mathcal{A}} (n_k^{(c)} n_l^{(c)} + m_k^{(c)} m_l^{(c)}), \\ \Gamma_{mn}^{(a)} &= \frac{4}{L^2} \sum_{kl} e^{-ikm} e^{ikn} W_{kl}^{\mathcal{A}} (m_k^{(c)} n_l^{(c)} - n_k^{(c)} m_l^{(c)}), \end{aligned} \quad (\text{A.3})$$

with $W_{kl}^{\mathcal{A}} = \sum_{n \in \mathcal{A}} e^{-i(k-l)n}$.

It is now easy to verify that the long-time limits of matrices (A.3), with m, n on a finite subsystem \mathcal{A} , are equivalent to their time averages

$$\bar{\Gamma}_{mn}^{(d)} = \sum_{\mathbf{k}} e^{-ik(m-n)} (2v_k^2 - 1)^2, \quad \bar{\Gamma}_{mn}^{(a)} = 0, \quad (\text{A.4})$$

leading indeed to construction (3.47), the correct ensemble at equilibrium.

Fig. 3.5.2 from the main text shows the scaling of entanglement entropy with system size (left panels) and time (right panels) for various values of the interaction range. It is clear that for longer interaction ranges (except for the special case $\alpha = 1$), the thermalization slows down, with a very slow approach to the GGE (dotted lines) for large subsystems.

A.2 Derivation of the correlation function

The decay of the correlation functions at large distances can be evaluated for $\alpha < 1$. The spectrum in the vicinity of the divergence can be approximated as $\epsilon_k \approx \xi^{(\alpha)} k^{\alpha-1}$, with $\xi^{(\alpha)} = \cos(\pi\alpha/2)\Gamma(1-\alpha)$ (see the Supplemental Material of [10]). Only modes close to the divergence will contribute at large distances.

Furthermore, we have that $\theta_k \approx -\pi/2$ around the divergence, such that at large $r = |m - n|$,

$$\langle c_m^\dagger c_n \rangle \approx i \langle c_m c_n \rangle \approx -\frac{1}{4\pi} \Re \left(\int_{-\pi}^{\pi} e^{-i(kr+2\epsilon_k t)} dk \right) \quad (\text{A.5})$$

The integral can be evaluated with a static-phase approximation and yields expression (3.32) from the main text, with

$$\begin{aligned} F(r, t) &= \frac{1}{2\sqrt{2\pi(2-\alpha)}} \left(2(1-\alpha)\xi^{(\alpha)} t \right)^\gamma r^{-\chi}, \\ \eta(r, t) &= \frac{\pi}{4} + (2-\alpha) \left(2\xi^{(\alpha)} t \right)^{2\gamma} \left((1-\alpha)r \right)^{1-2\gamma}. \end{aligned} \quad (\text{A.6})$$

See Fig. 3.4 in the main text for a comparison between the correlation function and this approximation.

Appendix B

Extra info on exciton-polaritons in planar microcavities

B.1 The quantum Langevin equation

We consider a large system, in which the system of interest is embedded, together with its environment and some coupling (see Chapter 4),

$$\hat{H} = \hat{H}_{\text{sys}} + \hat{H}_{\text{env}} + \hat{H}_{\text{coup}}. \quad (\text{B.1})$$

The reservoir is parametrized as a set of harmonic oscillators

$$\hat{H}_{\text{env}} = \sum_l \omega_l \hat{b}_l^\dagger \hat{b}_l. \quad (\text{B.2})$$

Here, l is some arbitrary index employed to label the modes and ω_l is the frequency of mode l . The coupling between the system of interest and the environment is then parametrized as

$$\hat{H}_{\text{coup}} = \sum_{j,l} \kappa_{jl} [\hat{a}_j \hat{b}_l^\dagger + \hat{a}_j^\dagger \hat{b}_l], \quad (\text{B.3})$$

where \hat{a}_j is some operator of the system and κ_{jl} are the couplings between system mode j and reservoir mode l .

We opt to capture the dissipative dynamics coming from the coupling with the reservoir in terms of an effective equation of motion for the operators \hat{a}_j of the system. To this end, we start by evaluating Heisenberg's equation of motion for the \hat{b}_l operators that make up the reservoir

$$i\partial_t \hat{b}_l = [\hat{b}_l, \hat{H}] \quad (\text{B.4})$$

$$= \omega_l \hat{b}_l + \sum_j \kappa_{jl} \hat{a}_j. \quad (\text{B.5})$$

This equation has a formal solution of the form,

$$\hat{b}_l(t) = e^{-i\omega_l t} \hat{b}_l(0) - i \sum_j \kappa_{jl} \int_0^t dt' e^{-i\omega_l(t-t')} \hat{a}_j(t'). \quad (\text{B.6})$$

In the same way, we can evaluate Heisenberg's equation of motion for the operator \hat{a}_j , which now consists of a part generated by Hamiltonian dynamics with \hat{H}_{sys} and a contribution from the coupling with the reservoir (B.3),

$$i\partial_t \hat{a}_j = [\hat{a}_j, \hat{H}] \quad (\text{B.7})$$

$$= [\hat{a}_j, \hat{H}_{\text{sys}}] + \sum_l \kappa_{jl} \hat{b}_l \quad (\text{B.8})$$

$$= [\hat{a}_j, \hat{H}_{\text{sys}}] + \sum_l \kappa_{jl} e^{-i\omega_l t} \hat{b}_l(0) - i \sum_l \kappa_{jl}^2 \int_0^t dt' e^{-i\omega_l(t-t')} \hat{a}_j. \quad (\text{B.9})$$

In the last line, we have substituted solution (B.6) for the reservoir operator \hat{b}_l . In principle, this equation is decoupled from any dynamics taking place in the reservoir; we merely need the initial values of the $\hat{b}_l(t)$ operators.

The important point to see is that, besides the unitary dynamics generated by \hat{H}_{sys} , we find two dissipative contributions to the dynamics of the system operator \hat{a}_j . The key assumption is now that the energy scales associated with the reservoir are much higher than any relevant scale in the system. The oscillations in the integral over time in (B.9) are therefore significantly faster than any time scale resolved within the system, so that they will largely cancel out.

In practice, we can then approximate

$$\sum_l \kappa_{jl}^2 \int_0^t dt' e^{-i\omega_l(t-t')} = \frac{\gamma_j}{2} \delta(t-t') \quad (\text{B.10})$$

making (B.9) local in time. With this assumption, we ensure that losses are treated on a *Markovian* level, i.e the loss processes are instantaneous and there is no memory of lost particles.

Additionally, we can approximate the rapid oscillations, contained in the second term of (B.9), as random noise that enters the system,

$$\sum_l \kappa_{jl} e^{-i\omega_l t} \hat{b}_l(0) = \sqrt{\gamma_j} \hat{\xi}_j(t). \quad (\text{B.11})$$

The noise here inherits the quadratic nature of the reservoir and is assumed to attain Gaussian statistics with correlation functions at zero temperature

$$\langle \hat{\xi}_j(t) \hat{\xi}_{j'}(t') \rangle = \langle \hat{\xi}_j^\dagger(t) \hat{\xi}_{j'}(t') \rangle = 0, \quad (\text{B.12})$$

$$\langle \hat{\xi}_j(t) \hat{\xi}_{j'}^\dagger(t') \rangle = \delta_{j,j'} \delta(t-t'). \quad (\text{B.13})$$

Substitution of the polariton field operator $\hat{\Psi}(\mathbf{r}, t)$ for the generic system operator \hat{a}_j in (B.7) then yields the quantum Langevin equation (5.21) from the main text.

B.2 The Bogoliubov transformation revisited

The Bogoliubov approximation provides an approximate description of a quantum field in terms of a coherent condensate with Gaussian quantum fluctuations on top. Although the formalism for a driven-dissipative fluid is very similar to the equilibrium case, we would like to draw the attention to a few notable differences.

For equilibrium atomic condensates the quantity ω_k from (5.27) is generally known as the quasiparticle spectrum and it indicates the frequency at which a particular Bogoliubov mode $\hat{\chi}_{\mathbf{k}}$ oscillates [99]. However, out of equilibrium one needs to take caution when this view is generalized. The reason is that, in contrast with an equilibrium condensate, the bare-particle dispersion $\varepsilon_{\mathbf{k}}$ is not necessarily a positive function of \mathbf{k} . In a driven-dissipative quantum fluid the condensate phase is set by the detuning δ , a tunable parameter in experiment, while at equilibrium it is fixed by the chemical potential μ , such that in that case $\Delta = 0$ holds exactly (see (5.24)).

B.2.1 Evolution of the quasiparticle operators

Following expression (5.25), the evolution of the particle operators $\hat{\phi}_{\mathbf{k}}$ can be formulated as

$$i\partial_t \begin{pmatrix} \hat{\phi}_{\mathbf{k}} \\ \hat{\phi}_{-\mathbf{k}}^\dagger \end{pmatrix} = \left(B_{\mathbf{k}} - i\frac{\gamma}{2} \right) \begin{pmatrix} \hat{\phi}_{\mathbf{k}} \\ \hat{\phi}_{-\mathbf{k}}^\dagger \end{pmatrix} + \begin{pmatrix} \hat{\xi}_{\mathbf{k}} \\ \hat{\xi}_{-\mathbf{k}}^\dagger \end{pmatrix}, \quad B_{\mathbf{k}} = \begin{pmatrix} \varepsilon_{\mathbf{k}} + \mu & \mu \\ -\mu & -\varepsilon_{\mathbf{k}} - \mu \end{pmatrix}. \quad (\text{B.14})$$

We can always write $B_{\mathbf{k}} = U_{\mathbf{k}} D_{\mathbf{k}} U_{\mathbf{k}}^{-1}$ with

$$D_{\mathbf{k}} = \begin{pmatrix} \omega_{\mathbf{k}} & 0 \\ 0 & -\omega_{\mathbf{k}} \end{pmatrix}, \quad U_{\mathbf{k}} = \begin{pmatrix} v_{1,\mathbf{k}}^{(+)} & v_{1,\mathbf{k}}^{(-)} \\ v_{2,\mathbf{k}}^{(+)} & v_{2,\mathbf{k}}^{(-)} \end{pmatrix}, \quad v_{1,\mathbf{k}}^{(\pm)} = -\frac{\mu}{\varepsilon_{\mathbf{k}} + \mu \pm \omega_{\mathbf{k}}} v_{2,\mathbf{k}}^{(\pm)}, \quad (\text{B.15})$$

such that $V_{\mathbf{k}}^{(\pm)} = (v_{1,\mathbf{k}}^{(\pm)}, v_{2,\mathbf{k}}^{(\pm)})^T$ are the left eigenvectors of $B_{\mathbf{k}}$ with eigenvalues $\pm\omega_{\mathbf{k}}$. Notice that $B_{\mathbf{k}}$ is in general not Hermitian and that therefore left and right eigenvectors do not necessarily coincide, nor must they form an orthogonal basis.

Without any loss of generality, we can now define new quasiparticle operators $\Xi_{\mathbf{k}} = U_{\mathbf{k}}^{-1} \Phi_{\mathbf{k}}$, with $\Xi_{\mathbf{k}} = (\hat{\chi}_{\mathbf{k}}^{(+)}, \hat{\chi}_{-\mathbf{k}}^{(-)})^T$ and $\Phi_{\mathbf{k}} = (\hat{\phi}_{\mathbf{k}}, \hat{\phi}_{-\mathbf{k}}^\dagger)^T$, which evolve in time as

$$\partial_t \begin{pmatrix} \hat{\chi}_{\mathbf{k}}^{(+)} \\ \hat{\chi}_{-\mathbf{k}}^{(-)} \end{pmatrix} = \left(D - i\frac{\gamma}{2} \right) \begin{pmatrix} \hat{\chi}_{\mathbf{k}}^{(+)} \\ \hat{\chi}_{-\mathbf{k}}^{(-)} \end{pmatrix} + \text{noise} \quad (\text{B.16})$$

B.2.2 Regular modes

If we want the $\hat{\chi}_{\mathbf{k}}^{(\pm)}$ to be operators that satisfy bosonic commutation relations, they need to fulfil two conditions. First of all they must be each others Hermitian conjugate, which leads to

$$v_{1,\mathbf{k}}^{(+)} = (v_{2,\mathbf{k}}^{(-)})^* \quad \text{and} \quad v_{2,\mathbf{k}}^{(+)} = (v_{1,\mathbf{k}}^{(-)})^*, \quad (\text{B.17})$$

such that we can choose to write

$$U_{\mathbf{k}} = \begin{pmatrix} u_{\mathbf{k}} & v_{\mathbf{k}}^* \\ v_{\mathbf{k}} & u_{\mathbf{k}}^* \end{pmatrix}. \quad (\text{B.18})$$

Secondly, the bosonic commutation relation $[\hat{\chi}_{\mathbf{k}}^{(+)}, \hat{\chi}_{-\mathbf{k}}^{(-)}] = 1$ tells us that

$$|u_{\mathbf{k}}|^2 - |v_{\mathbf{k}}|^2 = 1 \quad (\text{B.19})$$

After evaluation and making use of (B.15), the parameters u_k and v_k are found as,

$$u_k, v_k = \pm \sqrt{\frac{\epsilon_k + \mu}{2\omega_k} \pm \frac{1}{2}} \quad (\text{B.20})$$

In this way, we have derived the standard text book definition of the Bogoliubov transformation without making any assumptions other than the Bogoliubov operators being bosonic.

B.2.3 Diffusive-like modes

Diffusive-like modes are characterized by having $\epsilon_k < 0$, so that ω_k is purely imaginary and we can write $\omega_k = i\Gamma_k$ with Γ_k real. By making use of relation (B.15) we can now evaluate

$$|u_{\mathbf{k}}|^2 - |v_{\mathbf{k}}|^2 = |u_{\mathbf{k}}|^2 \left(1 - \frac{(\epsilon_{\mathbf{k}} + \mu)^2 + \Gamma_{\mathbf{k}}^2}{\mu^2} \right) = |u_{\mathbf{k}}|^2 \left(1 - \frac{(\epsilon_{\mathbf{k}} + \mu)^2 - \epsilon_{\mathbf{k}}(\epsilon_{\mathbf{k}} + 2\mu)}{\mu^2} \right) = 0 \quad (\text{B.21})$$

This clearly contradicts (B.19), meaning that either condition (B.17) or condition (B.19) cannot be satisfied. Henceforth, the Bogoliubov operators $\hat{\chi}_{\mathbf{k}}^{(\pm)}$ of diffusiv-like modes cannot be bosonic.

We can choose another parametrization (not unique) for the transformation matrix $U_{\mathbf{k}}$ from (B.15)

$$U_{\mathbf{k}} = \begin{pmatrix} r_{\mathbf{k}} & r_{\mathbf{k}}^* \\ s_{\mathbf{k}} & s_{\mathbf{k}}^* \end{pmatrix}, \quad s_{\mathbf{k}} = \frac{-\mu}{\epsilon_{\mathbf{k}} + \mu + i\Gamma_{\mathbf{k}}} r_{\mathbf{k}}, \quad (\text{B.22})$$

where we choose the normalization $s_{\mathbf{k}} r_{\mathbf{k}}^* - r_{\mathbf{k}} s_{\mathbf{k}}^* = i$, such that

$$U_{\mathbf{k}}^{-1} = i \begin{pmatrix} s_{\mathbf{k}}^* & -r_{\mathbf{k}}^* \\ -s_{\mathbf{k}} & r_{\mathbf{k}} \end{pmatrix}. \quad (\text{B.23})$$

With this choice of parametrization we derive after straightforward algebra from (B.15) that

$$s_k = \sqrt{\frac{\mu}{2\Gamma_k}}, \quad r_k = \frac{-\mu}{\epsilon_k + \mu + i\Gamma_k} \sqrt{\frac{\mu}{2\Gamma_k}}, \quad (\text{B.24})$$

B.3 The time evolution of the particle operators

We focus on the linear part of time evolution of an excitation. In general, we find that equation (5.25) can be solved by introducing time-dependent operators of the form

$$\hat{\phi}_{\mathbf{k}}(t) = e^{-\gamma t/2} \left(\eta_{\mathbf{k}}(t) \hat{\phi}_{\mathbf{k}}(0) + \zeta_{\mathbf{k}}(t) \hat{\phi}_{-\mathbf{k}}^\dagger(0) \right) + \text{noise} \quad (\text{B.25})$$

Here, $\eta_{\mathbf{k}}(t)$ and $\zeta_{\mathbf{k}}(t)$ are time-dependent Bogoliubov coefficients. When Δ is tunable, we can distinguish three different regimes that are separated in momentum space [100, 102].

- $\Delta < 0$: $\varepsilon_{\mathbf{k}}$ is positive for any \mathbf{k} and the quasiparticle spectrum $\omega_{\mathbf{k}}$ has a gap given by $\sqrt{|\Delta|(|\Delta| + 2\mu)}$. In the limiting case $\Delta \rightarrow 0$ the gap closes and we retrieve the familiar linear spectrum of an equilibrium condensate. Particle-like (hole-like) excitations oscillate with a frequency ω_k ($-\omega_k$), but are damped by γ , reflecting the overall finite lifetime of particles. The time-dependent Bogoliubov transformation is then found as

$$\eta_k(t) = |u_k|^2 e^{-i\omega_k t} - |v_k|^2 e^{i\omega_k t}, \quad \zeta_k(t) = 2i u_k v_k^* \sin(\omega_k t). \quad (\text{B.26})$$

- $0 < \Delta < 2\mu$: A disk of modes $k < \sqrt{2m\Delta}$ appears where $\varepsilon_{\mathbf{k}} < 0$. Modes in this region have a purely imaginary frequency $\omega_k = i|\omega_k|$ so that they are damped or amplified at a rate $\Gamma_k = |\omega_k|$. Therefore one branch of excitations will be strongly damped in time with a lifetime $1/(\gamma + 2\Gamma_k)$, while excitations on the other branch may have a much longer lifetime $1/(\gamma - 2\Gamma_k)$ and are parametrically amplified. Modes in this region are traditionally called *diffusive*-like [100]. We derive that their time evolution is governed by

$$\eta_k(t) = i \left(s_k r_k^* e^{\Gamma_k t} - s_k^* r_k e^{-\Gamma_k t} \right), \quad \zeta_k(t) = -2i |s_k|^2 \sinh(\Gamma_k t), \quad (\text{B.27})$$

with s_k and r_k given in (B.24). Note that, in order to have only exponentially damped diffusive modes, we must assert that $\gamma > 2\mu$.

- $2\mu < \Delta$: Same as above, but in this case the diffusive modes are found on a ring $\sqrt{2m(\Delta - 2\mu)} < k < \sqrt{2m\Delta}$, while modes in the inner disk $k < \sqrt{2m(\Delta - 2\mu)}$ oscillate with a real frequency ω_k , like usual. For these modes the time evolution is found as

$$\eta_k(t) = |u_k|^2 e^{i\omega_k t} - |v_k|^2 e^{-i\omega_k t}, \quad \zeta_k(t) = -2i u_k v_k^* \sin(\omega_k t), \quad (\text{B.28})$$

meaning that they oscillate with the reversed frequency $-\omega_k$ as compared to B.26, with u_k and v_k given in (B.20).

B.4 Main noise sources

In this Appendix, we discuss the influence of the dominant noise sources in the setup. First, we assume a homogeneous distribution of polaritons in the plane of the microcavity; this

can be distorted in the presence of cavity disorder. Second, interaction with a phonon bath may lead to pure dephasing of polaritons, thus altering the squeezing properties of the light. Eventually, this together with other relaxation mechanisms may result in a population of thermal polaritons in the microcavity.

B.4.1 Disorder

We may give an estimate for the effects of disorder by considering the Fourier transform $V_{\mathbf{k}}$ of a random potential, $V(\mathbf{r}) = \frac{1}{\sqrt{V}} \sum_{\mathbf{k}} V_{\mathbf{k}} e^{i\mathbf{k}\cdot\mathbf{r}}$, which is applied to the planar microcavity. We then find that the random potential enters into the evolution of the mean field in the rotating frame as

$$i\dot{\psi}(\mathbf{r}) = \left(-\frac{\nabla^2}{2m} + g|\psi(\mathbf{r})|^2 + V(\mathbf{r}) - \delta - i\frac{\gamma}{2} \right) \psi(\mathbf{r}) + F. \quad (\text{B.29})$$

When we restrict to evaluating the linear response of the mean field to disorder, we find that the non-uniform polariton field can be formulated as $\psi(\mathbf{r}) = \psi_0 + \frac{1}{\sqrt{V}} \sum_{\mathbf{k}} \delta\psi_{\mathbf{k}} e^{i\mathbf{k}\cdot\mathbf{r}}$. After substitution in (B.29) and collecting terms up to linear order in $\delta\psi_{\mathbf{k}}$ and $V_{\mathbf{k}}$, we find a set of linear equations for each mode

$$\mathcal{L}_k \begin{pmatrix} \delta\psi_{\mathbf{k}} \\ \delta\psi_{-\mathbf{k}}^* \end{pmatrix} = \begin{pmatrix} -V_{\mathbf{k}}\psi_0 \\ V_{-\mathbf{k}}\psi_0^* \end{pmatrix} \quad (\text{B.30})$$

with the response matrix

$$\mathcal{L}_k = \begin{pmatrix} \epsilon_k + gn_0 - i\frac{\gamma}{2} & g\psi_0^2 \\ -g\psi_0^{*2} & -\epsilon_k - gn_0 - i\frac{\gamma}{2} \end{pmatrix}, \quad (\text{B.31})$$

and $\epsilon_k = k^2/2m - \delta + Un_0$. By solving (B.30) we derive the response of the density distribution to the disorder potential in the linear regime

$$\delta n_{\mathbf{k}} = |\delta\psi_{\mathbf{k}}|^2 = V_{\mathbf{k}}^2 n_0 \frac{\epsilon_k^2 + \gamma^2/4}{(\omega_k^2 + \gamma^2/4)^2} \quad (\text{B.32})$$

with ω_k given in (5.27).

For this qualitative analysis we consider $\omega_k \approx \epsilon_k$, such that $\delta n_{\mathbf{k}} \approx V_{\mathbf{k}}^2 n_0 / ((\omega_k^2 + \gamma^2/4))$. When we compare this with the momentum distribution from coherent pair creation (5.31), we conclude that $\langle V^2 \rangle \Delta V_c \ll g \cdot \mu / 2$, where $\langle V^2 \rangle$ is the variation of the disorder potential and ΔV_c is the correlation volume of disorder. Plugging in numbers, we find that $V(\mathbf{r})$ should not vary more than $\sim 40 \mu\text{eV}$ over a scale of $1 \mu\text{m}$ for an interaction constant $g = 10 \mu\text{eV} \cdot \mu\text{m}^2$, in line with [82], and $\mu = 300 \mu\text{eV}$. Probably, this is the primary challenge to implement our proposal in experiment, based on values reported in Ref. [133].

B.4.2 Pure dephasing

When polaritons interact with a bath of phonons, this can be captured by introducing dissipation in the form of dephasing in the master equation (4.3). This amounts to adding a dissipator [86]

$$\mathcal{D}_{\text{deph}}[\hat{\rho}] = \frac{\gamma_{\text{deph}}}{2} \int d\mathbf{r} \left(2\hat{n}\hat{\rho}\hat{n} - \hat{\rho}\hat{n}^2 - \hat{n}^2\hat{\rho} \right), \quad (\text{B.33})$$

with $\hat{n} = \hat{\Psi}^\dagger \hat{\Psi}$ the local density operator and γ_{deph} is the rate associated to dephasing.

While this leaves the evolution of n_k in (5.29) unaffected, it changes the evolution of pair correlations as

$$i\partial_t c_k = \left(2\varepsilon_k + 2g|\psi_0|^2 - i(\gamma + \gamma_{\text{deph}}) \right) c_k + g\psi_0^2(2n_k + 1) \quad (\text{B.34})$$

The steady-state correlations from (5.31) with dephasing are then found as

$$n_k = \frac{1}{2} \frac{\frac{\tilde{\gamma}}{\gamma}(gn_0)^2}{\omega_k^2 - \gamma_{\text{deph}}/\gamma(gn_0)^2 + \tilde{\gamma}^2/4}, \quad c_k = -\frac{g\psi_0^2}{2} \frac{\varepsilon_k + gn_0 + i\tilde{\gamma}/2}{\omega_k^2 - \gamma_{\text{deph}}/\gamma(gn_0)^2 + \tilde{\gamma}^2/4}, \quad (\text{B.35})$$

with $\tilde{\gamma} = \gamma + \gamma_{\text{deph}}$.

When $\gamma_{\text{deph}} \ll \gamma$, we retrieve expressions (5.31) from the main text. In practice, our proposal does not rely on high-quality cavities, such that γ is not necessarily small compared to other energy scales (in particular, we need $\gamma \sim \mu$ for the results of Fig. 6.3). Therefore, we deem that it is not unrealistic to establish a setup with $\gamma_{\text{deph}} \ll \gamma$.

B.4.3 Other noise sources

As a consequence of other spurious relaxation processes, an incoherent population of polaritons can build up at the bottom of the excitation branch. This may result in an extra density of polaritons n_{inc} at nonzero k , not generated by coherent pair-creation, which is to be added to n_k in (5.31) and therefore reduces the squeezing of the output light. One way to circumvent this problem is to employ a pulsed excitation scheme. Then, the polariton population is expected to build up on the time scale of the polariton lifetime, while thermalization into the bottom of the lower polariton branch requires some relaxation process, which typically occurs on a much longer time scale.

Appendix C

Details on the construction of a hierarchy of equations

C.1 Derivation of the correlation hierarchy for the cavity array

With ansatz (5.22) from the main text, we find the equation of motion for the quantum fluctuations $\hat{\phi}_k$ (8.6). By repeatedly applying the product rule, one can obtain the equations of motion for the correlation functions of the quantum fluctuations. An alternative, completely equivalent approach would be to evaluate $\partial_t \langle \hat{O} \rangle = i \langle [\hat{H}, \hat{O}] \rangle + \text{tr} \{ \hat{O} \mathcal{D}[\hat{\rho}] \}$. Due to spatial homogeneity, only momentum-conserving operator products are included in this construction.

For a general correlation function $C = \langle \prod_k \hat{\phi}_k^{\dagger a_k} \hat{\phi}_k^{b_k} \rangle$ of order N , with $N = \sum_k (a_k + b_k)$, one can derive the following recurrence relation

$$\begin{aligned}
 i\frac{\partial C}{\partial t} = & \sum_q \left[\left(-(a_q - b_q) (\epsilon_q + 2U |\psi_0|^2) - i(a_q + b_q) \frac{\gamma}{2} \right) C \right] \\
 & + U\psi_0^2 \sum_q \left[\left(2b_q C \begin{bmatrix} a_{-q+} \\ b_{q-} \end{bmatrix} + b_{-q} (b_q - \delta_{q,-q}) C \begin{bmatrix} b_{q-} \\ b_{-q-} \end{bmatrix} \right) \right] \\
 & - U\psi_0^{*2} \sum_q \left(2a_q C \begin{bmatrix} a_{q-} \\ b_{-q+} \end{bmatrix} + a_q (a_{-q} - \delta_{q,-q}) C \begin{bmatrix} a_{-q-} \\ a_{q-} \end{bmatrix} \right) \\
 & + \frac{U\psi_0}{\sqrt{L}} \sum_{k,q} \left[2b_q C \begin{bmatrix} b_{q-} \\ a_{k-q+} \\ b_{k+} \end{bmatrix} + b_k (b_q - \delta_{q,k}) C \begin{bmatrix} b_{k-} \\ b_{q-} \\ b_{k+q+} \end{bmatrix} - a_k C \begin{bmatrix} a_{k-q+} \\ a_{q+} \\ a_{k-} \end{bmatrix} \right] \\
 & - \frac{U\psi_0^*}{\sqrt{L}} \sum_{k,q} \left[2a_q C \begin{bmatrix} a_{k+q+} \\ a_{q-} \\ b_{k-} \end{bmatrix} + a_k (a_q - \delta_{q,k}) C \begin{bmatrix} a_{k+q+} \\ a_{k-} \\ a_{q-} \end{bmatrix} - b_k C \begin{bmatrix} b_{k-} \\ b_{q+} \\ b_{k-q+} \end{bmatrix} \right] \\
 & + \frac{U}{L} \sum_{k,k',q} \left(2b_k C \begin{bmatrix} b_{k-} \\ a_{k'+} \\ b_{k-q+} \\ b_{k'+q+} \end{bmatrix} + b_{k'} (b_k - \delta_{k,k'}) C \begin{bmatrix} b_{k'-} \\ b_{k-} \\ b_{k-q+} \\ b_{k'+q+} \end{bmatrix} - 2a_k C \begin{bmatrix} a_{k-} \\ a_{k'-q+} \\ a_{k+q+} \\ b_{k'+} \end{bmatrix} \right) \\
 & - a_{k'} (a_k - \delta_{k,k'}) C \begin{bmatrix} a_{k'-} \\ a_{k'-q+} \\ a_{k+q+} \\ a_{k-} \end{bmatrix} \Big)
 \end{aligned}$$

Here, we adopted the notation, following Ref. [154],

$$C[a_{q\pm}] = \left\langle \hat{\phi}_q^{\dagger a_q \pm 1} \hat{\phi}_q^{b_q} \prod_{k \neq q} \hat{\phi}_k^{\dagger a_k} \hat{\phi}_k^{b_k} \right\rangle.$$

Up to third order, the explicit evaluation of the expression above yields the following equations of motion for the correlators.

- *First order:* A finite value for the zero-momentum component is found

$$\partial_t \langle \hat{\phi}_0 \rangle = (Un_0 - i\gamma/2) \langle \hat{\phi}_0 \rangle + U\psi_0^2 \langle \hat{\phi}_0^\dagger \rangle + \frac{2U\psi_0}{\sqrt{L}} \sum_k \langle \hat{\phi}_k^\dagger \hat{\phi}_k \rangle + \frac{U\psi_0^*}{\sqrt{L}} \sum_k \langle \hat{\phi}_k \hat{\phi}_{-k} \rangle + \frac{U}{L} \sum_{k,q} \langle \hat{\phi}_{k+q}^\dagger \hat{\phi}_q \hat{\phi}_k \rangle \quad (\text{C.1})$$

- *Second order:* We find for the evolution of the density of fluctuations

$$\begin{aligned}
 i\partial_t \langle \hat{\phi}_k^\dagger \hat{\phi}_k \rangle = & -i\gamma n_k + U\psi_0^2 \langle \hat{\phi}_k^\dagger \hat{\phi}_{-k}^\dagger \rangle - U\psi_0^{*2} \langle \hat{\phi}_k \hat{\phi}_{-k} \rangle \\
 & + \frac{2U}{\sqrt{L}} \sum_q \left(\psi_0 \langle \hat{\phi}_k^\dagger \hat{\phi}_q^\dagger \hat{\phi}_{k+q} \rangle - \psi_0^* \langle \hat{\phi}_{k+q}^\dagger \hat{\phi}_q \hat{\phi}_k \rangle \right) + \frac{U}{\sqrt{L}} \sum_q \left(\psi_0^* \langle \hat{\phi}_k^\dagger \hat{\phi}_q \hat{\phi}_{k-q} \rangle - \psi_0 \langle \hat{\phi}_{k-q}^\dagger \hat{\phi}_q^\dagger \hat{\phi}_k \rangle \right) \\
 & + \frac{U}{L} \sum_{q,l} \left(\langle \hat{\phi}_k^\dagger \hat{\phi}_q^\dagger \hat{\phi}_l \hat{\phi}_{k+q-l} \rangle - \langle \hat{\phi}_{k+q-l}^\dagger \hat{\phi}_l^\dagger \hat{\phi}_q \hat{\phi}_k \rangle \right). \quad (\text{C.2})
 \end{aligned}$$

C.2. Different truncation schemes and comparison

Likewise, for the anomalous averages

$$\begin{aligned}
i\partial_t \langle \hat{\phi}_k \hat{\phi}_{-k} \rangle &= (2\epsilon_k + 2U|\psi_0|^2 - i\gamma) \langle \hat{\phi}_k \hat{\phi}_{-k} \rangle + U\psi_0^2 \left(2\langle \hat{\phi}_k^\dagger \hat{\phi}_k \rangle + 1 \right) \\
&+ \frac{2U\psi_0}{\sqrt{L}} \sum_q \left(\langle \hat{\phi}_k \hat{\phi}_q^\dagger \hat{\phi}_{q-k} \rangle + \langle \hat{\phi}_q^\dagger \hat{\phi}_{q+k} \hat{\phi}_{-k} \rangle \right) + \frac{U\psi_0^*}{\sqrt{L}} \sum_q \left(\langle \hat{\phi}_k \hat{\phi}_q \hat{\phi}_{-k-q} \rangle + \langle \hat{\phi}_q \hat{\phi}_{k-q} \hat{\phi}_{-k} \rangle \right) \\
&+ \frac{U}{L} \sum_{q,m} \left(\langle \hat{\phi}_k \hat{\phi}_q^\dagger \hat{\phi}_l \hat{\phi}_{-k+q-l} \rangle + \langle \hat{\phi}_q^\dagger \hat{\phi}_l \hat{\phi}_{k+q-l} \hat{\phi}_{-k} \rangle \right). \tag{C.3}
\end{aligned}$$

- *Third order:* For the third-order correlation functions we can derive the equations of motion in the same way

$$\begin{aligned}
i\partial_t \langle \hat{\phi}_{k-q}^\dagger \hat{\phi}_q^\dagger \hat{\phi}_k \rangle &= \left(-\epsilon_{k-q} - \epsilon_q + \epsilon_k - U|\psi_0|^2 - \frac{3i}{2}\gamma \right) \langle \hat{\phi}_{k-q}^\dagger \hat{\phi}_q^\dagger \hat{\phi}_k \rangle \\
&- U\psi_0^{*2} \left(\langle \hat{\phi}_{q-k} \hat{\phi}_q^\dagger \hat{\phi}_k \rangle + \langle \hat{\phi}_{k-q}^\dagger \hat{\phi}_{-q} \hat{\phi}_k \rangle \right) + U\psi_0^2 \langle \hat{\phi}_{k-q}^\dagger \hat{\phi}_q^\dagger \hat{\phi}_{-k} \rangle \\
&+ \frac{2U}{\sqrt{L}} \sum_m \left(\psi_0 \langle \hat{\phi}_{k-q}^\dagger \hat{\phi}_q^\dagger \hat{\phi}_m^\dagger \hat{\phi}_{m+k} \rangle - \psi_0^* \langle \hat{\phi}_{k-q+m}^\dagger \hat{\phi}_m \hat{\phi}_q^\dagger \hat{\phi}_k \rangle - \psi_0^* \langle \hat{\phi}_{k-q}^\dagger \hat{\phi}_{q+m}^\dagger \hat{\phi}_m \hat{\phi}_k \rangle \right) \\
&+ \frac{U}{\sqrt{L}} \sum_m \left(\psi_0^* \langle \hat{\phi}_{k-q}^\dagger \hat{\phi}_q^\dagger \hat{\phi}_m \hat{\phi}_{k-m} \rangle - \psi_0 \langle \hat{\phi}_{k-q-m}^\dagger \hat{\phi}_m^\dagger \hat{\phi}_q^\dagger \hat{\phi}_k \rangle - \psi_0 \langle \hat{\phi}_{k-q}^\dagger \hat{\phi}_{q-m}^\dagger \hat{\phi}_m^\dagger \hat{\phi}_k \rangle \right) \\
&+ \frac{U}{L} \sum \left(\text{5th-order correlators} \right) \tag{C.4}
\end{aligned}$$

and

$$\begin{aligned}
i\partial_t \langle \hat{\phi}_{-k-q} \hat{\phi}_q \hat{\phi}_k \rangle &= \left(\epsilon_k + \epsilon_q + \epsilon_{k+q} + 3U|\psi_0|^2 - \frac{3i}{2}\gamma \right) \langle \hat{\phi}_{-k-q} \hat{\phi}_q \hat{\phi}_k \rangle \\
&+ U\psi_0^2 \left(\langle \hat{\phi}_{k+q}^\dagger \hat{\phi}_q \hat{\phi}_k \rangle + \langle \hat{\phi}_{-k-q} \hat{\phi}_{-q}^\dagger \hat{\phi}_k \rangle + \langle \hat{\phi}_{-k-q} \hat{\phi}_q \hat{\phi}_{-k}^\dagger \rangle \right) \\
&+ \frac{2U\psi_0}{\sqrt{L}} \sum_m \left(\langle \hat{\phi}_m^\dagger \hat{\phi}_{m-k-q} \hat{\phi}_q \hat{\phi}_k \rangle + \langle \hat{\phi}_{-k-q} \hat{\phi}_m^\dagger \hat{\phi}_{m+q} \hat{\phi}_k \rangle + \langle \hat{\phi}_{-k-q} \hat{\phi}_q \hat{\phi}_m^\dagger \hat{\phi}_{m+k} \rangle \right) \\
&+ \frac{U\psi_0^*}{\sqrt{L}} \sum_m \left(\langle \hat{\phi}_m \hat{\phi}_{-k-q-m} \hat{\phi}_q \hat{\phi}_k \rangle + \langle \hat{\phi}_{-k-q} \hat{\phi}_m \hat{\phi}_{q-m} \hat{\phi}_k \rangle + \langle \hat{\phi}_{-k-q} \hat{\phi}_q \hat{\phi}_m \hat{\phi}_{k-m} \rangle \right) \\
&+ \frac{U}{L} \sum \left(\text{5th-order correlators} \right) \tag{C.5}
\end{aligned}$$

Through its equations of motion, a correlator of order N couples to correlators up to order $N + 2$. In principle, this hierarchy of equations continues to infinite order if the number of particles is not conserved. Therefore, to obtain a closed set of equations, the hierarchy must be truncated in some way.

C.2 Different truncation schemes and comparison

We briefly discuss two different truncation schemes and motivate the choice for the one presented in the main text.

- *The hard cutoff (HC):* The most straightforward approach is to set all correlation functions of order N higher than N_c (i.e. orders $N_c + 1$ and $N_c + 2$) to zero in the

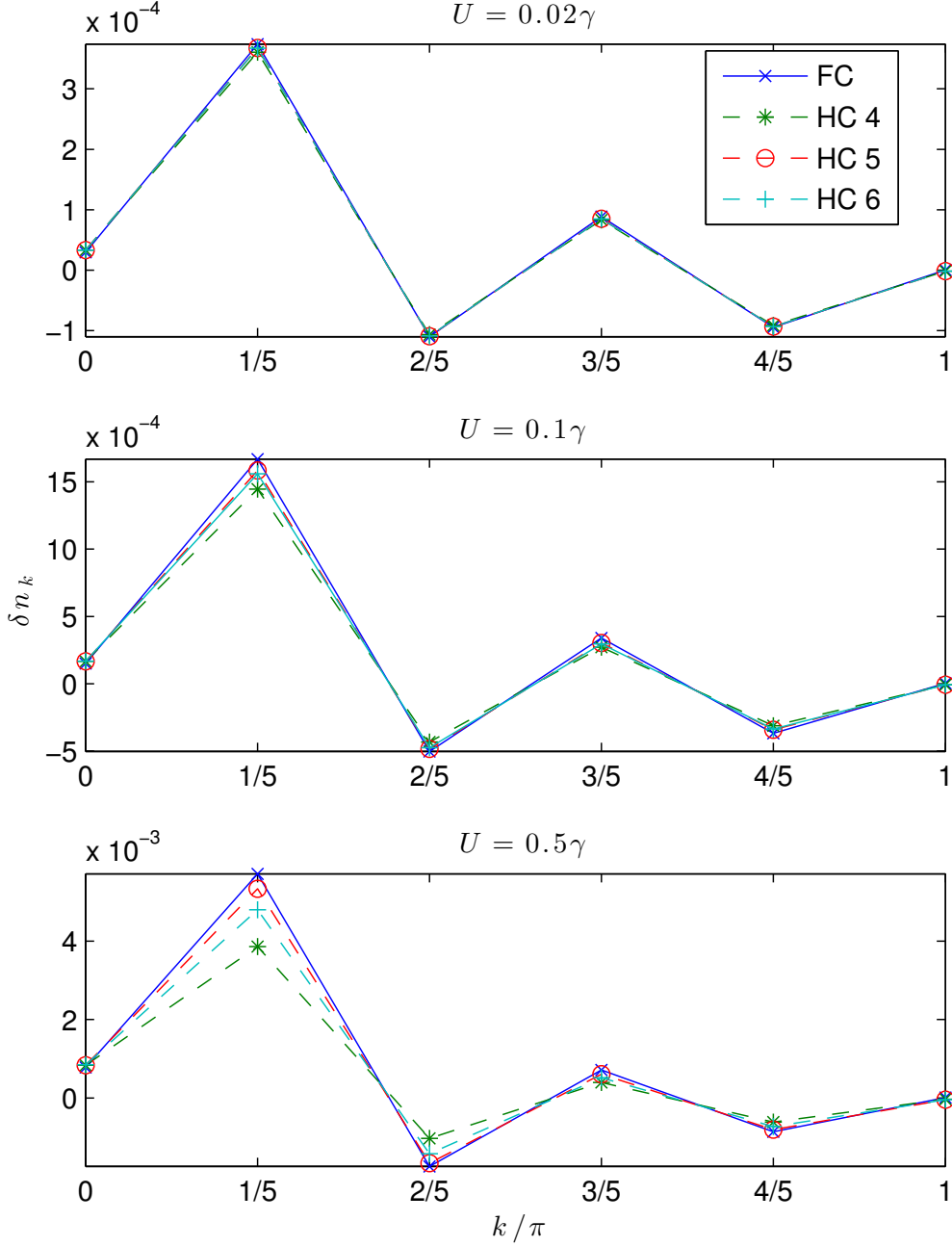


Figure C.1: The comparison of different truncation schemes for the quantity $\delta n_k = n_k - n_k^{\text{bog}}$, with n_k^{bog} the momentum distribution in the Bogoliubov approximation (8.10). We show the values of U that have been studied in the main text. The chain consists of only 10 cavities, such that higher-order truncations can be computed and compared. ‘FC’ stands for ‘factorized cutoff’: the method that has been outlined and employed in the main text. ‘HC’ stands for ‘hard cutoff’ and the integer indicates up to which order N_c normal-ordered correlation functions have been included in the hierarchy.

C.2. Different truncation schemes and comparison

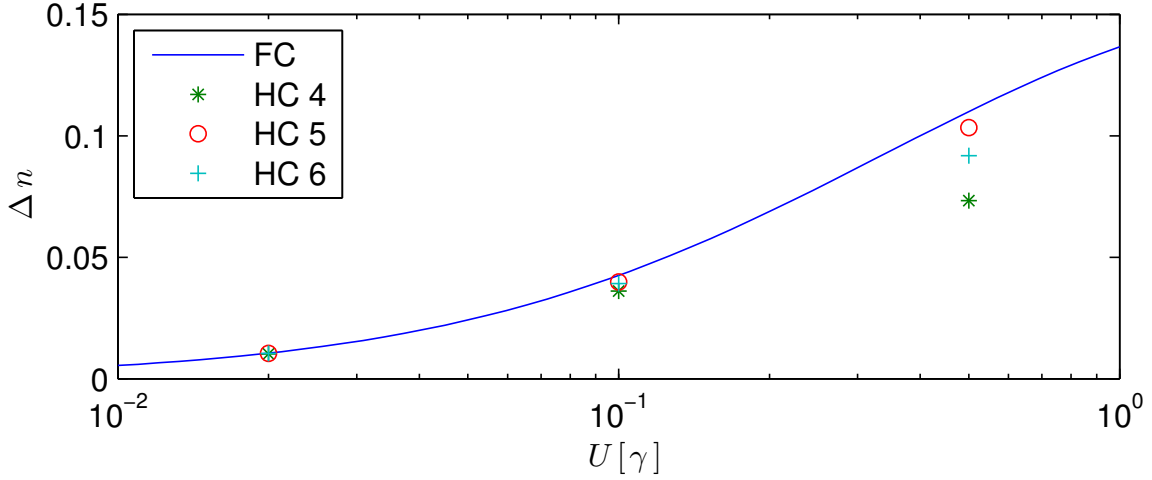


Figure C.2: The difference $\Delta n = 1/L \sum_k |n_k - n_k^{\text{bog}}|/n_k^{\text{bog}}$ as a function of the coupling constant U for different truncation schemes for a chain comprising 10 cavities.

equations of motion. The major benefit of employing this truncation scheme is that, by construction, it produces a linear system of equations, which is relatively easily solved numerically. This allows one to evaluate the result as a function of N_c for small enough system sizes. As discussed in Ref. [154], this approach is expected to be efficient when the number of excitations is small. More precisely, by pursuing this truncation scheme, one is implicitly assuming a small occupation of all modes $n_k < 1$, otherwise the factorizable part of the correlation functions quickly grows as a function of N and the calculation may not converge at high N_c . Nevertheless, even when $n_k < 1$ is satisfied, no a priori assumptions can be made about the connected part of the correlation functions. Therefore one must always verify convergence of the result by increasing N_c . Following Ref. [154], we refer to this truncation scheme as the ‘hard cutoff’.

- *The factorized cutoff (FC)*: The method employed in the manuscript differs in a few aspects from the one described above. First of all, we do not use the linearized equation for the first-order correlator $\langle \hat{\phi}_0 \rangle$ (C.1), but integrate in time the full Gross-Pitaevskii equation with back-reaction terms, i.e. Eq. (8.31), along with the different correlation functions. As explained in the main text, this has the advantage of having $\langle \hat{\phi}_0 \rangle = 0$ by definition, making correlators up to order 3 de facto connected, because their factorizable part vanishes. On the other hand, the field ψ_0 in equations (8.31)-(8.35) is now time dependent, so that the system of equations is no longer linear.

Furthermore, we perform two different approximations to close the system of equations at order $N = 3$, by consistently including the back-reaction of the $N = 4$ and $N = 5$ in the equations for the $N = 2$ and $N = 3$ correlation functions. While the normal

parts of higher order correlators were set to zero in the HC scheme, we start here by including them in factorized form

For a general $N = 4$ correlation function, bearing in mind that $\langle \hat{\phi}_0 \rangle = 0$, we find that it can be written as,

$$\begin{aligned} \langle \phi_m^\dagger \phi_l^\dagger \phi_q \phi_k \rangle &= \langle \phi_m^\dagger \phi_l^\dagger \phi_q \phi_k \rangle_c \\ &+ \langle \phi_l^\dagger \phi_{-l}^\dagger \rangle \langle \phi_k \phi_{-k} \rangle \delta_{l,-m} \delta_{k,-q} \\ &+ \langle \phi_q^\dagger \phi_q \rangle \langle \phi_k^\dagger \phi_k \rangle \left(\delta_{m,q} \delta_{l,k} + \delta_{m,k} \delta_{l,q} \right) \end{aligned}$$

and likewise for other fourth-order correlators. The subscript c (first line) denotes the connected, non-factorizable part of a correlator and is neglected in our truncation scheme. In the equations of motion for the second-order correlation function the factorization of the $N = 4$ correlators (see third line of (C.2) and (C.3)) into products of $N = 2$ correlators yields the Hartree-Fock-Bogoliubov-like terms in (8.31)-(8.32). In turn, for the third-order, the $N = 4$ correlators from (C.4) and (C.5), produce the drive terms $F_{k,q}^{(M,R)}$ from (8.36) and (8.37). Note that in the latter we have omitted factorizations of the form $\sim \frac{U\psi_0}{\sqrt{L}} c_q \sum_l n_l \delta_{k,0}$, and similar terms with $\sim \delta_{k,q}$ and $\sim \delta_{q,0}$, which drive the diagonal terms of $M(R)_{k,q}$. They are not related to Beliaev-Landau scatterings and we have checked that they merely give a negligible extra shift to ψ_0 and slightly renormalize the value of n_k and c_k in $k = 0$, while leaving points at $k \neq 0$ essentially unaffected.

Also the fifth-order correlator, entering in the equations of motion for the third-order correlator, can be approximated by its factorizable form, which produces a total of ten different products of 2nd and 3rd order correlators. Two different groups of terms arise with this procedure. For instance, the first of the three terms entering (C.4) is

$$\begin{aligned} \sum_{l,m} \langle \hat{\phi}_{k-q}^\dagger \hat{\phi}_q^\dagger \hat{\phi}_l^\dagger \hat{\phi}_m \hat{\phi}_{k+l-m} \rangle &\approx \\ \langle \hat{\phi}_{k-q}^\dagger \hat{\phi}_{k-q} \rangle \sum_l \langle \hat{\phi}_q^\dagger \hat{\phi}_l^\dagger \hat{\phi}_{l-q} \rangle &+ \dots \\ + \langle \hat{\phi}_{k-q}^\dagger \hat{\phi}_q^\dagger \hat{\phi}_k \rangle \sum_l \langle \hat{\phi}_l^\dagger \hat{\phi}_l \rangle &+ \dots \end{aligned} \quad (\text{C.6})$$

The dots indicate more terms of the same kind, with summations over a $N = 3$ (first line) or a $N = 2$ correlator (second line). Hence we conclude that, after gathering all those terms, they can be captured by making changes of the kind

$$|\psi_0|^2 \rightarrow |\psi_0|^2 + \frac{1}{L} \sum_l \langle \hat{\phi}_l^\dagger \hat{\phi}_l \rangle \quad (\text{C.7})$$

$$\psi_0 \rightarrow \psi_0 + \frac{1}{L} \sum_l \langle \hat{\phi}_q^\dagger \hat{\phi}_l^\dagger \hat{\phi}_{l-q} \rangle + \dots \quad (\text{C.8})$$

The second approximation consists of neglecting the corrections coming from the factorized fifth-order correlator, which is justified by assuming that the condensate

C.2. Different truncation schemes and comparison

density is much larger than the density of fluctuations. We have evaluated all these fifth-order contributions and verified that their influence on the second-order and third-order correlation function is negligible for the parameters that are used.

To check the consistency of the method we used in the main text, we compare it in Fig. C.1 and Fig. C.2 with the HC truncation scheme at higher orders for a chain of only 10 sites. This allows us to obtain results within a reasonable computation time for truncation orders up to $N_c = 6$ in the HC scheme. The factorized method from the main text appears to agree very well with the HC scheme for $N_c = 5$, even though we only included connected correlators up to order 3. From this we conclude that, at least in the parameter regime that we have considered, it is a good approximation to neglect both the connected $N = 4$ and the full $N = 5$ correlator. On the other hand, we see a large deviation from the HC with $N_c = 4$, even though both methods include correlators up to the same order $N = 4$. This can be attributed to the inaccuracy with which the fourth-order is evaluated in the HC scheme, i.e. by bluntly neglecting all higher-orders. Therefore the inclusion of the fourth order in factorized form directly, as was employed in our FC scheme, turns out to be a much better approximation than obtaining it through a HC scheme with $N_c = 4$.

From Fig. C.1 and Fig. C.2 we deduce that results obtained with different truncation schemes start to deviate from each other at $U/\gamma = 0.5$. This limits the range of parameters in which our approach provides a quantitatively accurate description. While for stronger U/γ , the error due to truncation of higher orders terms becomes increasingly important, still at $U/\gamma = 0.5$ we see that all truncation schemes reproduce at least qualitatively the same result; in particular, the $N_c = 3$ factorized cutoff still reasonably well agrees with the $N_c = 5$ HC scheme, and even with $N_c = 6$. We have therefore chosen to use the $N_c = 3$ factorized cut-off approximation for the study of Beliaev-Landau processes in larger systems, even though there is a small, but non-negligible quantitative deviation from higher-order HC schemes.

Keeping in mind that higher-order HC schemes are numerically cumbersome and can not be applied to large systems, our main motivation for sticking to the $N_c = 3$ factorized cut-off approximation is that, to our knowledge, no efficient methods exist to simulate driven-dissipative quantum dynamics in a system with intermediate interactions ($U = 0.5\gamma$) and a large particle number (128 cavities, each containing 20 photons on average). A possible alternative approach would be to develop a variational method with matrix product operators in the spirit of [68, 67], in which the matrix product state of the quantum excitations is determined self-consistently by coupling it back to the coherent condensate. This will hopefully be the subject of future work.

We therefore conclude that, even though we constructed a hierarchy in terms of correlation functions up to order 3 only, the accuracy is comparable to (or even better as) higher-order methods in the HC scheme. Obviously, the reduced numerical complexity in the developed truncation scheme realizes a significant computational speedup as compared

to these higher-order methods, thus allowing us to tackle much larger systems and address the physically most relevant questions.

C.3 Discretization of the hierarchy of correlation functions in three spatial dimensions

We provide some more info on how we parametrize the different correlation functions in three spatial dimensions for a practical implementation in chapter 9.

C.3.1 The kinetic equations

The delta distribution for energy conservation in expressions (9.36) and (9.37) from the main text can be further evaluated. The energy-conserving condition then translates into a delta distribution that fixes the scattering angle,

$$\delta(\omega_{\mathbf{k}} - \omega_{\mathbf{q}} - \omega_{\mathbf{k}-\mathbf{q}}) = \delta(\cos \theta - \cos \theta_{\mathbf{k},\mathbf{q}}) \left| \frac{\partial \omega_{\mathbf{k}-\mathbf{q}}}{\partial \cos \theta} \right|^{-1} \quad (\text{C.9})$$

$$= \frac{m}{kq} \frac{\omega_{\mathbf{k}} - \omega_{\mathbf{q}}}{\sqrt{\mu^2 + (\omega_{\mathbf{k}} - \omega_{\mathbf{q}})^2}} \delta(\cos \theta - \cos \theta_{\mathbf{k},\mathbf{q}}), \quad (\text{C.10})$$

Here, we have defined the energy-conserving scattering angle

$$\cos \theta_{\mathbf{k},\mathbf{q}} = \frac{1}{2kq} \left(k^2 + q^2 + \xi^{-2} - \sqrt{\xi^{-4} + (\omega_k - \omega_q)^2} \right), \quad (\text{C.11})$$

with $\xi^{-1} = \sqrt{2m\mu}$ the inverse healing length and ω_k the Bogoliubov frequency of the mode \mathbf{k} (see (9.10) from the main text).

Therefore, we find in three spatial dimensions that the evolution of the occupation numbers under the kinetic equations is given by

$$\begin{aligned} \partial_t n_k = & \frac{mg^2 n_0}{\pi k} \left\{ \int_0^k dq q \frac{\omega_k - \omega_q}{\sqrt{\mu^2 + (\omega_k - \omega_q)^2}} A_{q,|\mathbf{k}-\mathbf{q}|}^2 \left(n_{|\mathbf{k}-\mathbf{q}|} n_q - n_k (n_q + n_{|\mathbf{k}-\mathbf{q}|} + 1) \right) \right. \\ & \left. + \int_k^\infty dq q \frac{\omega_q - \omega_k}{\sqrt{\mu^2 + (\omega_k - \omega_q)^2}} A_{k,|\mathbf{k}-\mathbf{q}|}^2 \left(n_q (n_k + n_{|\mathbf{k}-\mathbf{q}|} + 1) - n_k n_{|\mathbf{k}-\mathbf{q}|} \right) \right\} \quad (\text{C.12}) \end{aligned}$$

and similar for the anomalous correlation function c_k . Note that we have replaced the three-dimensional label \mathbf{k} with the wave number k since the expressions are rotation invariant.

The expression written in form (C.12) is apt for discretization and integration after defining the occupation numbers on a grid and replacing the integrals with discrete summations. Note though, that the values $|\mathbf{k} - \mathbf{q}|$ do generally not lie on the same discretized grid for k , such that we need to interpolate from the sampled values. This poses no further problems since n_k , the occupation number of Bogoliubov modes, varies smoothly in function of k .

C.3.2 Discretization of the full hierarchy

In principle, a general third-order correlator in three spatial dimensions is represented by a tensor of rank 9, which is way beyond the memory of an ordinary computer for a satisfactory discretization.

We explicitly seek to retain scatterings that are not energy-conserving, as they constitute physics that is not contained in the kinetic equations, but collisions are always considered momentum-conserving in a homogeneous setup. This observation fixes one momentum and reduces the objects to tensors of rank 6, the way we have written them in (9.28).

If we now align one of the vectors, say the momentum k , along the x -axis, we know that the scattered momentum \mathbf{q} is characterized by its amplitude and the angle with respect to the momentum k . All in all, this makes that we can represent a third-order object $M_{\mathbf{k},\mathbf{q}}$ by three different parameters: amplitude of input momentum k , amplitude of scattered momentum q and the relative angle between them θ , making that we only need a tensor of rank 3

$$M_{\mathbf{k},\mathbf{q}} \equiv M(k, q, \cos \theta) \quad (\text{C.13})$$

and similar for $R_{\mathbf{k},\mathbf{q}}$.

Note that for each k and q we can find the angle of exact energy conservation through relation (C.11). For each entry k, q we therefore keep a list of values (order 100) of $\cos \theta$, ranging from 0 to 1, where we fix one element to the exact energy-conserving angle $\theta_{\mathbf{k},\mathbf{q}}$.

Given the values k, q and $\cos \theta$ we can then find the amplitude of the other scattered vector

$$|\mathbf{k} - \mathbf{q}| = k^2 + q^2 - 2kq \cos \theta. \quad (\text{C.14})$$

Also through interpolation we can then sample the values $n_{|\mathbf{k}-\mathbf{q}|}$, making that we need to keep a list of n_k and \tilde{c}_k and the third-order correlators $M_{\mathbf{k},\mathbf{q}}$ and $R_{\mathbf{k},\mathbf{q}}$, represented as tensors of rank 3, to carry out the integration of the full 3-dimensional hierarchy (9.29-9.32) from the main text.

C.4 Comparison between the hierarchy and the kinetic equations

We present a quantitative analysis of the short-time dynamics as generated by the full hierarchy of correlations and compare with the approximation that results in the kinetic description of the problem. When integrating the full hierarchy, we run into numerical issues and memory problems for long integration times or small discretization in momentum space. The hierarchy also takes into account non-resonant collisions, which means that we have to explicitly include the scattering angle between the ingoing and outgoing momenta (see Appendix C.3).

These simulations are done in 3D for a reduced number of k -modes ($N_k = 128$ or $N_k = 256$) in the radial direction to allow for a modest discretization of the scattering angle in the hierarchy ($N_c = 200$ or $N_c = 70$). In the kinetic formulation, the energy conserving condition fixes the scattering angle, so that we only have two variables k and q . This permits us to take a much larger discretization for the results presented in the main text, $N_k = 8192$.

C.4. Comparison between the hierarchy and the kinetic equations

C.4.1 The quasiparticle occupation numbers

In Fig. C.3, we show the evolution of the quasiparticle occupation numbers for a comparison between the hierarchy of correlation functions and the kinetic equations at short times $\sim 1/\mu$. We observe that the curve of $n_k(t)$ predicted by the kinetic equation differs in two distinct ways from that of the hierarchy: (i) the evolution at very short times is not well captured by the kinetic equation, which results in a small offset (controlled by the interaction strength na_s^3) between the two curves, conserved all along the evolution and (ii) contrary to the kinetic description, the hierarchy of correlations retains high-frequency components in $n_k(t)$. Those two differences are directly related to the two approximations on which kinetic equations are based: (i) they are valid only at long times and (ii) they are valid only on average over a time $\gg 1/\omega_k$.

This analysis shows that for times $\sim 1/\mu$ the kinetic equations show deviations at low wave numbers ($k \ll 1/\xi$). Conversely, higher momentum modes ($k \gtrsim 1/\xi$) allow for an accurate description in terms of a kinetic formulation of the problem. In the main text we focus on the density correlation function at distances of the order of the healing length, much smaller than the full size of the gas. Here, we conclude that at these distances an effective formulation of the problem in terms of kinetic equations, as applied in the main text, agrees very well with the integration in time of the full hierarchy, which is computationally much harder.

C.4.2 The density-density correlations at short times

As a final quantitative analysis, we check the result of both the hierarchy of correlation functions and the kinetic description for the density-density correlations at short times. As Fig. C.4 shows, the difference is virtually indistinguishable with the bare eye. The small offset that we found for the evolution of quasiparticle occupation numbers, is almost entirely masked by the large oscillations that dominate the short-time dynamics, before prethermalization. If we zoom in closely, we notice a small difference of the order of 1% between the two predictions. This provides our most convincing justification for the application of the kinetic equations from immediately after the interaction ramp, provided distances of the order of the healing length are targeted.

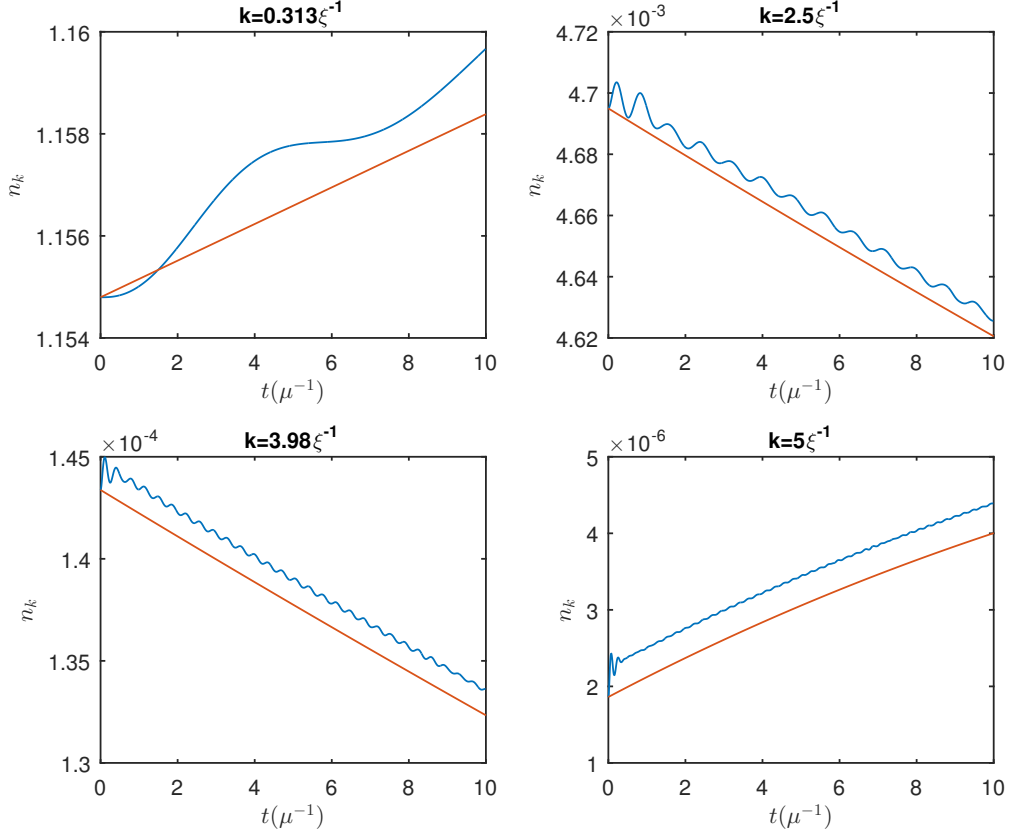


Figure C.3: A comparison of the quasiparticle occupation numbers $n_{\mathbf{k}}$ as produced by the integration of the hierarchy of correlation functions (blue lines) and the derived kinetic equation in the adiabatic limit (red lines) for the quench $g_i = 0 \rightarrow g_f = 0.05\mu\xi^3$ (corresponding to $n\xi^3 = 20$) in $\tau_s = 0.5\mu^{-1}$ (see initial momentum distribution on Fig. 9.3 of the main text). At low momenta, we notice a significant difference between the two predictions. At high momenta, however, the two results lie close to each other and the HOC produces a fast initial oscillation that then dephases, justifying the application of the kinetic description from right after the quench when short distances are considered. We used $N_k = 128$ and $N_c = 200$ with $k_{\max} = 10/\xi$.

C.4. Comparison between the hierarchy and the kinetic equations

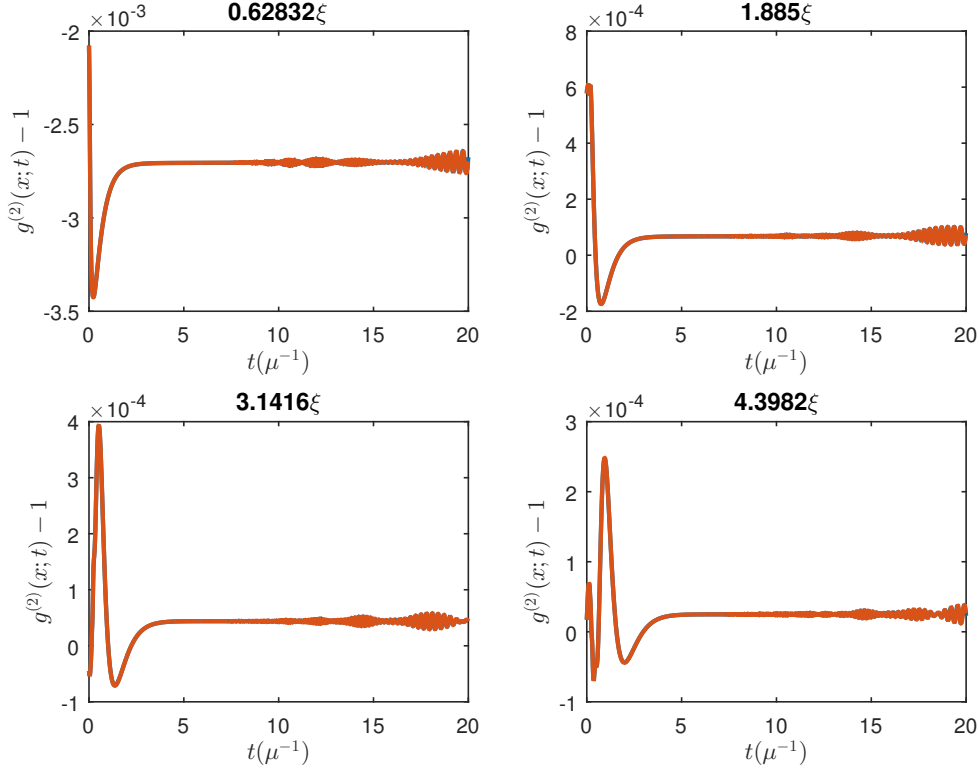


Figure C.4: The density-density correlations at short times for different distances, as indicated above the figures, after the ramp $g_i = 0 \rightarrow g_f = 0.05\mu\xi^3$ in $\tau_s = 0.5/\mu$. The blue line is the result obtained with the kinetic description and the red line with the full hierarchy. The same grid, composed of 256 radial modes, was used for the two simulations. As seen, both results cannot be distinguished with the bare eye. However, if we zoom in we find a difference of $\sim 1\%$. The fast oscillations at later times are due to an upcoming partial revival of this smaller system, expected to occur at $t \approx 26/\mu$ (corresponding to the slowest quasiparticle frequency). We need the smaller system for the integration of the hierarchy, but apart from that the parameters are the same as in Fig. 9.4 from the main text. Notice that $g^{(2)}(x; t = 0) \neq 0$ since we do not plot the evolution during the interaction ramp when $g^{(2)}(x; t)$ starts building up already. We used $N_k = 256$ and $N_c = 70$ with $k_{\max} = 10/\xi$.

Bibliography

- [1] A. Polkovnikov, K. Sengupta, A. Silva, and M. Vengalattore, “Colloquium,” *Rev. Mod. Phys.*, vol. 83, pp. 863–883, Aug 2011.
- [2] M. B. Hastings and T. Koma, “Spectral gap and exponential decay of correlations,” *Communications in Mathematical Physics*, vol. 265, pp. 781–804, Aug 2006.
- [3] M. B. Hastings, “An area law for one-dimensional quantum systems,” *Journal of Statistical Mechanics: Theory and Experiment*, vol. 2007, no. 08, p. P08024, 2007.
- [4] J. Eisert, M. Cramer, and M. B. Plenio, “Colloquium,” *Rev. Mod. Phys.*, vol. 82, pp. 277–306, Feb 2010.
- [5] S. R. White, “Density matrix formulation for quantum renormalization groups,” *Phys. Rev. Lett.*, vol. 69, pp. 2863–2866, Nov 1992.
- [6] F. Verstraete and J. I. Cirac, “Matrix product states represent ground states faithfully,” *Phys. Rev. B*, vol. 73, p. 094423, Mar 2006.
- [7] U. Schollwöck, “The density-matrix renormalization group,” *Reviews of modern physics*, vol. 77, no. 1, p. 259, 2005.
- [8] D. Perez-Garcia, F. Verstraete, M. M. Wolf, and J. I. Cirac, “Matrix product state representations,” *arXiv preprint quant-ph/0608197*, 2006.
- [9] D. Vodola, L. Lepori, E. Ercolessi, and G. Pupillo, “Long-range ising and kitaev models: phases, correlations and edge modes,” *New Journal of Physics*, vol. 18, no. 1, p. 015001, 2015.
- [10] D. Vodola, L. Lepori, E. Ercolessi, A. V. Gorshkov, and G. Pupillo, “Kitaev chains with long-range pairing,” *Phys. Rev. Lett.*, vol. 113, p. 156402, Oct 2014.
- [11] S. Bravyi, M. Hastings, and F. Verstraete, “Lieb-robinson bounds and the generation of correlations and topological quantum order,” *Physical review letters*, vol. 97, no. 5, p. 050401, 2006.
- [12] J. Eisert and T. J. Osborne, “General entanglement scaling laws from time evolution,” *Phys. Rev. Lett.*, vol. 97, p. 150404, Oct 2006.

- [13] A. Polkovnikov, “Microscopic diagonal entropy and its connection to basic thermodynamic relations,” *Annals of Physics*, vol. 326, no. 2, pp. 486–499, 2011.
- [14] J. M. Deutsch, “Quantum statistical mechanics in a closed system,” *Physical Review A*, vol. 43, no. 4, p. 2046, 1991.
- [15] M. Srednicki, “Chaos and quantum thermalization,” *Physical Review E*, vol. 50, no. 2, p. 888, 1994.
- [16] M. Rigol, V. Dunjko, and M. Olshanii, “Thermalization and its mechanism for generic isolated quantum systems,” *Nature*, vol. 452, no. 7189, pp. 854–858, 2008.
- [17] M. Rigol, “Quantum quenches and thermalization in one-dimensional fermionic systems,” *Physical Review A*, vol. 80, no. 5, p. 053607, 2009.
- [18] J.-S. Caux and F. H. Essler, “Time evolution of local observables after quenching to an integrable model,” *Physical review letters*, vol. 110, no. 25, p. 257203, 2013.
- [19] M. Rigol, V. Dunjko, V. Yurovsky, and M. Olshanii, “Relaxation in a completely integrable many-body quantum system: an ab initio study of the dynamics of the highly excited states of 1d lattice hard-core bosons,” *Physical review letters*, vol. 98, no. 5, p. 050405, 2007.
- [20] E. T. Jaynes, “Information theory and statistical mechanics,” *Physical review*, vol. 106, no. 4, p. 620, 1957.
- [21] D. Poilblanc, T. Ziman, J. Bellissard, F. Mila, and G. Montambaux, “Poisson vs. goe statistics in integrable and non-integrable quantum hamiltonians,” *EPL (Europhysics Letters)*, vol. 22, no. 7, p. 537, 1993.
- [22] A. Pal and D. A. Huse, “Many-body localization phase transition,” *Physical Review B*, vol. 82, no. 17, p. 174411, 2010.
- [23] T. Dauxois, S. Ruffo, E. Arimondo, and M. Wilkens, “Dynamics and thermodynamics of systems with long-range interactions: An introduction,” in *Dynamics and Thermodynamics of Systems with Long-Range Interactions*, pp. 1–19, Springer, 2002.
- [24] P. Pfeuty, “The one-dimensional ising model with a transverse field,” *ANNALS of Physics*, vol. 57, no. 1, pp. 79–90, 1970.
- [25] G. Mussardo, *Statistical field theory: an introduction to exactly solved models in statistical physics*. Oxford University Press, 2010.
- [26] S. Sachdev, *Quantum phase transitions*. Wiley Online Library, 2007.

Bibliography

- [27] E. Lieb, T. Schultz, and D. Mattis, “Two soluble models of an antiferromagnetic chain,” in *Condensed Matter Physics and Exactly Soluble Models*, pp. 543–601, Springer, 2004.
- [28] E. Fradkin, “Jordan-wigner transformation for quantum-spin systems in two dimensions and fractional statistics,” *Physical review letters*, vol. 63, no. 3, p. 322, 1989.
- [29] P. Jordan and E. P. Wigner, “über das paulische äquivalenzverbot,” in *The Collected Works of Eugene Paul Wigner*, pp. 109–129, Springer, 1993.
- [30] P. Calabrese, F. H. L. Essler, and M. Fagotti, “Quantum quench in the transverse-field ising chain,” *Phys. Rev. Lett.*, vol. 106, p. 227203, Jun 2011.
- [31] A. Y. Kitaev, “Unpaired majorana fermions in quantum wires,” *Physics-Uspekhi*, vol. 44, no. 10S, p. 131, 2001.
- [32] D. Porras and J. I. Cirac, “Effective quantum spin systems with trapped ions,” *Physical review letters*, vol. 92, no. 20, p. 207901, 2004.
- [33] M. Van Regemortel, D. Sels, and M. Wouters, “Information propagation and equilibration in long-range kitaev chains,” *Phys. Rev. A*, vol. 93, p. 032311, Mar 2016.
- [34] A. S. Buyskikh, M. Fagotti, J. Schachenmayer, F. Essler, and A. J. Daley, “Entanglement growth and correlation spreading with variable-range interactions in spin and fermionic tunneling models,” *Physical Review A*, vol. 93, no. 5, p. 053620, 2016.
- [35] M. Foss-Feig, Z.-X. Gong, C. W. Clark, and A. V. Gorshkov, “Nearly linear light cones in long-range interacting quantum systems,” *Phys. Rev. Lett.*, vol. 114, p. 157201, Apr 2015.
- [36] E. H. Lieb and D. W. Robinson, “The finite group velocity of quantum spin systems,” in *Statistical Mechanics*, pp. 425–431, Springer, 1972.
- [37] B. Nachtergaele, H. Raz, B. Schlein, and R. Sims, “Lieb-robinson bounds for harmonic and anharmonic lattice systems,” *Communications in mathematical physics*, vol. 286, no. 3, pp. 1073–1098, 2009.
- [38] P. Calabrese and J. Cardy, “Time dependence of correlation functions following a quantum quench,” *Physical review letters*, vol. 96, no. 13, p. 136801, 2006.
- [39] A. Einstein, B. Podolsky, and N. Rosen, “Can quantum-mechanical description of physical reality be considered complete?,” *Physical review*, vol. 47, no. 10, p. 777, 1935.
- [40] Z.-X. Gong, M. Foss-Feig, S. Michalakis, and A. V. Gorshkov, “Persistence of locality in systems with power-law interactions,” *Phys. Rev. Lett.*, vol. 113, p. 030602, Jul 2014.

- [41] G.-C. Wick, “The evaluation of the collision matrix,” *Physical review*, vol. 80, no. 2, p. 268, 1950.
- [42] I. Peschel, “Calculation of reduced density matrices from correlation functions,” *Journal of Physics A: Mathematical and General*, vol. 36, no. 14, p. L205, 2003.
- [43] J. Schachenmayer, B. Lanyon, C. Roos, and A. Daley, “Entanglement growth in quench dynamics with variable range interactions,” *Physical Review X*, vol. 3, no. 3, p. 031015, 2013.
- [44] M. G. Nezhadhighi and M. Rajabpour, “Entanglement dynamics in short-and long-range harmonic oscillators,” *Physical Review B*, vol. 90, no. 20, p. 205438, 2014.
- [45] M. M. Wolf, F. Verstraete, M. B. Hastings, and J. I. Cirac, “Area laws in quantum systems: Mutual information and correlations,” *Phys. Rev. Lett.*, vol. 100, p. 070502, Feb 2008.
- [46] L. Cevolani, G. Carleo, and L. Sanchez-Palencia, “Protected quasilocality in quantum systems with long-range interactions,” *Phys. Rev. A*, vol. 92, p. 041603, Oct 2015.
- [47] D. Sels and M. Wouters, “Stationary ensemble approximations of dynamic quantum states: Optimizing the generalized gibbs ensemble,” *Phys. Rev. E*, vol. 92, p. 022123, Aug 2015.
- [48] J. Eisert, M. Friesdorf, and C. Gogolin, “Quantum many-body systems out of equilibrium,” *Nature Physics*, vol. 11, no. 2, pp. 124–130, 2015.
- [49] B. Rauer, S. Erne, T. Schweigler, F. Cataldini, M. Tajik, and J. Schmiedmayer, “Recurrences in an isolated quantum many-body system,” *arXiv preprint arXiv:1705.08231*, 2017.
- [50] T. Langen, S. Erne, R. Geiger, B. Rauer, T. Schweigler, M. Kuhnert, W. Rohringer, I. E. Mazets, T. Gasenzer, and J. Schmiedmayer, “Experimental observation of a generalized gibbs ensemble,” *Science*, vol. 348, no. 6231, pp. 207–211, 2015.
- [51] W. Verstraelen, D. Sels, and M. Wouters, “Unitary work extraction from a generalized gibbs ensemble using bragg scattering,” *Phys. Rev. A*, vol. 96, p. 023605, Aug 2017.
- [52] J. W. Britton, B. C. Sawyer, A. C. Keith, C.-C. J. Wang, J. K. Freericks, H. Uys, M. J. Biercuk, and J. J. Bollinger, “Engineered two-dimensional ising interactions in a trapped-ion quantum simulator with hundreds of spins,” *Nature*, vol. 484, no. 7395, pp. 489–492, 2012.
- [53] P. Jurcevic, B. P. Lanyon, P. Hauke, C. Hempel, P. Zoller, R. Blatt, and C. F. Roos, “Quasiparticle engineering and entanglement propagation in a quantum many-body system,” *Nature*, vol. 511, no. 7508, pp. 202–205, 2014.

Bibliography

- [54] M. Cheneau, P. Barmettler, D. Poletti, M. Endres, P. Schauß, T. Fukuhara, C. Gross, I. Bloch, C. Kollath, and S. Kuhr, “Light-cone-like spreading of correlations in a quantum many-body system,” *Nature*, vol. 481, no. 7382, pp. 484–487, 2012.
- [55] D. Jaksch, C. Bruder, J. I. Cirac, C. W. Gardiner, and P. Zoller, “Cold bosonic atoms in optical lattices,” *Phys. Rev. Lett.*, vol. 81, pp. 3108–3111, Oct 1998.
- [56] E. H. Lieb and W. Liniger, “Exact analysis of an interacting bose gas. i. the general solution and the ground state,” *Physical Review*, vol. 130, no. 4, p. 1605, 1963.
- [57] E. H. Lieb, “Exact analysis of an interacting bose gas. ii. the excitation spectrum,” in *Condensed Matter Physics and Exactly Soluble Models*, pp. 617–625, Springer, 2004.
- [58] E. H. Lieb, R. Seiringer, and J. Yngvason, “One-dimensional bosons in three-dimensional traps,” in *The Stability of Matter: From Atoms to Stars*, pp. 909–912, Springer, 2003.
- [59] H.-P. Breuer and F. Petruccione, *The theory of open quantum systems*. Oxford University Press on Demand, 2002.
- [60] J. Dalibard, Y. Castin, and K. Mølmer, “Wave-function approach to dissipative processes in quantum optics,” *Physical review letters*, vol. 68, no. 5, p. 580, 1992.
- [61] T. Sauter, W. Neuhauser, R. Blatt, and P. Toschek, “Observation of quantum jumps,” *Physical review letters*, vol. 57, no. 14, p. 1696, 1986.
- [62] S. Gleyzes, S. Kuhr, C. Guerlin, J. Bernu, S. Deleglise, U. B. Hoff, M. Brune, J.-M. Raimond, and S. Haroche, “Quantum jumps of light recording the birth and death of a photon in a cavity,” *Nature*, vol. 446, no. 7133, pp. 297–300, 2007.
- [63] S. Finazzi, A. Le Boité, F. Storme, A. Baksic, and C. Ciuti, “Corner-space renormalization method for driven-dissipative two-dimensional correlated systems,” *Physical review letters*, vol. 115, no. 8, p. 080604, 2015.
- [64] F. Verstraete, J. J. Garcia-Ripoll, and J. I. Cirac, “Matrix product density operators: simulation of finite-temperature and dissipative systems,” *Physical review letters*, vol. 93, no. 20, p. 207204, 2004.
- [65] R. Orus and G. Vidal, “Infinite time-evolving block decimation algorithm beyond unitary evolution,” *Physical Review B*, vol. 78, no. 15, p. 155117, 2008.
- [66] H. Weimer, “Variational principle for steady states of dissipative quantum many-body systems,” *Phys. Rev. Lett.*, vol. 114, p. 040402, Jan 2015.
- [67] J. Cui, J. I. Cirac, and M. C. Banuls, “Variational matrix product operators for the steady state of dissipative quantum systems,” *Physical review letters*, vol. 114, no. 22, p. 220601, 2015.

- [68] E. Mascarenhas, H. Flayac, and V. Savona, “Matrix-product-operator approach to the nonequilibrium steady state of driven-dissipative quantum arrays,” *Physical Review A*, vol. 92, no. 2, p. 022116, 2015.
- [69] C. Gardiner and P. Zoller, *Quantum noise: a handbook of Markovian and non-Markovian quantum stochastic methods with applications to quantum optics*, vol. 56. Springer Science & Business Media, 2004.
- [70] H. Paul, “Photon antibunching,” *Rev. Mod. Phys.*, vol. 54, pp. 1061–1102, Oct 1982.
- [71] R. H. Brown and R. Q. Twiss, “A test of a new type of stellar interferometer on sirius,” *Nature*, vol. 178, no. 4541, pp. 1046–1048, 1956.
- [72] R. H. Brown and R. Q. Twiss, “Correlation between photons in two coherent beams of light,” *Nature*, vol. 177, no. 4497, pp. 27–29, 1956.
- [73] K. M. Birnbaum, A. Boca, R. Miller, A. D. Boozer, T. E. Northup, and H. J. Kimble, “Photon blockade in an optical cavity with one trapped atom,” *Nature*, vol. 436, no. 7047, pp. 87–90, 2005.
- [74] A. Imamolu, H. Schmidt, G. Woods, and M. Deutsch, “Strongly interacting photons in a nonlinear cavity,” *Physical Review Letters*, vol. 79, no. 8, p. 1467, 1997.
- [75] A. Faraon, I. Fushman, D. Englund, N. Stoltz, P. Petroff, and J. Vučković, “Coherent generation of non-classical light on a chip via photon-induced tunnelling and blockade,” *Nature Physics*, vol. 4, no. 11, pp. 859–863, 2008.
- [76] A. Reinhard, T. Volz, M. Winger, A. Badolato, K. J. Hennessy, E. L. Hu, and A. Imamoglu, “Strongly correlated photons on a chip,” *Nature Photonics*, vol. 6, no. 2, pp. 93–96, 2012.
- [77] A. J. Hoffman, S. J. Srinivasan, S. Schmidt, L. Spietz, J. Aumentado, H. E. Türeci, and A. A. Houck, “Dispersive photon blockade in a superconducting circuit,” *Physical review letters*, vol. 107, no. 5, p. 053602, 2011.
- [78] C. Lang, D. Bozyigit, C. Eichler, L. Steffen, J. Fink, A. Abdumalikov Jr, M. Baur, S. Philipp, M. da Silva, A. Blais, *et al.*, “Observation of resonant photon blockade at microwave frequencies using correlation function measurements,” *Physical review letters*, vol. 106, no. 24, p. 243601, 2011.
- [79] C. Noh and D. G. Angelakis, “Quantum simulations and many-body physics with light,” *Reports on Progress in Physics*, vol. 80, no. 1, p. 016401, 2016.
- [80] M. J. Hartmann, “Quantum simulation with interacting photons,” *Journal of Optics*, vol. 18, no. 10, p. 104005, 2016.

Bibliography

- [81] M. Bamba, A. Imamoğlu, I. Carusotto, and C. Ciuti, “Origin of strong photon antibunching in weakly nonlinear photonic molecules,” *Phys. Rev. A*, vol. 83, p. 021802, Feb 2011.
- [82] G. Muñoz-Matutano, A. Wood, M. Johnson, X. V. Asensio, B. Baragiola, A. Reinhard, A. Lemaitre, J. Bloch, A. Amo, B. Besga, *et al.*, “Quantum-correlated photons from semiconductor cavity polaritons,” *arXiv preprint arXiv:1712.05551*, 2017.
- [83] T. C. H. Liew and V. Savona, “Single photons from coupled quantum modes,” *Phys. Rev. Lett.*, vol. 104, p. 183601, May 2010.
- [84] H. Flayac and V. Savona, “Input-output theory of the unconventional photon blockade,” *Physical Review A*, vol. 88, no. 3, p. 033836, 2013.
- [85] H. Flayac, D. Gerace, and V. Savona, “An all-silicon single-photon source by unconventional photon blockade,” *Scientific reports*, vol. 5, p. srep11223, 2015.
- [86] H. Flayac and V. Savona, “Unconventional photon blockade,” *Physical Review A*, vol. 96, no. 5, p. 053810, 2017.
- [87] I. Carusotto and C. Ciuti, “Quantum fluids of light,” *Reviews of Modern Physics*, vol. 85, no. 1, p. 299, 2013.
- [88] M.-A. Lemonde, N. Didier, and A. A. Clerk, “Antibunching and unconventional photon blockade with gaussian squeezed states,” *Physical Review A*, vol. 90, no. 6, p. 063824, 2014.
- [89] J. Keeling, F. Marchetti, M. Szymańska, and P. Littlewood, “Collective coherence in planar semiconductor microcavities,” *Semiconductor science and technology*, vol. 22, no. 5, p. R1, 2007.
- [90] M. Baeten, *Microcavity polaritons in the presence of a two-dimensional electron gas*. PhD thesis, University of Antwerp, 2015.
- [91] S. Koghee, *The dynamical Casimir effect in exciton-polariton quantum fluids*. PhD thesis, University of Antwerp, 2016.
- [92] M. V. Regemortel, “Binary polariton fluids,” 2013.
- [93] J. Kasprzak, M. Richard, S. Kundermann, A. Baas, P. Jeambrun, J. Keeling, F. Marchetti, M. Szymańska, R. Andre, J. Staehli, *et al.*, “Bose–einstein condensation of exciton polaritons,” *Nature*, vol. 443, no. 7110, pp. 409–414, 2006.
- [94] J. Baumberg, P. Savvidis, R. Stevenson, A. Tartakovskii, M. Skolnick, D. Whittaker, and J. Roberts, “Parametric oscillation in a vertical microcavity: A polariton condensate or micro-optical parametric oscillation,” *Physical Review B*, vol. 62, no. 24, p. R16247, 2000.

- [95] J. Lebreuilly, M. Wouters, and I. Carusotto, “Towards strongly correlated photons in arrays of dissipative nonlinear cavities under a frequency-dependent incoherent pumping,” *Comptes Rendus Physique*, vol. 17, no. 8, pp. 836–860, 2016.
- [96] P. Drummond and D. Walls, “Quantum theory of optical bistability. i. nonlinear polarisability model,” *Journal of Physics A: Mathematical and General*, vol. 13, no. 2, p. 725, 1980.
- [97] W. Casteels, F. Storme, A. Le Boité, and C. Ciuti, “Power laws in the dynamic hysteresis of quantum nonlinear photonic resonators,” *Physical Review A*, vol. 93, no. 3, p. 033824, 2016.
- [98] S. Rodriguez, W. Casteels, F. Storme, N. C. Zambon, I. Sagnes, L. Le Gratiet, E. Galopin, A. Lemaître, A. Amo, C. Ciuti, *et al.*, “Probing a dissipative phase transition via dynamical optical hysteresis,” *Physical Review Letters*, vol. 118, no. 24, p. 247402, 2017.
- [99] L. Pitaevskii and S. Stringari, *Bose-Einstein condensation and superfluidity*, vol. 164. Oxford University Press, 2016.
- [100] I. Carusotto and C. Ciuti, “Probing microcavity polariton superfluidity through resonant rayleigh scattering,” *Physical review letters*, vol. 93, no. 16, p. 166401, 2004.
- [101] A. Berceanu, E. Cancellieri, and F. Marchetti, “Drag in a resonantly driven polariton fluid,” *Journal of Physics: Condensed Matter*, vol. 24, no. 23, p. 235802, 2012.
- [102] M. Van Regemortel and M. Wouters, “Negative drag in nonequilibrium polariton quantum fluids,” *Physical Review B*, vol. 89, no. 8, p. 085303, 2014.
- [103] X. Busch, I. Carusotto, and R. Parentani, “Spectrum and entanglement of phonons in quantum fluids of light,” *Physical Review A*, vol. 89, no. 4, p. 043819, 2014.
- [104] S. L. Danilishin and F. Y. Khalili, “Quantum measurement theory in gravitational-wave detectors,” *Living Reviews in Relativity*, vol. 15, no. 1, p. 5, 2012.
- [105] B. P. Abbott, R. Abbott, T. Abbott, M. Abernathy, F. Acernese, K. Ackley, C. Adams, T. Adams, P. Addesso, R. Adhikari, *et al.*, “Observation of gravitational waves from a binary black hole merger,” *Physical review letters*, vol. 116, no. 6, p. 061102, 2016.
- [106] M. Van Regemortel, S. Ravets, A. Imamoglu, I. Carusotto, and M. Wouters, “Engineering gaussian states of light from a planar microcavity,” *arXiv preprint arXiv:1712.08012*, 2017.
- [107] S. Beliaev, “Energy spectrum of a non-ideal bose gas,” *Sov. Phys. JETP*, vol. 34, no. 2, p. 299, 1958.

Bibliography

- [108] N. Katz, J. Steinhauer, R. Ozeri, and N. Davidson, “Beliaev damping of quasiparticles in a bose-einstein condensate,” *Physical review letters*, vol. 89, no. 22, p. 220401, 2002.
- [109] P. Nozières and D. Pines, *Theory of quantum liquids*. Hachette UK, 1999.
- [110] L. Pitaevskii and S. Stringari, “Landau damping in dilute bose gases,” *Physics Letters A*, vol. 235, no. 4, pp. 398–402, 1997.
- [111] S. Giorgini, “Damping in dilute bose gases: A mean-field approach,” *Physical Review A*, vol. 57, no. 4, p. 2949, 1998.
- [112] G. Kónya, G. Szirmai, D. Nagy, and P. Domokos, “Photonic tuning of beliaev damping in a superfluid,” *Physical Review A*, vol. 89, no. 5, p. 051601, 2014.
- [113] H. Kurkjian, Y. Castin, and A. Sinatra, “Landau-khalatnikov phonon damping in strongly interacting fermi gases,” *EPL (Europhysics Letters)*, vol. 116, no. 4, p. 40002, 2016.
- [114] E. Hodby, O. Marago, G. Hechenblaikner, and C. Foot, “Experimental observation of beliaev coupling in a bose-einstein condensate,” *Physical review letters*, vol. 86, no. 11, p. 2196, 2001.
- [115] Z. Ristivojevic and K. Matveev, “Decay of bogoliubov excitations in one-dimensional bose gases,” *Physical Review B*, vol. 94, no. 2, p. 024506, 2016.
- [116] S. Tsuchiya and A. Griffin, “Damping of bogoliubov excitations in optical lattices,” *Physical Review A*, vol. 70, no. 2, p. 023611, 2004.
- [117] L. M. Sieberer, S. D. Huber, E. Altman, and S. Diehl, “Dynamical critical phenomena in driven-dissipative systems,” *Phys. Rev. Lett.*, vol. 110, p. 195301, May 2013.
- [118] T. Ramos, H. Pichler, A. J. Daley, and P. Zoller, “Quantum spin dimers from chiral dissipation in cold-atom chains,” *Phys. Rev. Lett.*, vol. 113, p. 237203, Dec 2014.
- [119] Y. Yanay and A. A. Clerk, “Reservoir engineering of bosonic lattices using chiral symmetry and localized dissipation,” *arXiv preprint arXiv:1710.10318*, 2017.
- [120] A. Amo and J. Bloch, “Exciton-polaritons in lattices: A non-linear photonic simulator,” *Comptes Rendus Physique*, vol. 17, no. 8, pp. 934 – 945, 2016. Polariton physics / Physique des polaritons.
- [121] M. Fitzpatrick, N. M. Sundaresan, A. C. Li, J. Koch, and A. A. Houck, “Observation of a dissipative phase transition in a one-dimensional circuit qed lattice,” *Physical Review X*, vol. 7, no. 1, p. 011016, 2017.
- [122] V. Bouchiat, D. Vion, P. Joyez, D. Esteve, and M. Devoret, “Quantum coherence with a single cooper pair,” *Physica Scripta*, vol. 1998, no. T76, p. 165, 1998.

- [123] J. Mooij, T. Orlando, L. Levitov, L. Tian, C. H. Van der Wal, and S. Lloyd, “Josephson persistent-current qubit,” *Science*, vol. 285, no. 5430, pp. 1036–1039, 1999.
- [124] J. M. Martinis, S. Nam, J. Aumentado, and C. Urbina, “Rabi oscillations in a large josephson-junction qubit,” *Physical review letters*, vol. 89, no. 11, p. 117901, 2002.
- [125] J. Koch, M. Y. Terri, J. Gambetta, A. A. Houck, D. Schuster, J. Majer, A. Blais, M. H. Devoret, S. M. Girvin, and R. J. Schoelkopf, “Charge-insensitive qubit design derived from the cooper pair box,” *Physical Review A*, vol. 76, no. 4, p. 042319, 2007.
- [126] M. H. Devoret, A. Wallraff, and J. M. Martinis, “Superconducting qubits: A short review,” *arXiv preprint cond-mat/0411174*, 2004.
- [127] A. A. Houck, H. E. Türeci, and J. Koch, “On-chip quantum simulation with superconducting circuits,” *Nature Physics*, vol. 8, no. 4, pp. 292–299, 2012.
- [128] E. Wigner, “On the quantum correction for thermodynamic equilibrium,” *Physical review*, vol. 40, no. 5, p. 749, 1932.
- [129] A. Polkovnikov, “Phase space representation of quantum dynamics,” *Annals of Physics*, vol. 325, no. 8, pp. 1790–1852, 2010.
- [130] K. Vogel and H. Risken, “Quasiprobability distributions in dispersive optical bistability,” *Physical Review A*, vol. 39, no. 9, p. 4675, 1989.
- [131] T. Köhler and K. Burnett, “Microscopic quantum dynamics approach to the dilute condensed bose gas,” *Phys. Rev. A*, vol. 65, p. 033601, Feb 2002.
- [132] J. O. Andersen, “Theory of the weakly interacting bose gas,” *Rev. Mod. Phys.*, vol. 76, pp. 599–639, Jul 2004.
- [133] F. Baboux, D. De Bernardis, V. Goblot, V. Gladilin, C. Gomez, E. Galopin, L. L. Gratiet, A. Lemaître, I. Sagnes, I. Carusotto, *et al.*, “Unstable and stable regimes of polariton condensation,” *arXiv preprint arXiv:1707.05798*, 2017.
- [134] S. Inouye, M. Andrews, J. Stenger, H.-J. Miesner, D. Stamper-Kurn, and W. Ketterle, “Observation of feshbach resonances in a bose–einstein condensate,” *Nature*, vol. 392, no. 6672, pp. 151–154, 1998.
- [135] C. Chin, R. Grimm, P. Julienne, and E. Tiesinga, “Feshbach resonances in ultracold gases,” *Rev. Mod. Phys.*, vol. 82, pp. 1225–1286, Apr 2010.
- [136] A. Rançon, C.-L. Hung, C. Chin, and K. Levin, “Quench dynamics in bose-einstein condensates in the presence of a bath: Theory and experiment,” *Phys. Rev. A*, vol. 88, p. 031601, Sep 2013.

Bibliography

- [137] A. Rançon and K. Levin, “Equilibrating dynamics in quenched bose gases: Characterizing multiple time regimes,” *Phys. Rev. A*, vol. 90, p. 021602, Aug 2014.
- [138] C.-L. Hung, V. Gurarie, and C. Chin, “From cosmology to cold atoms: observation of sakharov oscillations in a quenched atomic superfluid,” *Science*, p. 1237557, 2013.
- [139] A. Sinatra, Y. Castin, and E. Witkowska, “Coherence time of a bose-einstein condensate,” *Phys. Rev. A*, vol. 80, p. 033614, Sep 2009.
- [140] Y. Castin and R. Dum, “Low-temperature bose-einstein condensates in time-dependent traps: Beyond the $u(1)$ symmetry-breaking approach,” *Phys. Rev. A*, vol. 57, pp. 3008–3021, Apr 1998.
- [141] S. S. Natu and E. J. Mueller, “Dynamics of correlations in a dilute bose gas following an interaction quench,” *Phys. Rev. A*, vol. 87, p. 053607, May 2013.
- [142] G. Menegoz and A. Silva, “Prethermalization of weakly interacting bosons after a sudden interaction quench,” *Journal of Statistical Mechanics: Theory and Experiment*, vol. 2015, no. 5, p. P05035, 2015.
- [143] I. Carusotto, R. Balbinot, A. Fabbri, and A. Recati, “Density correlations and analog dynamical casimir emission of bogoliubov phonons in modulated atomic bose-einstein condensates,” *The European Physical Journal D-Atomic, Molecular, Optical and Plasma Physics*, vol. 56, no. 3, pp. 391–404, 2010.
- [144] V. Dodonov, “Current status of the dynamical casimir effect,” *Physica Scripta*, vol. 82, no. 3, p. 038105, 2010.
- [145] G. T. Moore, “Quantum theory of the electromagnetic field in a variable-length one-dimensional cavity,” *Journal of Mathematical Physics*, vol. 11, no. 9, pp. 2679–2691, 1970.
- [146] S. Koghee and M. Wouters, “Dynamical casimir emission from polariton condensates,” *Physical review letters*, vol. 112, no. 3, p. 036406, 2014.
- [147] C. Wilson, G. Johansson, A. Pourkabirian, M. Simoen, J. Johansson, T. Duty, F. Nori, and P. Delsing, “Observation of the dynamical casimir effect in a superconducting circuit,” *Nature*, vol. 479, no. 7373, pp. 376–379, 2011.
- [148] I. Carusotto, S. Fagnocchi, A. Recati, R. Balbinot, and A. Fabbri, “Numerical observation of hawking radiation from acoustic black holes in atomic bose–einstein condensates,” *New Journal of Physics*, vol. 10, no. 10, p. 103001, 2008.
- [149] R. Balbinot, A. Fabbri, S. Fagnocchi, A. Recati, and I. Carusotto, “Nonlocal density correlations as a signature of hawking radiation from acoustic black holes,” *Physical Review A*, vol. 78, no. 2, p. 021603, 2008.

- [150] J. Steinhauer, “Observation of quantum hawking radiation and its entanglement in an analogue black hole,” *Nature Physics*, vol. 12, no. 10, p. 959, 2016.
- [151] E. Altman, E. Demler, and M. D. Lukin, “Probing many-body states of ultracold atoms via noise correlations,” *Physical Review A*, vol. 70, no. 1, p. 013603, 2004.
- [152] M. Van Regemortel, W. Casteels, I. Carusotto, and M. Wouters, “Spontaneous beliaev-landau scattering out of equilibrium,” *Phys. Rev. A*, vol. 96, p. 053854, Nov 2017.
- [153] M. Van Regemortel, H. Kurkjian, I. Carusotto, and M. Wouters, “Prethermalization to thermalization crossover in a dilute bose gas following an interaction ramp,” *arXiv preprint arXiv:1803.07459*, 2018.
- [154] W. Casteels, S. Finazzi, A. Le Boité, F. Storme, and C. Ciuti, “Truncated correlation hierarchy schemes for driven-dissipative multimode quantum systems,” *New Journal of Physics*, vol. 18, no. 9, p. 093007, 2016.